GEOTECHNOLOGIEN

GEOTECHNOLOGIEN
Science Report

Mineral Surfaces – From Atomic Processes to Industrial Application

Status Seminar
26-27 October 2010
Johannes-Gutenberg-Universität
Mainz

Programme & Abstracts

No. 16

GEOTECHNOLOGIEN
Science Report

Mineral Surfaces – From Atomic Processes to Industrial Application

Status Seminar
26-27 October 2010
Johannes-Gutenberg-Universität, Mainz

Programme & Abstracts

No. 16

Impressum

Editorship / Schriftleitung
Dr. Ute Münch, Werner Dransch

ISSN 1619-7399

Die Deutsche Bibliothek – CIP Einheitsaufnahme

GEOTECHNOLOGIEN
Mineral Surfaces – From Atomic Processes to Industrial Application
Status Seminar
26-27 October 2010
Johannes Gutenberg-Universität Mainz
Programme & Abstracts –
Potsdam: Koordinierungsbüro GEOTECHNOLOGIEN, 2010
(GEOTECHNOLOGIEN Science Report No. 16)
ISSN 1619-7399

Distribution / Bezug
Koordinierungsbüro GEOTECHNOLOGIEN
Telegrafenberg
14473 Potsdam, Germany
Fon +49 (0)331-288 10 71
Fax +49 (0)331-288 10 77
www.geotechnologien.de
geotech@gfz-potsdam.de

Preface

Processes of the mineral surfaces take place at atomic and molecular length scales. Elementary reactions such as dissolution and the growth and mineral transformations, adsorption and ion exchange are important for a variety of geological processes. Even with technical procedures weathering reactions are taken advantage of: e.g. in fixation of pollutants on mineral surfaces, in corrosion processes, or in the activation and making of industrial minerals more functional.
The aim of the research is to understand and quantitatively assess mineral surfaces in their full complexity in terms of new processes and products to alter chemical, physical and biological functionalization. Clay minerals are of particular interest due to their specific charge distributions. Also biotechnological processing procedures and the development of bioactive mineral surfaces are investigated.

The understanding of all these different processes and reactions is expected to find new economic possibilities to clean drinking water in polluted areas, improving ceramics and other consumer goods as well as to discover new bone replacement materials.
Since April 2008 thirteen collaborative projects on the topic of »mineral surfaces« have been funded by the Federal Ministry of Education and Research (BMBF) with a volume of nearly 8 million Euros.

The main objective of the status seminar is to bring scientists and industrial partners together to discuss new ideas and find new possibilities for cooperation and synergies.

Ute Münch
Hartmut Fueß

Table of Contents

Scientific Program
Status Seminar »Mineral Surfaces«
26–27 October 2010, Universität Mainz

26. October 2010

13.00 – 13.15	Welcome
13.15 – 14.00	HYDROPHOBINS – Using hydrophobins to prevent microbial biofilm growth on mineral surfaces
14.00 – 14.45	BioMin – Functionalized mineral surfaces: Sorption mechanisms of growth-stimulating proteins on surfaces of bone substitutes based on calcium phosphates
14.45 – 15.30	HydraSmec – Understanding processes at the hot smectite-water interface for tailoring industrial bentonite applications
15.30 – 16.00	*Coffee and Poster*
16.00 – 16.45	The impact of mineral and rock surface topography on colloid retention
16.45 – 17.30	Surface and Wetting Properties of Diagenetic Minerals and Sedimentary Grains in Reservoir Rocks (NanoPorO)
17.30 – 18.15	Reactivity of Calcite/Water-Interfaces (RECAWA):Molecular level process understanding for technical applications
18.15 – 19.00	Identification and modification of the surface properties of calcite fillers as a basis for new, highly filled adhesives
about **19.30**	*Dinner*

27. October 2010

08.30 – 09.15	InProTunnel: Interfacial Processes between Mineral and Tool Surfaces – Causes, Problems and Solutions in Mechanical Tunnel Driving
09.15 – 10.00	SIMSAN – Simulation-supported development of process-stable raw material components and suspensions for the production of ceramic sanitary ware on the basis of modified mineral surfaces
10.00 – 10.45	Control mechanisms of clays and their specific surface area in growing media – assessment of clay properties and their parametrization for the optimization of plant quality
10.45 – 11.15	*Coffee Break*
11.15 – 12.00	SURFTRAP – Development and Optimisation of a Process to Biosynthesize Reactive Iron Mineral Surfaces for Water Treatment Purposes
12.00 – 12.45	MicroActiv – Optimization of water purification technology for arsenic and antimony scavenging by microbially-activated Fe-oxide minerals
12.45 – 13.30	Microstructural Controls on Monosulfide Weathering and Heavy Metal Release (MIMOS)
13.30 – 13.45	*Final Discussion*

HYDROPHOBINS – Using hydrophobins to prevent microbial biofilm growth on mineral surfaces

Rieder A. (1), Schwartz T. (1), Obst U. (1), Bollschweiler C. (2), Gutt B. (3), Zoller J. (3), Fischer R. (3)*

(1) Department of Microbiology of Natural and Technical Surfaces, Institute of Functional Interfaces (IFG), Karlsruhe Institute of Technology (KIT), e-mail: thomas.schwartz@kit.edu

(2) BASF SE, e-mail: claus.bollschweiler@basf.com

(3) Department of Microbiology, Institute for Applied Biosciences, Karlsruhe Institute of Technology (KIT) e-mail: reinhard.fischer@kit.edu

*Coordinator of the project

Introduction

Microbial biofilms are an extremely successful way of life. Bacteria and fungi benefit in this symbiotic life form of metabolic exchange, protection and genetic flexibility. They produce a matrix of organic molecules in which they are embedded and which offers new habitats to other organisms, such as other bacteria or fungi. Biofilms cannot be avoided to colonize surfaces in unsterile habitats. So, they can be found everywhere in nature and in technical systems, but they play an ambivalent role. On the one hand biofilms are essential to degrade and transform water contaminations, but on the other hand they can diminish product qualities and damage capital equipment. Biofilms can cover medical equipment such as catheters and pathogenic bacteria, which may be living in the biofilms, are a continuous source of infection of the patients. In addition, the metabolism of the biofilm microorganisms may change the composition of the fluids or contaminate them with their products. As biofilms are all-round, the understanding of the biofilm formation and its manipulation are of prime importance in microbiology and material sciences.

The choice of a material and the corresponding surface properties like mechanical properties, structure, polarity, and chemistry influence the binding of various molecules and cells. The surface properties affect the biocompatibility of a material and consequently also bacterial adhesion, and biofilm growth. In this project hydrophobins are used as a novel modification of surfaces to change surface properties like hydrophobicity and thus might have an effect on biofilm formation.

Hydrophobins are fungal proteins, which self-assemble on hydrophobic as well as hydrophilic surfaces into extremely stable monolayers. Recombinant hydrophobins provide the opportunity to use these highly surface-active proteins for large-scale surface coatings. Hydrophobins are non-toxic and can be used for surface modification and functionalization (with e.g. enzymes) of industrial relevant materials like steel, plastics, and ceramics.

In this project hydrophobin coated surfaces and their properties are studied with respect to bacterial cell adhesion, cell differentiation, and cellular growth with the aim to influence biofilm formation.

In the first part of the project recombinant hydrophobins were produced and purified. Different surfaces were coated with hydrophobins and characterized, since the coating efficiency is the basis for subsequent biofilm formation studies. Biofilms were grown on natural as well as hydrophobin coated surfaces and different methods were established to analyse biofilm formation.

Since the hydrophobin coated surfaces did not reduce microbial growth, we designed modified fusion hydrophobins and attached cationic antimicrobial peptides (AMPs) to the hydrophobins.

1. Hydrophobins

Hydrophobins are small proteins with about 100 amino acids, which are produced by filamentous fungi. In nature they coat the surface of fungal spores to ease the growth out of the ground and to protect the spore itself. It is recently known that hydrophobins also prevent the human immune recognition of airborne fungal spores.

There are two classes of hydrophobins, which only differ in the arrangement of eight highly conserved cysteine residues. Self-assembled monolayers formed by class I hydrophobins are more stable than those formed by class II hydrophobins. For our research we are using DewA, which is produced by *Aspergillus nidulans* and belongs to the class I hydrophobins. Since hydrophobins are highly surface-active they can easily be used for surface modification and functionalization. Until recently, the use of hydrophobins for large-scale surface coatings has been prevented by the fact that they had to be isolated from fungal cultures in a lengthy process. Recently the BASF SE achieved a breakthrough and established an expression system for the large-scale production of hydrophobins.

1.1 Fusion hydrophobins

Based on the large-scale industrial production, it is now possible to obtain large amounts of hydrophobins in a comparatively short time, but due to their characteristics, the hydrophobins had to be produced as so called fusion hydrophobins. The BASF SE provides two fusion hydrophobins for surface coating. The available fusion hydrophobins are composed of the class I hydrophobin DewA of *Aspergillus nidulans* and a fusion partner. The fusion partner is the synthase yaaD of *Bacillus subtilis* in complete respectively shortened form (Figure 1). The synthase is used to lead the hydrophobin into the inclusion bodies in *Escherichia coli* for the purification. H*Protein B has the shortest version of yaaD which still works as a leader. The fusion hydrophobins have a mass of 47 kDa respectively 19 kDa, whereas the hydrophobin part itself has a mass of only 10 kDa. In fusion hydrophobin H*Protein A the hydrophobin part forms 20%, in H*Protein B 50% of the total protein mass.

1.2 Modification of the fusion hydrophobins

Because of the lack of being antimicrobial by itself, we modified the fusion hydrophobins. We used cationic antimicrobial peptides (AMPs), which are only 9 to 50 amino acids in size and are proven to be active against bacteria and even against yeasts and filamentous fungi. They are an alternative to antibiotics and do not affect human cells. Until now there is no resistance known. The AMPs were fused to the N-terminus of the long and short version of the *yaaD* in the expression vector pQE60 (Figure 2). The modified plasmids (pHHC-011, pHHC-012, pF1-011 and pF1-012) were transformed into *E. coli* BL21. The induction of the expression was performed with 0.5mM IPTG (Isopropyl β-D-1-thiogalactopyranoside) at OD_{600} 0.6 to 1.0; we let the culture grow over night. The purification of the modified fusion hydrophobins

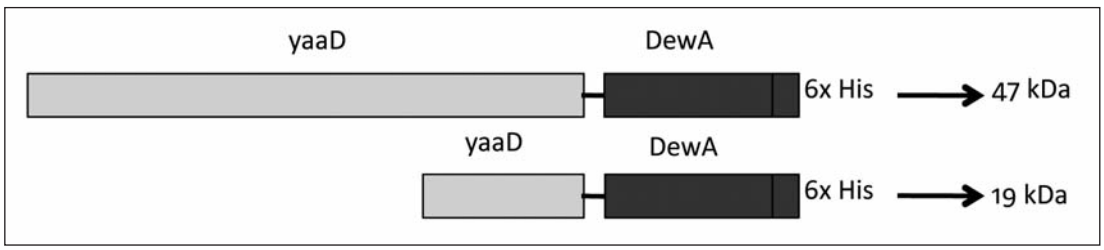

Figure 1: The fusion hydrophobins consist of the synthase yaaD in complete (H*Protein A) respectively shortened (H*Protein B) form, the class I hydrophobin DewA and a C-terminal His-tag.

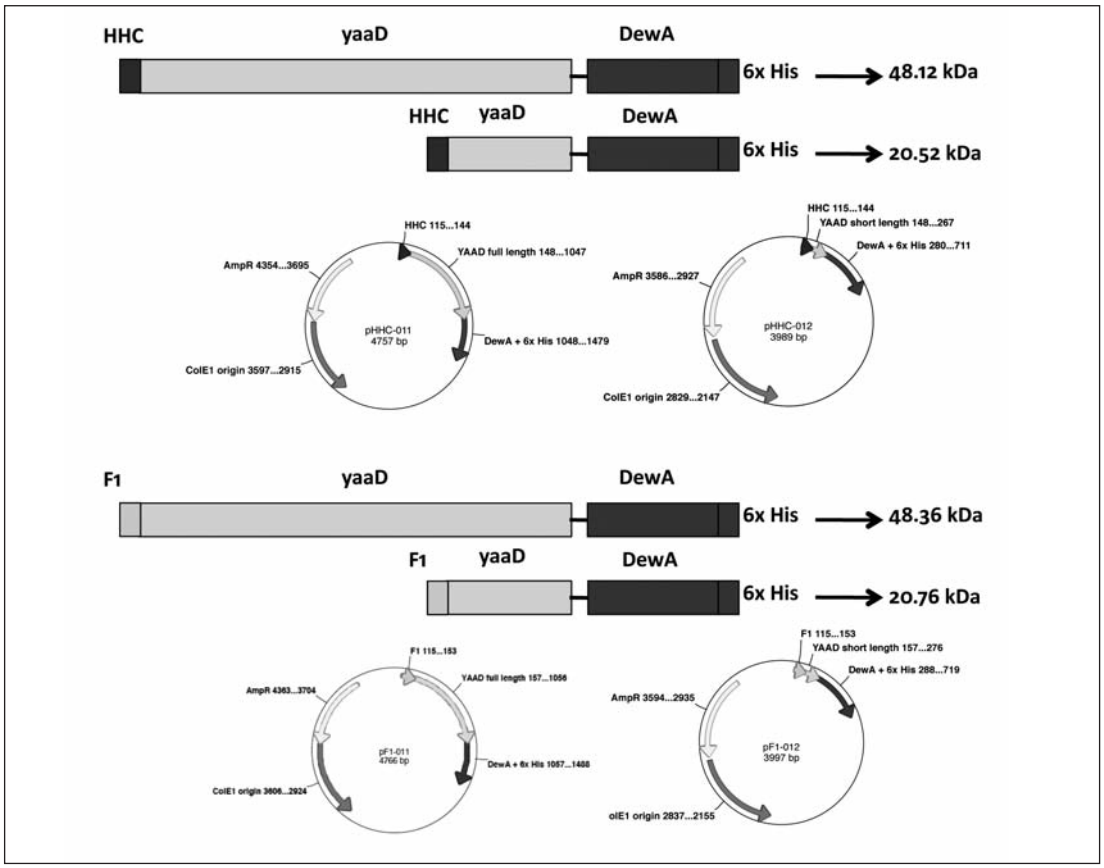

Figure 2: Fusion hydrophobins with cationic antimicrobial peptides. We fused the AMP to the N-terminal site of the yaaD. After biochemical calculations the AMPs are on the top of the coated surfaces and the contact point for biofilms.

was done by an approved protocol of the BASF SE, where a pH-shift from 12 to 9 dissolves the modified fusion hydrophobins out of the IBs. After centrifugation the dissolved proteins remain in the supernatant, which was lyophilized afterwards. The molecular masses of the modified fusion proteins are only a little larger, because of the small size of the AMPs. The modified fusion hydrophobins have a mass of about 48 kDa and 20 kDa, respectively (Figure 3).

1.2.1. Testing the functionality of the modified fusion hydrophobins

We used different organisms, gram-positive and gram-negative bacteria and eukaryotes (*S. pneumoniae, B. subtilis, E. coli, P. putida and A. nidulans*) to show the functionality of the modified fusion hydrophobins. We performed killing curves (*A. nidulans, B. subtilis, S. pneumoniae*) and peptide activity tests (*A. nidulans, B. subtilis, S. pneumoniae, P. putida*) to show this. First we tested if only the fusion hydrophobins have an effect on the growth of microorganisms. We used the strain *B. subtilis* TMB488, which is a reporter strain for the two-component system LiaFSR and is inducible by cell envelope stress by antibiotics, which have an effect on the lipid II cycle (*Jordan et al., 2007*). Using different concentrations of the fusion hydrophobin we could not detect a growth inhibition (Figure 4). We found the same results with the other organisms. Killing curves were performed using the modified fusion hydrophobins, but there was no difference in the growth recognizable.

Because of these results we decided to perform peptide activity assays in microtiter plates. Peptide activity assays were performed earlier to check the antimicrobial activity of the AMPs F1 and HHC in A. nidulans (*Mania et al., 2010*). We found MICs (**M**inimal **I**nhibitory **C**oncentrations) of about 1µg/ml respectively about 5µg/ml, so we decided to use these AMPs for modification.

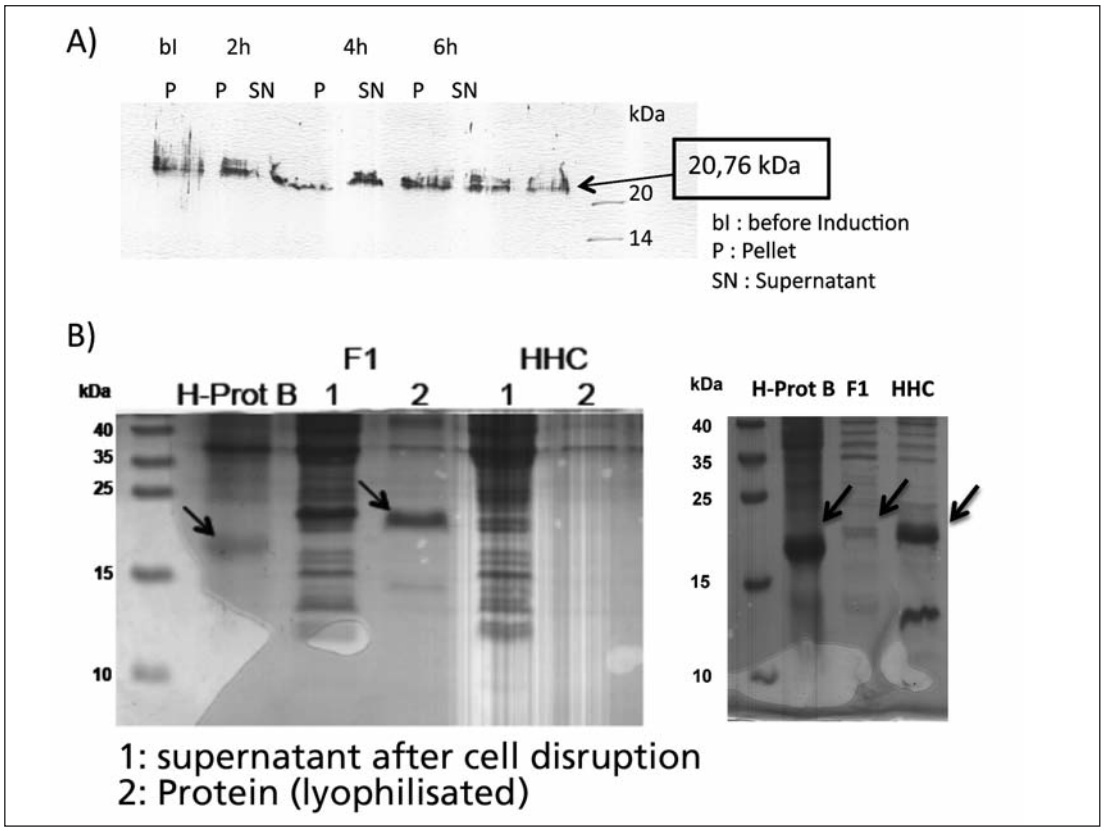

Figure 3: Over expression analysis. A) Western blot: The modified fusion hydrophobin F1-012 serves as an example for a western blot. The modified fusion hydrophobins were transformed with *E. coli* BL21 an expression strain. With induction by 0.5mM IPTG the modified fusion proteins were expressed and could be detected by the 6x-His tag. There is a clear band at about 20kDa, which corresponds to the mass of the modified fusion hydrophobin. B) SDS-Gels: By over expression the modified fusion proteins were enriched and applied on 15-15% SDS Gels. Of the lyophilized protein powder we applied 10µg/ml in each column. As comparison serve the fusion hydrophobins we got from the BASF SE.

In each column of the plate, one peptide is diluted from top to bottom to roughly identify the MIC. This is done in Minimal Medium (MM) with glucose as sole carbon source and resazurin as indicator of viability. Resazurin is a blue dye that turns pink when it is reduced, for example by respiration of living microorganisms in the medium. Each well is inoculated with a defined amount of spores (105 spores) of an A. nidulans wild type strain (RMS011). First we tested all the AMPs we have in our stock (F1, HHC, #15, #29, Bac2a, C6, D5, E6, Indolicidin and Kai13) and then we tested the modified fusion hydrophobins. There was no growth inhibition of the F1 and HHC fusion hydrophobin in any tested organism (Figure 5, and data not shown), although the peptides alone were highly active. This suggested an inhibitory effect of the fused hydrophobin.

1.2.2. Modification of fusion hydrophobins with a surface-tethered peptide

Meanwhile Hilpert et al. (2009) found some AMPs, which work better while they are tethered to surfaces. One of these peptides, KaiH, consists of 12 amino acids (WIVVIWRRKRRR) and has a mass of 1.7 kDa. We attached this peptide to the N-terminus of the shortened and full-length version of the yaaD and cloned it also in the pQE60 vector (Figure 6). As a negative control we chose a peptide slightly changed peptide, hW (WIVVIWRAKRRR), and attached it also to the shortened and full-length versions of the yaaD. The over expression and purification will be done according to the same protocol as before.

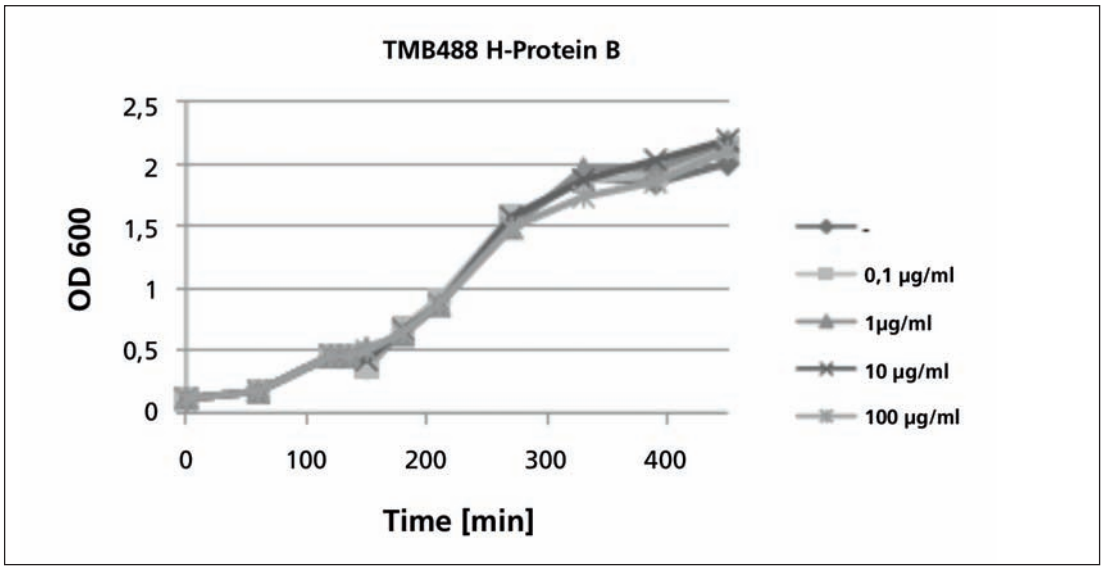

Figure 4: Growth curve of B. subtilis TMB488. The strain grew in LB-Media (lysogenic broth) with 5µg/ml chloramphenicol. A 100ml culture was inoculated at OD_{600} 0.1 with a preculture of *B. subtilis* TMB488. Then let it grow until OD_{600} 0.6 when it was splited into five 10ml cultures. To each of these cultures we gave a different concentration of fusion hydrophobins (0.1µg/ml, 1µg|ml, 10µg/ml and 100µg/ml). One of these grew without any add-on.

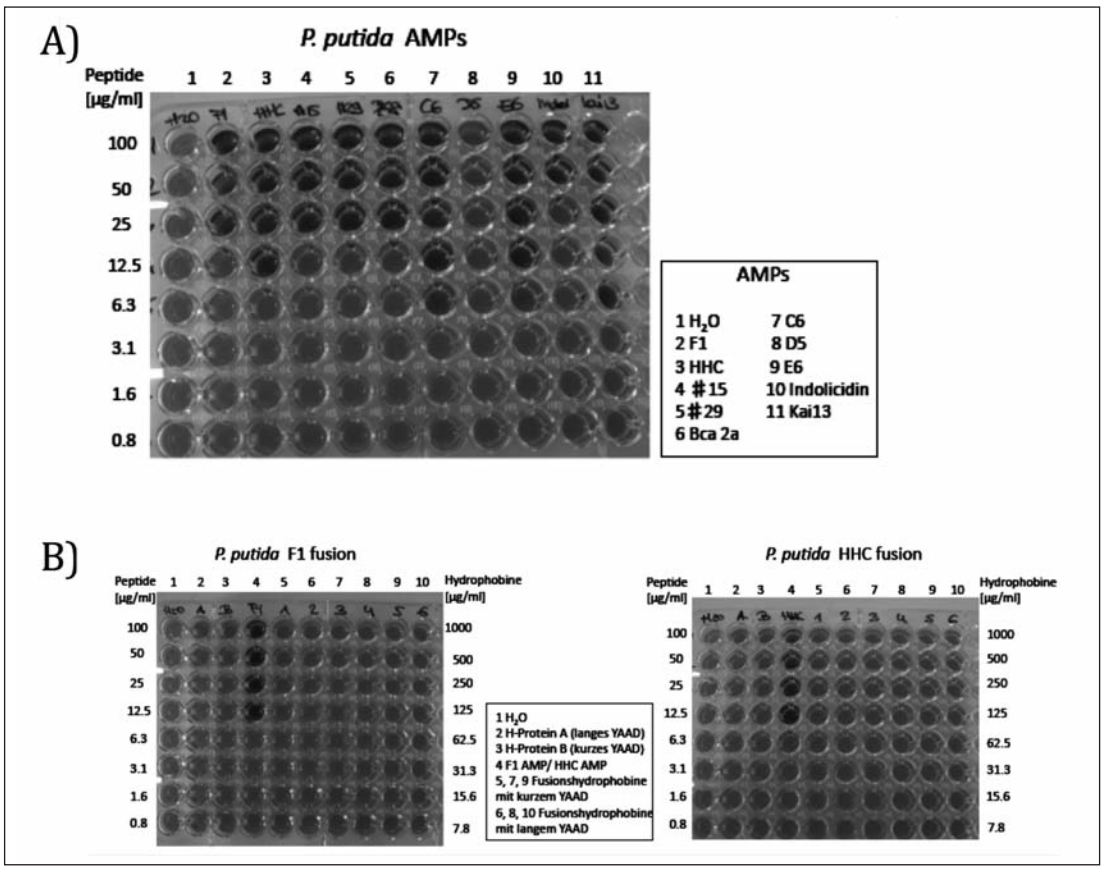

Figure 5: Peptide activity assays with P. putida. A) Testing 10 different AMPs for antimicrobial activity. As control serves aqua dest. In each column there is another peptide with decreasing concentration. B) In a second step the modified fusion proteins (5-10) were tested. In each column there is another modified fusion protein with decreasing concentration. As control serve the AMP (F1 or HHC), aqua dest. and the fusion hydrophobins from the BASF SE.

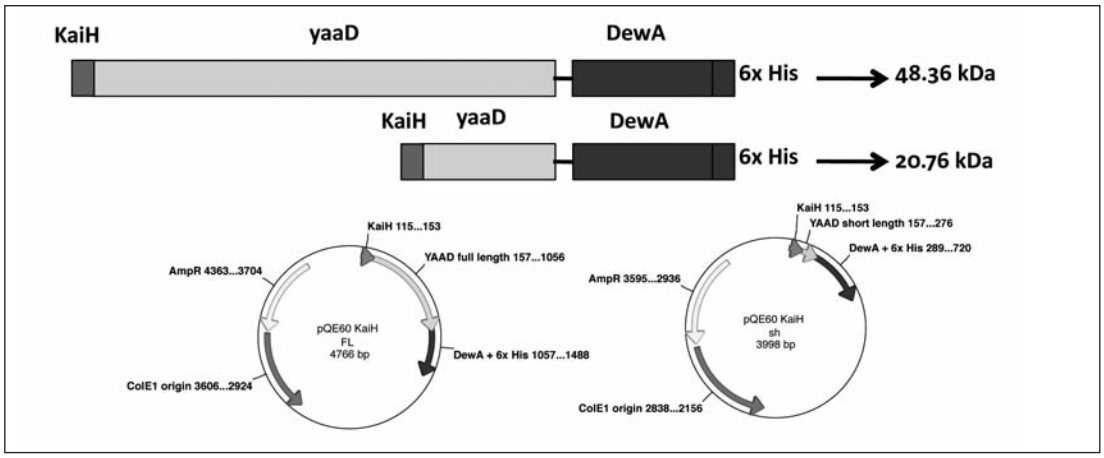

Figure 6: Modified fusion hydrophobins with the cationic antimicrobial peptide KaiH. Fusion of the AMP to the N-terminal side of yaaD and cloning in the pQE60 vector.

2. Characterization of hydrophobin coated surfaces

In this project hydrophobin coated surfaces and their properties are studied with respect to bacterial cell adhesion, cell differentiation, and cellular growth with the aim to influence biofilm formation.

In a first step unmodified recombinant fusion hydrophobins were used and a coating protocol was developed. The hydrophobin coated surfaces were characterized under various aspects.

2.1 Surface coating with hydrophobins

Glass surfaces were used as reference material for coating experiments. Glass is a very hydrophilic material and thus comparable to ceramic materials. The glass surfaces were coated with the fusion hydrophobins H*Protein A and H*Protein B. The used concentration of the hydrophobin solution was 10µM. The glass surfaces were coated according to *Janssen et al. (2004)*. The hydrophobins were solved in buffer (50mM Tris-HCl, 1mM $CaCl_2$, pH 8). Subsequently, the surfaces were cleaned with ethanol and incubated for 1-16 hours at 23-80 °C in the hydrophobin solution. During the incubation the hydrophobins self-assembled on the surface in α-helical conformation. The surfaces were rinsed with distilled water and dried at room temperature. Half of the surfaces was further treated for the induction of a β-sheet shift. The β-sheet conformation of the hydrophobin coating is said to be more stable than the α-helical conformation. For this the surfaces were incubated for 10 minutes at 80 °C in 2 % SDS-solution, subsequently rinsed with distilled water and dried.

Different parameters like incubation temperature and incubation time might influence the self-assembly behavior and the postulated monolayer of hydrophobins. These parameters were changed to analyze the fundamental characteristics of fusion hydrophobins on surfaces.

2.2 Characterization of hydrophobin coated surfaces

Different surface analysis methods were applied for the characterization of hydrophobin-coated surfaces and the clarification of the influence of the variable coating parameters. The hydrophobin-coated surfaces were analyzed in matters of change of surface hydrophobicity and homogeneity of the coating. In addition also the adsorption characteristics of hydrophobins were studied.

Change of surface hydrophobicity

Contact angle measurement (CA) is a simple-to-adopt method for surface analysis. It is used to detect the presence of films or coatings and to determine their properties. The contact angle describes the shape of a liquid droplet resting on a solid surface and thus gives information about the wettability of the surface. The more a liquid droplet spreads, the smaller is the contact angle and the more hydrophilic

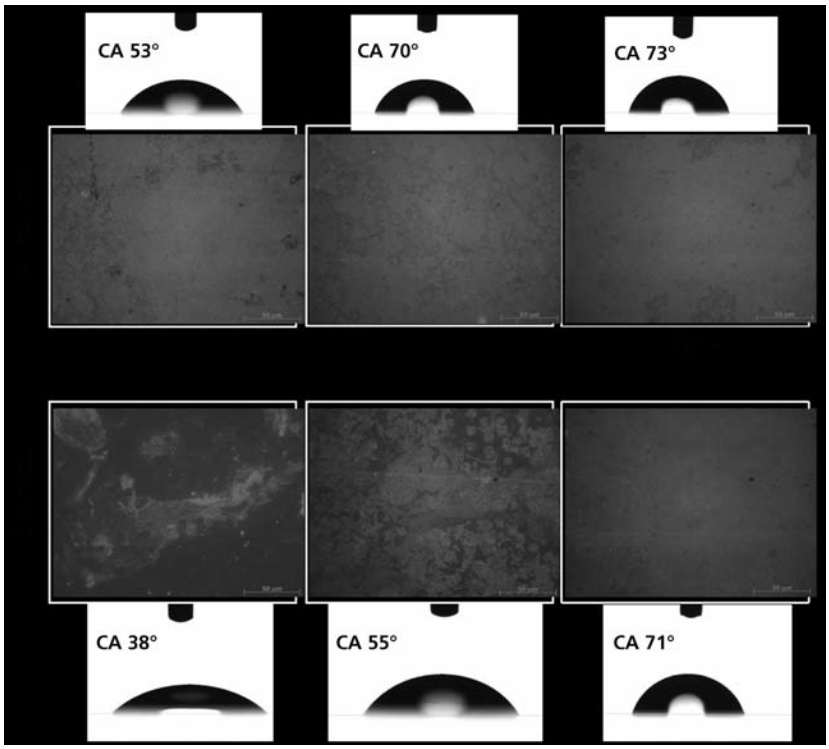

Figure 7: Contact angles and immunofluorescence microscopy are applied to monitor the change of surface hydrophobicity and coating homogeneity of hydrophobin coated surface. The fusion hydrophobins H*Protein A and H*Protein B adhere in a temperature and time dependent manner. The longer the incubation time the more homogenous is the coating in alpha-helical and beta-sheet conformation. Less surface hydrophobicity is lost with the induction of the beta-sheet shift at long incubation times.

is the surface. Since hydrophobins are amphiphilic proteins, which self-assemble on surfaces the contact angel of uncoated vs. coated, surfaces is changed and used as a parameter for the efficiency of the coating.

For contact angel measurements the *Contact Angle System OCA20* and the software *SCA20* (Dataphysics, Filderstadt, Germany) were used. The contact angle of a 5 µl water droplet (sessile drop technique) was calculated with the Laplace-Young equation. The contact angle was determined on at least five different spots on the surface.

The hydrophobin coating changed the wettability of the glass surface. Glass is a hydrophilic material (contact angle 11° ± 2°). With the self-assembly of the hydrophobins on the glass surface it became more hydrophobic. The change of the surface wettability was dependent on the incubation time, the incubation temperature and the hydrophobin conformation.

H*Protein A and H*Protein B changed the wettability of the glass surface in a very similar way. Longer incubation times and an increased temperature resulted in significant hydrophobicity changes of about 60° (Figure 7). The induction of the β-sheet shift caused losses of up to 20° of primarily achieved surface hydrophobicity. Here a big influence of incubation temperature and incubation time was noticed. Coatings prepared at room temperature lose much more hydrophobicity compared to coatings at 80 °C. The longer the incubation time the more stable was the coating and the less was lost with the induction of the β-sheet shift.

These results indicated that the longer the incubation time and the higher the incubation temperature the more efficient and stable was the hydrophobin coating. A **long incubation time** (16h) and **high incubation temperature** (80°C) **increased** the **surface hydrophobicity** of hydrophobin coated surfaces significantly.

In addition to the surface hydrophobicity also the stability of hydrophobin coatings was determined with contact angel measurements. The surface hydrophobicity of freshly coated surfaces was compared to the surface hydrophobicity of surfaces stored at room temperature for up to five weeks. The coating was stable and no change was detected in surface hydrophobicity over time.

Homogeneity of hydrophobin coating

To determine the homogeneity of the hydrophobin coating immunofluorescence microscopy was applied. Immunofluorescence microscopy is often used in biology and medicine to visualize proteins and their distribution. The proteins act as antigens and can be detected with fluorescent labeled antibodies. They are studied using a fluorescence or confocal microscope.

For the detection of the hydrophobin layer on the surface a primary Anti-his antibody was used which specifically binds to the His-tag of the proteins. A secondary fluorescent labeled antibody binds to the Fc region of the primary antibody and could be detected with the fluorescence microscope.

The characteristics of H*Protein A and H*Protein B on glass surfaces were very similar. Surface coatings prepared at room temperature in α-helical protein conformation were homogenous with just a few holes and cracks. The longer the incubation time the more homogenous was the coating, but the differences were insignificant. After the induction of the β-sheet shift the surface coating was very disordered. On glass surfaces coated for one respectively six hours at room temperature no hydrophobin coating was detectable with immunofluorescence microscopy after the β-sheet shift. These results were in accord with the contact angle data, which showed that a lot of hydrophobicity was lost on these surfaces.

The surfaces which were coated at 80 °C were much more homogenous compared to the surfaces coated at room temperature. There were slight differences between the various incubation times, but all coatings in α-helical conformation were homogenous (Figure 7). After the induction of the β-sheet shift big differences occurred. The longer the incubation time the more homogenous was the coating. These results confirmed the contact angle data. The longer the incubation time and the higher the incubation temperature the more homogenous was the coating in the α-helical and the β-sheet conformation. It was essential to incubate the materials for **16 hours at 80 °C** in the protein-solution to form a **homogenous hydrophobin-layer in α-helical and β-sheet conformation**.

To confirm the results of the immunoflurescence microscopy AFM (atomic force microscope) measurements were applied. The measurement were performed in the measurement cell of an MFP-3D BioAFM (Asylum, Mannheim) having a commercial Si_3N_4 cantilever of

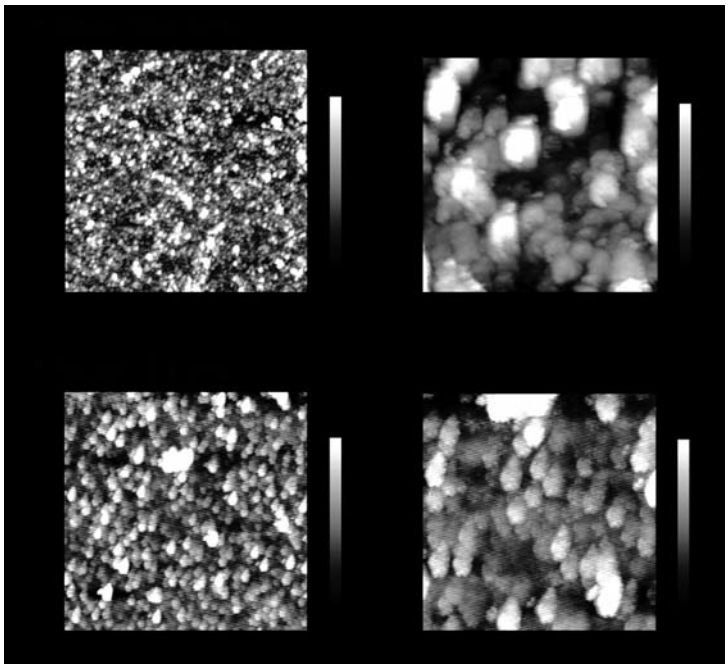

Figure 8: AFM height images of glass surfaces coated with H*Protein A and H*Protein B in alpha helical conformation for 16 hours at 80 °C. The proteins self assemble on the surfaces in ordered globular structures.

a normal spring constant of 0,56 N/m (nano and more) in air. The microscope was operating in an AC-mode, where the tip was scanned back and forth at 0° along the horizontal line in a scan range of 10 µm. The AFM was used with a 5 µm z-range and 150 µm x- and y-range scanner (type J Digital instruments). Topographic images were evaluated with the Scanning Probe Image Processor (SPIP).
On glass surfaces hydrophobins adhered in ordered protein layers. Surface coatings performed at 80 °C with H*Protein A and H*Protein B in alpha-helical and beta-sheet conformation showed a globular protein adsorption pattern (Figure 8). These results were in accordance with the immunfluorescence microscopy. Also at the **nano level** hydrophobin coatings performed for **16 hours at 80 °C** were **homogenous**.

Adsorption characteristics of hydrophobins

The adsorption characteristics of fusion hydrophobins were monitored with QCM-D (quartz crystal microbalance with dissipation) measurements. QCM is a very sensitive tool to detect changes in weight and thus a helpful method to sense adsorption processes on surfaces. The quartz crystal microbalance determines a mass per unit area by measuring the change in frequency of a quartz crystal resonator. The resonance is disturbed by the addition or removal of a small mass due to, for example, protein deposition at the surface of the acoustic resonator. It can be used under vacuum, in gas phase and in liquid environments. In addition to measuring the frequency, the dissipation is measured. The dissipation is a parameter quantifying the damping in the system, and is related to the sample's viscoelastic properties.
The adsorption of H*Protein A and H*Protein B (10µM in 50mM Tris-HCl, 1mM $CaCl_2$, pH 8) were analyzed on a SiO_2 coated quartz crystal. The protein layer thickness and the absorbed mass were calculated with the Voigt vicoelasitc model. The protein adsorption was monitored for up to 16 hours at 20 °C and a flow rate of 50 µl/min. The stability of the formed protein layer was determined by rinsing with 2% SDS solution.
H*Protein A formed a layer of 17 ± 3 nm and H*Protein B of 14 ± 2 nm on the SiO_2 surface. After 1 hour of incubation the maximum layer thickness was already reached. No more changes were observed during further incubation. These results were in accordance with the data of the contact angle measurements and the immunofluorescence microscopy. To achieve a homogenous hydrophobin coating and a significant change of the surface hydrophobicity short incubation times were sufficient. The formed coating thickness of 17 ± 3 nm respectively 14 ± 2 nm matched the expected thickness of hydrated monolayers of fusion hydrophobins. The fact that even with a longer incubation time no changes of the larger thickness were monitored, pleads for the formation of a stable monolayer.
The adhered protein mass was 17 ± 3 mg/m^2 for H*Protein A and 14 ± 2 mg/m^2 for H*Protein B (Figure 9). Unfortunately the formed protein layer was not stable under these conditions. After rinsing with 2% SDS solution the hydrophobin layer was detached completely. As already mentioned, the temperature plays an important role in the formation of a stable hydrophobin layer. Contact angle measurement and immunofluorescence microscopy have shown that higher temperatures (80 °C) were necessary to form stable monolayers. The QCM experiments were performed at 20 °C. This might result in this nonstable hydrophobin layer.

Various surface analysis methods were established and applied for the characterization of hydrophobin coated surfaces. At a later stage of this project these techniques will also be used for the characterization of surface coatings with modified fusion hydrophobins. The influence of the modification on the surface performance of the fusion hydrophobins will be determined.

3. Analysis of microbial biofilm formation on different surfaces

Biofilms were grown on natural as well as

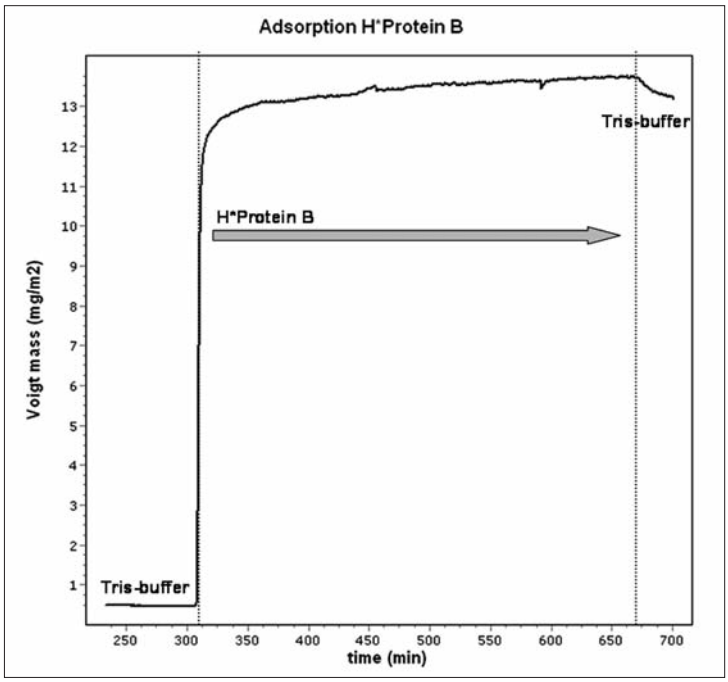

Figure 9: Adsorption of hydrophobin H*Protein B (10µM) in Tris buffer (50mM Tris, 1mM $CaCl_2$, pH 8.0) on SiO_2 surface monitored with QCM-D. The adsorped mass was quantified with Voigt viscoelastic model.

hydrophobin coated surfaces with single species and natural mixed populations. Different methods were applied and established to analyze the bacterial and fungal population in terms of population composition, microbial density and spatial distribution. Additionally the interaction of bacteria and fungi in biofilms was monitored.

3.1 Bacterial biofilm formation

Microbial biofilms represent a special, very successful life form of bacteria. The microorganisms benefit in this symbiotic life form from metabolic exchange, genetic flexibility and protection, which a biofilm offers in comparison to planktonic growth. Nearly all bacterial species are able to exhibit this type of growth firmly adhering to a substrate, in addition to the planktonic freely floating growth variety.

A special characteristic of all biofilms, besides firm adhesion to one site, is their highly structured character (*Costerton et al. 1999, Costerton et al. 2001.*) The development of a biofilm proceeds in various chronological steps. These are dependent on the involved bacterial species external factors and also surface characteristics. The first step, the initial adhesion is reversible. With the production of a matrix of organic molecules, the extracellular matrix, the adhesion gets irreversible. The bacteria are embedded in the extracellular matrix, which also offers new habitats to other organism such as other bacteria or fungi. The biofilm starts to mature and to form three-dimensional structures. A mature biofilm releases single cells, which again adhere to the substrate and start the biofilm life cycle again.

In order to characterize the influence of hydrophobin coated surfaces on bacterial biofilm formation the primary adhesion as well as mature biofilms grown on uncoated and coated surfaces were analyzed.

Primary adhesion

The primary adhesion is the first and consequently the crucial step at the change from planktonic to sessile growth.

Primary adhesion of Escherichia coli on hydrophobin coated and uncoated glass slides

To analyze the primary bacterial adhesion a **GFP-tagged *E. coli*** strain (*E. coli* BW3110, pJOE 4056.2 His e-GFP) was used. After induction of the promoter with 0.2% Rhamnose the »green fluorescent protein« (GFP) is stable expressed intracellular. The bacteria can be detected with the epifluorescence microscope without further labeling steps.

E. coli was grown in biofilm reactor on hydrophobin coated and uncoated glass slides and

the bacterial adhesion was monitored at different time points for **up to 24 hours**. The biofilm was washed in 0.89 % NaCl to remove loosely attached microorganisms and subsequently analyzed with epifluorescence microscopy.
More bacteria adhered on hydrophobin coated glass slides compared to uncoated glass slides.

Quantification of biofilm growth
For the quantification of the first steps of the biofilm formation a crystal violet assay was applied. Individual cavities of a 96-well microtiter plate (polystyrol) were coated with H*Protein A and H*Protein B according to the established protocol. The **GFP-tagged *E. coli*** (*E. coli* BW3110, pJOE 4056.2 His e-GFP) was grown overnight and diluted in sterile growth medium (OD_{600nm} 0.25). 100 µl bacterial suspension were portioned in each cavity and incubated at 37 °C for **up to 6.5 hours**. The adhered bacteria were stained with crystal violet and the biofilm formation could be quantified with the determination of the optical density at 590nm.
At most time points a higher adhesion of *E. coli* was detected on hydrophobin coated surfaces compared to uncoated surfaces. After just 0.5 hours a significant higher bacterial adhesion on the various hydrophobin coated surfaces was monitored. This effect diminished and even inverted after 6.5 hours. Now more bacteria adhered on hydrophobin coated surfaces compared uncoated polystyrol (Figure 10).

Mature biofilm
The mature **bacterial biofilms** were grown in **wastewater effluent** on hydrophobin coated and uncoated glass slides for up to **four weeks** and subsequently analyzed in terms of population composition, microbial density and spatial distribution.

Population analyses
Molecular biological population analyses like PCR-DGGE (polymerase chain reaction with subsequent denaturing gradient gel electrophoresis) allow studying the diverse population of bacteria in wastewater biofilms. Population analyses were used to detect variations in the composition of the bacterial population on hydrophobin coated and uncoated surfaces. For the analysis of the bacterial population the biofilm DNA was isolated and amplified in a PCR-reaction with the primer set 27f and 517r targeting the eubacterial 16S rDNA. The 16S rDNA of prokaryotes is the most conserved (least variable) gene and for this reason used to identify bacteria. The initial PCR-reaction resulted in a mixture of PCR amplicons which all have the same length (526 bp). Sequence variations like differences in GC content and distribution were used to separate these amplicons in a denaturing gradient gel electrophoresis. Here each band represents one bacterial species. DGGE banding patterns can be used to visualize variations in microbial diversity and provide a rough estimate of the richness

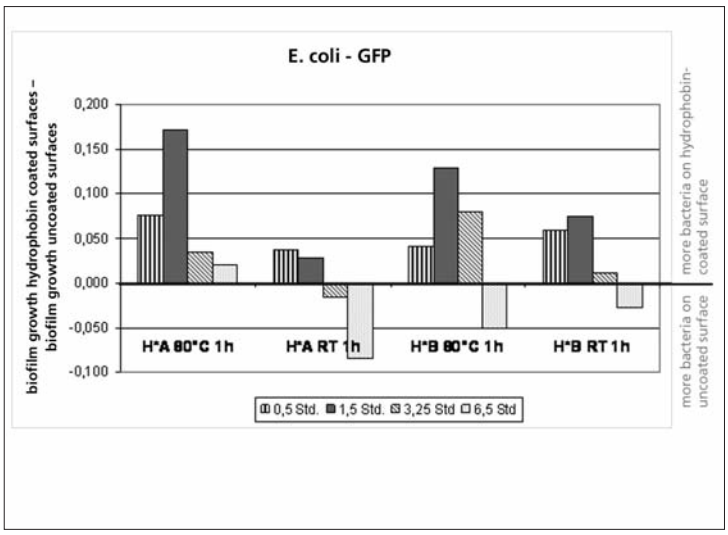

Figure 10: The primary adhesion of *E. coli* was monitored at different time points and quantified with crystal violet staining.
The differences in the biofilm growth on hydrophobin coated and uncoated surfaces are shown. At early time points (0.5 h) significantly more bacteria adhere on hydrophobin coated surfaces.

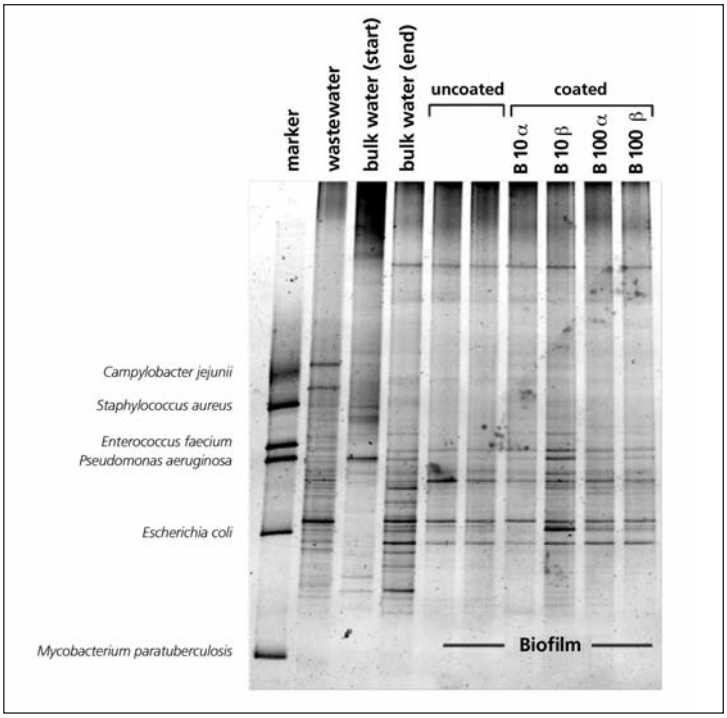

Figure 11: DGGE profiles of amplified partial 16S rRNA genes of planktonic wastewater bacteria (right) and wastewater biofilms (left). The bands obtained from different pure cultures of hygienically relevant bacteria serve as reference marker (left): *Campylobacter jejunii, Staphylococcus aureus, Enterococcus faecium, Pseudomonas aeruginosa, E. coli, Salmonella enterica, Mycobacterium paratuberculosis* (top to bottom). The banding pattern of wastewater biofilms on uncoated and coated materials showed no significant differences.

and abundance of predominant microbial community members. The bacterial population was analyzed with PCR-DGGE (Figure 11). The planktonic bacterial population (left) differed clearly from the biofilm population (right). No significant differences were visible in the banding pattern of biofilms grown on different surfaces. The bacteria adhered with the same preference to natural and hydrophobin coated surfaces.

Microbial density

A further characteristic of biofilm growth is besides the population composition the number of bacteria growing in a biofilm. Colony forming units (CFU) were used to estimate the growth density. The biofilm was washed in 0,89 % NaCl to remove loosely attached microorganisms, scraped of the surface with a sterile cell scraper, resuspended in sterile PBS and serial diluted. Suitable dilution steps were plated in triplicates on DEV-agar. They were incubated for up to 7 days at 37 °C. The bacterial colonies were counted and the number of bacteria per square cm was calculated. A lot of bacteria grew on the uncoated and hydrophobin coated surfaces, but there was no significant difference in the cell numbers on various materials.

Spatial distribution of biofilm growth

Biofilms were stained directly on the surface with the DNA intercalating fluorescent dyes Syto9 to scan the spatial distribution of biofilm growth. Prior to fluorescent staining the biofilm was washed in 0.89 % NaCl to remove loosely attached microorganisms. Syto9 solution was dropped on the biofilm sample to stain all present microorganisms. The sample was incubated for 20 minutes in the dark at room temperature and subsequently washed carefully with water. The slides were prepared with the mounting media citifluor and a coverslip for fluorescence microscopy.
No significant differences were observed in the spatial distribution of the biofilm growth on uncoated and hydrophobin coated surfaces.

Different steps of biofilm development were monitored on hydrophobin coated and uncoated surfaces. Hydrophobin coated surfaces influence the primary bacterial adhesion. The bacteria are attracted by the hydrophobin coated surfaces and adhere in higher numbers as on uncoated surfaces. But the impact of hydrophobin coated surfaces on biofilm formation seems to be time dependent. In mature biofilms (4 weeks) no differences in biofilms

established on natural and hydrophobin coated surfaces could be detected.
The established techniques for the biofilm characterization will further be applied to characterize the influence of modified hydrophobins on biofilm formation. The hydrophobins will be modified with antimicrobial peptides to enhance their effect on biofilm formation.

3.2 Fungal biofilm formation

In addition to bacteria there are also fungi inside of a biofilm. When the mature biofilm is formed, fungi joined the biofilm. To analyze the fungal populations in biofilms we use native biofilms. A native biofilm is a biofilm, which can be found in the natural environment and harbors more than one microorganism species. In a native biofilm, protozoan, algae, bacteria and fungi can be found.

Design of a clone library

To analyze and identify the fungal population of a biofilm a molecular biological approach was used and a clone library was designed. A clone library offers the advantage that also fungi, which are not able to grow on agar plates, can be detected and identified. With a clone library it is possible to estimate the abundance of single fungal species in biofilms. For the generation of the clone library the complete biofilm DNA was isolated and amplified in a PCR-reaction with the primer set ITS1 and ITS4. These primers are specific for the ITS-region of eukaryotes. The ITS-region is well suited for the identification of fungi since it has a higher variability than other regions of the rDNA. The PCR products were cloned in Escherichia coli and tested with a colony PCR (primer set M13/T7) and the restriction enzyme

Table 1: Isolated fungi and protozoa from native biofilms.
A clone library was designed for the isolation of the fungi with the amplified ITS-region in E. coli. The sequences were analyzed by a M13/T7 PCR, a digestion and by the online-tool BLAST. Plant 1 and 2 are the different places in the purification plant of Karlsruhe/Neureut. Plant 1 is the place in the mechanical treatment direct after the rack and the second place was in the biological treatment of the plant. Influent biofilm is a biofilm, which was incubated in influent wastewater for one month. The isolates from the biofilm of the lake are also listed in the table.

Species	Order	Season	Origin
Achlya sp.	Saprolegniales	Winter	Plant 1
Anguillospora longissima		Winter	Lake
uncultured Blastocladiomycota		Spring	Plant 2
Candida boidinii	Saccharomycetales		Influent biofilm
Candida pelliculosa	Saccharomycetales	Winter	Plant 1
Candida tropicalis	Saccharomycetales	Winter, Spring	Plant 1
Cladosporium cladosporioides	Capnodiales	Winter	Lake
Fusarium merismoides var. merismoides	Hypocreales	Fall	Plant 1
Galactomyces geotrichum	Saccharomycetales	Spring	Plant 1
Geotrichum sp. (Galactomyces sp.)	Saccharomycetales	Spring, Fall	Plant 1
Mortierella sp.	Mortierellales	Winter	Plant 1
Mucor racemosus	Mucorales		Influent biofilm
Nectria lugdunensis	Hypocreales	Winter	Lake
Penicllium commune	Eurotiales		Influent biofilm
Pichia anomala	Saccharomycetales	Winter	Plant 1
Phoma herbarum		Winter	Lake
Phythium sp.	Pythiales	Winter	Plant 1
Protoventuria alpina	Helotiales	Summer	Plant 1
Rhinocladiella atrovirens	Chaetothyriales	Spring	Plant 1
Rhodotorula mucilaginosa	Sporidiobolales	Spring	Plant 2
Saccharomyces cerevisiae	Saccharomycetales	Spring	Plant 1
Sporobolomyces lactosus	Erythrobasidiales	Fall	Plant 1
Sporobolomyces symmetricus	Erythrobasidiales	Spring	Plant 1
uncultured Tremellomycetes		Winter	Plant 1
Trichosporon sp.	Tremellales	Winter, Spring	Plant 1
Trichosporon cutaneum	Tremellales	Winter	Plant 1
Trichosporon domesticum	Tremellales	Summer	Plant 1
Trichosporon montevideense	Tremellales	Winter	Plant 1
Cyclidium glaucoma	Pleuronematida	Spring	Plant 2
Entamoeba sp.	Entamoebida	Spring	Plant 1
Oxytricha sp.	Stichotrichida	Spring	Plant 2
Paramecium tetraurelia	Peniculida	Spring	Plant 2
Zoothamnium sp.		Winter, Spring	Plant 1, 2
Zoothamnium plumula		Winter	Plant 1

MspI. Clones, which showed different banding patterns on an agarose gel after the restriction digest, were sequenced.

The isolated and identified fungi and protozoa from wastewater biofilms and biofilm from a lake in Karlsruhe-Leopoldshafen are listed in table 1. In addition to these isolates, 111 clones were sequenced which were not described so far. All isolates of the biofilm from the plant in autumn, the Alb, the effluent and the Rhein were species, which are not described so far. Most of the undescribed clones belong to the genus Candida and Trichosporon, which can be shown in a genealogical tree. Until now it is in general not much known about fungi in biofilms. These clones are very interesting since they might be fungi preferably growing in biofilms (Table 1). There was no significant difference in the fungal population on uncoated and hydrophobin coated materials.

Spatial distribution of biofilm growth

Biofilms were stained with Calcofluor directly on the surface of glass slides. Calcofluor binds specifically to chitin and cellulose and stains fungi and algae. Prior to fluorescent staining the biofilm was washed in 0.85% NaCl to remove loosely attached microorganisms. For the staining of fungi and algae a small volume of 0.1% Calcofluor and 15 % KOH were dropped on the biofilm and subsequently washed with 70 % ethanol and water. The samples were analyzed with the fluorescence microscope (Figure 12).

3.3 Interaction of bacteria and fungi in biofilms

Fluorescence *in situ* hybridization (FISH) was applied to analyze the distribution and interaction of bacteria and fungi in biofilms. FISH is a technique used to detect and localize the presence of specific DNA sequences in situ. FISH uses specific fluorescent-labelled probes that bind to only those parts of the genome with

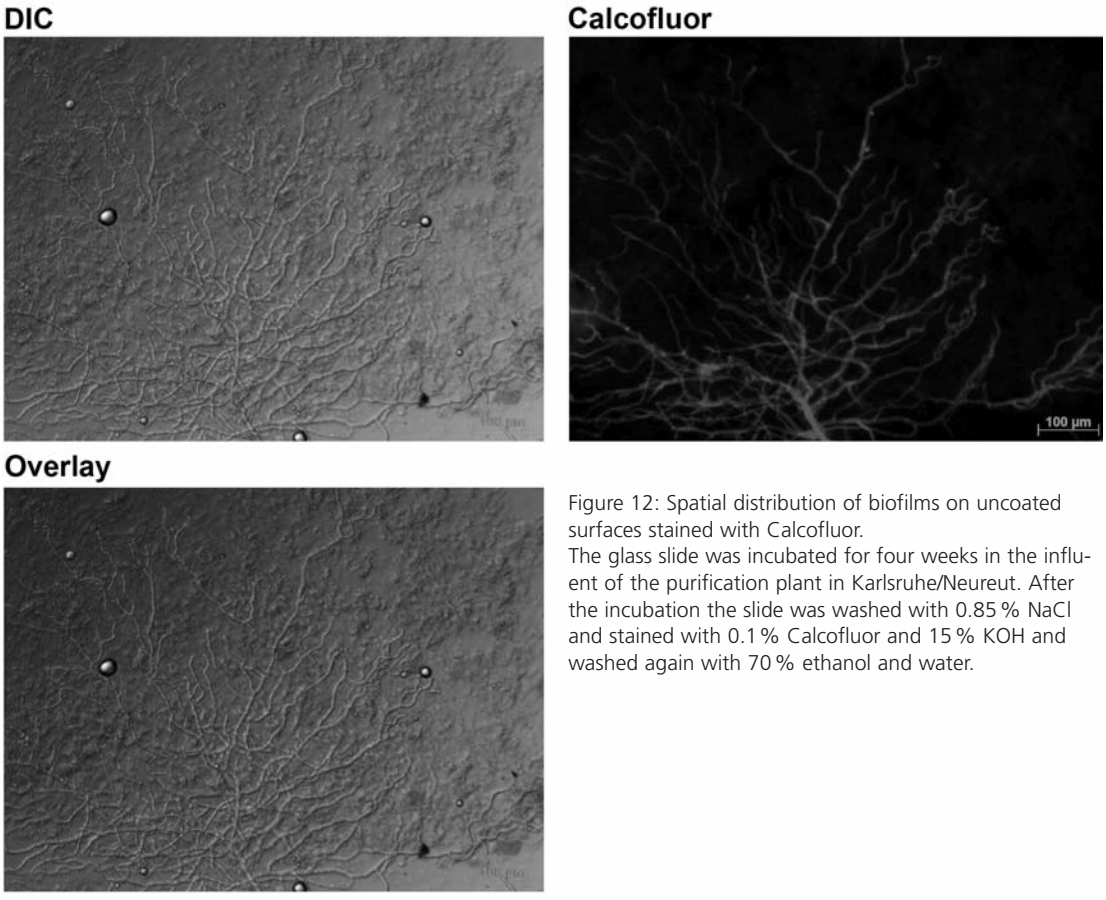

Figure 12: Spatial distribution of biofilms on uncoated surfaces stained with Calcofluor.
The glass slide was incubated for four weeks in the influent of the purification plant in Karlsruhe/Neureut. After the incubation the slide was washed with 0.85 % NaCl and stained with 0.1 % Calcofluor and 15 % KOH and washed again with 70 % ethanol and water.

which they show a high degree of sequence similarity. With this technique different microorganism groups can be stained in situ with diverse fluorescent dyes.

To analyze the interaction of bacteria and fungi two different probes were applied. EuUni was labeled with Fluorescein and bound to a highly conserved region of the eukaryotic 18S rRNA. The prokaryotic 16S rRNA was detected with the Cy3 labeled probe Eub338. The FISH was done as described *Baschien et al. 2008*. The biofilms were fixed, dehydrated and afterwards hybridized with the probes. The samples were analyzed with the fluorescence microscope. For our investigations we used glass slides, which were directly incubated in the influent of the plant Karlsruhe/Neureut and in the Alb (effluent of the plant). Figure 13 shows a FISH of a biofilm, which was incubated in the influent of the plant. The slide was incubated for four weeks, washed with 0,85 % NaCl to remove loosely attached microorganisms and hybridized with both probes.

References

Baschien, C., Manz, W., Neu, T.R., Marvanová, L., Szewzyk, U. (2008). In situ detection of freshwater fungi in an alpine stream by new taxon-specific fluorescence in situ hybridization probes. AEM, Oct. 2008, p. 6427-6436

Costerton, J.W., Stewart, P.S., Greenberg, E.P. (1999). Bacterial Biofilms: A Common Cause of Persistent Infections. Science 284, 1318 – 1322.

Costerton, J. W., Damgaard, H. N., K. -J. Cheng (2001). Cell Envelope Morphology of Rumen Bacteria. J Bacteriol. 118, 1132-1143.

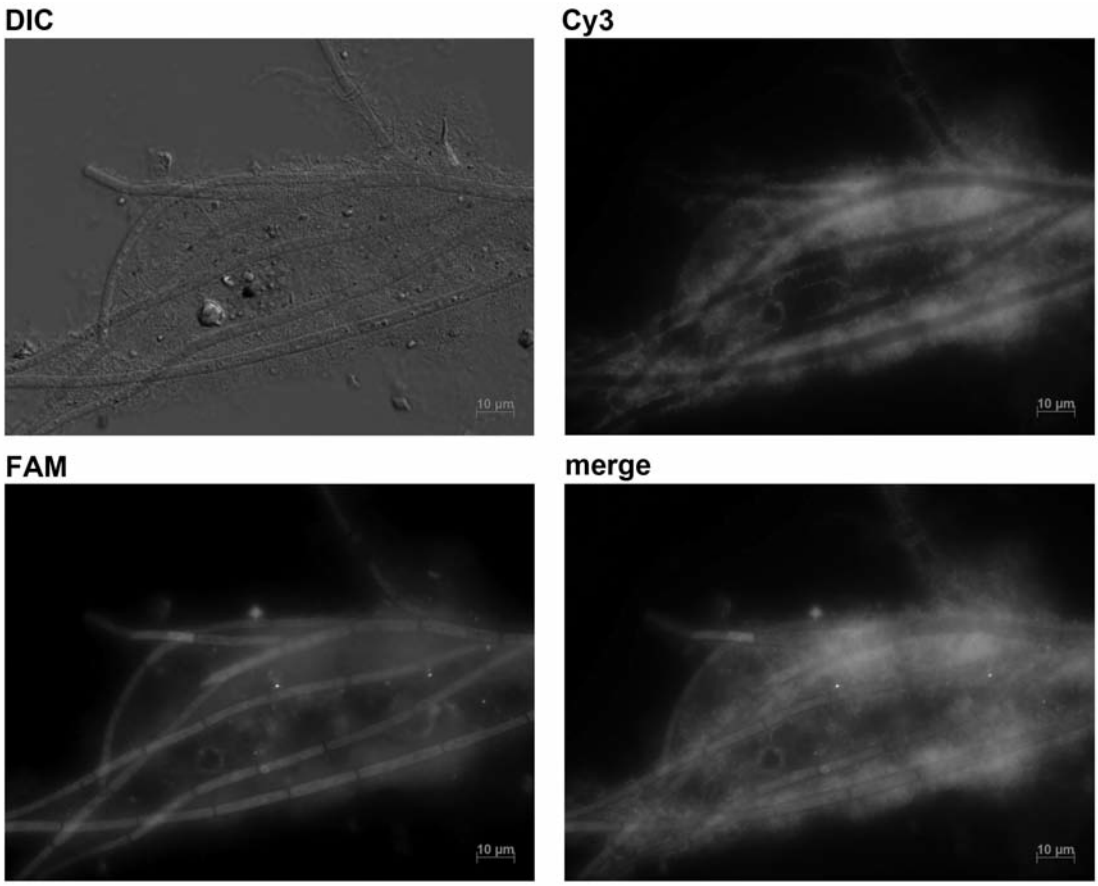

Figure 13: Fluorescence in situ hybridization with a biofilm of the purification plant.
The glass slide was incubated for four weeks in the influent of the purification plant Karlsruhe/Neureut. Afterwards FISH was carried out with the specific probes for fungi and bacteria. The biofilms were fixed, dehydrated and hybridized with the probes. Shown in red is the bacteria specific probe (Cy3), in green the fungi specific probe (FAM).

Hilpert, K., Elliott, M., Jenssen, H., Kindrachuk, J., Fjell, C.D., Körner, J., Winkler, D.F., Weaver, L.L., Henklein, P., Ulrich, A.S., Chiang, S.H., Farmer, S.W., Pante, N., Volkmer, R., Hancock, R.E. (2009). Screening and characterization of surface-tethered cationic peptides for antimicrobial activity. Chem Biol. 2009 Jan 30;16(1):58-69.

Janssen, M.I., van Leeuwen, M.B., van Kooten, T.G., de Vries, J., Dijkhuizen, L., Wosten, H.A. (2004). Promotion of fibroblast activity by coating with hydrophobins in the beta-sheet end state. Biomaterials 25 (14), 2731-2739

Jordan, S., Rietkötter, E., Strauch, M.A., Kalamorz. F., Butcher, B.G., Helmann, J.D., Mascher, T. (2007). LiaRS-dependent gene expression is embedded in transition regulation in Bacillus subtilis. Microbiology 153, 2530-2540

Mania, D., Hilpert, K., Ruden, S., Fischer, R., Takeshita, N. (2010). Screening for antifungal peptides and their modes of action in Aspergillus nidulans. Not yet published.

BioMin – Functionalized mineral surfaces: Sorption mechanisms of growth-stimulating proteins on surfaces of bone substitutes based on calcium phosphates: Second status report

Lindner M. (1), Koczur K. (1), Kirsten A. (1), Oliveira A. (2), Seifert G. (2), Gemming S. (3), Zurlinden K. (4), Meißner M. (4), Jennissen H.P. (4), Müller-Mai C. (5), Fischer H. (1)*

(1) Department of Dental Materials and Biomaterials Research, RWTH Aachen University Hospital, e-mail: hfischer@ukaachen.de

(2) Department of Chemistry, Theoretical Chemistry, TU Dresden, e-mail: gotthard.seifert@chemie.tu-dresden.de

(3) Institute of Ion Beam Physics and Materials Research, Research Center Dresden-Rossendorf, e-mail: s.gemming@fzd.de

(4) Institute of Physiological Chemistry, Biochemical Endocrinology, University of Duisburg-Essen, e-mail: hp.jennissen@uni-duisburg-essen.de

(5) Clinic for Surgery, Department of Trauma Surgery and Orthopaedics, Knappschaftskrankenhaus Bochum-Langendreer, e-mail: ch.mueller-mai@kk-bochum.de

* Coordinator of the project

Abstract

The manufactured samples of amorphous and recrystallized bioactive glass 45S5 were sterilized for further investigations especially for the *in vivo* testing. Two common sterilization procedures for solid bodies, steam sterilization and hot air sterilization, were tested. After the steam sterilization the surface topography and the chemical content at the surface of the samples changed. This effect could not be observed after hot air sterilization. Hence, hot air sterilization procedure was chosento sterilize the samples. We developed a manufacturing process to produce porous β-tricalcium phosphate specimens. NH_4HCO_3 was successfully used to create pores inside the samples. The advantage of this material is that it decomposes at low temperature (60 °C) and so only can affect the samples a short temperature range from room temperature up to 60 °C. Hence, no cracks where detected at the surface and the core of the samples. Different kind of pore sizes and amount of porosity was created in the ceramic parts by using this porosifying agent. The bounding ability of the BMP-2 (Bone Morphogenic Protein) of amorphous and recrystallized bioactive glass was characterized by two different concentrations of the BMP-2 in the immersion fluid. The results show that a doubling of the concentration of the BMP-2 in the immersion fluid resulted in the two-fold amount of BMP-2 at the surface of the amorphous and the recrystallized bioactive glass. However, the release of the BMP-2 showed a difference with respect to these two materials. Both materials show an initial burst phase in the release of the bone morphogenetic protein from the surface of about two days followed by a sustained release. During the initial burst phase more BMP-2 was released from the recrystallized surface compared to amorphous surface of the bioactive glass. As experimental results on the BMP-2 activity on mineral surfaces indicate that a non-covalent attachment to an unpolar surface functionalization yields the best coverage, the relevant

structural characteristics of BMP-2 under osteogenic conditions were studied by molecular dynamics simulations with a biological force field. An analysis of the local flexibility of BMP monomers and dimers in solution and on a non-polar functionalization revealed major structure changes at the N-terminus, close to the α-helix, and around the disulfide bridge in the dimer. As all secondary structure elements remained intact in the bonded dimer, the results indicate that the flexible areas in-between may facilitate the docking of BMP-2 to surfaces, but are not involved in sterically driven osteogenic activity. Electronic structure calculations suggest alkylphosphonic acids and nucleotides as suitable surface functionalizations, which bind to the mineral surface with the polar part and expose an unpolar part to attach. The amorphous and recrystallized bioactive glass coated and not coated with BMP, respectively, were implanted in New Zealand white rabbits for four different implantation times (7, 28, 84, 168 days). 6 implants were used for one kind of material and implantation time, i. e. overall 96 cylindrical implants (3.96 mm diameter, 8.1 mm height) have been inserted. At present, the evaluations of specimens prior implantation and at 7 days were completed. Due to the implantation procedure a gap healing was observed, leading to a delay in bone formation in comparison to former studies in the same animal model with bioactive implants. Up to 7 days after implantation no bone-bonding was observed in any of the specimens. All of the materials (amorphous, crystalline each with and without BMP-coating) displayed no obvious changes in surface density and structure up to now indicating a lower surface reactivity as known from 45S5 bioactive glass. At 7 days the highest expression of an early marker, which indicates that the bone matrix is activated, was observed at the amorphous coated implants. Therefore, stimulation in bone formation around the BMP-coated implants is possible. Subsequently, we will histologically analyze the samples of longer implantation times to confirm this observation.

Introduction

Our research joint project focuses on the interface between implant material and biological environment. More precisely we want to compare the interaction of an amorphous material (bioactive glass) und a crystalline material (recrystallized bioactive glass) with bone tissue. The bioactivity and subsequently the bone remodelling process weakens especially when greater bone defects have to be restored by this class of material. It is known that the growth of bone tissue can significantly be stimulated by so called Bone Morphogenetic Proteins (BMPs). In our project we want to compare the coupling ability and the desorption kinetics of the BMPs on the amorphous and the crystalline surface. Tests in vitro, in vivo and additionally computational simulation of the coupling process will create further knowledge of the interaction of the BMPs with the mineral surface and the biological environment. This knowledge is important for the development and manufacturing of tailored bone substitute implants, so that degradation of the substitute material and build-up of new bone tissue can go hand-in-hand in vivo. In the following chapters the results are presented that have been achieved within the first fifteen month of our joint project.

Sterilization of amorphous and recrystallized bioactive glass

The manufactured and analyzed samples of amorphous and recrystallized bioactive glass (see science report 2009) must be sterilized before further experiments like the immobilization of BMP-2 on the surface and the in vivo testing can be carried out. Therefore a standard sterilization procedure for solid state bodies of a steam autoclave (120 °C, 1h) was used. The surface of the samples was examined before and after the sterilization process using a scanning electron microscope (SEM) and energy dispersive X-ray analysis (EDX). After the sterilization process the surface topography of the samples changed compared to the surface of the samples which were not sterilized with hot steam (Fig. 1, Fig. 2). Because the surface topography changed after the

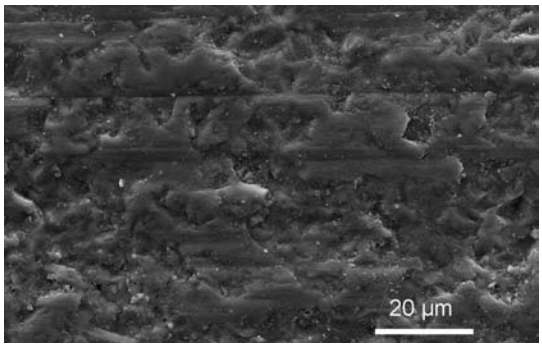

Figure 1: Analysis of the microstructure of a recrystallized bioactive glass surface after grinding without subsequent sterilization.

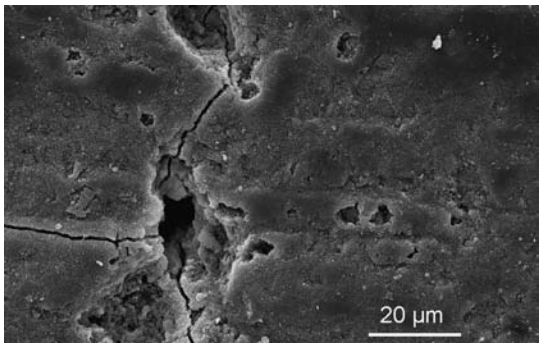

Figure 2: Analysis of the microstructure of a recrystallized bioactive glass surface after grinding and subsequently sterilized with steam.

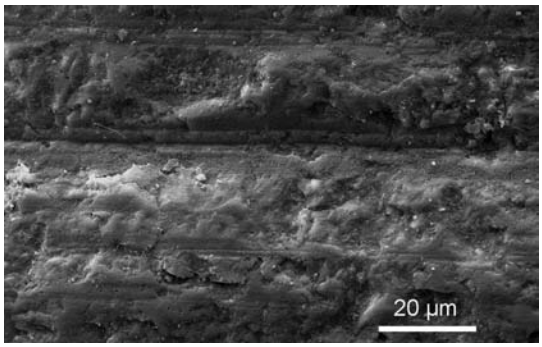

Figure 3: Analysis of the microstructure of a recrystallized bioactive glass surface after grinding and subsequently sterilized with hot air.

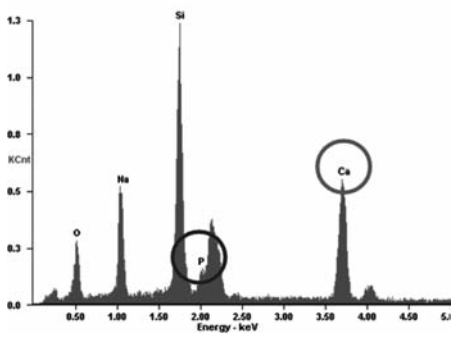

Figure 4: EDX-analysis of a recrystallized bioactive glass surface after grinding without subsequent sterilization.

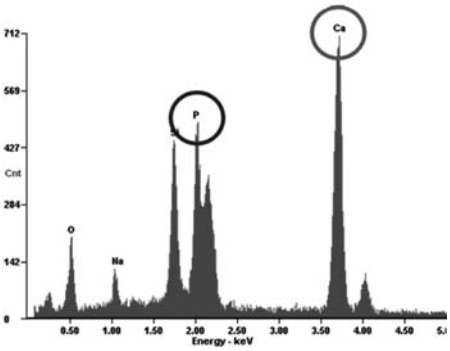

Figure 5: EDX-analysis of a recrystallized bioactive glass surface after grinding and subsequently sterilized with steam. An enrichment of Ca and P could be detected.

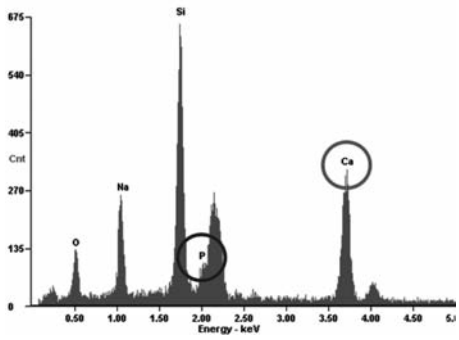

Figure 6: EDX-analysis of a recrystallized bioactive glass surface after grinding and subsequently sterilized with hot air. No enrichment of Ca and P could be detected.

steam sterilisation, another suitable standardized sterilization process had to be found which has no or only a marginal effect to our specimens. One adequate sterilization process proved successfully was the hot air sterilization method (180 °C, 2h). After the hot air sterilization process the surface topography did not change compared to the surface of the samples which were not sterilized (Fig. 1, Fig. 2).

Furthermore the method of steam sterilization did not only influence the surface topography of the samples. This method changed also the chemical composition at the surface. The EDX-

analysis showed an enrichment of phosphor and calcium at the surface of the samples which were sterilized by the steam sterilization method compared to the specimens which were not sterilized (Fig. 4, Fig. 5). The samples treated using the method of hot air sterilization did not show an enrichment of phosphor and calcium at the surface and provided the same chemical content on the surface like the samples which were not sterilized (Fig. 4, Fig. 6).

Now that there was found a sterilization procedure which did not influence the surface of the specimen, 124 cylindrical samples (3.96±0.03 mm diameter, 8.1±0.1 height) were manufactured for the in vivo experiments. 96 specimens were implanted, 16 bakkup samples were fabricated and 12 cylinders were used for checking the amount of the adsorbed BMP-2.

Fabrication and characterization of porous β-tricalcium phosphate (β-TCP) specimens

β-tricalcium phosphate (β-$Ca_3(PO_4)_2$) is one of the most investigated biodegradable ceramic materials for medical applications to support bony defects. The pore size and the amount of porosity are one of the most important parameters for using this material for bone replacement. Different procedures have been developed to synthesize porous ceramic parts. Nearly all techniques to establish porosity in a ceramic specimen use a porosifying agent which burns out during the sintering process and creates the desired porosity in the manufactured part. Therefore, one main property of the porosifying agent is, that it completely disappears during firing process. For that reason organic substances like oil or carbon based materials are common materials to create porosity in ceramic specimen. As first attempts to create porosity, it was used a polyurethane foam. One disadvantage using polyurethane is the higher thermal expansion of the polyurethane compared to the ceramic. This resulted in cracks in the part before the sintering process could start. A sample was heated up to only 200 °C instead up to the sintering temperature of 1100 °C. The foam did not burn out because of the low temperatures and large cracks were visible at the surface of the samples.
Because of the described problems with the polyurethane foam we decided to test other materials for creating the porosity in the samples. One of these materials was NH_4HCO_3. The advantage of this material was that it decomposes at low temperatures (60 °C) to NH_3, H_2O and CO_2. Hence there was only a small temperature range (room temperature up to 60 °C) when this material could interact with the ceramic material. This material was tested by mixing powder of β-TCP and NH_4HCO_3 together with different weight ratios. Tablets were pressed of this material and the sintering processes was performed. A pressing device with a diameter of 12 mm was used to press cylindrical specimen of a height of about 1 mm and 18 mm. Using NH_4HCO_3 as a porosifying agent, the samples showed no cracks at the surface after the sintering process. The manufactured parts were analyzed in comparison to specimens which were made of β-TCP only (Tab. 1).

The results in Table 1 show, that the amount of porosity of the sample is about 38 vol.-% when no NH_4HCO_3 is used. This porosity is caused by the sintering process of the β-TCP particles which results in pores smaller than 10 µm (Fig. 7 and Fig. 8).

The SEM micrographs of the sintered specimen with NH_4HCO_3 showed clearly the difference in the microstructure of the manufactured specimen compared to the parts made of β-TCP only. The fracture surface of a ceramic part made of 50 % β-TCP, 50 % NH_4HCO_3 < 50µm shows the pores which are caused by the porosifying agent (Fig. 9 and Fig. 10)
Using more NH_4HCO_3 results in specimens with over 80 vol.-% porosity. The mechanical strength of these parts was very low. Even handling these parts for further investigations resulted in small pieces which cracked from the samples.

Table 1: Resulting porosity for different particle size and different amounts of NH_4HCO_3.

material [wt.-%]	porosity [vol.-%]
100 % β-TCP	38.0
50 % β-TCP, 50 % NH_4HCO_3 < 50µm	57.1
30 % β-TCP, 70 % NH_4HCO_3 < 50µm	81.0
50 % β-TCP, 50 % NH_4HCO_3 < 710µm	63.6

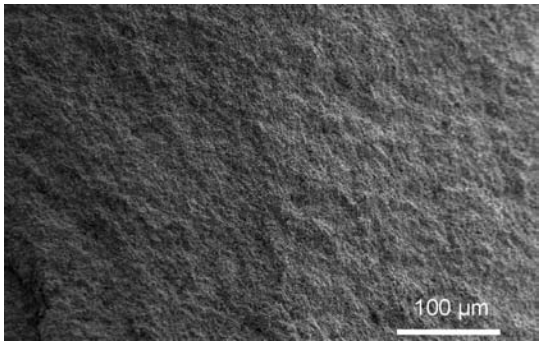

Figure 7: Overview of a fracture surface a sintered specimen made of β-TCP. No pores can be detected at this magnification.

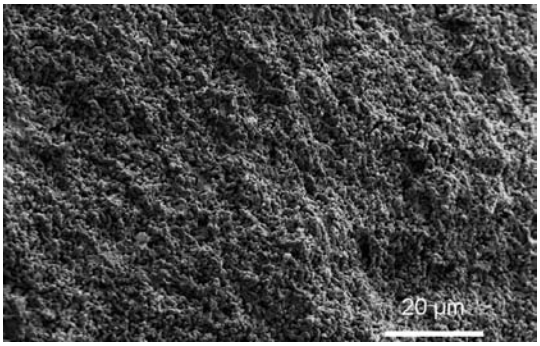

Figure 8: Microstructure of a fracture surface a sintered specimen made of β-TCP. Only small pores (< 10 µm) can be detected.

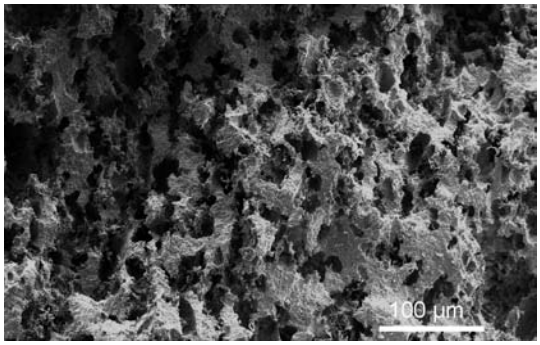

Figure 9: Overview of a fracture surface a sintered sample made of 50 % β-TCP, 50 % NH_4HCO_3 < 50µm. In comparison to Fig. 10 pores of 50 µm can be detected.

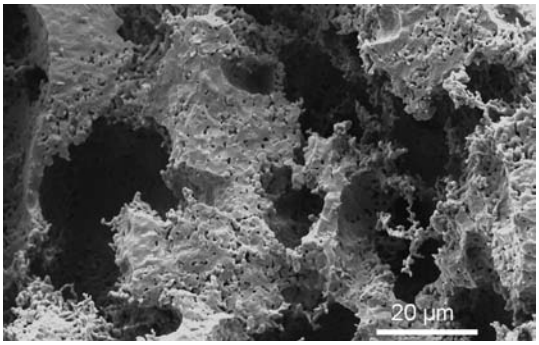

Figure 10: Microstructure of a fracture surface a sintered sample made of 50 % β-TCP, 50 % NH_4HCO_3 < 50 µm. In comparison to Fig. 8 the pores in the size of 50 µm can be detected.

Now that there was found a suitable porosifying agent the next goal was to create different defined pore sizes in the samples. Therefore, the NH_4HCO_3 was grinded and the particle size distribution was analyzed before, during and after the milling process (Tab 2). The material was milled dry with ZrO_2 milling balls on a rolling platform.

The meaning of the value d_{10} is, that 10 vol.-% of the particles are smaller (or equal) than the given value; analog for d_{50} and d_{90}. The results show a proper milling process by the time of 9 hours. When now NH_4HCO_3 of different milling times is used to create the porosity in the parts, different sizes of pores are the result. Also we wanted to obtain a material with only a short range in pore size distribution. Therefore the NH_4HCO_3 can be sieved with two sieves at the same time. For example a sieve of 63 µm mesh is stuck on top of a sieve of a 45 µm mesh and the NH_4HCO_3 is sieved. The particles which do not pass the 45 µm and remain on the top of this sieve have a particle size between 45 µm and 63 µm. Hence the over all range of this particle size distribution is only 18 µm. If this material now is used as a

Table 2: Specific values of the particle size distribution depending on the milling time (NH_4HCO_3).

milling time [h]	d_{10} [µm]	d_{50} [µm]	d_{90} [µm]
0	24.8	244.0	647.8
1	7.4	70.9	378.4
2	6.1	45.7	182.2
4	3.9	25.1	103.5
6	4.6	25.5	85.8
9	3.4	15.6	37.9

porosifying agent, it will lead to same small distribution in pore size of the manufactured ceramic part.

Immobilization of BMP-2 on cylindrical bioactive glass 45S5 samples

First experiments for investigating the immobilization and the controlled release of BMP-2 from bioactive glass were carried out by using miniplates containing of amorphous and crystalline bioactive glass respectively. Results of these experiments were shown in our last report.

In contrast for animal experiments cylindrical samples were used. So it was necessary to investigate the immobilization and the controlled release of BMP-2 from these cylindrical samples. First investigations show unsteady results which could explained by microscopic investigations. REM measurements illustrate

Table 3: Immobilization of BMP-2 on cylindrical samples of bioactive glass.

BMP-2 Concentration [mg/ml]	amorphous glass [µg/cm²]	recrystallized glass [µg/cm²]
0.1	1.10 ± 0.19	1.24 ± 0.85
0.2	2.22 ± 0.12	2.08 ± 0.16

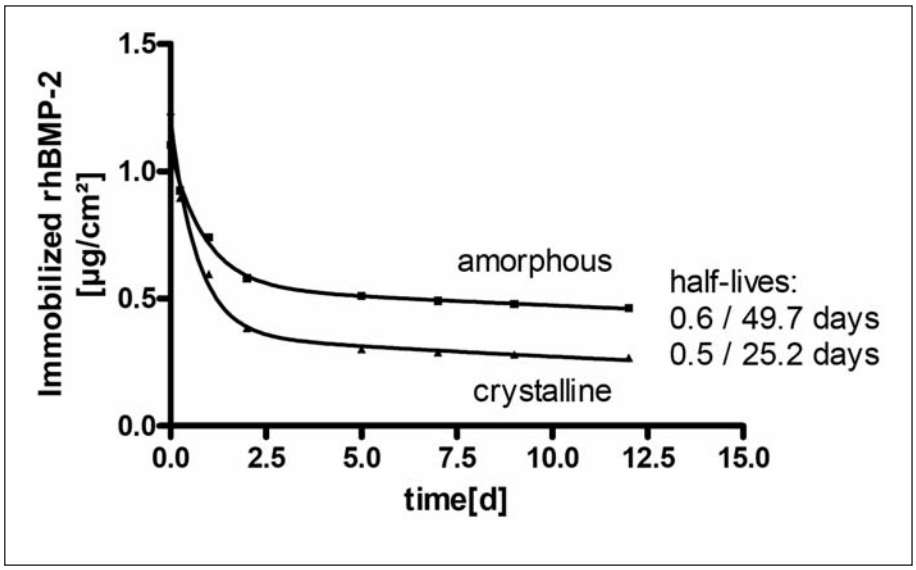

Figure 11: Release of BMP-2 from cylindrical bioactive glass samples.

Table 4: Amount of bound BMP-2 on cylindrical samples used for animal experiments

Period of observation [d]	amorphous glass [µg/cm²]	recrystallized glass [µg/cm²]
7 *	2.95 ± 0.37	3.76 ± 0.38
28	4.68 ± 1.39	3.91 ± 0.85
84	1.20 ± 0.06	1.84 ± 0.28
168 *	2.95 ± 0.37	3.76 ± 0.38

* prepared concerted

gaps and holes on the surface as a consequence of the steam sterilisation process.
After changing to the hot air sterilisation process cylindrical samples with an undamaged surface could be used for pre-experiments and animal experiments.
Depending on BMP-2 concentration in the incubation solution 1.1 - 2.2 µg BMP-2 per cm² glass surface were bound (tab. 3).

Furthermore the release of BMP-2 from these surfaces was examined (see Figure 11). A great part of immobilized protein is released from the surface during first two days.

In a »press-fit-experiment« cylindrical samples were put into rabbit bones comparable to the operation process. We could show, that only ca. 10 % of immobilized protein were lost during this procedure.

Unfortunately the amount of bound protein on samples used for animal experiments differs from the results of the pre-experiments and also among themselves although all terms and conditions were constant. Table 4 shows these data for all parts of the animal experiment.

Adsorption and desorption of BMP-2 on bioactive glass 45S5 and silica glass miniplates

The fabricated and sterilized bioactive glass 45S5 was used to the adsorption of BMP-2 from the mineral surface. It is the aim of this work to bestow osteoinductivity by immobilizing BMP-2 on a glass surface. The binding of BMP-2 to an implantable bioactive glass surface (45S5 specification) by a radiotracer method and to a model silica glass surface by evanescent wave technology will be described here.Amorphous bioactive glass (45S5 specification, Ra ~ 0.9 µm) was prepared in polished miniplate form (5 x 10 x 1 mm) for BMP-2 binding measurements by radiotracer technology. Highly polished silica glass (Suprasil I, Ra ~ 1-3 nm) in form of round plates (∅ = 36 mm, 0.9 mm thick). Ultra hydrophilic surfaces (θ 0-10°) were prepared with chromosulfuric acid (CSA). ^{125}I-BMP-2 (0.1 mg/ml) was adsorbed on bioactive glass for 17 hours according to and unlabelled BMP-2 (0.1 mg/ml, 3.8 µM) on Suprasil for 5 min in a TIRF-rheometer (Trp fluorescence) by air-bubble technology. Adsorption was performed in 20 mM Na acetate buffer pH 4.5 (buffer A) in both cases. After binding to bioactive glass for 17 h ^{125}I-BMP-2 was desorbed for 11 days in phosphate buffered saline pH 7.4 (buffer B, PBS). On Suprasil after obtaining equilibrium in ca. 5 min BMP-2 was desorbed in buffer A for 20 h.

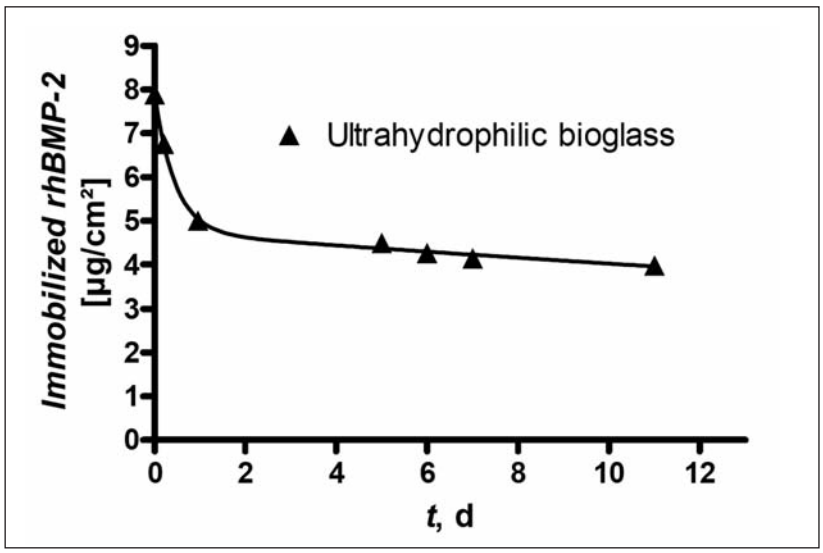

Figure 12: Release of BMP-2 from the surface of polished amorphous bioactive glass (bioactive glass). The data was fitted to a two-phase exponential decay function (r^2 = 0.99)

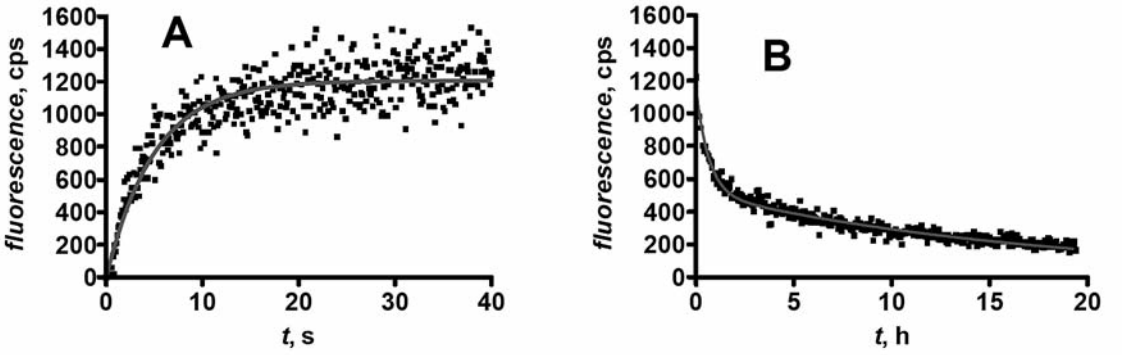

Figure 13: Adsorption (A) and Desorption (B) of BMP-2 on suprasil silica glass measured by TIRF-rheometry. Desorption was measured after 5 min of adsorption.

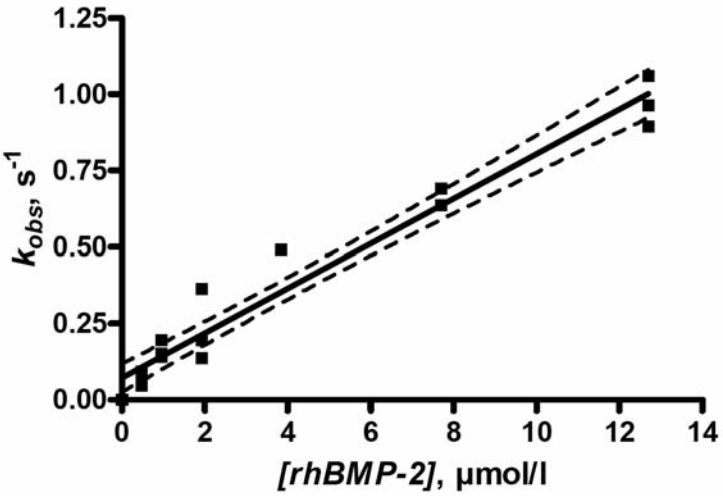

Figure 14: k_{obs}-Plot of the k_{obs} values vs the BMP-2 concentration for the calculation of the initial kinetic constants.

As shown in Fig. 12, BMP-2 is adsorbed on the ultra-hydrophilic (~8 µg/cm^2). The release of BMP-2 occurs in the form of a two phase exponential first order decay reaction. The first exponential corresponds to a burst phase with a half-life ($t_{1/2}$) of ~ 0.3 days (k_{-1} = 2.7 x 10^{-5} s^{-1}). The second phase corresponds to a sustained release phase with a half life of ~ 42 days (k_{-2} = 1.9 x 10^{-7} s^{-1}). For biological activity the samples loaded with BMP-2 were allowed to release BMP-2 for three days into the cell culture medium. From the dose-response curves the $K_{0.5}$ values for released BMP-2 were determined to 11-20 nM (control values 5-10 nM) indicating a high biological activity of released BMP-2.

Fig. 13A shows the adsorption kinetics of BMP-2 on silica glass in the TIRF-rheometer. Adsorption occurs as a single exponential (k_{obs} = 0.199 s^{-1}) without a mass transport limitation. Desorption after 5 minutes (Fig. 13B) proceeds as atwo phase exponential decay (k_{-1} = 4.3 x 10^{-4} s^{-1};$t_{1/2,1}$ = 0.45 h and k_{-2} = 1.6 x 10^{-5} s^{-1};$t_{1/2,2}$ = 12.2 h). Thus for k_{-2} the desorption rate is 42 times higher on Suprasil than on bioactive glass.

Figure 14 shows the kinetic constants of initial BMP-2 binding (encounter complex) to Suprasil: k_{+1} = 7.98 x 10^4 M^{-1}s^{-1}, k_{-1} = 0.071 s^{-1} and a binding constant of K = 1.1 x 10^6 M^{-1}.
From the k_{+1} = 7.98 x 10^4 M^{-1}s^{-1} of BMP-2 binding on Suprasil (Fig. 14) and the k_{-2} = 1.9 x 10^{-7} s^{-1} of desorption on bioactive glass (Fig. 12) an apparent binding constant K´ = 4.2 x 10^{11} M^{-1} can be calculated. This high apparent

binding constant for sustained release, compared to the encounter complex, may be due to conformational changes during the 17 h incubation step.

Simulation of solvent and surface effects on BMP-2 monomer and dimer

Bone morphogenetic proteins such as BMP-2 actively participate in the bone remodeling process by stimulating osteoblast differentiation and by regulating osteoblast and osteoclast activities. Experimental evidence suggests that this activity relies on specific structural characteristics, because also fragments of BMPs exhibit osteogenic activity [D1]. Results obtained by the BIOMIN project partners on the BMP-2 activity on bioactive glass and bioceramic surfaces with polar and non-polar functionalized surfaces indicate that a non-covalent attachment of BMP-2 to an unpolar surface functionalization yields the best coverage. These findings were the starting point for systematic molecular dynamics simulations which aim at determining the relevant structural characteristics of BMP-2 under physiological, osteogenic conditions. Such detailed knowledge of the functional BMP-2 substructure is essential for devising biologically tailored implants with better remodeling properties and yields a perspective for a better, more direct medicamentation of bone cancer.

The present molecular dynamics simulations were carried out with the established, biologically oriented force field CHARMM27 and the NAMD simulation package, which allow to systematically incorporate the conditions at the bone remodeling site in a step-wise manner. In collaboration with the experimentally working BIOMIN partners we have determined three focus areas, which lead to subsequently more complex model structures and modeling conditions and thus allow to systematically expand our understanding of the biological activity of BMP-2 during regrowth: first is to determine the structural stability of the BMP dimer and the monomers which form BMP-2 in aqueous solution and at body temperature, second is to rationalize the osteogenically most favorable interaction of BMP-2 with the functionalized mineral surface of the bone substitute ceramics, and third is to identify the specific active structural motifs within the BMP-2 geometry and their steric, polar and non-polar features.

Results from the first step were reported already last year, thus we summarize only the major findings: The optimum BMP-2 structure, composed of two equal strands of 114 amino acids each and bonded via a disulfide bridge of the cystein residue number 78 was determined and compared with a non-bonded dimer and the monomer, because the latter two structures would be more easily accessible by synthetic methods than the complete BMP-2 protein. Further findings from those calculations were that major structural rearrangements occur on the time scale of several nanoseconds, which poses the necessity for adequately long simulation times and that water stabilizes all structures and most pronouncedly the dimeric forms of BMP-2. The outcome of this task within the BIOMIN collaboration has been documented in several contributions to scientific conferences and journals [D2-D6].

During the second project year, which is reported here, first the study of the structural stability was concluded with more detailed data on flexible and rigid parts of the BMP, and major progress was achieved in focus area two, which concerns the interaction of BMP-2 with differently functionalized mineral surfaces.

To finish the structural study of BMP in monomeric and dimeric forms, a detailed, residue-resolved analysis of the local flexibility was performed, which revealed that major structure changes occur around the disulfide bridge and the flexible N-terminus of the amino acid chain under physiological conditions. Fig. 15 shows the time-averaged root mean square deviation (rmsd) of the residue positions as function of the residue number. The rmsd values of the monomer, the non-bonded dimer and the disulfide-bridged dimer in aqueous surrounding, T = 37 °C, are displayed from top to bottom. The spatially and time-averaged rmsd values of the three structures are indicated as dashed lines. With a value of 2 Å, the bonded dimer exhibits a lower overall flexibility than

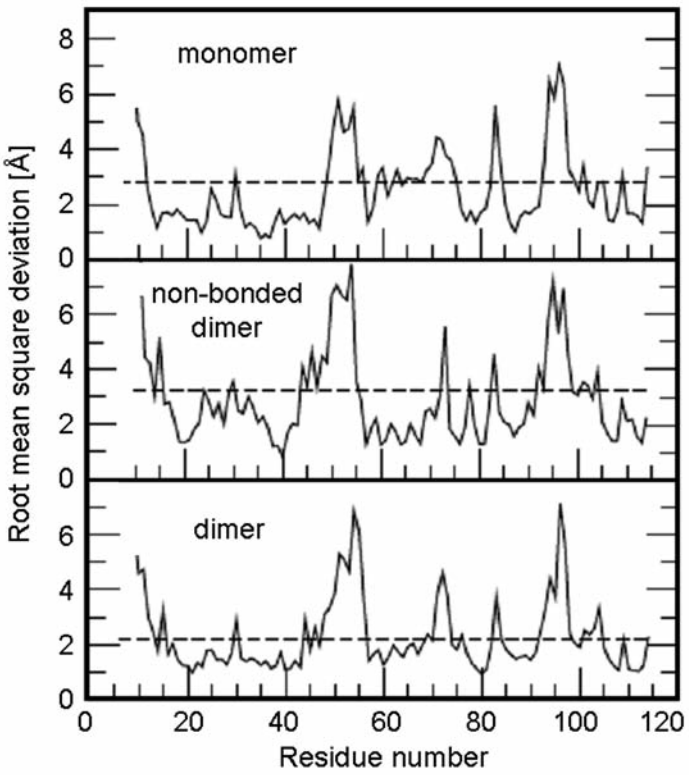

Figure 15: Time-averaged root mean square deviation (rmsd) of the residue position as function of the residue number along the amino acid chain of BMP-2. The curves show the rmsd of the monomer, the non-bonded dimer and the bonded dimer from top to bottom (solid lines) along with the spatially averaged values (dashed lines). Residue 1 is the N-terminus.

the monomer and the non-bonded dimer (both about 3 Å). In the spatially resolved curves, residue 114 corresponds to the rather rigid C terminus, whereas residues 1 to 10 belong to the highly flexible part at the N-terminus which reaches rmsd values of up to 14 Å (monomer), 18 Å (non-bonded dimer), and 12 Å (dimer). Those rsmd values are beyond the displayed range, which was adapted to the overall smaller variations along the polypeptide chain. This result indicates that the N-terminus can not be involved in an osteogenic activity, which relies on purely steric effects. However, the flexibility may facilitate the docking of BMP-2 to surfaces or receptors via the N-terminus, hence its flexibility may be of secondary, chemically driven physiological relevance.
Other flexible areas with rmsd values of up to 6 Å comprise the residues around the disulphide bridge at amino acid number 78 (region II) and two non-polar regions between residues 40 to 60 (region I) and residues 90 to 100 (region III). To analyze the inherent steric changes, the secondary structure of the system was determined by applying the standard routines, here program STRIDE [D7], which is part of the MD simulation and visualization package. The original experimental assignment comprises nine separate beta-sheet units, β1 to β9, and one beta-sheet, β5a, attached to the alpha helix α3. These rigid subunits are joined by flexible parts, which are several amino acids wide [D8]. If the experimental secondary structure is derived by means of the MD analysis routines, the rigid subunits are determined in close agreement with the experimental assignment. Differences concern the neighboring sheets β6 and β7 and also β8 and β9, which are found to combine into two longer sheets, and β5a, which is missing in the MD-derived analysis.

Fig. 16 depicts the secondary structure schematically for the original experimental assignment (exp.), the re-analysis of that data by the MD routines (*exp.), the monomer, and each strand of the non-bonded and bonded dimers, separately. Triangles denote amino acids that participate in a beta sheet, circles indicate the position of residues which belong to an alpha helix. For all model systems the secondary features agree excellently with the ones of the experimental data. As sole difference only the bonded dimer matches the reference length of β2, whereas β2 is too long in the other struc-

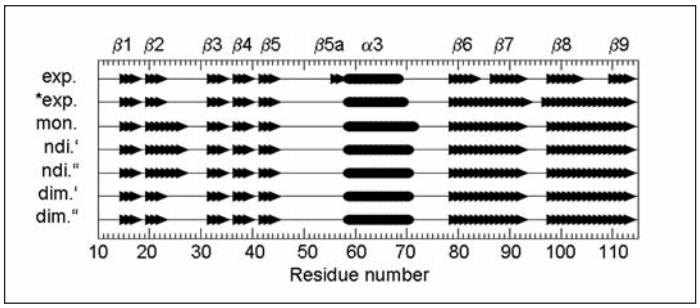

Figure 16: Secondary structure of BMP-2. The curves show beta sheet areas (triangles) and alpha helix areas (circles) of the experimental structure (exp.) in its original assignment, along with the subunits found by the automatized numerical procedure for the experimental structure (*exp.), the monomer (mon.) and both strands of the non-bonded (ndi' and ndi") and of the bonded dimer (dim.' and dim.") from top to bottom. The numbering of beta sheet and alpha helix areas is indicated above the graph; residue 1 is the N-terminus.

tures. This analysis allows correlating the peaks in Fig. 15 to residues which do not participate in secondary structure elements. Regions I and II brace the alpha helix, thus this analysis implies that the rigid helix moves as a whole relative to the rest of the protein. This mechanism may facilitate BMP-2 bonding to non-polar surfaces. The peaks in region III imply that all four beta sheets β6 to β9 can move relative to one another, hence the flexibility of the area is reproduced well by the simulation despite the assignment as two larger beta sheets.

For the second step, studying the interaction of BMP monomer and dimers with differently functionalized mineral surfaces, adsorption on model surfaces was investigated by molecular dynamics. As simple model for a mineral surface with non-polar aprotic functionalization a regular, self-assembled bilayer of POPC (POPC = 1-palmitoyl-2-oleoyl-phoshatidyl-choline) was equilibrated at body temperature. As POPC would attach to a mineral surface via the polar phosphatidyl-choline moiety and expose the non-polar palmitoyl and oleoyl chains towards the liquid phase, a bilayer which exposes the alkyl chains was chosen as first model. In contact with an aqueous solution of BMP-2 the protein then employs its non-polar fragments to anchor on the alkyl-functionalized surface via van-der-Waals interactions. Initial cursory simulations pursued during the first reporting period have been extended to simulations of up to 30.000 ps simulation time and confirmed the previous findings. After an initial period of a few nanoseconds a non-polar region of the protein starts interacting with the surface. The final BMP-2 adsorption site is an upright position coordinated via the alpha helix area of one of the monomers, and still exposing the other one. Under the given conditions BMP-2 is form-stable, i.e. it maintains its active ternary and quaternary structure. The monomer, in contrast, looses its ternary structure and spreads on the surface. For the dimer the disulfide bridge and additional non-polar interactions between the two strands occur, which stabilize the bonded dimer and corroborate the trend to lower rmsd values obtained for the dimer in solution.

Simulation of hydrophobic functionalization on bioceramics

Insight into the atomistic processes at the biofunctionalized mineral surface can be achieved by molecular dynamics simulations, whereas and a quantum-mechanical treatment is required for specific details of the structure and the structure-property relation. In line with the MD simulations of BMP-2 on non-polar surfaces we have investigated the local structural and electronic changes at oxide surfaces with aprotic and weakly polar to non-polar functionalization. The first system addresses the modification of a titanium dioxide surface by adsorption of the nucleotide cytidine. Calculations with the density-functional-based tight-binding (DFTB) method show that on the rutile (110) surface cytidine favors anchoring with two oxygen atoms of its phosphate part. Adsorption occurs preferentially at two neighboring five-fold coordinated Ti atoms along the [001] direction, thus opening a pathway to an ordered adsorption of unpolar substances along [001]. The electronic densities of state show that the aro-

matic part of the cytidine residue remains unchanged upon adsorption on rutile. This implies that no significant changes occur in the nanotube binding capacity by p-stacking of the aromatic part, hence, nucleotide-functionalized oxide surfaces are ideal substrates for the ordered, stable and electronically and chemically inert immobilization of larger unpolar moieties [D9].

As second system self-assembled monolayers of different alkylphosphonic acids on corundum α-Al_2O_3 (0001), bayerite β-$Al(OH)_3$ (001) and boehmite γ-AlOOH (010) surfaces were studied by DFTB calculations. Mono-, bi-, and tridentate adsorption modes were considered. In addition, the organization of single adsorbed molecules was compared to the organization at full surface coverage. The height (thickness) of the self-assembled monolayers is always shorter than the length of the phosphonic acid molecules due to tilting of the alkyl chains. Tilt angles at full surface coverage are very similar to the tilt angle of a single adsorbed molecule, which indicates that the density of the self-assembled monolayers is limited by the density of adsorption sites. The lateral interactions between alkyl chains are evidenced by small torsions of the adsorbed molecules, which may serve to minimize the repulsion forces between interchain hydrogen atoms. Similar tilt angles were obtained for mono-, bi-, and tridentate adsorptions. Hence, the coordination mode is not related to the molecule tilting, which implies that dense unpolar functional films can be formed on arbitrarily shaped mineral surfaces [D10].

Classical modeling of structure formation in aqueous solutions

A reaction-diffusion-type formulation of the bone remodelling process in terms of Turing structures had been set up during the first reporting period. This model has been successfully tested for structure formation in ionic solutions and describes brine channel formation in aqueous salty solutions close to the phase transition temperature in very good agreement with experimental data [D11].

In vivo investigations

After production and BMP-coating of bioactive implants animal experiments were planned to evaluate the tissue response to the implants. A comparison between coated and non-coated implants was performed. Different qualitative and quantitative histological methods were used to describe the tissue response to the implants and the material response after implantation. The main question to be answered is whether the BMP-coatings do stimulate bone growth around two different types of bioactive implant material of similar chemical composition or not. Two different types of implant materials were used in this project. One consisted of an amorphous glas, which was close to 45S5 bioactive glass and the second material was a partially crystalline glass-ceramic of the same composition. Each group of material was either used as produced or after coating with BMP (Bone Morphogenetic Protein). The diameter of the implants was 3.96 mm und the length was 8 mm.The implants were intended to fit exactly to the drill hole to minimize loss of the coating during insertion. The burr displayed an outer diameter of 3.95 mm.Pathogen free New Zealand white rabbits were used for the experiments (Charles River).They were held separately in either plastic or wire cages according to the German Tierhaltungsverordnung BGBl. ll Nr.485/2004 idF BGBl. ll Nr. 530/2006.They got a standard 12 hour night and day rhythm, and their diet consisted of pressed dry pellets (Smith®) to which 25 mg/kg salinomycinsodium were added.

Prior to the operation the implants were sterilized by using dry heat. One half of the implants was coated with BMP. The animals were anesthetized with a Ketamin (0.35 ml per kg) and Xylazin (0.17 ml per kg), which was given intra muscularly. Whilst performing the surgery an additional Isoflurane anesthesia was given through a respiration mask. 0.5 ml Gentamycin per Rabbit was injected to prevent Infection, as well as 0.3 ml Rimadyl for pain management. After shaving the legs up to the hip joint and disinfecting the area with

Braunoderm, an incision was made medially to the knee joint. The patella was luxated laterally after cutting through the medial retinaculum. A hole was then drilled in a sagittal direction into the trabecular bone of the distal epiphysis of the femur (diamond coated cylindric hollow drill, outer diameter of 3.95 mm). The cooling of the device was assured through NaCl-solution which was sprayed onto the drill with a syringe. After implantation, the Patella was forced back in its normal position. For the suture of the retinaculum a Dacron 0 Vicryl® thread was used, and to close the skin the suture material was 3-0 Mersilene®. The skin was closed with a continuous suture technique and a securing single suture. The animals had surgery on both knees to make sure the stress is the same on both knees, and the animal does not fall into a relieving posture.
The animals were put in a deep anesthesia with 2.5 ml Ketamin, 1 ml Xylazin and they got 1.3 ml of Fentanyl. additionally to that the rabbits were given Isoflurane. The skin was cut with a scissor, then the Knee joint was laid bare and the ligaments were cut through. The patella was lifted up and the distal femur was separated from the femoral diaphysis. Diamond coated cutting disks were used to cut the distal piece of the femur right underneath the implant. Then the condyles on both sides of the bone were cut off to open the intertrabecular spaces for immersion fixation. The last step was cutting off the trimmed piece from the rest of the femur. The cooling was also done with NaCl through a syringe. The Animals were then put to death by injecting 2 ml of T61 (Embutramid) intra venously whilst still in deep anesthesia. Data of operations, used implants and sacrifice of the animals are given in Table 5.
For histological characterization of the host response to the implants and the concomitant material response after insertion different methods were applied. The complete evaluation of each specimen comprised conventional light microscopy (LM) after staining with Giemsa and von Kossa-Fuchsin as well as histomorphometry, immunohistochemistry (IHC), scannning- (SEM) and transmisssion electron microscopy (TEM).

The tissue blocks were fixated in Histochoice and embedded in plastic. Then they were glued upon slices and cut with a saw (Leica sp 1600). The cuts are about 30 µm thick and were ground and polished. Each specimen for conventional LM was cut with the surrounding trabecular bone from ventral to dorsal. The first 6 got staining for IHC (Osteocalcin, Osteopontin, Osteonectin, Bone Sialoprotein, Alcaline Phosphatase and Collagen1), one was left for SEM-BSE; two got the Giemsa stain, two the von Kossa Fuchsin reaction and another one was left as a reserve. The procedure of cutting the slices is demonstrated in Table 6.

For IHC, slices 1-6 were deacrylated and incubated with specific antibodies (Osteonectin AON-1-s, Bone Sialoprotein WVID1 (9C5)-s,

Table 5: Date of implantation/explantation according to the four groups of materials. Per implant material and time point 3 animals were operated on and 6 implants have been inserted. Thus, using 4 implant materials (amorphous, crystalline, amorphous BMP-coated, crystalline BMP-coated) a total of 48 animals and 96 implants were used.

Implantation	Implantation time	Material	Explantation
18.01.2010	168 days	**amorphous, crystalline with BMP**	05.07.2010
19.01. 2010	168 days	amorphous, crystalline without BMP	06.07.2010
20.01.2010	7 days	**amorphous, crystalline with BMP**	27.01.2010
21.01.2010	7 days	amorphous, crystalline without BMP	28.01.2010
12.04.2010	84 days	**amorphous, crystalline with BMP**	05.07.2010
13.04.2010	84 days	amorphous, crystalline without BMP	06.07.2010
17.05.2010	28 days	**amorphous, crystalline with BMP**	05.07.2010
18.05.2010	28 days	amorphous, crystalline without BMP	06.07.2010

Table 6: Sequence of the slices produced be sawing and grinding. The numbers star form ventrally (1) and stop at the dorsal aspect of the specimens (12).

Slice Nr.	1-6	7	8	9	10	11	12
Staining	IHC	reserve	SEM	Kossa	Giemsa	Kossa	Giemsa

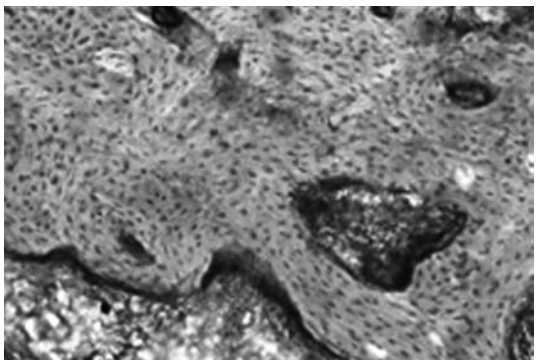

Figure 17: Amorphous implant, 7 days, BMP-coated. Surrounding bone with generalized and strong coloration for OC.

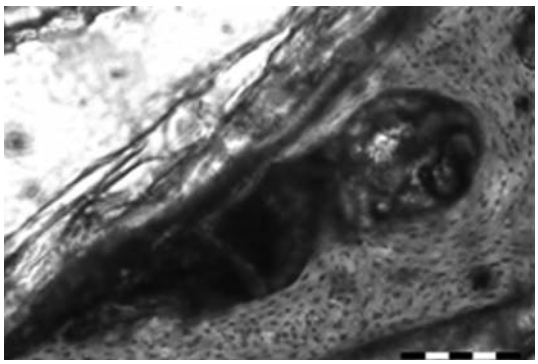

Figure 18: Amorphous implant, 7 days, no coating. The coloration for OC is generalized but moderate.

Osteopontin MPIIIB10 (1)-s, Alkaline Phosphatase B4-78-s, Collagen 1 M-38-s from the University of Iowa and Osteocalcin [OCG3], ab13420-50 from abcam. The slices were stained with AEC (liquid3-amino-9-ethylcarbazole), counterstained (Mayer´s haematoxylin) and mounted (Kaisers glyceringelantine, coverslips).
The samples are fixated with Glutaraldehyde and Cacodylate buffer, drained in an ascending alcoholic line and dried with HMDS (Hexamethyldisilazane). To discover alterations of implant surfaces one implant of each type and implantation time as well as one implant of each type prior and after coating was used for SEM analysis. The TEM-samples were fixated as the SEM-specimens and embedded in Spurr. Cutting and evaluation start in October 2010.
At 7 days all of the cut specimens showed a gap between the implant and the surrounding bone, although it was intended to create an intimate contact between the preexisting tissue and the implants. The gap between the old preexisting bone and the implant surface was up to 600 µm wide. Those spaces are filled with soft tissue in some cases and in others they were empty due to shrinking artefacts. New bone trabeculae were not observed in the drill hole which is attributed to the short time period. Bone-implant contacts were observed only exceptionally were old bone trabeculae reached the surface. Obvious differences in the tissue response between amorphous and crystalline implants and between coated and non-coated implants as well were not observed. Looking at the cross-cut implants the crystalline specimens appeared to be denser than the amorphous ones. In both materials, coated or non-coated, parts of the brittle material were lost due to the sawing process. The interface between bone and tissue was in most of the cases intact, pointing to an intimate contact between implant surface and tissue. Obvious differences in the density of all of the implants between the outermost surface and the centre were not observed.
At 7 days only slight differences in antibody reactions could be seen between the 4 implant materials. The only marker that showed significant colouring was Osteocalcin (Fig. 17, 18). There were only slight differences between amorphous and crystalline implants. But with both implant types, there was a stronger reaction to Osteocalcin (OC) with coated amorphous as well as crystalline implants. In all groups the mineralized bone matrix was coloured red which indicates a high level of activity of the OC in this area. The doted coloration ranged between mild and severe and it was always generalized. OC is an early marker, which indicates that the bone matrix is activated. In one of the cuts also osteocytes were coloured

moderate and generalized in the mineralized bone matrix which implicates their activity of building the bone.

With Alkaline Phosphatase only one (crystalline, no coating) cut showed a mild localized expression in the fibrinous matrix. Collagen 1 could not be detected in any of the slices. BSP (Bone sialoprotein) showed in one cut a localized mild expression (crystalline, BMP-coating), another one a localized moderate expression in the fbrinous matrix. For ON (osteonectin) in only one cut a localized mild expression in the fibrinous matrix was observed. For OP (osteopontin) no reddish coloration was visible.
Implants prior to implantation: The surface structure has been characterized before and after coating. Generally, the amorphous implants appeared slightly smoother than the crystalline ones. Implants at 7 days: All the 4 implant types showed similar tissue components on their surfaces. These comprised fibrinous structures between bone and the implant material. In further enlarged photomicrographs one could find erythocytes in this fibrinous net. Changes in the surface structure of the implants were only observed in amorphous types with and without coatings as cracks on the surface.Procession of the TEM-specimens will start in October.
At present, evaluation of specimens prior to implantation and at 7 days using LM, IHC and SEM as well were completed. The following observations have been made:

1. Due to the implantation procedure a gap healing was observed, leading to a delay in bone formation in comparison to former studies in the same animal model with bioactive implants. Up to 7 days after implantation no bone-bonding was observed in any of the specimens.
2. All of the materials (amorphous, crystalline each with and without BMP-coating) displayed no obvious changes in surface density and structure up to now indicating a lower surface reactivity as known from 45S5 bioactive glass.
3. At 7 days the highest expression of OC was observed at the amorphous coated implants. Therefore, stimulation in bone formation around the BMP-coated implants is possible. Further evaluation of later time-points is necessary, to assure this observation.

References

[D1] Senta H, Park H, Bergeron E, Drevelle O, Fong D, Leblanc E, Cabana F, Roux S, Grenier G, Faucheux N, Cyt. Growth Fact. 20 (2009) 213-222.

[D2] Fischer H, Koczur K, Lindner M, Jennissen HP, Zurlinden K, Meißner M, Müller-Mai C, Seifert G, Oliveira A, Morawetz K, Gemming S, GeoDresden 2009, 30.09.-02.10.2009, Dresden.

[D3] Oliveira A, Seifert G, Gemming S, Proc. 12th Intern. Symp. Biomater. Biomech, 17.-19.03.2010, Essen.

[D4] Seifert G, Oliveira A, Gemming S, Proc. 12th Intern. Symp. Biomater. Biomech, 17.-19.03.2010, Essen.

[D5] Oliveira AF, Gemming S, Seifert G, BIOmaterialien (2010) submitted.

[D6] Oliveira AF, Gemming S, Seifert G, J. Phys. Chem. B, (2010) submitted.

[D7] Philips JC et al., J. Comp. Chem. 26 (2005) 1781-1802; McKerell AD, et al., J. Phys. Chem. B 102 (1998) 3586-3616; Frishman D, Argos P, Prot. Struct. Funct. Genet. 23 (1995) 566-579.

[D8] Scheufler C, Sebald W, Hülsmeyer M, J. Mol.Biol. 287 (1999) 103-115.

[D9] Gemming S, Enyashin AN, Frenzel, J, Seifert G, Int. J. Mater. Sci. 101 (2010) 758-64
[D10] Luschtinetz R, Oliveira AF, Duarte HA, Seifert G, Z. Anorg. Allg. Chem. 636 (2010) 1506-1512.

[D11] Kutschan B, Morawetz K, Gemming S, Phys. Rev. E 81 (2010) 036106.

HydraSmec – Understanding processes at the hot smectite-water interface for tailoring industrial bentonite applications

Stanjek H. (1)*, Meister D. (1), Steinkemper U. (2), Wolff H. (2), Diedel R. (3), Habäck M. (3), Grefhorst C. (4), Böhnke S. (4), Schmidt E. (5), Latief O. (5), Schmahl W. (6), Jordan G. (6), Eulenkamp C. (6)

(1) Clay and Interface Mineralogy, RWTH Aachen University (CIM), e-mail: helge.stanjek@cim.rwth-aachen.de

(2) Institut für Gießereitechnik GmbH, Düsseldorf (IfG), e-mail: steinkemper@ifg.net

(3) Forschungsinstitut für Anorganische Werkstoffe- Glas/Keramik-GmbH, Höhr-Grenzhausen (FGK), e-mail: diedel@fgk-keramik.de, manuela.habaeck@fgk-keramik.de

(4) S & B Industrial Minerals GmbH, Marl (S&B), e-mail: c.grefhorst@ikominerals.com, s.boehnke@ikominerals.com, p.oberschelp@ikominerals.com

(5) Stephan Schmidt KG (SSKG), Dornburg-Langendernbach, e-mail: othmar.latief@schmidt-tone.de, eva.schmid@schmidt-one.de

(6) Department für Geo- und Umweltwissenschaften, Sektion Kristallographie, LMU München (LMU), email: constanze.eulenkamp@lrz.uni-muenchen.de, jordan@lmu.de,

* Coordinator of the project

Introduction

The adhesive properties of smectites are widely used in many industrial applications. These properties are mainly due to the reversible expansion and contraction of their interlayer spaces as a function of water activity. Being part of moulding sands, smectites are responsible for the required mechanical strength of moulds. Due to the need of industry for castings of increasing complexity but decreasing weight, it becomes essential to tailor moulding-sand mixtures beyond their current abilities. So far, however, it has not been discovered in detail why changes occurring during the casting process are partially reversible in the laboratory, but not in the circuit of the moulding sands. In general at temperatures below 300 °C and in the laboratory, de- and rehydration are reversible processes. It is therefore important to understand the complex kinetics of de- and rehydration of smectites and their influence on the mechanical behaviour of the moulding sands, before improvements can be achieved.

Smectites are also widely used as adsorbents, e.g., for water. Lower water adsorption capacities and reduced adsorption rates of industrially-dried bentonites compared with bentonites dried to the same water content in the laboratory show that the kinetics of drying apparently influences interface processes. Smectites exposed to hot water vapour do not fully rehydrate in contrast to dry-heated smectites, which is another important aspect. Due to contact angle measurements, increasing hydrophobicity could be observed after vapour treatment, which, however, might depend on physical changes of aggregation (pore volume). Nevertheless, other parameters such as CEC or X-ray diffraction patterns of the 00l-reflexes did not show any conspicuous changes. Initial investigations led to the assumption that coordination of Al^{3+}-Ions can be made responsible for these processes. However this has to be confirmed. Not only the hydration energy of the cations, but also size and charge as well as the water to smectite ratio, achievement/attainment of dispersion, speed of drying and further variables have an influence on the

dynamics of dehydration (and possibly rehydration).
The objective of the current project is the detailed examination of the aforementioned basic mechanisms from atomic to industrial scale in order to understand them as well as to optimize the casting processes. The following is a summary of the experiments and first interpretations of the results carried out by the project partners.

Bentonite characterisation
The rather initial X-ray characterization of the bentonite samples done in 2008 has now been advanced for the raw bentonites (Table 1).

For testing purposes we included the 001 of smecite in the fitting procedure, whereas *Ufer et al. (2008)* omitted this first peak. The iron contents of the octahedral sheets were refined unconstrained.

All bentonites have montmorillonite contents > 0.8 g/g. Mica and kaolinite were present in small amounts except for bentonite C, where the kaolinite contents varied within two charges from 0.14 to 0.2 g/g. Calcite was detected in bentonites D, E and W, respectively. The presence of carbonates was also evident in the STA/TG measurements.

The XRD contents of montmorillonite correlate with the contents determined with methylene blue sorption (Fig. 1), but at least one of the methods gives systematic deviations.

The mineralogical composition was checked against the chemical analyses (Fig. 2). For all samples Fe_2O_3 was overestimated by the mineral composition by a factor of two to three, whereas Al_2O_3 and SiO_2 were correspondingly underestimated.

Obviously, the phase contents seem to be biased especially for the iron contents. Therefore,

Table 1: Quantitative phase contents in g/g of all raw bentonites and some size fractions. Additional minor phases such as cristobalite, brookite, feldspars and others were omitted in this table.

Sample	Bentonite	Size fraction	Cation	Montmorillonite	Quartz	Muscovite 2M1	Kaolinite Ideal	Calcite
BeC_080910_r_Stanjek	C	Total	Ca	0.74	0.02	0.01	0.20	0.00
BeC-FR-08-0910	C	Total	Ca	0.79	0.03	0.01	0.14	0.00
BeC_080910_r_schkl40_M	C	< 40 µm	Mg	0.74	0.01	0.02	0.22	0.00
BeC_080910_r_attgr2	C	> 2 µm	Mg	0.50	0.04	0.01	0.25	0.00
BeD_080907_r_Stanjek	D	Total	Na	0.91	0.02	0.00	0.00	0.02
BeD-FR-08-0907	D	Total	Na	0.90	0.02	0.01	0.00	0.02
BeD_090617_r	D	Total	Na	0.90	0.02	0.00	0.00	0.03
BeD_090630_r	D	Total	Na	0.91	0.02	0.00	0.00	0.02
BeD_090630_r_attkl2_Mg	D	< 2 µm	Mg	1.00	0.00	0.00	0.00	0.00
BeD_090630_r_attgr2	D	> 2 µm	Ca	0.75	0.02	0.00	0.00	0.06
BeE_080908_r_Stanjek	E	Total	Na	0.84	0.07	0.03	0.00	0.01
BeE-FR-08-0908	E	Total	Na	0.82	0.08	0.03	0.02	0.01
BeE_080908_attgr2	E	> 2 µm	Na	0.39	0.23	0.06	0.00	0.00
BeH_090819_r	H	Total	Na	0.96	0.03	0.00	0.00	0.01
BeW_080909_r	W	Total	Na	0.75	0.04	0.02	0.00	0.02
BeW-FR-08-909	W	Total	Na	0.88	0.04	0.02	0.00	0.02
BeW_080909_rschkl40_M	W	< 40 µm	Mg	0.87	0.02	0.01	0.00	0.01
BeW_080909_r_attgr2	W	> 2 µm	Mg	0.43	0.16	0.02	0.00	0.08

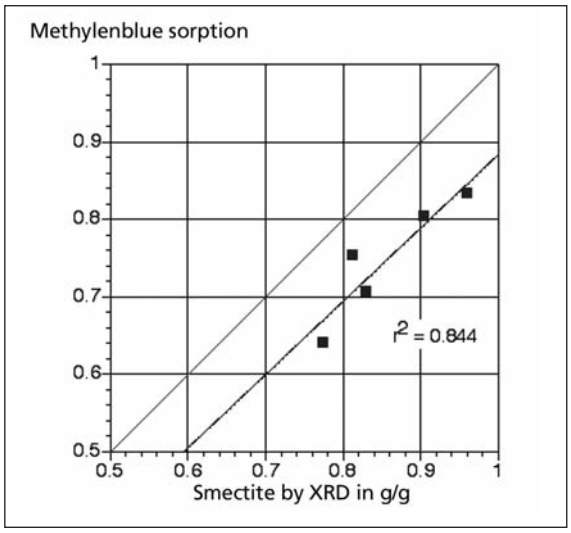

Figure 1: Smectite contents determined by X-ray diffraction versus methylene blue adsorption.

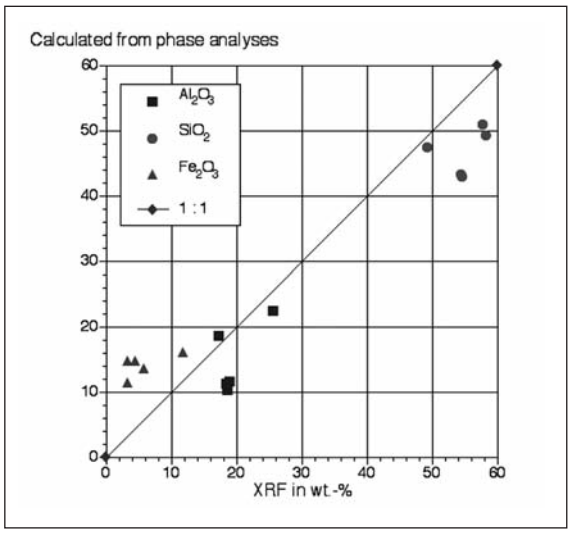

Figure 2: Contents of Al_2O_3, SiO_2 and Fe_2O_3 calculated from the Rietveld analyses and plotted against the contents determined by X-ray fluorescence spectroscopy.

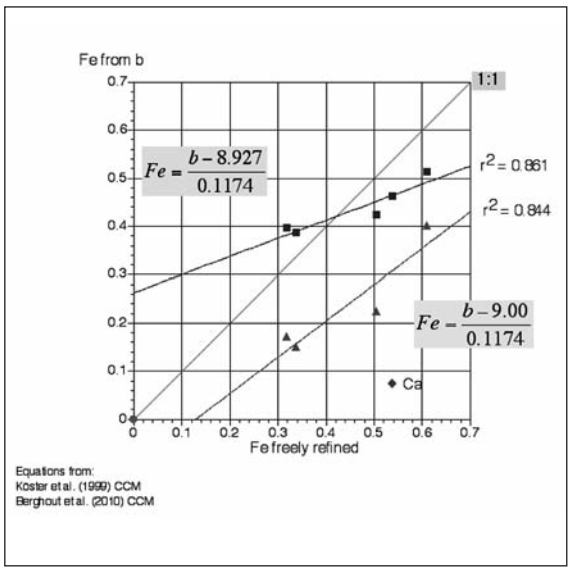

Figure 3: Plot of Fe contents constrained to two variants of an equation (blue and green box) versus Fe contents determined by freely refining the octahedral site occupancies. Note that bentonite C is a non-activated Ca-bentonite marked with Ca in the figure (only green equation). The other bentonites have Na in their interlayer space.

the fits were repeated by constraining the octahedral iron contents to the cell edge length b using the equation Fe = (b – 8.972)/ 0.1174 (*Köster et al., 1999*). A significant correlation was found (Fig. 3), but the intercept seems not reasonable.

A more reasonable trend was obtained by increasing slightly the constant 8.927 (green box in Fig. 3). Recently, MD calculations confirmed that the cell edge length b responds to the kind of interlayer cation and the hydration state (*Berghout et al., 2010*). Their b values, however, where with 9.04 – 9.08 Å for the hydrated states even larger than the refined ones of our samples. Therefore, we artifically selected 9.00 Å as the constant. The general discrepancies between mineralogical and chemical composition require more and detailed investigations.

Cast experiments

In the first year of the project, optimization of the cast experiments were done (see Report 2008). In 2009, three cast experiments were performed at the IfG. To get sand samples with the same »thermal history«, the round configuration of the moulds have been changed into a rectangular configuration. To improve the sampling of the moulding sand, a split flask was designed (Fig 4). This flask can be opened after the casting has finished (Fig. 5). In this way the samples can be taken across the whole mould.

Moulding sand, cast iron and casting temperature have been defined previously: moulding material is quartz sand, type F32, mixed with one of five kinds of bentonite (~ 0.08 g/g) and with water (~0.035 g/g). For the neutron diffraction experiments, pure bentonite was placed adjacent to the hollow space filled later on with the metal melt (Fig. 6).

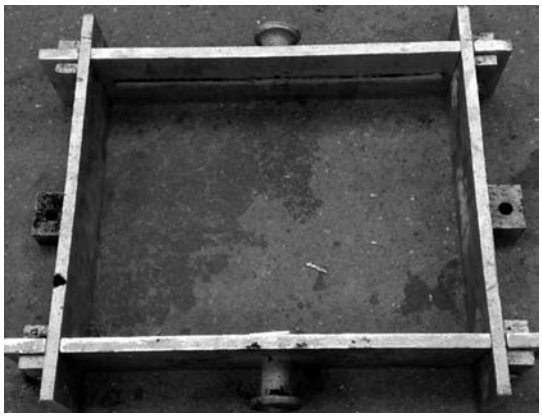

Figure 4: Split flask

Figure 5: Detail of split flask

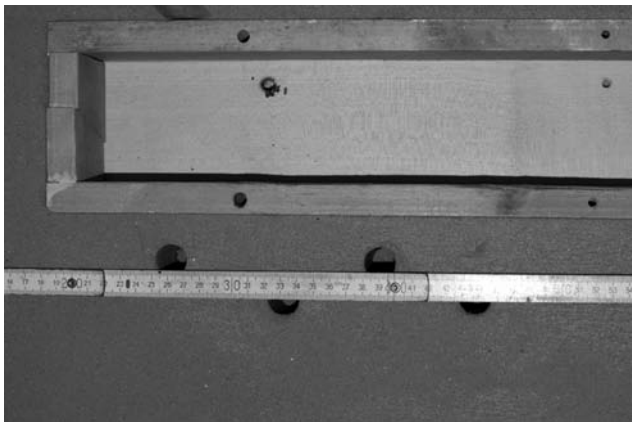

Figure 6: Cast model with wooden insert (removed before closing the form) and holes for placing pure bentonite dedicated for the neutron diffraction experiments.

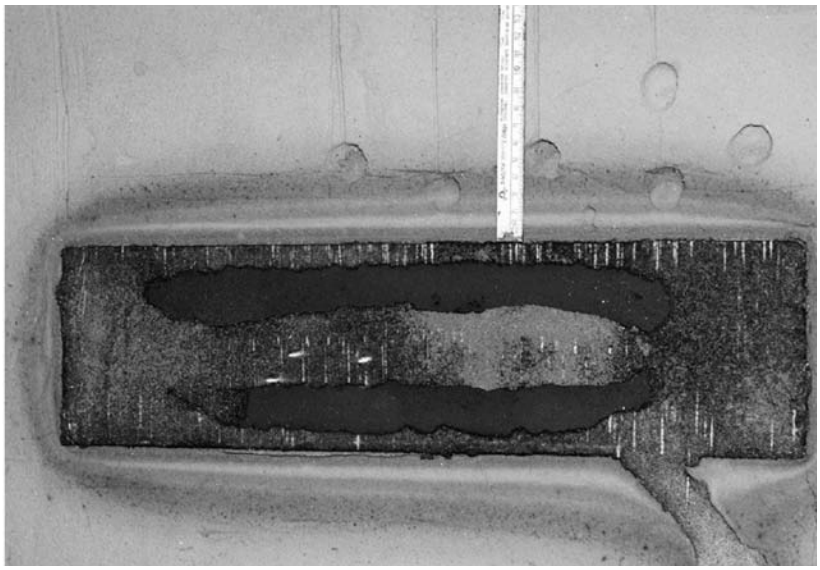

Figure 7: Casting box showing the iron casting and the bentonite holes. Note the zoning around the cast iron. Samples were taken starting adjacent to the cast iron (zone 1) and proceeding towards the outer range (zone 5).

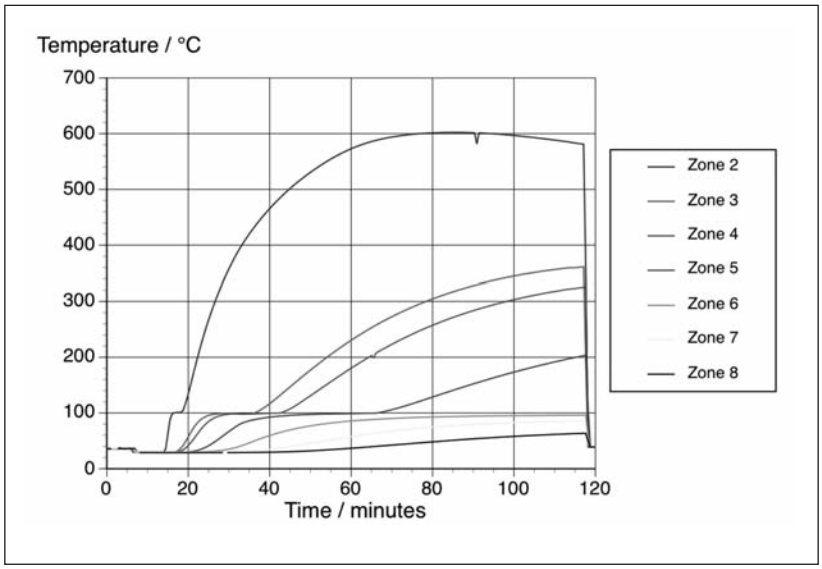

Figure 8: Temperature profiles of casting experiment from 19.8.2009. The data of zone 1 are not shown because the temperature sensor failed shortly after the beginning of the cast process. Note that zones 2 to 5 remained for a certain time at 100 °C and then experienced higher temperatures, whereas zone 6 and higher did not exceed 100 °C.

The five sampled zones ranged from 0-2, 2-3, 3-4.5, 4.5-7, 7-10, and 10.5-17.5 cm, respectively (Fig. 7). The temperature profiles are visualized in Fig. 8. Possible changes in the hydration pattern were minimized by freezing the samples in liquid nitrogen and keeping them in a freezer at -18 °C till further analyses.

Cation exchange capacities

The cation exchange capacities (CEC) were measured in a time series with time steps of 15, 30, 45, 60, 120 and 180 minutes on the raw bentonite and on two moulding sand-mixtures after the cast experiment. The objective of this CEC analysis was to find out, whether heating causes clay interlayer contraction, which would result not only in decreased CEC values at short exchange times, but also in a different exchange kinetic. It was already shown in 2009 that the Cu-Trien exchange reached its final value already after 15 minutes exchange time. The zones, however, varied in the absolute amounts of the CEC.

Meanwhile, the smectite contents of the sand mixtures (FR32 and bentonite D) were determined by XRD. Due to the low contents of smectite in the sand (0.08-0.10 g/g) the accuracy of the smectite content was checked on a pure quartz sample. The Rietveld refinement of this pure quartz resulted in approximately 0.02 g/g

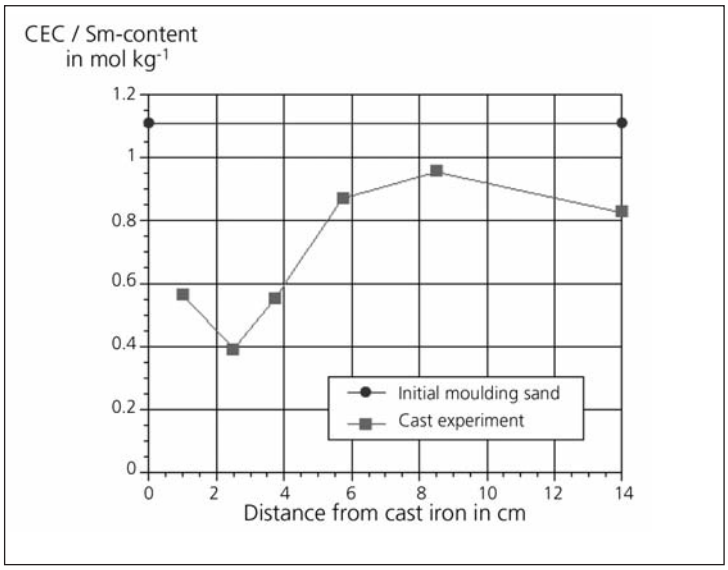

Figure 9: The cation exchange capacities are normalized to the smectite content from XRD. Note that even the outermost zone does not reach the value of the initial mixture (blue line). Bentonite H, experiment 19.08.2009.

smectite. This offset is mainly due to the overlapping of smectite reflections with strong quartz reflections, where minor misfits in the peak profile results in an overestimation of smectite. Therefore, the smectite contents of the sand mixtures were corrected by this bakkground value.

Figure 9 shows that the smectite contents decrease with decreasing distance to the cast iron except for the first zone, which differs also in the CEC value from the second zone. Since the smectite contents vary less than the CEC, the CEC normalized to the smectite content show a pronounced increase with increasing distance (Figure 9).

Two aspects deserve attention: Although the most distant zone had a smectite content similar to the initial material, the original CEC was not measured within an exchange time of one hour. It is also striking that no 10 Å phase was detected by XRD, although the diminished CEC values could result from irreversible layer contraction. The current explanation for this discrepancy is the possible influence of the kinetics of rehydration of possibly contracted interlayers. The CEC values were determined on material, which was defrosted immediately before the analysis. The XRD analyses, however, required grinding in ethanol (with some water), which had to evaporate afterwards. This treatment could have provided time for re-expansion of contracted interlayers. This hypothesis can be checked by CEC measurements with exchange times much longer than one hour.

For all samples, the loss on ignition (> 1100 °C) was determined by STA. The results correlate well with the findings from residual moisture detection. The mass change is decreasing with decreasing distance to the cast body and it correlates significantly with the smectite contents from XRD (Fig. 10). The regression line, however, does not intercept next to zero. A theoretical calculation shows that the first two samples could have released only structural OH groups, whereas the samples of zones 3 to 6 and the initial sample contained additional interlayer water (see the dividing green line in Fig. 10). Furthermore, about one third of the smectite has obviously transformed into a phase, which escaped quantification by XRD. It is tempting to assign this amount to the cis-trans character of bentonite H: The current fitting resulted in 0.7 cis- and 0.3 transvacant layers. This agrees with the maximum temperatures reached in the different zones (Fig. 8). In zone 1 a partial dehydroxylation was likely because of Tmax > 600 °C. In zone 2, which reached 600 °C, the remaining smectite retained its theoretical OH content. The next zones had T < 350 °C, which seems too low for a dehydroxylation, but it should be noted that

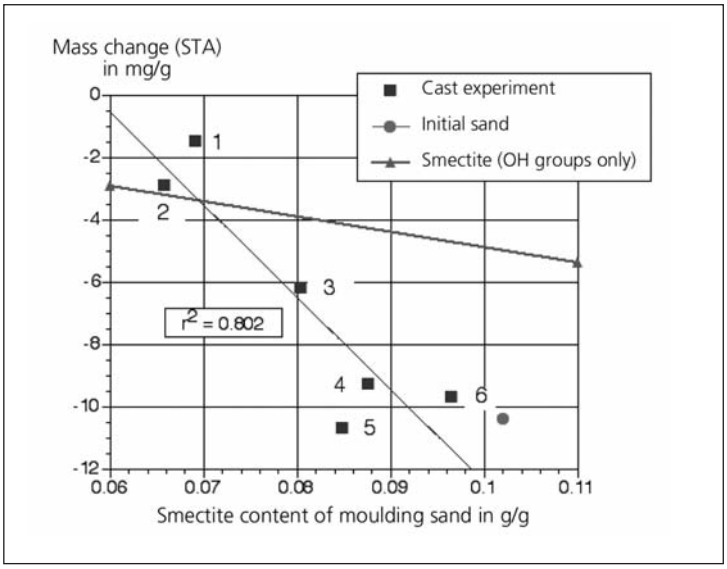

Figure 10: Plot of mass changes determined with Simultaneous Thermal Analysis (STA) versus smectite contents of the moulding sands determined by XRD. The green line demarks the theoretical mass loss of a fully dehydrated Na smectite.

for kinetic reactions a too low temperature can be balanced (at least, in parts) by longer reaction times. This hypothesis remains to be checked.

Neutron radiography

To investigate the dehydration of the moulding sand (pore water, smectite interlayer water) in detail with neutron radiography, we designed a special casting simulation experiment to in-situ visualize the loss of water. Instead of pouring a hot metal melt into a casting mould, the experimental set up consists of a casting mould (Fig. 11) which is dropped on a hot copper block (Fig. 12). The design of the sand box with a Cu-bottom plate ensures an ideal heat transfer corresponding to the thermal shock-like heat induction during a real casting process. Thermocouples were placed within the moulding sand to provide simultaneously information on the temporal temperature gradients. They were set in direct contact and in one, two, three, four and five centimeter distance to the Cu-bottom plate (Fig. 13). The experiments have been performed in the research reactor FRM II in Garching with the instrument ANTARES.

In a first set of neutron radiography experiments we tested the functionality of the simulation experiment, the sand box charging and moulding material rehydration conditions. Also possible sand thicknesses and different bentonite contents were checked to achieve the best contrast in the radiographs.

The experiments allowed us to successfully simulate the shock-heating of the mould material in an industrial casting process. We were able to visualize fluxes of water during the dehydration process with high temporal and spatial resolution. But the experiments revealed also that the moulding material was neither homogeneously loaded nor homogeneously rehydrated. Zones of different density and with different water contents were visible in the radiographs.

For a better data evaluation a second set of experiments was necessary, where we implemented the following modifications:

– optimization of the homogeneity of the mould material (an improved compaction mechanism/procedure while loading the sand mould was essential to avoid zones of different density within the moulding material).
– improved rehydration process (right after the addition of the water, which was lost by dehydration, the sands were homogenized for 3 minutes with a blender).
– utilization of thermocouples with higher resolution at fixed reference positions in all experiments (allowed a precise comparison of the thermal parameters in the different experimental runs).

We performed five evaluable experiments (compare table 2). The mould thickness of 7cm and a bentonite content of 12 wt% were kept constant in all experiments. The casting mould

Figure 11: Top view of sand box

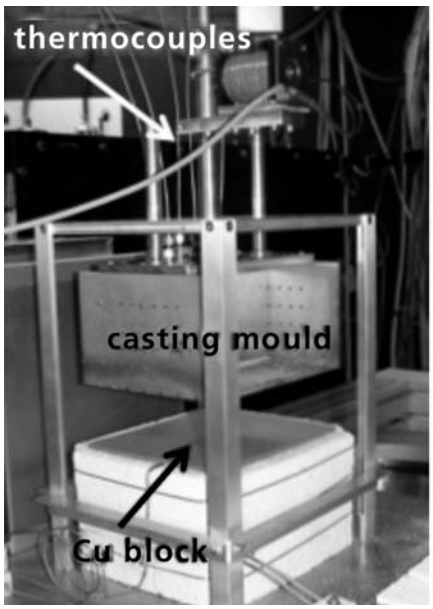

Figure 12: Casting simulation experiment

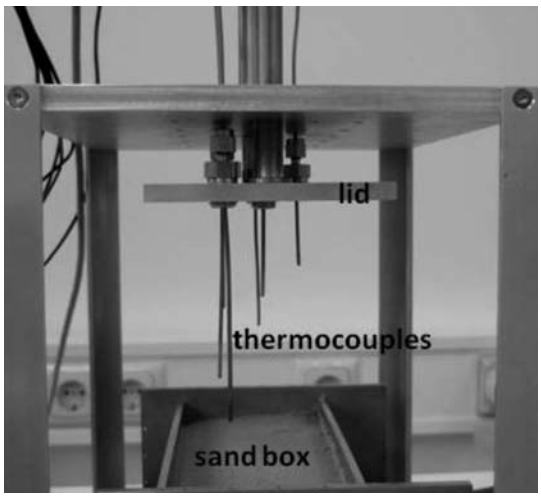

Figure 13: Thermocouples placed in different depths

was dropped onto the hot Cu plate when ~650 °C were reached. The charging of the mould and compaction of the mould material were carried out in the same way to ensure the same homogeneous density conditions for all experiments. The experiments were focused on the following aspects:

– effect of multiple cycles of previous dehydration/rehydration on the performance of the moulding sand
– effect of 2wt% carbonaceous material as a functional additive to the moulding sand
– performance of different types of bentonite (W: natural Na-bentonite, D: soda activated Ca-bentonite)

The radiographs (Fig. 14) show in general the removal of water from the mould. The process initiates at the heat source at the bottom. The grey scale depends on the water amount in the moulding sand. The dehydrated material appears light-grey while the hydrated material is dark-grey. The experiments revealed a progressive movement of water in the sand and resolved a broad transitional zone from the pristine hydration state of the sand to a fully dehydrated state. At this transitional zone positions can be determined which on one hand relate to the onset of pore water dehydration and on the other hand relate to the completion of interlayer dehydration.

The evaluation of radiographic experiments revealed the following results:
The optimization of the loading procedure and rehydration process was successful and reproducibly yielded a homogeneous and equally distributed moulding material in the sand box. The temperature-time data at fixed points of reference in the different experiments showed that the thermal history of all experiments matched (within the remaining data error) and that the thermal parameters (conductivity, heat flow) in different sands were constant (Fig. 15). A constant compaction and homogeneity of the different sand moulds in the different experimental runs can, thus, be inferred and the kinetic dehydration parameters of different experimental runs were directly comparable.

Table 2: Performed experiments and used moulding sands.
Exp.: experiment number
a: bentonite type.
b: additive (2 wt% of carbona-ceous material).
c: condition of moulding sand prior to radiographic experiment.
* Experimental data were not evaluable.

Exp.	a	b	c	sample name
1	W	-	4 x dehy. & rehy.	W_rec
2	W	C	3 x dehy. & rehy.	WC_rec
3	W	-	raw	W_raw
4	W	C	raw	WC_raw
5*	D	-	3 x dehy. & rehy.	D_rec
6	D	C	3 x dehy. & rehy.	DC_rec

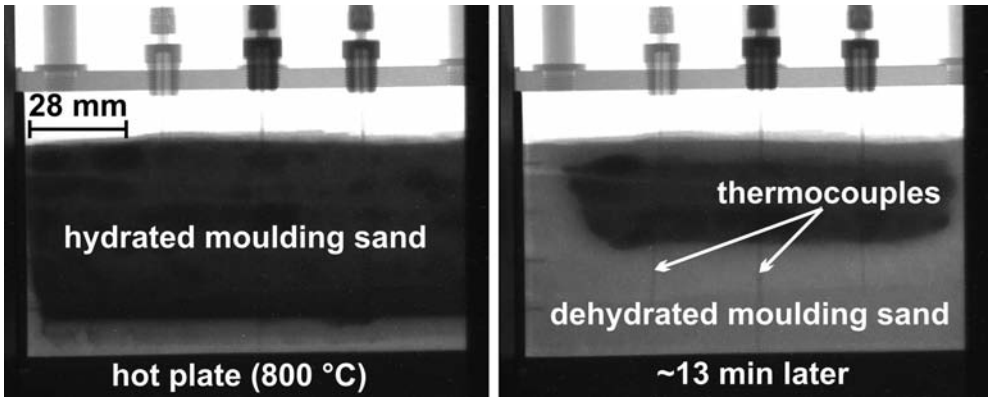

Figure 14: Two Neutron radiographs showing the dehydration of moulding sand.

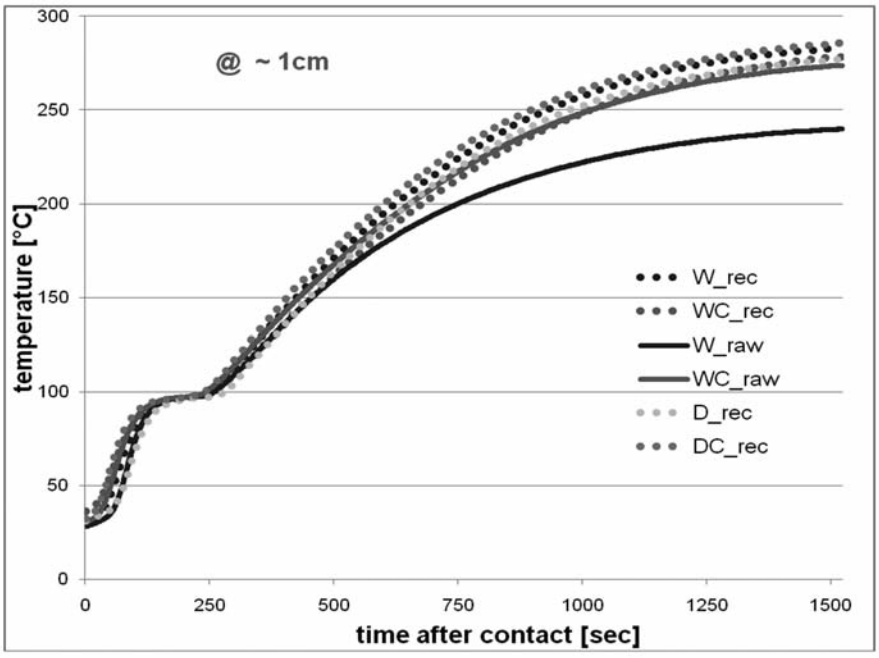

Figure 15: Comparison of temperature developments of all experiments at ~1 cm distance to the bottom Cu-plate. The thermal history of all experiments matches within the remaining data error.

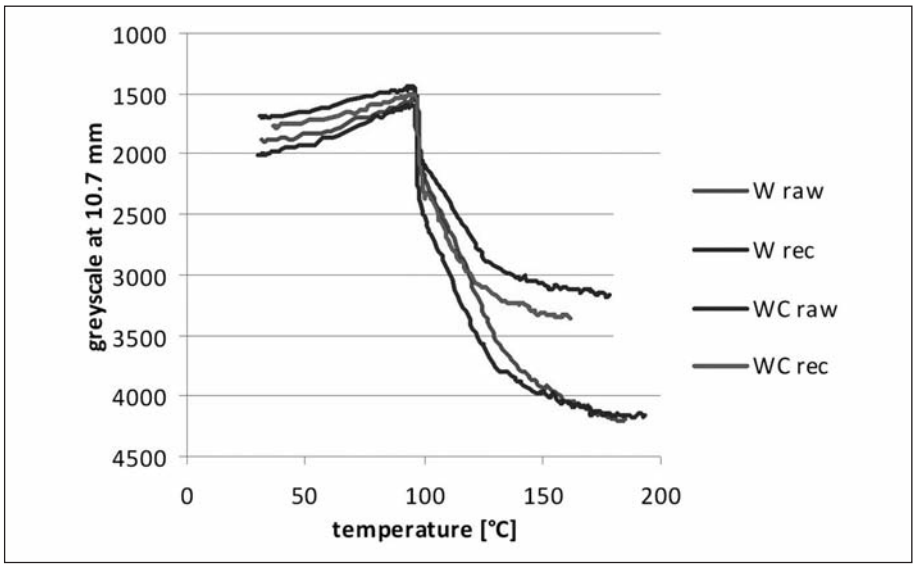

Fig. 16: Image grey scale, representing the amount of water, versus temperature measured at ~ 1cm distance to Cu-bottom plate. The recycled samples show the tendency to dry slightly faster as the corresponding raw material, more water is released at 100 °C.

The evaluation of the amount of water in the different moulds (represented by image grey scales as a measure of the intensity of neutron scattering) versus distance from the hotplate at the bottom, time, and temperature revealed:

- In all runs, the general behavior was that the dehydration started with a vaporization of pore water at about 100 °C. On top of this range, an enrichment of water in the areas <100 °C could be observed. This water accumulation may be caused by steam pushing pore water upwards and condensing in the areas <100 °C.
- Dehydration was not completed at 100 °C. A decrease of neutron scattering intensity could be observed up to about 170 °C. This decrease very likely correlated with the release of water from the clay interlayers via the pore system (Fig. 16).
- The comparison of raw and recycled sands revealed that from recycled sands more water was released around 100 °C while the total amount of water was almost constant in both types of experiments. As a consequence the recycled sands were drying slightly faster.
- Sands with carbon containing additives scatter the neutron beam much stronger at temperatures >100 °C than additive free sands – although scattering <100 °C is almost identical. These differences may indicate interaction of C with water or hydrogen >100 °C which retard the H-release.

The amount of material obtained from the radiography experiment was only sufficient for mineralogical analyses, but not for the mechanical tests such as compactibility. Therefore, a new experimental setup was designed, which will allow to mimick the radiography experiment on a much larger scale. It consists of fireclay bricks and a copper plate, which is heated to 600 °C in a furnace. Then the bricks are placed in a frame. On top of them the copper plate rests. Both layers are kept at the desired temperature by blow torches placed below (Fig. 17). The flask filled with moulding sand is then placed on the copper plate. The temperature evolution in the mould is monitored by thermocouples. After obtaining the desired temperatures in the moulding sand, the flask can be removed quickly from the copper plate and cooled down for subsequent sampling.

Neutron powder diffraction

The raw and the recycled moulding sands with bentonite W and WC show *d* (001) values of about 19 Å (Fig. 19), but subtle differences in

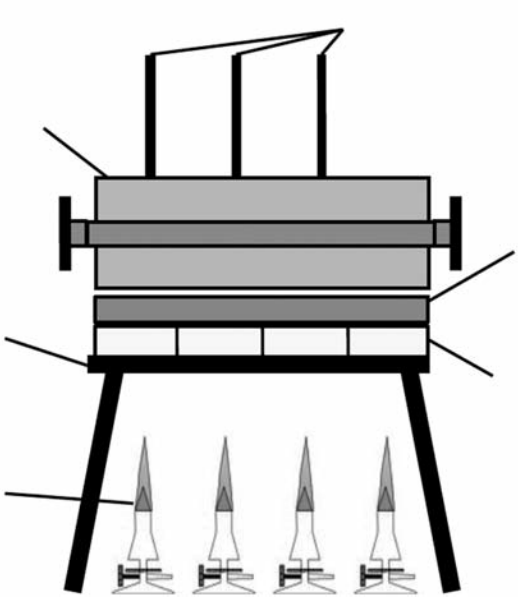

Figure 17: Scheme of the heating system

Figure 18: Pilot test of the heating system

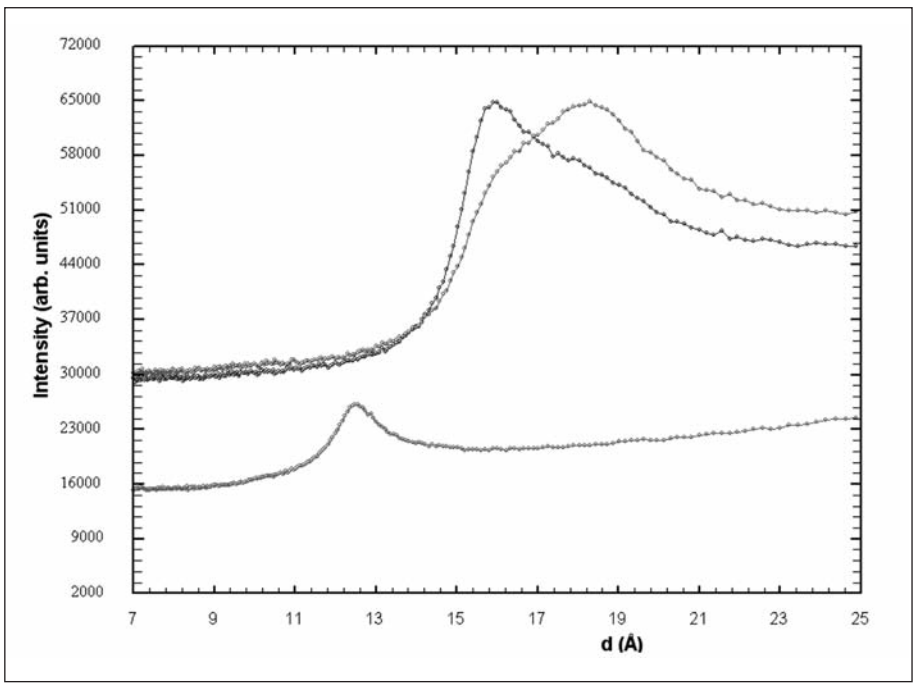

Fig. 19: Neutron powder diffraction pattern of moulding sand with 12%wt Bentonite D (measured at DMC, PSI).

peak shape indicate the presence of higher *d*-values in recycled smectites. These differences might be related to the different water release visible in the neutron radiographs. Dehydrated smectites, directly measured after the casting simulation, reveal d values of about 12.3 Å. The differences in the hydration states of bentonite D containing moulding sand is significant (Fig. 20). Again the recycled sand with a*d* (001) maximum at about 18.8 Å shows higher d values than the raw material.

Industrial drying

Following the initial characterization of several bentonites, two raw materials were selected for further testing. Quantities of about 100 tons each were activated with 2.5 % soda and stored on a stockpile. The homogeneity of the raw material mixture was documented by sampling and analysing chemical and mineralogical contents. Samples taken before milling consisted of large chunks of clay, which had a pronounced variability in their mineralogical composition (Table 3).

Milling of these clays was done in a MPS 100, a cylinder ball mill. Establishing constant milling condition required the processing of about 20 tons of material. The mill inlet was fed with pre-mixed material, which was pre-dried to about 30 %-wt. water content. Coarse material such as rock fragments or too large aggregates were removed during the mil passage. Monitoring of the size distributions and the temperatures at various times showed that the outgoing material had residual water contents of less than 7 %-wt. Moreover, temperatures reached 110 °C, which is above the recommended maximum temperature of 90 °C for drying bentonites. The different particle size classes 04 and 07 differed substantially in their water uptake as measured by Enslin-Neff. Furthermore, the swelling volumes of class 04 is significantly higher than that of class 07.

Table 3: Mineralogical analyses of three clay chunks (S.D.: Standard deviation, CV: coefficient of variation).

Sample	Quarz	Smectite Ca	Microcline Intermediate	Monalbite	Kaolinite Ideal
Be1_100312	0.139	0.711	0.049	0.101	0.000
Be2_100312	0.037	0.824	0.071	0.069	0.000
Be3_100312	0.060	0.681	0.133	0.092	0.034
Average	0.078	0.739	0.085	0.087	0.011
S.D.	0.044	0.061	0.036	0.013	0.016
CV in %	55.7	8.3	42.1	15.4	141

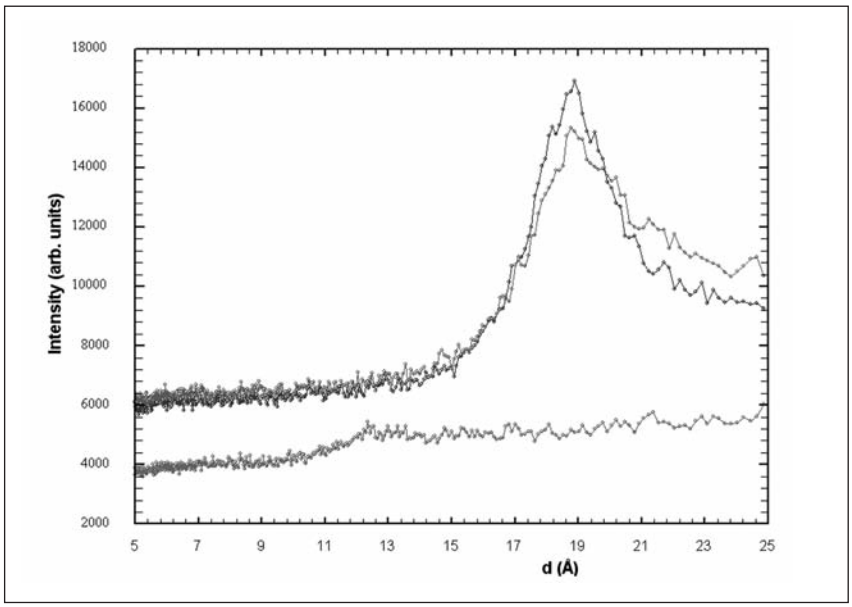

Figure 20: Neutron powder diffraction pattern of moulding sand WC with 12%wt bentonite and 2 wt% C (measured at SPODI, FRM II) show different hydration states.

Summary
In the research project HYDRASMEC small-scale industrial experiments provided samples, which were used to identify the potential processes, which lead to differences between hot steam interaction in industrial applications versus laboratory procedures. X-ray diffraction measurements in combination with time-resolved CEC measurements revealed that the smectites dehydrate depending on the temperature and water pressure regime, but show also rehydration dynamics, which have not been fully investigated yet. The kinetics of the dehydration process has been assessed with neutron radiography, which allowed to establish a two-dimensional time-position characterization of the water redistribution process in a mould sand. Conditions for posible steam interaction have also been identified in the industrial drying process.

References
Berghout, A., Tunega, D. and Zaoui, A. (2010) Density functional theory (DFT) of Na/Mg/Ca/Sr/Ba-exchanged montmorillonites. Clays and Clay Minerals 58, 174-187.

Bickmore, B.R., Hochella, M. E. Jr., Bosbach D., and Charlet L. (1999). Methods for performing atomic force microscopy imaging of clay minerals in aqueous solutions. Clays and Clay Minerals, 47, 573- 581.

Köster, H. M., Ehrlicher, U., Gilg, H. A., Jordan, R., Murad, E. and Omnich, K. (1999) Mineralogical and chemical characteristics of five nontronites and Fe-rich smectites. Clay Minerals 34, 579-599.

Ufer, K., Stanjek, H., Roth, G., Dohrmann, R., Kleeberg, R. and Kaufhold, S. (2008) Quantitative phase analysis of bentonites by the Rietveld method. Clays and Clay Minerals 56, 272-282.

The impact of mineral and rock surface topography on colloid retention

Fischer C. (1,2)*, Darbha G.K. (1), Michler A. (1), Schäfer T. (3), Lüttge A. (2)

(1) Georg-August-Universität Göttingen, Abt. Sedimentologie/Umweltgeologie, Goldschmidtstr. 3, D-37077 Göttingen, Email: cornelius.fischer@geo.uni-goettingen.de

(2) Rice University, Dept. of Earth Science & Dept. of Chemistry, 6100 Main Street, Houston, Texas 77251-1892, U.S.A., Email: aluttge@rice.edu

(3) Institut für Nukleare Entsorgung,Forschungszentrum Karlsruhe, Postfach 3640, 76021 Karlsruhe, Email: schaefer@ine.fzk.de

* Coordinator of the project

Abstract

Overall goal of this GEOTECHNOLOGIEN project called »The impact of mineral and rock surface topography on colloid retention« is a systematic approach to determine, characterize, and quantify the interaction between rough mineral surfaces and colloidal particles. A previous systematic study using pitted calcite single crystal surfaces yielded results about the general correlation between surface roughness parameters and the efficiency of colloidal retention under electrostically unfavorable conditions (*Darbha et al. 2010*). Here we present results about (i) the controlled variation of colloidal retention at well-defined, artificial surface structures, (ii) the characterization and quantification of sources and sinks of natural particles in a quasi-closed system that is used as a test site for field experiments, and (iii) the quantitative experimental results about the retention of particles on natural rock surfaces that allows for a predictive approach to natural systems. In detail, the following results are discussed in this report:

(i) As an analog to rough mineral surfaces with halfpores in the submicron size, the deposition behavior of latex colloids was studied on a regular pit pattern (pit diameter = 400 nm, pit spacing = 400 nm, pit depth = 100 nm). Effects of hydrodynamics and colloidal interactions in transport and deposition dynamics of a colloidal suspension were investigated in a parallel plate flow chamber. The experiments were conducted at pH ~6.6 under both favorable and unfavorable conditions (in terms of electrostatic forces) using carboxylate functionalized colloids to study the impact of surface topography on particle retention. The influence of particle diameter variation (0.3-2 µm) on retention of monodisperse as well as polydisperse suspensions as a function of flow velocity over a wide range was studied. The impact of surface topography deviations was found to be more significant for smaller colloids (0.3 and 0.43 µm). Larger colloids (1 and 2 µm) beyond a critical velocity of 7×10^{-5} and 3×10^{-6} m/s tend to detach from the surface irrespective of the impact of roughness since drag forces exceed adhesion forces. For polydisperse suspensions, an increase in both polydispersity and fluid flow velocity resulted in the decrease of colloid deposition efficiency due to enhanced double layer repulsions. Hematite colloids of quasi-spherical shape with diameters of about 950 nm showed a higher deposition flux compared to spherical latex colloids of equivalent size. These experimental results provide quantitative constraints for the prediction of particle retention as a function of fluid-flow

velocity, polydispersity, and particle shape and size.

(ii) The investigation of the source (iron sulfide-bearing rocks), the processes of particle generation (oxidative weathering, acidic mine water conditions, mine water mixing), the particle transport, and the deposition of particles at water-rock interfaces within the well-defined system of an abandoned alum slate mine enables a first-order approach for balancing of particle retention at rough surfaces in nature. The quantification of particle concentration in the mine outflow as well as the quantification of the deposited material enables an estimation of the kinetics of particles retention within such a system. For comparison, experiments were conducted to get laboratory results about the kinetics of particle retention using substrates with similar ranges of topography variations.

(iii) Colloid adsorption experiments at natural rock samples were performed using black slate and micrite limestone as substrates. Micrite samples were etched to obtain variances in surface roughness and topography. Generally, surface steps at grain boundaries are the major cause for the overall roughness variations. A positive correlation between surface roughness of micrite surfaces and the surface-normalized density of adsorbed particles was found. For surface sections < 20 µm, a remarkable dispersion of the surface-normalized particle density was found. We conclude that the variance in surface reactivity responsible for the recognized variance in particle deposition is caused by the density of grain boundaries of the rock material. An analog experiment using a grid pattern with varying grid line density confirmed this conclusion: A strong correlation between line density and adsorbed particle density was found. The results presented here show the quantitative impact of surface topography variations on colloid retention under electrostically unfavorable conditions. An important application of these results is their utilization as an input parameter for predictive approaches to the fate of colloids in the environment.

1. Introduction

Understanding the colloidal particle deposition mechanism at fluid-solid interfaces is important to address a variety of environmental and industrial processes. Important examples are the protection of particle adsorption in semiconductor manufacturing (*HEROUX et al., 1996*), the control of colloidal deposition (such as polypeptides) in bio-engineering (*ZHENG et al., 2004*), the transport of pathogenic microorganisms (*BALES et al., 1991*) and heavy metals (*BAUMANN et al., 2006*) in the aquatic system, as well as the prediction of colloid formation and deposition in nuclear waste repositories (*SCHAFER et al., 2004; SCHAFER et al., 2009*). Numerous studies have been conducted to investigate the significant factors governing the particle retention mechanisms in the subsurface environments focusing on fluid phase composition (*PRESCOTT et al., 2002; SCHALDACH et al., 2006*), the properties of colloids and media (*ZHUANG et al., 2005*), and physical and chemical conditions of the flow (*JOHNSON et al., 2007; JOHNSON and TONG, 2006; TONG and JOHNSON, 2006; TORKZABAN et al., 2007*).

The transport and deposition of colloidal particles in porous media such as sediments or sedimentary rocks under unfavorable conditions is of great importance to understand the capture of particles in the environment (*BRADFORD and TORKZABAN, 2008; CHANG and CHAN, 2008*). Although there are various hypothesis proposed in the literature to explain the deviation from the traditional classical filtration theory (*BRADFORD et al., 2003; BRADFORD and TORKZABAN, 2008*), until now the fate of colloid transport and retention is still poorly understood. As a consequence, the quantitative prediction of particle retention in nature (at mineral, rock and soil surfaces) is still almost impossible. In many natural processes, the deposition of colloids on surfaces is explained by chemical and charge heterogeneity of surfaces, impurities etc. (*FILBY et al., 2008*). Under *unfavorable* conditions, however, where repulsive electrostatic forces between mineral surface and particles prevail, an increase of the importance of roughness for deposition of col-

loids was concluded and the quantitative impact of surface roughness has to be included into predictive considerations (*ALONSO et al., 2009; DARBHA et al., 2010*). This is also underlined by the fact that a multitude of minerals (both sedimentary grains and mineral colloids) carry a negative surface charge under neutral pH conditions, that results in the common situation of electrostatically unfavorable conditions (*KOSMULSKI, 2002; KOSMULSKI, 2004; KOSMULSKI, 2006; KOSMULSKI, 2009*). Although theoretical and experimental investigations suggest an enhanced colloid deposition with increasing surface roughness, it is often disregarded. Recent experimental work conducted at field sites (*GECKEIS et al., 2004; MORI et al., 2003*) and in the laboratory (*DELOS et al., 2008*) in the context of colloid mediated radio nuclide migration depicted the deposition of colloids at rough rock and mineral surface under favorable conditions. More detailed, batch sorption experiments were performed to study the interaction of gold nanoparticles with rough granite interfaces (*ALONSO et al., 2009; ALONSO et al., 2007*). The experimental comparison of favorable vs. unfavorable electrostatic conditions showed non-negligible colloidal retention at the crystalline rock under unfavorable electrostatic conditions influenced by surface roughness. Results of experiments performed by Das and co-authors demonstrated that surface roughness provides a large enough restraining torque in predicting the hydrodynamic detachment of particles (*DAS et al., 1994*). In the experiments carried out for colloid straining and filtration in saturated porous media, the surface roughness of the grains caused an increased colloidal retention due to enhanced collision efficiency by a factor of 2 to 3 (*AUSET and KELLER, 2006*). Calculations of DLVO interaction energy between a sphere and simulated membrane surfaces predict the significant reduction in the energy barrier with increasing surface roughness (*HOEK and AGARWAL, 2006; HOEK et al., 2003*). Most of the theoretical work is based on interfacial study between positive protrusions and spherical colloids where the particle is several orders of magnitude larger in size compared to the asperity (*BHATTACHARJEE et al., 1998; MARTINES et al., 2008*). The importance of interaction between a surface with negative asperities (pits/holes/etch pits) was investigated in context to the recent colloid probe technique experiments on a rough membrane composed of peaks and valleys (*BOWEN and DONEVA, 2000*). While results predict that peaks have a decreased magnitude of EDL repulsions compared to valleys, the adhesion rate was found to be higher for valleys compared to peaks (*BHATTACHARJEE et al., 1998; HOEK et al., 2003; MARTINES et al., 2008*). Furthermore, experimental results show that the van der Waals (vdW) contact interactions of a Polystyrene latex sphere and a rough silicon substrate reduced the interaction energy by 90% because of the effective larger separation distance between them (*COOPER et al., 2000*). This is according to a recent colloid deposition study on a rough mineral surface (etched calcite) were etch pit walls were the preferred adsorption sites (*DARBHA et al., 2010*). Moreover, the deposition rate was shown to be a function of etch pit depth and density.

In the light of these observations and calculations, deeper insight into the interaction between particles and rough surfaces is required. The questions how surface roughness variations of the substrate can influence the colloidal deposition, what fundamental processes are related to the removal of fine particles from rough surfaces in a hydrodynamic flow, as well as what are the preferred sites for particle adsorption related to substrate surface roughness or charge variations are still unanswered. More specifically, the interplay between (i) applied hydrodynamics, (ii) the variation of colloid size and polydispersity, and (iii) substrate surface topography variation (roughness) during the complex deposition process requires deep quantitative insight.

Here we report the results of our investigations during the second year of the GEOTECHNOLOGIEN project: »The impact of mineral and rock surface topography on colloid retention«. In detail, this overview provides information about the following investigations:

(i) Influence of varying surface charge, hydrodynamic conditions, and polydispersity on particle retention on well-defined synthetically surfaces (silicon wafer surfaces, APTES and oxidized) that mimic natural mineral and rock surfaces
(ii) Mineral vs. latex particle adsorption
(iii) Natural colloids : Shape, size and aggregation as constraints to particle adsorption experiments
(iv) Natural rocks as adsorbents: The example of micrite limestone
(v) Influence of pit wall density variation on particle retentions: An analog study
(vi) Outlook: The evolution of fluid-rock interfaces and the formation of grain coatings

2. Methods and Material

2.1. Colloidal Particles

Carboxylate polystyrene latex colloids (d= 0.3, 0.43, 1, 2 µm) were purchased from Postnova Analytics. The hematite (α-Fe_2O_3) colloids were synthesized by the forced hydrolysis of $FeCl_3$ (*MATIJEVIC and SCHEINER, 1978; RAMING et al., 2002*). For preparation, an aqueous suspension of 0.0315 M $Fe_2Cl_3 \cdot 6H_2O$ in 0.005 M HCl was placed in a hot oven at 100°C for 1 week. The resulting sample was allowed to cool and was centrifuged several times by resuspending the colloids to avoid any excess $FeCl_3$ or other impurities. The size of the hematite colloids was 955 ± 96 nm.

2.2. Silicon wafer samples

Silicon wafers with (100) orientation were purchased from AMO GmbH. Wafers were cleaned using acetone and isopropanol followed by piranha acid. After a thorough rinsing in water the wafers left in air for complete oxidation for 5 to 7 days. For surface functionalization with APTES (*Aldrich, USA*), the substrates were cleaned with piranha acid and rinsed with water. Subsequently, they were dried under a flow of pure nitrogen. The dry substrates were then immersed in a 10 % APTES in methanol solution for 60 min followed by thorough rinsing in methanol and again dried under flow of nitrogen (*VAN LOENHOUT et al., 2009*). Layer thikness is ~0.9 nm and ~0.6 nm for SiO_2 and APTES, respectively (*MITCHELL et al., 1994; VAN LOENHOUT et al., 2009*). Typical dimension of the silicon sample was 4 mm x 4 mm x 0.68 mm.

2.3. Rock samples

Slate rock samples were cleaved and cut to obtain subsamples with dimensions of 4 mm x 4 mm x 1 mm. Micrite samples were cut to a size of 10mm x 5mm x 5mm. The surface was polished. Subsamples were etched for 60' and 120'. Resulting surface root-mean-square roughness (*Rq*) was 70 nm, 85 nm, and 100 nm, respectively.

2.4. Zeta potential and photon correlation spectroscopy

Zeta potentials and photon correlation spectroscopy (PCS) measurements of the colloids were performed using a ZetaPlus (Zeta Potential Analyzer, Brookhaven Instruments). The Smoluchowski equation was applied to convert electrophoretic mobility measurements of the colloids to zeta potentials. The ζ-potential measurements were performed at pH = 6.6 in 10^{-2}M NaCl. The respective zeta potential values for 0.3, 0.43, 1, 2 µm were -52, -63, -45, -47 mV, respectibely. The constant average diameters for the polydisperse colloid mixture(s) from the PCS measurements showed that suspensions were stable during the duration of the experiments. The zeta potential of the hematite colloids was -25 ± 5 mV.

The ζ-potential of both oxidized and APTES functionalized silicon wafer sample surfaces was determined by a streaming potential analyzer (Anton Paar Surpass Electrokinetic Analyzer) with plane-parallel channel cell method at ionic strength of 10^{-2} M NaCl solution. The point of zero charge (PZC) for oxidized silicon surfaces was found to be at pH ~ 3-4 and the PZC of the APTES functionalized silicon surfaces was found to be at pH ~8.7 (*WU et al., 2006*).

2.5. SEM analysis of natural particles as well as adsorbed material

A Cryo-FE-SEM, FEI Quanta 200 FEG, with

Edax EDX detector was used to investigate shape and chemical composition of natural particles. Slurry of suspended particles was put on a glass sample holder and dried.

2.6. Laser Particle Sizer (LPS)

Natural material was sampled from encrustations. The solid samples were elutriated. Suspensions were separated into grain size classes < 2 µm and ≥ 2 µm using the Atterberg method. The particle size distribution (PSD) of the resuspended colloids was analyzed with a laser particle analyser from Beckman & Coulter (Laser Particle Sizer (LPS) LS 13320). Analyzed particle size range was 0.04 µm to 2000 µm. The particle analyzer applies the technology of elastic light scattering (ELS) for particle size characterization. The size calculation is based on either Fraunhofer diffraction or the Mie theory. To get information of particle size in the sub-micrometer range a so called polarization intensity differential scattering (PIDS) technology is implemented in the particle analyzer. Several optical models can be applied to optimize the PSD results, depending on the nature of the solid, the suspending fluid and the wavelength of the incident laser beam. Very critical values are both the refractive index and the adsorption coefficient. The physical constants were taken from the literature (*CARPER, 1999*). In the case of particle aggregates, particularly for the poorly crystalline Fe oxides hydroxides, an effective refractive index was calculated after the suggestions in literature (*GREGORY, 2009*) and applied to the collected data. This approach takes into account the typical difference between the refractive index of a single solid particle and a particle aggregate. The aggregate may show a clearly lower density than the single grain and hence a lower refractive index. According to these considerations, the effective refractive index can be obtained from the ratio (*f*, volume fraction) of the total solid volume of the aggregate and the total volume of the aggregate (enclosing volume):

$$f = k^{\frac{D-3}{3}}$$

D = fractal dimension, k = number of particles. For the iron oxides a fractal dimension (D) of 2.5 was chosen and the particle number was set to 50'000 for 500 nm spherical aggregates (according to *Gregory, 2008*). The volume weighted relative refractive index, *mF*, is given by

$$m_F = f(m-1)+1$$

with m = relative real refractive index (single grain/suspension medium). So we obtain an effective refractive index, RI_{eff}

$$RI_{eff} = m_F \times RI_{fluid}$$

For the PSD analysis of the iron oxides a RI_{eff} of 1.47 is chosen. An adsorption coefficient of 0.1 is taken. This is an appropriate value for iron oxide as well as for silicateaggregates (*CARPER, 1999*).

2.7. XRD analysis of natural particles

Mineral particles from precipitation experiments as well as from resuspended grain coating material were analyzed using a Philips X'Pert MPD diffractometer that was equipped with a PW 3373/00 Cu LFF x-ray tube and a PW 3050/10 goniometer. The chosen scan range for poorly crystalline iron oxides hydroxides was from 10 – 70° 2Θ with a step size of 0.04° 2Θ, time per step was 20 s. Better crystallized material from encrustations were analyzed with a scan range of 2 - 75° 2Θ, step size 0.02° 2Θ, time per step 2 s.

2.8. ICP-OES

The concentration of Fe, S, P, Si, Al, Ca, Na, K, Mg, Mn, Zn, Cu, Mo of mine water samples and of precipitation samples was measured using a ICP-OES (PerkinElmer, Optima 4300 DV). Filtration of the mine water and from the precipitation experiments was performed using a filter with pore size of 0.025 µm. The filter cakes were digested with $HClO_4$ before analysis.

2.9. Flow-through experiments

The colloidal deposition experiments using silicon wafer samples were conducted in a rectangular parallel-plate channel fluid cell made of Teflon. The inner dimensions of the cell were 60 mm x 10 mm x 3.4 mm. The substra-

te was oriented parallel to the flow direction. After use, the particle suspension was discarded. For comparison and in order to quantify the influence of half pores on the substrate surface, the colloid deposition experiments were conducted for both plane and rough substrates. Exposition time was 40 min. The Peclet number and the Reynolds number for the parallel plate flow chamber were calculated based on the following equations (*BAKKER et al., 2002*):

$$Pe = \frac{3Q_{pp}r_c^{\,3}}{4wb^3D_\infty}$$

$$Re = \frac{\rho Q_{pp}}{(w+2b)\upsilon}$$

(Q_{pp}: flow rate; r_c: particle radius; w: width of the flow chamber; b: half-depth of a parallel plate flow chamber, D_{oo}: particle diffusion coefficient; ρ: fluid density, and v: viscosity)

The flow rate in cell was adjusted to obtain the required Peclet number. For experiments with individual colloid deposition experiments the implemented Peclet number range was 10^{-4} to 1. For the here applied flow rates, the Reynolds numbers is in the range of 0.004 to 26.

Adsorption experiments with micrite surface were performed in a Teflon flow-through cell. Particle concentration was adjusted to 24 x 10^6 and 24 x 10^7 particles/ mL in 10^{-2} M NaCl solution and pH = 9 was adjusted using 0.01M NaOH. Before the micrite surface was exposed to a colloidal suspension, it was polished and subsequently etched in a flow-through cell for 60 and 120 min in 0.0004M H_2SO_4 solution (pH = 4.7) to produce a variance in surface roughness of the micrite samples. A systematic calcite dissolution study by *Lea et al.* (2001) showed that dissolution kinetics is significantly reduced by an increased carbonate concentration (>900 µM) in the solution. Therefore, in order to minimize the dissolution of calcite during the deposition experiments, and to avoid the instability of the colloidal system due to the released calcium into the system, a concentration of 700 µM of $NaHCO_3$ was added to the colloidal solution.

To sustain electrostically unvaforable conditions close to the PZC of calcite, the experiments were conducted at the close point of zero charge of calcite (pH_{pzc}=8.8-8.9) (*SCHMIDT et al., 2009; SOMASUNDARAN and AGAR, 1967*). Experiments were performed at room temperature (22 °C).

2.10. Vertical Scanning Interferometry (VSI)

The characterization and quantification of surface topography and roughness variations was carried out using a ZeMapper vertical scanning interferometer, manufactured by Zemetrics Inc., Tucson, AZ. VSI is an optical surface scanning method that provides a large field of view of up to several mm^2 and a vertical resolution of < 1 nm and a lateral resolution of about 200 nm (*LUTTGE et al., 1999*). For our measurements we applied white-light interferometry mode as well as blue-light monochromatic phase-shift mode. Several Mirau objectives were utilized. SPIP software (Image Metrology A/S) was used for surface data analysis as well as for particle characterization and quantification. Statistical topography parameters, so-called roughness parameters (*e.g., DONG et al., 1992; DONG et al., 1993; DONG et al., 1994a; DONG et al., 1994b*), were applied to evaluate surface topography data obtained by VSI measurements. We applied converged roughness parameters (*FISCHER and LÜTTGE, 2007*) to get information about size, frequency, and distribution of surface building blocks responsible for variations in surface topography variations.

2.11. Quantification of colloidial deposition at calcite surfaces

The individual number of colloids adsorbed was counted using SPIP software datasets. The kinetics of the colloidal deposition was determined by calculating the dimensionless Sherwood number (Sh) (*KLINE et al., 2008*),

$$Sh = \frac{J\,a_p}{C_0\,D_\infty}$$

where a_p is the radius of the particle, C_0 is the bulk colloidal concentration, D_∞ is the bulk dif-

fusion coefficient and, *J* is the deposition flux and was found by determining the initial slope of the number of deposited colloids versus time and the value was normalized to the area under consideration.

2.12. 3D computed tomography of newly-formed minerals in sandstones

A Phoenix x-ray Nanotom (180 kV / 15W nanofocus computed tomography (nano CT) system) was used to get spatial information about the distribution of iron oxide encrustation in sandstones. Sandstone samples were cut to a size of 3 mm x 3 mm x 3 mm. Samples were mounted to a glass stick. Resulting voxel size of the obtained data set was 3 µm x 3 µm x 3 µm.

3. Results and Discussion

This chapter provides information about three main parts of our research performed during the second year of this project period. The first section shows results from our experimental work about particle adsorption at well-defined, machined surface structures (chapter 3.1). The second section (chapter 3.1) provides information about both sources and sinks of colloids at a location used as a »natural laboratory« to study the fate of particles in the environment. Chapters 3.1 - 3.4 present and compare results obtained from experiments using both natural rock as well as well-defined machined sample surfaces as adsorbent.

3.1. Impact of surface functionalization, surface topography, and particle size on particle retention

Favorable conditions (APTES coated surfaces) vs. unfavorable conditions (silicon oxide layer): Regardless of particle diameter, the colloid deposition flux is always higher for APTES coated surfaces compared to a silicon oxide surfaces (Fig. 1). The simple reason for this result is the existence of attractive vs. repulsive electrostatic forces (positively charged silica surface with exposed amino groups vs. negatively charges silicon oxide surfaces) (*KLINE et al., 2008*).
More interesting is the size-depending behavior of J as well as the difference in *J* for rough vs. smooth surfaces. A minimum of deposition flux J was found for 1 µm colloids (Fig. 1). The slight increase in *J* for colloids with d = 2 µm vs. d = 1 µm could be caused by the common interception (Fig. 2). In the absence of an energy barrier, for non-Brownian particles the gravitational force is not an important factor (*ELIMELECH, 1994*). The 0.3 µm colloids experienced the highest ratio in *J* for smooth vs. rough surface deposition (pit diameter = 400 nm, pit spacing = 400 nm, pit depth = 100 nm). The *J* ratio decreases with an increase in particle size. Thus, it can be noticed that the effect of surfa-

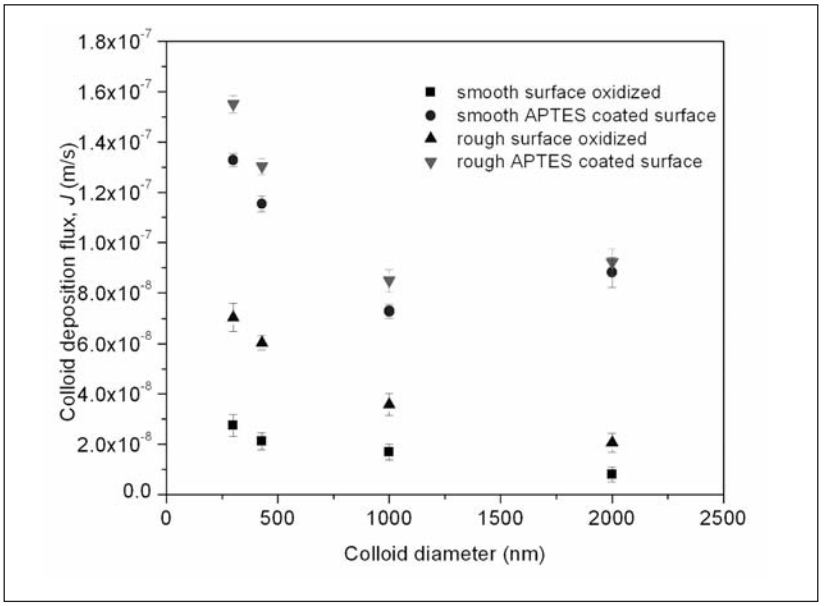

Figure 1: Comparison of colloid deposition flux of carboxylated latex colloids of different sizes (constant fluid flow velocity = 1.3 x 10^{-5} m/s) for smooth and rough surfaces. The influence of surface roughness on particle retention is reduced for larger colloids and under electrostatically favorable conditions.

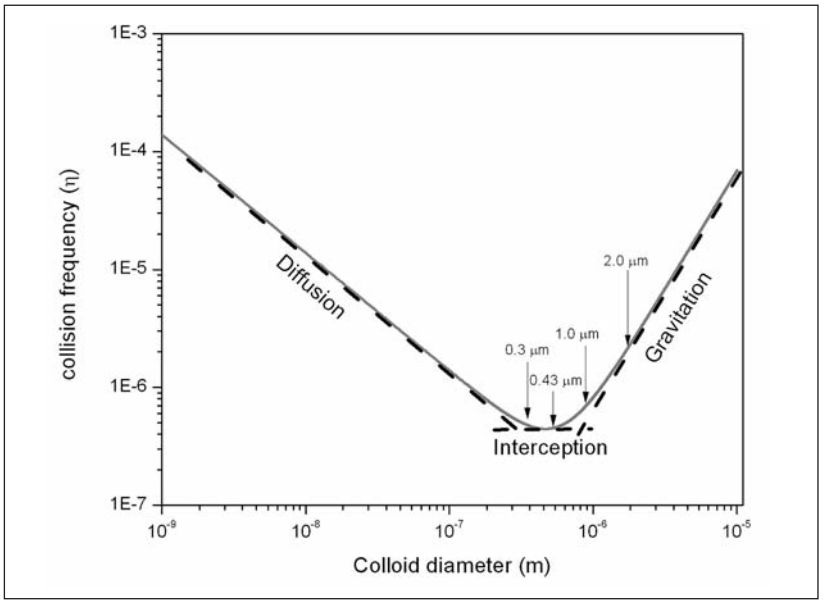

Figure 2: Collision frequency efficiency for a single collector at fluid velocity 1.3 x 10^{-5} m/s, viscosity = 8.9 x 10-4 Pa s, colloid density = 1.05 g/cm^3, fluid density = 1 g/cm^3.

ce roughness is more pronounced for smaller colloids compared to larger colloids. Compared to the classical filtration theory (CFT) (Fig. 2), the observed colloid deposition behavior is in partial agreement with the predictions of CFT. Filtration theory does not consider the surface charge effects, physical forces acting at the interface, and substrate surface geometry for calculation. The theory assumes that colloids were irreversibly retained in the primary minimum of the DLVO interaction energy distribution (*BRADFORD and TORKZABAN, 2008; ELIMELECH and OMELIA, 1990; JOHNSON et al., 2007; JOHNSON and TONG, 2006*). Hence, the here observed differences in size-dependant colloid deposition rates between experimental results and calculations according to the filtration theory can be explained by the influence of surface topography deviations.

According to fundamental studies about physical forces acting during particle-surface interaction (*BRADFORD and TORKZABAN, 2008*), several mechanisms may play a role either for attachment or detachment, such as rolling, dragging, lifting (Fig. 3). As reported in the literature, rolling plays an important role to remove a particle from the surface under laminar flow conditions. Particle rolling can be initiated regardless of its size even at the smallest flow rates (i.e., at lowest Reynolds numbers) (*BURDICK et al., 2001*). In order to remove a particle from the surface, the hydrodynamic torque applied to the particle must exceed that of the adhesion torque (*TORKZABAN et al., 2007*). Unlike a smooth surface, a rough surface can change the center of rotation and therefore in case of a rough surface a larger applied torque is required to remove a particle from the surface (*BURDICK et al., 2005*). Because of the here discussed influence of hydrodynamic forces on the efficiency of particle retention, a detailed experimental approach was performed to quantify the impact of fluid-flow velocity variation on the deposition of particles at rough surfaces. The results are reported in chapter 3.6 and compared to the particle deposition results using micrite surfaces.

The impact of polydispersity on the efficiency of particle retention at rough surfaces was investigated. A general result is that an increase in polydispersity leads to a decrease in the deposition efficiency. Moreover, as the polydispersity increases (from 0.3-0.43 µm vs. 1-2 µm) the difference in deposition efficiency between smooth vs. rough surfaces decreases. This can be explained by the hydrodynamic interactions between particles (i.e., the so-called hydrodynamic blocking effect (*ADAMCZYK et al., 1995; DABROS, 1989*)). When a particle approaches to an already adsorbed particle, it will be redirected from the initial (shortest) path due to EDL repulsions. For our investiga-

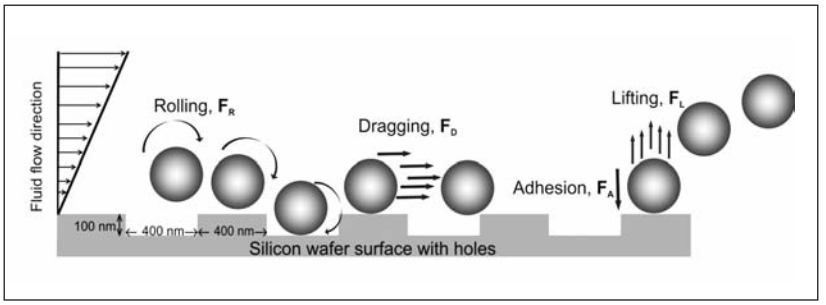

Figure 3: Schematic profile diagram to visualize the common forces at a fluid-solid body interface. As an example, a particle with d = 0.3 µm is shown at the structured surface applied for the study reported here.

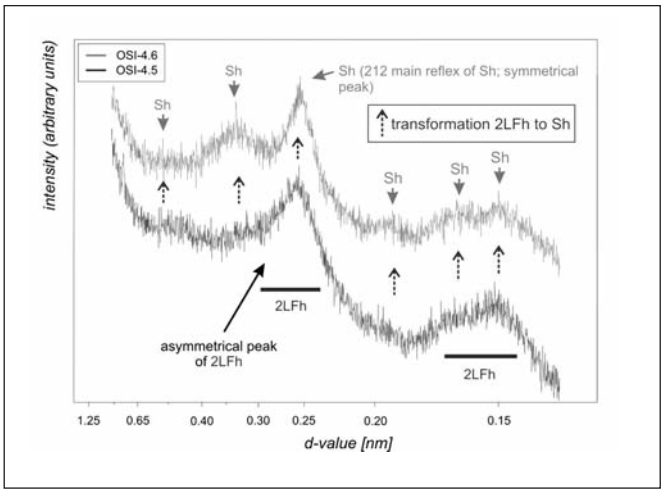

Figure 4: Precipitation experiments using mine water (pH = 2.5) showed the occurrence of 2L Ferrihydrite (Fh) as first precipitations after increase of pH to 2.8. Subsequently, the pH was increased to 4.5. In this pH-range ferrihydrite is not stable with respect to schwertmannite (Sh).

tions, the hydrodynamic blocking was found to be significant for rough surfaces under flow conditions with Pe > 1. The resulting shadow area is a narrow zone with an extension in the size range of the attached particle (*VAN LOENHOUT et al., 2009*). Hence, the electrohydrodynamic blocking increases with an increase in particle size.

Hematite colloids were used for comparison experiments. The experiments were carried out to quantify differences in the adsorption behavior of similar-sized and similar-shaped particles of different mineralogy. We observed an increased deposition of hematite colloids compared to polystyrene was observed. Again, the already discussed influence of roughness was reported for both favorable and unfavorable conditions. For a given fluid velocity (1.3 x 10^{-5} m/s), the deposition ratios (rough vs. smooth surfaces) under electrostically unfavorable conditions were calculated to be 5.47 (hematite) vs. 2.41 (polystyrene). A potential reason of the remarkable difference in retention efficiency could be the difference of the particles surface topography (*DRELICH, 2006; HOEK and AGARWAL, 2006; MARTINES et al., 2008*).

3.2. Natural colloids in an alum slate mine system

Precipitation of particles

The origin, transport, and retention of iron oxide/hydroxides was studied in an abandoned alum slate mine. During oxidative weathering, iron sulfides are removed from the black, organic-rich alum slate (*FISCHER et al., 2009*). Source for iron oxide colloids in this system is the dissolved matter in the acidic mine water of the Morassina mine, Thüringisches Schiefergebirge (*FISCHER et al., 2007*). At sample site »Oberer See«, the acidic water (pH ~ 2.5) contains relatively high concentrations of iron and sulfur. Precipitation experiments in the laboratory using sampled mine water showed the occurrence of first precipitations after increase of pH to 2.8. Subsequently, the pH was increased to 4.5. The precipitations consisted of a 2-line ferrihydrite (2LFh) (Fig. 4). In the mentio-

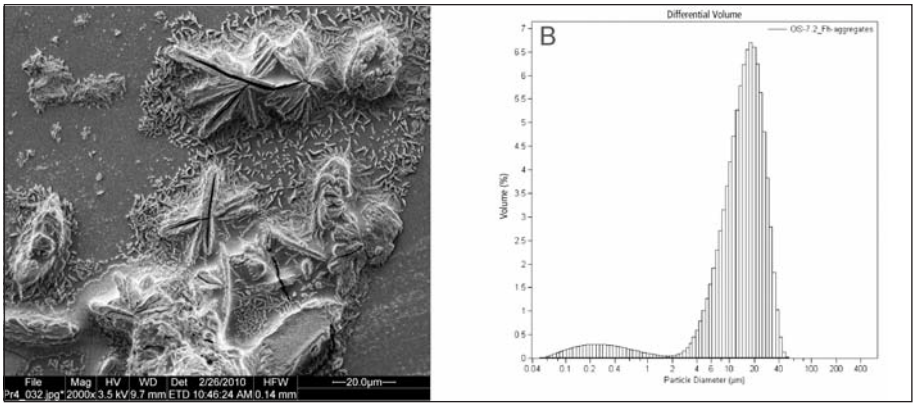

Figure 5: Schwertmannite was formed during precipitation experiments in the laboratory using sampled mine water (left: SEM image, right: LPS particle size analysis)

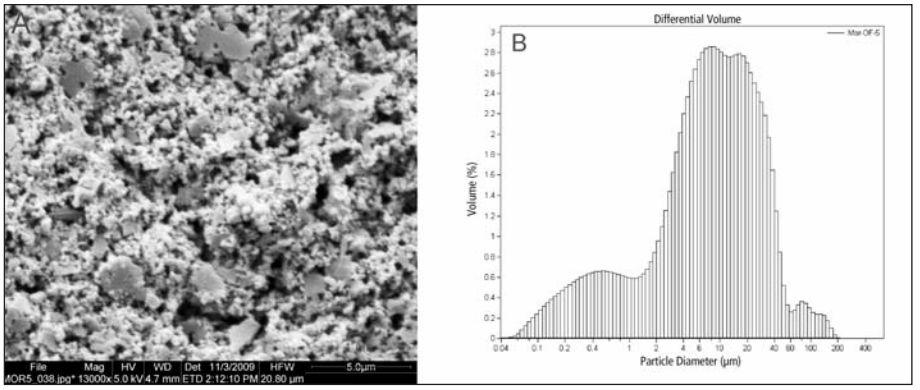

Figure 6: Particles sampled from encrustations formed in the streambed of the minewater of the Morassina outflow (left: SEM image of 2-line ferrihydrite (2LFh) particles and aggregates, right: LPS particle size analysis.

ned pH-range (2.5 – 4.5), ferrihydrite (Fh) is not stable with respect to schwertmannite (Sh). The XRD- and ICP-OES-analysis showed that there is a slow (in the range of months) transformation from 2-line ferrihydrite to Sh. This transformation came along with an incorporation of sulfate and hence with a decrease in pH. The initial precipitation of 2-line ferrihydrite instead of the thermodynamically favored schwertmannite was caused by high rates of hydrolysis in the laboratory experiments (135 µmol OH / mmol Fe / min). Under natural conditions however the direct precipitation of ferrihydrite has not been observed in sulfate-rich environments. This is caused by common slow hydrolysis rates in natural systems. Such hydrolysis conditions may also prevail for the most sections of the Morassina mine. Ullrich et al. (2005) showed that the dominant secondary minerals inside the mine consist of schwertmannite (Fig. 5) or XRD-amorphous iron-phosphate-sulfate phases.

Particle coatings (encrustations)

Iron oxide encrustations were sampled in a mine water streambed. Encrustations consist of pure 2-line ferrihydrite. SEM images show the spherical shape of 2-line ferrihydrite particles (Fig. 6). Particle diameter is around 200 - 500 nm. The spherical particles may also form aggregates with diameters of up to several microns. Aggregates may have an isometric as well as a platy shape. The XRD results show that the flaky-shaped particles do not consist of sheet silicates. Particle size distribution was analyzed using laser particle sizer (LPS). The results show for virtually all subsamples a bimodal size distribution. The first size mode confirms the size range of about 200 – 500 nm, visible in SEM images. The second size mode shows however a large portion of aggregated colloidal particles. According to the XRD results, the applied optical model to evaluate the data collected by LPS was calculated for Fh aggregates. For a detailed discussion of calculation of the optical constraints for porous aggregates analyzed by LPS see *Gregory (2009)*.

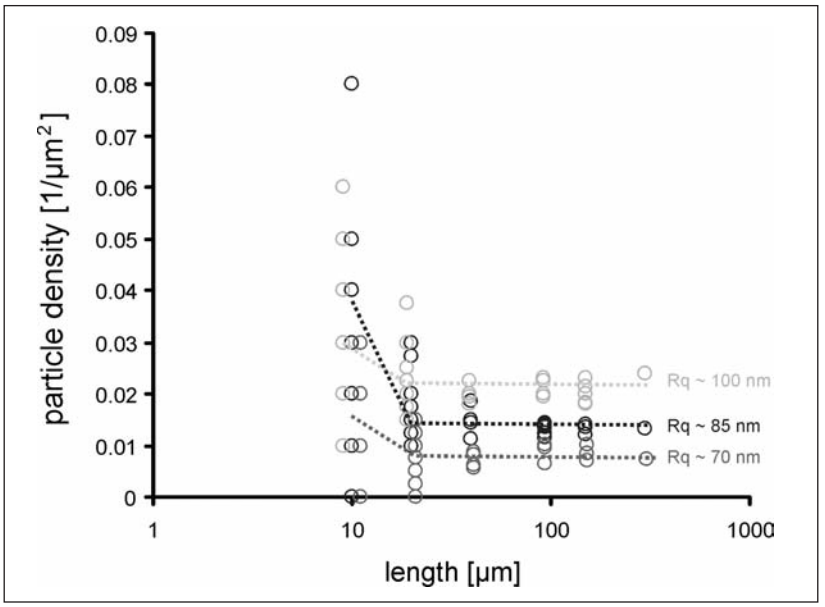

Figure 7: Surface area-normalized particle density on rough micrite surfaces as a function of field-of-view. Note the broad dispersion of particle density for surface sections < 20 µm.

Currently, in-situ adsorption experiments are performed in the streambed to get information about the adsorption kinetics of particles in the mine water. Substrate material of different types of lithographic structures on silicon samples was exposed to the mine water. The in-situ experiments mimic the topographic range known from natural rock surfaces (*FISCHER et al., 2008*). Due to the well-defined differences in pit size, shape, and spacing the expected results will provide important constraints for the evaluation of the results obtained by laboratory experiments.

3.3. Particle adsorption experiments: The micrite surface

Adsorption experiments were performed utilizing a suspension of latex colloids (d = 1 µm) in a flow-through cell. Experiments were carried out close to the PZC of calcite (pH = 8.9, see *Darbha, 2010*) under electrostatically slightly unfavorable conditions (pH ~ 9). The three applied micrite limestone samples showed surface roughness values of *Rq* = 70 nm, *Rq* = 85 nm, and *Rq* = 100 nm, respectively. After adsorption, the spatial distribution of the particle density on micrite surfaces was analyzed as a function of field-of-view. The result shows a relatively broad range (Fig. 7). Particularly, surface sections < 20 µm show a significant increase of the density range. The observed range was found for all of the roughness types (Fig. 7). According to previous results about adsorption at rough surfaces, the mean values of particle density (for large field-of-view sections) show a strong and positive correlation to the root-mean-square roughness Rq. The increase of density dispersion was found for all roughness types as a function of the decrease of the field of view. In fact, there is also an increase of the dispersion range with increasing roughness. The process of dispersion is however not completely governed by roughness variations. We therefore conclude that the dispersion reflects an intrinsic property of the rock that could be related to the density of grain boundaries of this very dense, nonporous rock. We also conclude that this result could act as a general explanation for the spatial inhomogeneity of particle density at rock surfaces after adsorption under electrostatically unfavorable conditions.

3.4. An analog experiment: The impact of lattice-»constant« variation of a machined, well-defined silicon surface on particle retention

The conclusion about the impact of grain boundaries that modulates the roughness variations of the etched rock surface was checked via an analog experiment. A silicon wafer was

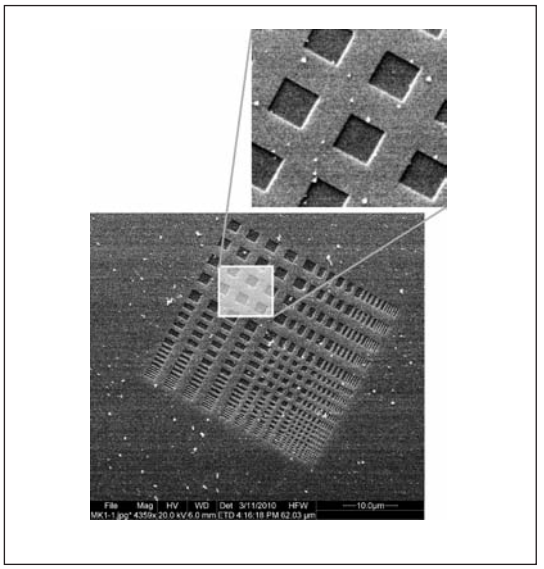

Figure 8: A silicon wafer was machined with pits of constant depth (100 nm) and a step-wise variation of the spacing of its pit pattern. Particle adsorption experiments using latex colloids (d = 60 nm, d = 100 nm) were performed using this sample as an analog for the variation in grain boundary density of mineral aggregates.

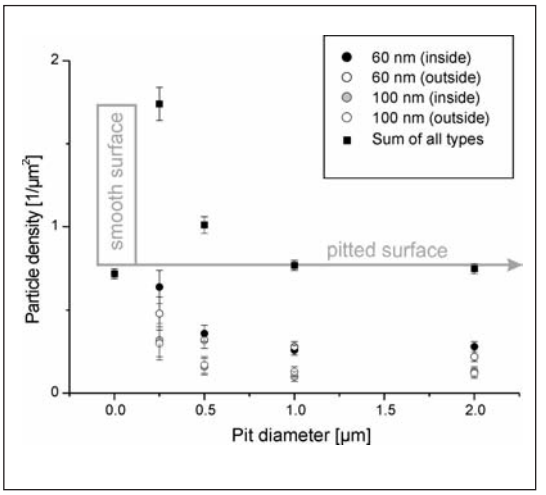

Figure 9: Surface area-normalized particle density (60 nm and 100 nm particles in pits, 60 nm and 100 nm particles outside of pits) as a function of pit size of the analyzed sample region

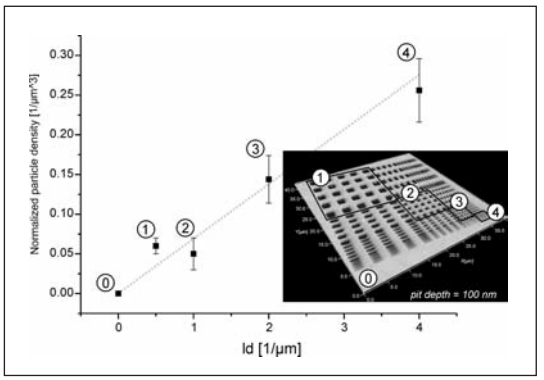

Figure 10: Surface area-normalized particle density as a function of pit wall density (line density, ld)

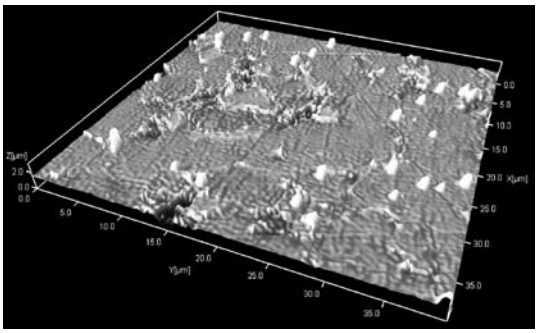

Figure 11: Visualization of adsorbed latex colloids (bright dots) on a micrite surface. The particles adsorbed at grain boundaries of the calcite grain aggregates. The grain boundaries form surface steps (h ~ X0 nm-X00 nm) generated during calcite dissolution.

machined with pits of constant depth (100 nm) and a step-wise variation of the spacing of its pit pattern (Fig. 8). Two types of particles (d = 60 nm, d = 100 nm) were utilized for adsorption experiments in a flow-through cell. Again, the number and surface-normalized density of adsorbed particles was analyzed. As a first result, the overall amount and distribution of adsorbed particles shows a negative correlation to the pit size (Fig. 9). Particle density was also quantified as a function of pit density, i.e., the density of lines or pit walls on a given surface section (Fig. 10). The positive correlation between the normalized particle density and the surface line density provides a robust confirmation the conclusion made in the previous chapter about the impact of grain boundaries on particle retention (Fig. 11).

3.5. Kinetics of particle adsorption on micrite, impact of particle concentration, and fluid-flow velocity on the deposition of particles on a rough micrite surface

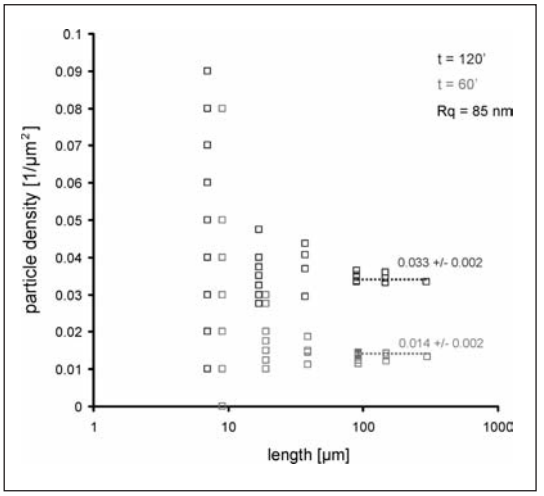

Figure 12: Adsorption of 1µm latex colloids on rough micrite surfaces. Surface area-normalized particle density is shown as a function of field-of-view. Exposition time was 60' and 120', respectively.

Repetitive experiments were performed utilizing micrite surfaces with *Rq* = 85 nm in a flow-through cell to study the impact of parameter variation on the efficiency of particle retention at a rough rock surface.

Mean values of particle density data measured at large field-of-view yielded 0.014 µm ± 0.002 µm² after duration of 60' (Fig. 12). After 120', the density increased to 0.033 ± 0.002 µm². No saturation was found during this short period of adsorption. The preferred sites of adsorption, i.e., the surface steps at grain boundaries are still almost unoccupied after an exposition period of 120'. The dispersion of particle density was however similar for both reaction periods. This underlines again the importance of specific sites that are important for the adsorption of particles on rock surfaces under unfavorable conditions (Fig. 11).

The variation in particle concentration of the applied suspension has no congruent impact on the mean density of adsorbed particles: The increase of concentration by an order of magnitude resulted in an increase of the mean particle density of just about 5. Also the density range is relatively small for small sections (l = 10 µm). We conclude that the simple increase in particle concentration is not able to provide a congruent increase in the particles surface impact probability (see also discussion about the shadow effect, chapter 3.1).

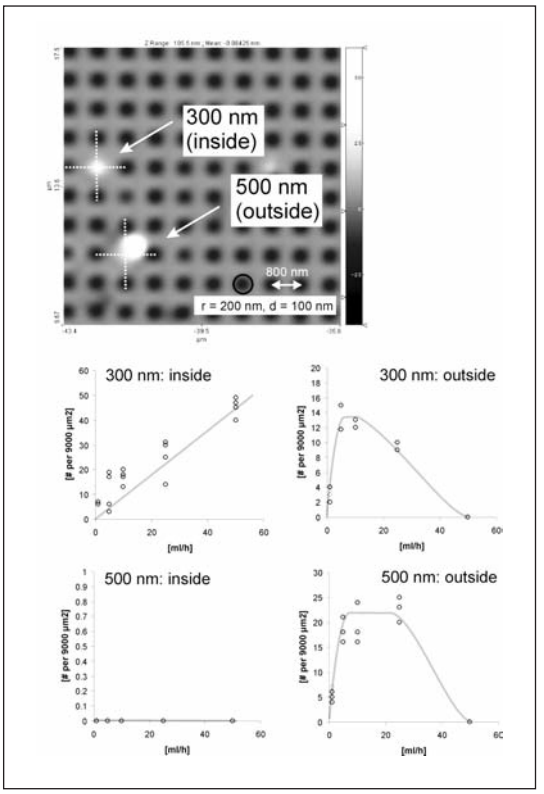

Figure 13: Surface-normalized particle density as a function of fluid-flow velocity. Adsorption experiments were carried out using regular pitted silicon wafer samples and latex colloids (d = 300 nm, d = 500 nm)

The variation in fluid flow velocity has a congruent impact on the mean density of adsorbed particles. This is, however, an inverse correlation: The 10-fold increase in fluid-flow velocity results in a reduction of the mean density of adsorbed particles. Because of this remarkable result the impact of fluid flow velocity variation on the deposition of particles was object of a detailed study (see next section).

3.6. Impact of fluid-flow velocity on the adsorption of particles at rough surfaces

A detailed experimental approach showed the impact of fluid-flow velocity variation on the deposition of particles at rough surfaces. Experiments were carried out using a regular pit pattern on silicon wafers (pit diameter = 400 nm, pit spacing = 400 nm, pit depth = 100 nm). Particle diameters were 300 nm and 500 nm, respectively. The number of particles within pits and outside of pits was analyzed as a function of fluid-flow velocity (Fig. 13). The

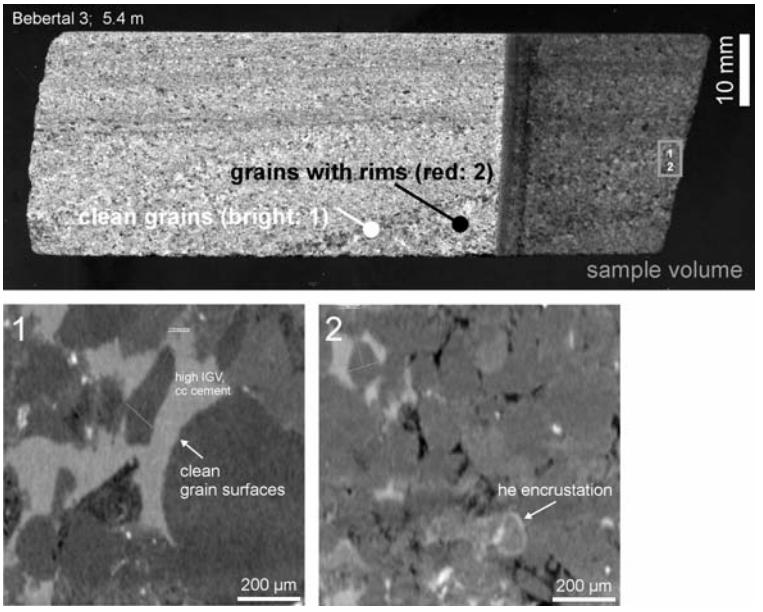

Figure 14: Example of two types of grain coatings in sandstone. Bright laminae (1) consist of grains with clean surface, high intergranular volume (IGV), and high amounts of cements. Hematite grain coatings (2) are responsible for a different diagenetic evolution that leads to remarkable lower IGV. The upper image is an optical micrograph. Images (1) and (2) were collected using an industrial 3D computed tomography system (Phoenix x-ray Nanotom)

impact of fluid-flow velocity on the efficiency of particle retention is very different for particles inside vs. outside of pits. Particles outside of pits attached close to pit walls.

For small particles (d = 300 nm) deposited in pits, a positive and linear correlation was found between particle density and fluid-flow velocity (Fig. 13). Particles attached to the surface outside of pits show however a more complicated behavior as a function of fluid flow-velocity: Both particle sizes show an initial positive correlation. Subsequently, a saturation plateau was found. Here, a further increase of fluid-flow velocity does not result in a further increase of particle retention. Above a critical velocity, the net particle retention decreases as a function of fluid-flow velocity. Further increase of fluid-flow velocity results in no net deposition of particles. The fluid-flow range that results in the reported particle density plateau is similar but not equal for both particle types. The results about particle adsorption as a function of fluid-flow velocity discussed in the previous section represent two points of the complicated function presented here, the plateau situation (lower velocity) as well as the negative correlation (higher velocity).

4. Outlook: The evolution of fluid-rock interfaces and the formation of grain coatings

The results presented here show a variety of input parameters that are able to govern the retention of colloids at rough surfaces under electrostatically unfavorable conditions. Knowledge and application of the parameter ranges investigated here enable quantitative predictions of particle retention in nature and allow for a prediction of dominating processes dur - ing fluid-rock interaction.

The example of sandstone diagenesis (Fig. 14) provides an example how the evolution of particle coatings at fluid-rock interfaces governs the further diagenetic evolution. For the example shown here, the formation of thick iron oxide coatings on sand grains hinder the precipitation of high-volume cement minerals, such as calcite or quartz. During burial diagenesis, the iron oxide-rich sandstone experienced therefore a higher reduction of the intergranular volume compared to the sandstone without iron oxide coatings.

The quantitive data about particle retention may therefore also provide predictive conclusions about the evolution of fluid-rock interfaces.

5. Acknowledgements

The authors thank André Filby and Johannes Lützenkirchen (Institut f. Nukleare Entsorgung (INE), Forschungszentrum Karlsruhe, Germany), Tim Salditt and Mike Kanbach (Institut für Röntgenphysik, Univ. Göttingen), Michael Seibt and Volker Radisch (Institut für Halbleiterphysik, Univ. Göttingen), Stephan Herminghaus and Matthias Schroeter (MPI für Dynamik und Selbstorganisation, Göttingen), Rolf S. Arvidson and Everett Salas (Rice Univ., Houston) for analytical help and fruitful discussions. We thank for financial support (grant # 03G0719A) coming from GEOTECHNOLOGIEN R&D program.

6. References

Adamczyk, Z., Siwek, B., and Szyk, L., 1995. Flow-Induced Surface Blocking Effects in Adsorption of Colloid Particles. J Colloid Interf Sci 174, 130-141.

Alonso, U., Missana, T., Patelli, A., Ceccato, D., Albarran, N., Garcia-Gutierrez, M., Lopez-Torrubia, T., and Rigato, V., 2009. Quantification of Au nanoparticles retention on a heterogeneous rock surface. Colloid Surface A 347, 230-238.

Alonso, U., Missana, T., Patelli, A., Rigato, V., and Ravagnan, J., 2007. Colloid diffusion in crystalline rock: An experimental methodology to measure diffusion coefficients and evaluate colloid size dependence. Earth and Planetary Science Letters 259, 372-383.

Auset, M. and Keller, A. A., 2006. Pore-scale visualization of colloid straining and filtration in saturated porous media using micromodels. Water Resour Res 42, -.

Bakker, D. P., Busscher, H. J., and van der Mei, H. C., 2002. Bacterial deposition in a parallel plate and a stagnation point flow chamber: microbial adhesion mechanisms depend on the mass transport conditions. Microbiol-Sgm 148, 597-603.

Bales, R. C., Hinkle, S. R., Kroeger, T. W., Stocking, K., and Gerba, C. P., 1991. Bacteriophage Adsorption during Transport through Porous-Media – Chemical Perturbations and Reversibility. Environ Sci Technol 25, 2088-2095.

Baumann, T., Fruhstorfer, P., Klein, T., and Niessner, R., 2006. Colloid and heavy metal transport at landfill sites in direct contact with groundwater. Water Research 40, 2776-2786.

Bhattacharjee, S., Ko, C. H., and Elimelech, M., 1998. DLVO interaction between rough surfaces. Langmuir 14, 3365-3375.

Bowen, W. R. and Doneva, T. A., 2000. Atomic force microscopy studies of membranes: Effect of surface roughness on double-layer interactions and particle adhesion. J Colloid Interf Sci 229, 544-549.

Bradford, S. A., Simunek, J., Bettahar, M., Van Genuchten, M. T., and Yates, S. R., 2003. Modeling colloid attachment, straining, and exclusion in saturated porous media. Environ Sci Technol 37, 2242-2250.

Bradford, S. A. and Torkzaban, S., 2008. Colloid transport and retention in unsaturated porous media: A review of interface-, collector-, and pore-scale processes and models. Vadose Zone Journal 7, 667-681.

Burdick, G. M., Berman, N. S., and Beaudoin, S. P., 2001. Describing hydrodynamic particle removal from surfaces using the particle Reynolds number. Journal of Nanoparticle Research 3, 455-467.

Burdick, G. M., Berman, N. S., and Beaudoin, S. P., 2005. Hydrodynamic particle removal from surfaces. Thin Solid Films 488, 116-123.

Carper, J., 1999. The CRC Handbook of Che - mistry and Physics. Libr J 124, 192-+.

Chang, Y. I. and Chan, H. C., 2008. Correlation equation for predicting filter coefficient under unfavorable deposition conditions. Aiche J 54, 1235-1253.

Cooper, K., Gupta, A., and Beaudoin, S., 2000. Substrate morphology and particle adhesion in reacting systems. J Colloid Interf Sci 228, 213-219.

Dabros, T., 1989. Interparticle Hydrodynamic Interactions in Deposition Processes. Colloid Surface 39, 127-141.

Darbha, G. K., Schäfer, T., Heberling, F., Lüttge, A., and Fischer, C., 2010. Retention of Latex Colloids on Calcite as a Function of Surface Roughness and Topography. Langmuir 26, 4743-4752.

Das, S. K., Schechter, R. S., and Sharma, M. M., 1994. The Role of Surface-Roughness and Contact Deformation on the Hydrodynamic Detachment of Particles from Surfaces. J Colloid Interf Sci 164, 63-77.

Delos, A., Walther, C., Schafer, T., and Buchner, S., 2008. Size dispersion and colloid mediated radionuclide transport in a synthetic porous media. J Colloid Interf Sci 324, 212-215.

Dong, W. P., Sullivan, P. J., and Stout, K. J., 1992. Comprehensive Study of Parameters for Characterizing 3-Dimensional Surface-Topography.1. Some Inherent Properties of Parameter Variation. Wear 159, 161-171.

Dong, W. P., Sullivan, P. J., and Stout, K. J., 1993. Comprehensive Study of Parameters for Characterizing 3-Dimensional Surface-Topography. 2. Statistical Properties of Parameter Variation. Wear 167, 9-21.

Dong, W. P., Sullivan, P. J., and Stout, K. J., 1994a. Comprehensive Study of Parameters for Characterizing 3-Dimensional Surface-Topography. 3. Parameters for Characterizing Amplitude and Some Functional-Properties. Wear 178, 29-43.

Dong, W. P., Sullivan, P. J., and Stout, K. J., 1994b. Comprehensive Study of Parameters for Characterizing 3-Dimensional Surface-Topography. 4. Parameters for Characterizing Spatial and Hybrid Properties. Wear 178, 45-60.

Drelich, J., 2006. Adhesion forces measured between particles and substrates with nanoroughness. Miner Metall Proc 23, 226-232.

Elimelech, M., 1994. Effect of Particle-Size on the Kinetics of Particle Deposition under Attractive Double-Layer Interactions. J Colloid Interf Sci 164, 190-199.

Elimelech, M. and Omelia, C. R., 1990. Kinetics of Deposition of Colloidal Particles in Porous-Media. Environ Sci Technol 24, 1528-1536.

Filby, A., Plaschke, M., Geckeis, H., and Fanghanel, T., 2008. Interaction of latex colloids with mineral surfaces and Grimsel granodiorite. Journal of Contaminant Hydrology 102, 273-284.

Fischer, C., Karius, V., and Thiel, V., 2007. Organic matter in black slates shows oxidative degradation within only a few decades. Journal of Sedimentary Research 77, 355-365.

Fischer, C., Karius, V., Weidler, P. G., and Lüttge, A., 2008. Relationship between micrometer to submicrometer surface roughness and topography variations of natural iron oxides and trace element concentrations. Langmuir 24, 3250-3266.

Fischer, C. and Lüttge, A., 2007. Converged surface roughness parameters – A new tool to quantify rock surface morphology and reactivity alteration. Am J Sci 307, 955-973.

Fischer, C., Schmidt, C., Bauer, A., Gaupp, R., and Heide, K., 2009. Mineralogical and geochemical alteration of low-grade metamorphic black slates due to oxidative weathering. Chemie der Erde - Geochemistry 69, 127-142.

Geckeis, H., Schafer, T., Hauser, W., Rabung, T., Missana, T., Degueldre, C., Mori, A., Eikenberg, J., Fierz, T., and Alexander, W. R., 2004. Results of the colloid and radionuclide retention experiment (CRR) at the Grimsel Test Site (GTS), Switzerland – impact of reaction kinetics and speciation on radionuclide migration.

Radiochim Acta 92, 765-774.

Gregory, J., 2009. Optical monitoring of particle aggregates. J Environ Sci-China 21, 2-7.

Heroux, J. B., Boughaba, S., Ressejac, I., and Meunier, M., 1996. CO_2 laser-assisted removal of submicron particles from solid surfaces. J Appl Phys 79, 2857-2862.

Hoek, E. M. V. and Agarwal, G. K., 2006. Exten - ded DLVO interactions between spherical particles and rough surfaces. J Colloid Interf Sci 298, 50-58.

Hoek, E. M. V., Bhattacharjee, S., and Elimelech, M., 2003. Effect of membrane surface roughness on colloid-membrane DLVO interactions. Langmuir 19, 4836-4847.

Johnson, W. P., Li, X. Q., and Yal, G., 2007. Colloid retention in porous media: Mechanistic confirmation of wedging and retention in zones of flow stagnation. Environ Sci Technol 41, 1279-1287.

Johnson, W. P. and Tong, M. P., 2006. Observed and simulated fluid drag effects on colloid deposition in the presence of an energy barrier in an impinging jet system. Environ Sci Technol 40, 5015-5021.

Kline, T. R., Chen, G. X., and Walker, S. L., 2008. Colloidal deposition on remotely controlled charged micropatterned surfaces in a parallel-plate flow chamber. Langmuir 24, 9381-9385.

Kosmulski, M., 2002. The pH-dependent surface charging and the points of zero charge. J Colloid Interf Sci 253, 77-87.

Kosmulski, M., 2004. pH-dependent surface charging and points of zero charge – II. Update. J Colloid Interf Sci 275, 214-224.

Kosmulski, M., 2006. pH-dependent surface charging and points of zero charge III. Update. J Colloid Interf Sci 298, 730-741.

Kosmulski, M., 2009. pH-dependent surface charging and points of zero charge. IV. Update and new approach. J Colloid Interf Sci 337, 439-448.

Lea, A. S., Amonette, J. E., Baer, D. R., Liang, Y., and Colton, N. G., 2001. Microscopic effects of carbonate, manganese, and strontium ions on calcite dissolution. Geochim Cosmochim Ac 65, 369-379.

Luttge, A., Bolton, E. W., and Lasaga, A. C., 1999. An interferometric study of the dissolution kinetics of anorthite: The role of reactive surface area. Am J Sci 299, 652-678.

Martines, E., Csaderova, L., Morgan, H., Curtis, A. S. G., and Riehle, M. O., 2008. DLVO interaction energy between a sphere and a nano-patterned plate. Colloid Surface A 318, 45-52.

Matijevic, E. and Scheiner, P., 1978. Ferric Hy - drous Oxide Sols .3. Preparation of Uniform Particles by Hydrolysis of Fe(Iii)-Chloride, Fe(Iii)-Nitrate, and Fe(Iii)-Perchlorate Solutions. J Colloid Interf Sci 63, 509-524.

Mitchell, D. F., Clark, K. B., Bardwell, J. A., Lennard, W. N., Massoumi, G. R., and Mitchell, I. V., 1994. Film Thickness Measurements of Sio2 by Xps. Surf Interface Anal 21, 44-50.

Mori, A., Alexander, W. R., Geckeis, H., Hauser, W., Schafer, T., Eikenberg, J., Fierz, T., Deguel - dre, C., and Missana, T., 2003. The colloid and radionuclide retardation experiment at the Grimsel Test Site: influence of bentonite colloids on radionuclide migration in a fractured rock. Colloid Surface A 217, 33-47.

Prescott, S. W., Fellows, C. M., Considine, R. F., Drummond, C. J., and Gilbert, R. G., 2002. The interactions of amphiphilic latexes with surfaces: the effect of surface modifications and ionic strength. Polymer 43, 3191-3198.

Raming, T. P., Winnubst, A. J. A., van Kats, C. M., and Philipse, A. P., 2002. The synthesis and magnetic properties of nanosized hematite

(alpha-Fe2O3) particles. J Colloid Interf Sci 249, 346-350.

Schafer, T., Geckeis, H., Bouby, M., and Fanghanel, T., 2004. U, Th, Eu and colloid mobility in a granite fracture under near-natural flow conditions. Radiochim Acta 92, 731-737.

Schafer, T., Seher, H., Hauser, W., Walther, C., Degueldre, C., Yamada, M., Suzuki, M., Missana, T., Alonso, U., Trick, T., and Blechschmidt, I., 2009. The Colloid Formation and Migration (CFM) project at the Grimsel Test Site (Switzerland): Results from the homologue tests. Geochim Cosmochim Ac 73, A1168-A1168.

Schaldach, C. M., Bourcier, W. L., Shaw, H. F., Viani, B. E., and Wilson, W. D., 2006. The influence of ionic strength on the interaction of viruses with charged surfaces under environmental conditions. J Colloid Interf Sci 294, 1-10.

Schmidt, M., Heberling, F., Finck, N., Stumpf, T., Schlegel, M., Dardenne, K., and Bosbach, D., 2009. Institute for Nuclear Waste Disposal Annual Report 2008. In: Geckeis, P. D. H. (Ed.). Forschungszentrum Karlsruhe GmbH, Karlsruhe, Karlsruhe.

Somasundaran, P. and Agar, G. E., 1967. Zero Point of Charge of Calcite. J Colloid Interf Sci 24, 433-+.

Tong, M. P. and Johnson, W. P., 2006. Excess colloid retention in porous media as a function of colloid size, fluid velocity, and grain angularity. Environ Sci Technol 40, 7725-7731.

Torkzaban, S., Bradford, S. A., and Walker, S. L., 2007. Resolving the coupled effects of hydrodynamics and DLVO forces on colloid attachment in porous media. Langmuir 23, 9652-9660.

Ullrich, B., Hantsch, K. U., Müller, K., Seidel, H., and Ullrich, B., 2005. Sekundärmineralbildungen des Alaunschieferbergwerkes »Morassina« bei Beiträge zur Geologie von Thüringen N.F. 12, 41-69.

van Loenhout, M. T. J., Kooij, E. S., Wormeester, H., and Poelsema, B., 2009. Hydrodynamic flow induced anisotropy in colloid adsorption. Colloid Surface A 342, 46-52.

Wu, Z. J., Xiang, H., Kim, T., Chun, M. S., and Lee, K., 2006. Surface properties of submicrometer silica spheres modified with aminopropyltriethoxysilane and phenyltriethoxysilane. J Colloid Interf Sci 304, 119-124.

Zheng, H. P., Berg, M. C., Rubner, M. F., and Hammond, P. T., 2004. Controlling cell attachment selectively onto biological polymer-colloid templates using polymer-on-polymer stamping. Langmuir 20, 7215-7222.

Zhuang, J., Qi, J., and Jin, Y., 2005. Retention and transport of amphiphilic colloids under unsaturated flow conditions: Effect of particle size and surface property. Environ Sci Technol 39, 7853-7859.

Surface and Wetting Properties of Diagenetic Minerals and Sedimentary Grains in Reservoir Rocks (NanoPorO)

Altermann W. (1)*, Drobek T. (1), Frei M. (1), Heckl W.M. (2), Kantioler M. (1), Phuong K.L. (1), Stark R.W. (3), Strobel J. (4)

(1) LMU, Geology, Sedimentology, Crystallography, wlady.altermann@iaag.geo.uni-muenchen.de, tanja.drobek@lrz.uni-muenchen.de, michaela.frei@iaag.geo.uni-muenchen.de, markus@kantioler.de, Kimphuong.Lieu@lrz.uni-muenchen.de

(2) TU Munich, TUM School of Education & Deutsches Museum München, w.heckl@deutsches-museum.de

(3) TU Darmstadt, Center of Smart Interfaces, stark@csi.tu-darmstadt.de

(4) RWE Dea, Hamburg, Joachim.Strobel@rwe.com

* Coordinator of the project

Introduction

Current secondary oil recovery measures allow for the recovery of a maximum of about 33 % of the oil in a reservoir. The remaining almost two third of the energy carrier are lost due to decreasing pressure, pore blocking, water invasion or hydrocarbon fluid adhesion to the rock. Therefore, fluids weakening the adhesion of hydrocarbons to pore walls and increasing permeability of the rock by e.g. mineral cement dissolution, are injected to the deposits in order to augment production. All such measures however, including enhanced oil recovery (EOR) methods such as the injection of supercritical CO_2 may increase the recovery factor of the original oil in place by further 10 % only. Consequently, most of the hydrocarbon wealth in oil and gas reservoirs cannot be extracted and is lost to future generations. It is thus of high importance to understand the fundamental wetting processes in the pore space, to better develop the potential of oil and gas production from reservoir rocks and to secure the fossil energy supply.

In siliciclastic oil and gas reservoir rocks, the pore space typically faces mineralogically varying sedimentary grains and various diagenetic minerals. Most common are mineral surfaces of quartz, feldspar, phyllosilicates, carbonates and iron oxides and hydroxides. This mineralogy surrounding the pore space, and the surface chemistry, topography and roughness on the micro and nano-scale rule the wetting behavior and adhesion properties of hydrocarbon fluids, water, or CO_2 to the pore walls. The dispersion, migration, adhesion and reactivity of fluids in rocks depends also on pressure and temperature conditions, nevertheless, particularly the morphology of pore walls and the pore and pore-throat shapes, have a significant impact on the behavior of the water-gas contact depth (WGC) and on the potential recovery of hydrocarbons from the given reservoir rock.

Each episode of fluid transport through the rock leaves a significant and characteristic trace in cement mineralogy, pore morphology, permeability, but often also in sediment grain or bioclast alteration. Such processes can be defined down to the nanoscale and play a crucial role in further mobility of hydrocarbons in rocks *(Hassenkam et al., 2009*). Sediment wetting varies with the alteration of the surfaces and depends on surface roughness, surface charges, and the chemical composition of the liquid phase (*Al-Futaitsi et al., 2003; Al-Futaisi and Patzek, 2004*). The interfacial tension of

the fluids strongly depends on the composition of the coexisting phases (*Sutjiadi-Sia et al., 2008*). In addition, the presence of a supercritical (sc)CO_2 phase can affect the wetting properties of the other phases due to mass exchange as a function of pressure (*Foullac et al., 200; Sutjiadi-Sia et al., 2008; Jäger and Pietsch, 2009*). It is, however, not clear how the specific conditions of the reservoir (p, T, surface chemistry and morphology) affect the interfacial tension of the relevant fluids. To understand the fundamental physico-chemistry helps to design new technologies for tertiary exploitation measures and for CO_2-storage (Carbon Capture and Storage: CCS). In this project we investigate the relationship between various minerals or grains facing the pore space, to fluids in reservoir rocks and to CO_2 and scCO_2 (*Altermann et al., 2008*). In the following we report on the geological and physical characterization of the reservoir rock under investigation and on the characterization of wetting of rough model surfaces in scCO_2.

Characterisation of the rocks and the pore space

The RWE Dea AG, Hamburg, provided cores and plugs of sandstone reservoir rocks with varying physical properties such as permeability, porosity, grain sizes and mineralogy from north German oil and gas deposits. The samples are well indurated, but still slightly friable, fine to medium grained, with sparry cements and with abundant pale and dull grains (see e.g. Fig. 1). From each sample several petrographic sections were obtained. The porosity was stained blue but no other stains (e.g. for feldspars or carbonates) were applied. In thin section, the samples may show some indistinct alternating lamination of coarser and finer grains and partly with differing cement and open pore space volume. Some samples however, exhibit very distinct lamination defined by grain size, mineralogy and porosity changes. Most sandstone samples are structurally medium mature but compositionally heterogeneous and immature. The grains are very well to well rounded, sometimes sub-rounded when finer, but appear also facetted, subrounded to poorly rounded because of dissolution under pressure, along grain to grain contacts (sutured contacts) and because of grain dissolution along boundaries during diagenesis (comp. below). The sorting of grain sizes and elongation are moderate to poor. Most grains are rather subspheroidal although distinctly

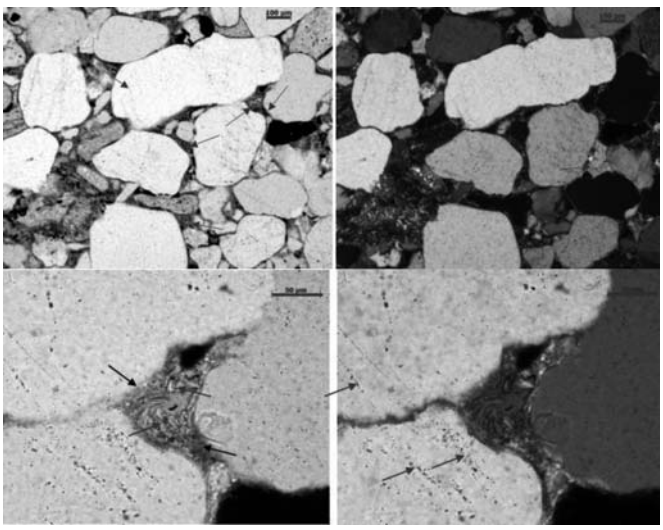

Figure 1: Grain under single (left side) and double (right side) polarised light. Scale in the upper right corners is 100µm. Chlorite is filling the pore space overgrowing hematite skins and the grains as pointed out by the arrows in picture on the left. The open pore space in the upper right corner of the upper picture pair displays haematite followed by chlorite growing tangentially into the open pore (enlargement in the lower pictures). The large elongated quartz grain in the upper part of the upper picture is syntaxially overgrown by quartz cement. The original grain boundary is pointed out by the arrow. In the upper right picture, calcite cement (right arrow) is also visible. The left arrow points to an altered feldspar with sericite inclusions. Sericite matrix can be also found between some grain boundaries. In the lower, enlarged view chlorite growing tangentially (arrows) is overgrowing haematite skins (arrows). The open pore space displays small fans of chlorite facing the open pore. Fluid inclusion trails can be seen in the quartz grains (pointed out by arrows in the lower right picture. Sutured grain contact can be recognised between the two grains on left hand side of the lower pictures.

elongated grains occur as well. The elongation seems not to depend on the grain composition. The sorting varies from laminae to laminae but is always not very high and smaller grains always are compacted between larger grains, with rare coarse sand sizes and common fine and medium grain sizes present. Rounding of grains strongly depends on the size, fine sand being significantly less rounded and less spheroidal than medium and coarse sand grains. All these properties are somewhat obliterated by widespread syntaxial quartz and albite overgrowth, which appears unambiguous only when observed under crossed polarisator.

Grain composition is of about 60 % to 70 % quartz grains. Albite, plagioclase and K-feldspar grains are also present and common. Quartzite, recrystallised chert, vein quartz and igneous rock fragments constitute less than 5 % of the grain content, the composition of the sandstones hints towards a cratonic source with mixed sedimentary and igneous rocks. This is supported by the presence of detrital phyllosilicates (muscovite and altered, greenish biotite) compacted between the quartz, feldspar and rock fragment grains. Few rounded, detrital, opaque ore grains (heavy minerals) were also found. The matrix varies between silt size detrital grains, clay minerals (primary and as alteration products of some unknown, probably volcanic and igneous rock fragment precursor), and patches and interstices with haematitic filling (possible alteration).

All samples exhibit a complicated polyphase diagenetic history. Sutured contacts and grain dissolution features evidence significant fluid movement during diagenesis. The diagenetic minerals were precipitated from migrating brians in the pore space, as synthaxial and normal quartz overgrowth cement, but also very commonly as albite cements, confirmed by EDAX analyses (see Fig. 2 and 3). Very often, the first generation of cement/matrix is that of chlorite and clay minerals and /or haematite skins sur-

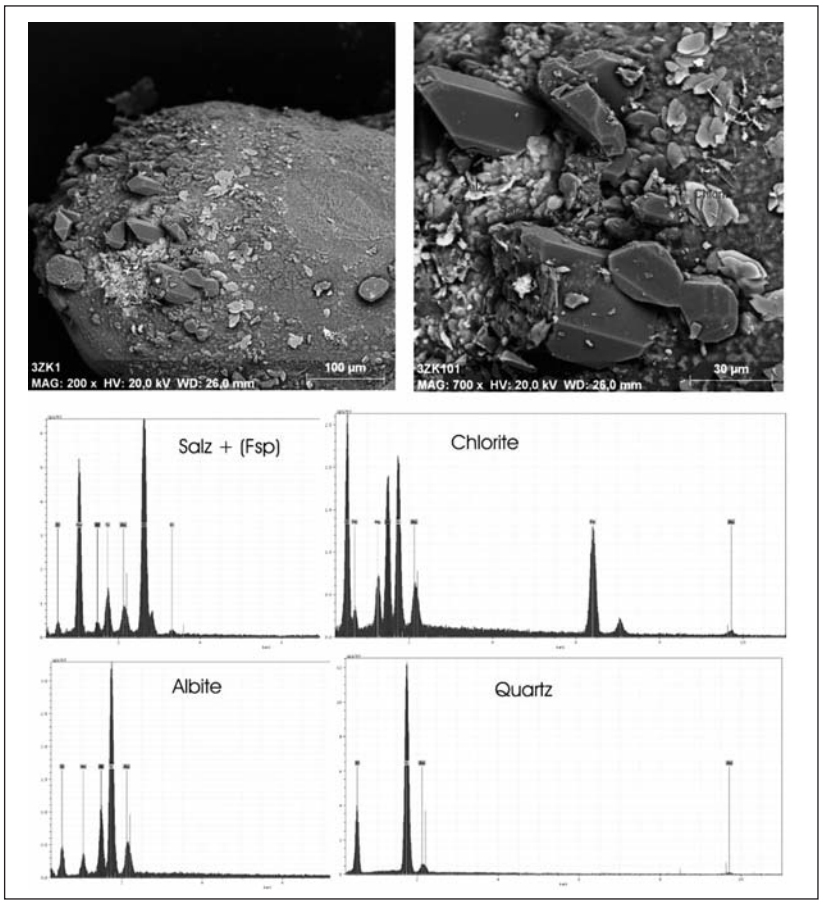

Figure 2: The left upper SEM micrograph displays an overview of the grain surface with idiomorphic minerals growing on the grain into the open pore space. The right hand image shows a close up view of this overgrowth, displaying idiomorphic mineral habitus of chlorite, quartz, albite (not well developed) and halite skin (Salz) and the respective EDX measurements. In the halite diagram (upper left) feldspar content is visible below the halite encrustation and thus Al and K peaks are visible as well.

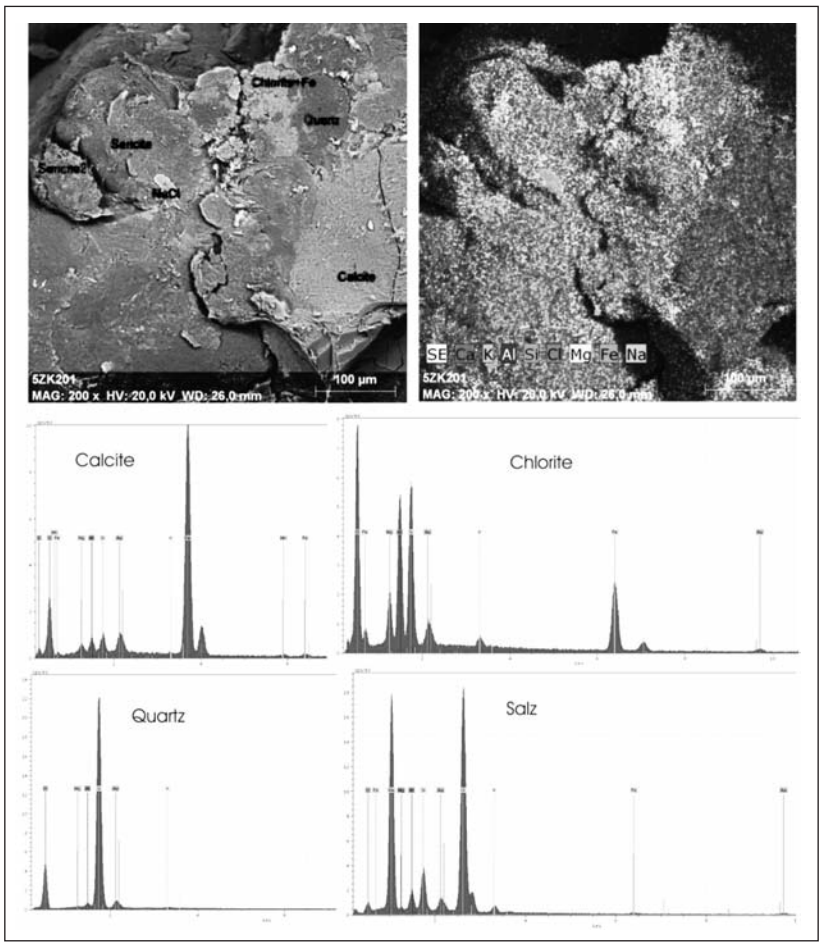

Figure 3: The left picture displays an overview of grain and cements with respective spots of EDX analysis, as shown in diagrams below. Chlorite, sericite, calcite, halite (Salz, NaCl) and quartz were found. The right hand picture displays an EDX elemental map of the view in left picture. The large area of calcite cement appears on the right side of the picture. Most of the other area is occupied by quartz cement.

rounding the grains. In a later diagenesis quartz and albite coatings were generated. Clay minerals, chlorite, haematite coats are present as the second and third cement generation as well. Partial decementation – dissolution of these neomorphic minerals, is evident in laminae, where such cements are much thinner and very irregular, leaving out abundant open pore space and by partial filling of the interstices with calcite, as most probably the latest stage of cementation. This is particularly clear where calcite is the only remaining pore filling cement and in direct contact to the detrital grains, but passing (overlapping) laterally onto quartz and albite cements. In such cases, it becomes apparent that the process was not a gradual replacement of former cements by calcite, but instead, the early cements were partly dissolved and transported aside in solution, and only subsequently, calcite was precipitated from migrating fluids. Calcite together with other cements thus, often fills resorption embayments but also dissolution pits in the grains.

SEM investigations were performed on single grains broken off from the core samples, pikked with pincers, mounted on a conventional SEM mount carrier disk with double-sided stikking tape, and coated with sputtered carbon. Elemental mapping was conducted by the EDX. In most cases cements fully cover the grains by multiple coats of various minerals. The outer most layers very often exhibit idiomorphic crystals facing the open pore space. The involved minerals are clay mineral platelets, albite twins, chlorite fans, idiomorphic, pseudohexagonal quartz needles and abundant salt (halite - NaCl) as hoppers and skins. The faces of these idiomorphic crystals are absolutely flat and smooth on sub micrometer scale. Where the coatings build a tangential skin without idiomorphic faces, the roughness is just below 1µm scale and can be well observed by the SEM. Typical crystalline surfaces with pitted regular crystallographic pattern are recognizable. As could be expected from the evaluation of the cements under optical micro-

Figure 4: The LSM and optical photographs show cements of different shape within a pore of the investigated sandstone. On the left hand side albite blades are visible. In the center of the pore needles of illite grow into the pore space on quartz overgrowth of a clastic grain. Some of the needles seem also to grow from the albite surface.

scope, only calcite does not produces idiomorphic crystals. It has been observed as broken surfaces only, because it is the latest stage of cementation usually filling the pore space as one crystal, poikilotopic infill of several neighboring pores.

AFM investigations were performed on single grains or small, cemented and bond grain groups of 2-10 grains, mounted on a small metal plate sample carrier and fixed by a commercial nail varnish. The video camera mounted on the AFM table allows for a high magnification observation of the grains (500x). It was difficult, but nevertheless possible, to relocate the same spots under the AFM and SEM. The measured surface roughness of the sample depends on the scale of observation. At all scales however, the roughness is significant and the topography as shown in the profiles in both directions, vertically and horizontally, is always steep and distinct. This provides problems as to the choice of the right AFM tip. The measurement precision achieved in vertical direction was of up to few tens of nm on ideal surfaces; surfaces of steep and high roughness however, were not possible to measure exactly.

Further roughness and topography measurements were performed by a digital laser scanning microscope (laser profilometer, LSM Keyence). The LSM delivers digitally sandwiched surface images of the sample, with high depth of focus and a quantitative topography data set in µm resolution (Fig. 4). The advantage of such measurements is the ability of the LSM to exactly resolve even very steep topography, although the resolution is by an order of magnitude lower than that of an AFM or a light interferometer. Fig. 5 shows an example where the grain surface is covered by cement and hematite. Additionally, needles (illite) grow into the pore space. Such needles can affect the fluid transport in the porous network and retain hydrocarbons. This example also shows that a microscopic inspection of the pore space is essential to identify relevant morphological features and that the complicated surface

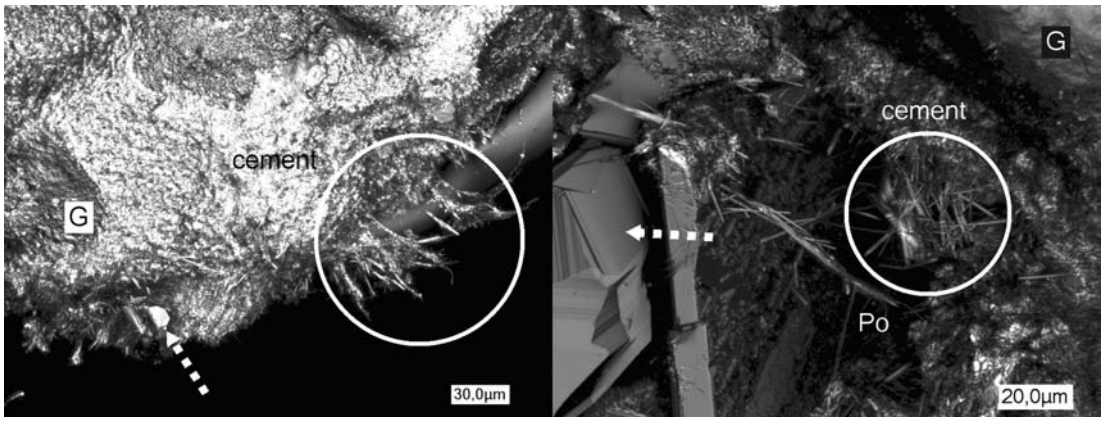

Figure 5: (left) Boundary of grain and part of grain surface (G) The grain covered by hematite skin has been stressed at the concave areas (dissolution depressions) and cement has overgrown the surface subsequently, while at the pore boundary illite needles (circle) are growing into the open pore space (Po). The sub-euhedral minerals with platy habitus are albite (dotted arrow in the right picture).

topography can not be simply described or measured by an AFM on a larger (>10 µm) scale.

As it is often difficult to identify very small grains or cements by optical microscopy, and almost impossible to identify the mineralogy by the AFM or LSM, therefore the above investigations were supported by micro-Raman spectroscopy in order to aid the mineral identification, performed mostly on thin sections and on single grain mounts. Our micro–Raman device is attached to a confocal microscope, which allows for three-dimensional imaging and for simultaneous chemical analysis. The confocal configuration leads to a small sample volume, from which Raman scattering can be recorded. Lateral and vertical cross-sections of the sample can easily be generated with high spatial resolution, whereby lateral and vertical 1-µm-thick optical slices are acquired from the surface to the maximum depth of 25 µm. The technical set up [confocal Raman microscope, alpha300 R; WITec GmbH, Ulm, Germany, frequency doubled Nd:YAG laser (532 nm, P_{max} = 22.5 mW) and a 100× objective (Nikon, NA=0.90, 0.26 mm working distance)] is described in detail in Kremer et al. (in press).

Due to the above described properties, the pore space in the investigated samples is very heterogeneous and has a wide range of mineralogical and roughness characteristics. The observed variety of the open pore morphology depends strictly on the shape of the detrital grains, on the vesicular cement minerals of tangential and needle-like habitus and on the fringing dissolution and pressure dissolution of the grains, that are mostly densely packed and grain supported. It is thus chiefly the diagenetic history and not the sedimentary history in these samples that rules the gross and nanomorphology of the pores. In order to simplify the search for a suitable target for experiments, the pores were classified according to the key mineralogy, into four main classes, each comprising several subclasses:

1) Not overgrown, rare grain surface/pore space contacts of varying mineralogy, but mainly quartz, feldspar and common volcaniclasts and heterogeneous rock fragment surfaces.
2) Quartz cement/pore space contact of botryoidal or hypidiomorphic quartz.
3) Calcite cement/pore space contact of varying shapes but mostly blocky and needle shaped or irregular, corroded calcite.
4) Heterogenous haematite, illite, chlorite albite cement/pore space contacts of differing morphologies.

Small Angle Neutron Scattering

A combination of small angle neutron scatte-

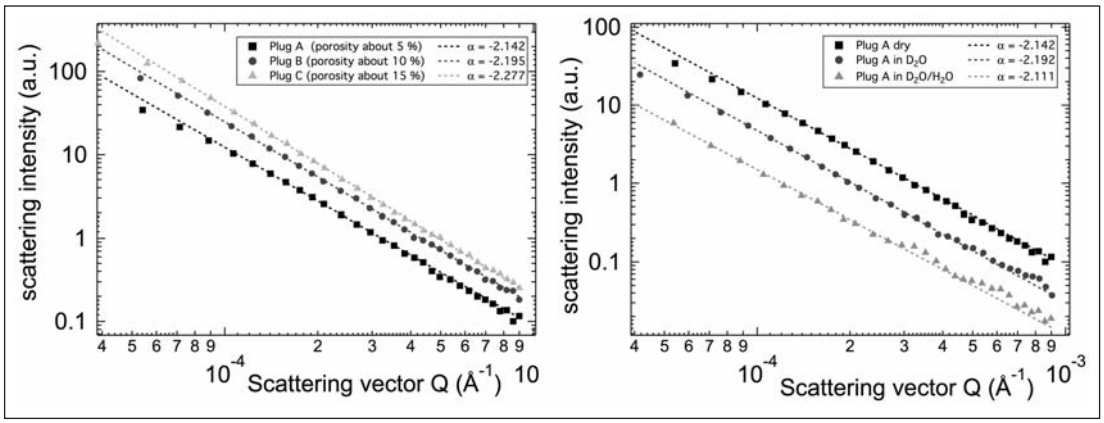

Figure 6: (left) Ultra small angle neutron scattering data of different plug samples from a quartz sandstone reservoir rock of a north German gas deposit. The intensities show a power law behaviour. With an exponent of about -2.2, indicating a mass fractal topography. (right) Filling the pores with D_2O or a contrast-matching mixture of D_2O and H_2O reduces the scattering intensity.

ring (SANS) and ultra-small angle neutron scattering (USANS) experiments on dry and partially wetted reservoir rock samples has been carried out at the Institut Laue-Langevin (ILL), in Grenoble, France in September 2010. The measurements will give insight into the interplay between texture, pore surface roughness, size distribution of the cement overgrowth and the distribution of connate water in the pore network.

Molecular scale interactions between fluids and mineral surfaces have a crucial impact on pore volume estimation, on the understanding of hydrocarbon migration, and on the possible degree of exploitation. These interactions also influence the assessment of CO_2 storage capacity and retention mechanisms or of the potential of geothermal energy generation in aquifers (*Pruess and Azaroual, 2006; Pruess, 2008*). The study aims to reveal nanoscale processes in the pore- space of sedimentary rocks in order to explain the migration processes and the permeability for fluids, gas and supercritical CO_2 within sedimentary rocks.

For reservoir rocks it is important to study the intact porous network within a representatively large volume of a bulk sample. Sandstones, mainly composed of quartz grains, show diverse heterogeneous textures, accessory minerals, and varying grain sizes of 5 ~ 100 m. Notably, capillary bound water in the pore system appears to reduce the permeability. The penetration power of neutrons allows to investigate the porosity of such bulk samples with SANS. This method is more powerful in combination with ultra small angle neutron scattering (USANS) for the study of the microstructure of rocks over a large range of scales (*Radlinski, 2006; Triolo et al., 2000; Sen et al., 2002*). The fractal dimension derived from the SANS/USANS data can be correlated to microscopy data (*Wong and Howard, 1986; Wong and Bray, 1988; Radlinski et al., 2004; Anovitz et al., 2009*) and used as a parameter for the correlation of porosity and permeability of rocks in conjunction with their pore topology (*Pape et al., 1999; Pape and Clauser, 2000*). At the beam lines D11 and S18 at ILL SANS and USANS experiments were carried out on the same set of samples. Pore filling and capillary condensation of fluids in porous media was observed with SANS and USANS by using contrast-matching H_2O/D_2O mixtures (*Broseta et al., 2001; Erko et al., 2010*).

In Figure 6 (left) data measured on sandstone reservoir rock samples of different depth and different porosity are shown. The scattering intensities follow a power law behavior, which is typical for porous rocks with an exponent of about -2.2, which corresponds to a mass fractal topography of the pore space with a

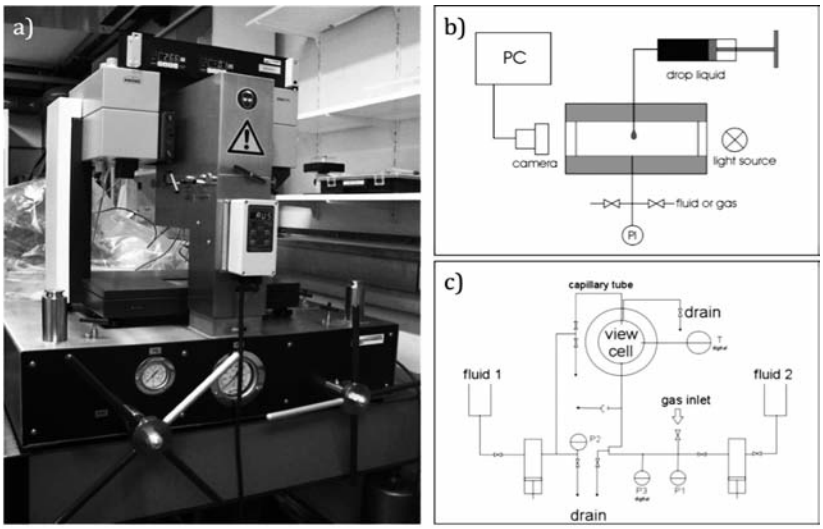

Figure 7: High Pressure View cell (Krüss GmbH, Hamburg, Eurotechnica, Bargteheide). The cylindrical cell has two optical windows. A drop can be placed on the sample surface through a capillary. The cell can be filled with two different gaseous or fluid media. Liquid CO_2 can be pressurized up to 69 MPa and heated to 180 °C. The cell is equipped with a contact angle measurement system.

dimension of 2.2. Filling the pores with D_2O or a mixture of D_2O and H_2O, contrast-matching to quartz and feldspar, massively reduced the scattering intensity. The remaining scattering contrast is mainly caused by the surfaces of calcite cement, heavy minerals and other minor constituents of the rock.

Wettability of rough surfaces at reservoir conditions

The wettability of the reservoir rock has a large influence on the productivity of a hydrocarbon reservoir. In oil fields, depending on the type of wetting characteristics of the rocks, different technologies for developing a field are necessary. One of the most prominent effects of the micro- and nano-morphology on wetting is the super-hydrophobicity, better known as the »lotus effect« on glass or ceramics (*Barthlott and Neinhuis, 1997; Neinhuis and Barthlott, 1997; Spori et al., 2008*). The lotus effect is caused by an only partial wetting of the rough surface profile by the liquid phase in the so-called Cassie-Baxter regime (*Wenzel, 1936; Cassie and Baxter, 1944*). So far, however, it is not clear how the presence of a supercritical phase and mass transport between the wetting and the supercritical phase affect superhydrophobicity.

To investigate the fundamental processes of wetting under reservoir conditions we have applied a high pressure / high temperature contact angle goniometer (Fig. 7). The instrument has a cylindrical high pressure view cell (HPVC), which can be filled with different fluid or gaseous media. It is possible to study wettability of surfaces and surface tension of different media with the sessile drop and pendant drop method. Experiments can be carried out at realistic reservoir conditions of up to 69 MPa and 180 °C with different fluids and CO_2.

To study the effect of temperature and pressure on the wettability of rough surfaces, a model surface was created that resembles the surface of a lotus leaf (Fig. 8). We used a ceramic aluminum oxide replica of a two-step-photolithographic pillar structure. The sample was coated with a chemically stable, hydrophobic fluorosilane layer. Dynamic contact angle (CA) measurements of water drops in fluid as well as supercritical CO_2 were performed at different temperature and pressure conditions. The pillar surface shows a superhydrophobic behavior with advancing CA of 150-160°, with a slight increase of the CA with pressure (0.1 MPa^{-1}) and a hysteresis of about 15° (Fig. 9). The contact angles at 100 °C show larger slope (0.4 MPa^{-1}) and increased hysteresis (25°) than the data measured at room temperature. The temperature and pressure dependence of the contact angle can be influenced by the interfacial tension of the phases as well as buoyancy effects due to variations of the density.

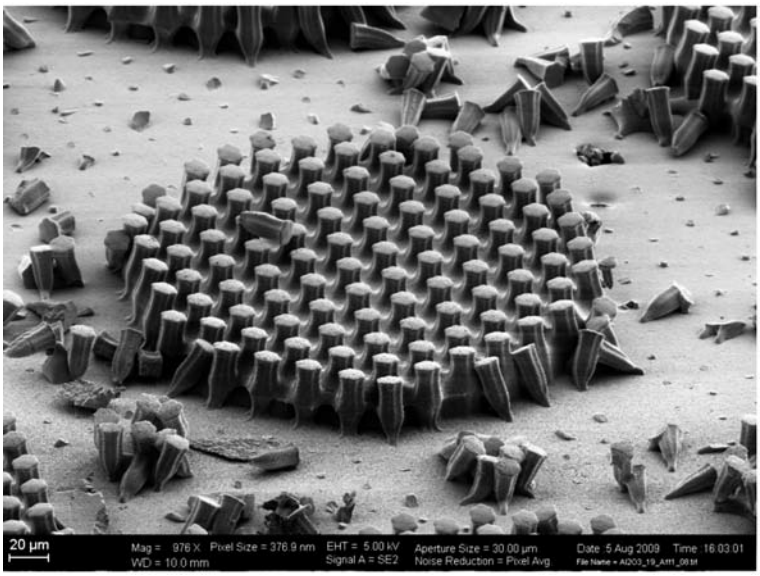

Figure 8: SEM image of a ceramic replica of a pillar structure. The large pillars have a diameter of 100 µm, the small ones 10 µm. The sub-micron scale topography of the sample is dominated by the grain size of the aluminium oxide particles of the slurry used for casting. Due to the undercut shape of the master, part of the small pillars broke off at separation of the replica from the negative (D. Spori, ETH Zurich).

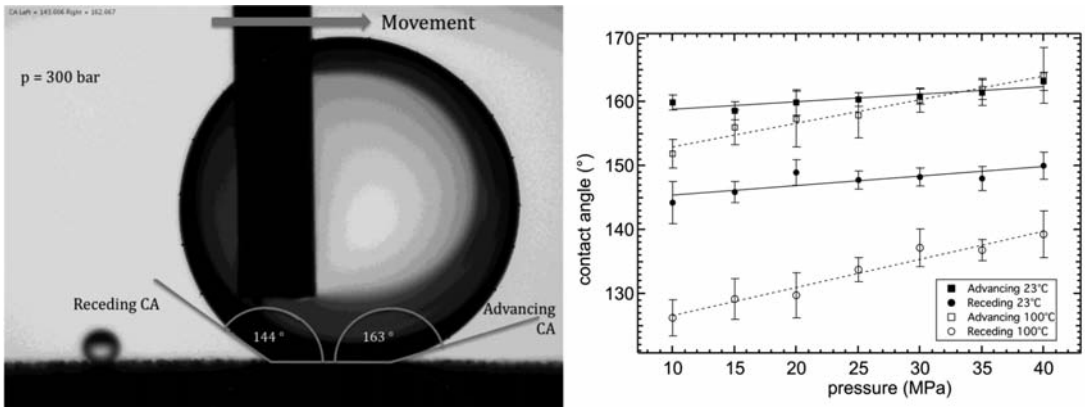

Figure 9: (left) Microphotograph of a water drop on the superhydrophobic pillar structure in liquid CO_2. The surface was moved with respect to the capillary, to measure the advancing and receding contact angle. (right) Contact angles of water in CO_2 at different temperatures and pressures. The data at 100 °C (supercritical CO_2) show a higher slope (0.4°/MPa) and a stronger hysteresis (25°) than the data at room temperature (0.1°/MPa and 15°).

The experiment shows that wetting phenomena caused by surface morphology can also occur under reservoir conditions. Main impact on the details of the wetting (contact angle, hysteresis) can be expected from variations in mass density or surface tension due to mass transfer with the supercritical phase.

Conclusions

The pore space morphology of reservoir rocks depends on the size and shape of the clastic debris and can be drastically changed during diagenesis due to influence of factors such as compaction, cementation, and pressure dissolution. The above observations have led to the conclusions that the pore surfaces at the first phase are rather smooth on a µm scale, and the pores are well-connected facilitating migration of fluids. The subsequent stages of diagenesis, including fluid migration itself, have changed and complicated however, the pore spaces morphology. Pores were filled by minerals and new micro-pores were opened by dissolution of diagenetic minerals. In addition, the grains and cements were partially dissolved, forming new pores within some sedimentary layers or laminae. The overgrowth on clastic grains by secondary minerals produced rough surfaces, leading to more rugged pore surfaces. The flow capacity of hydrocarbon fluids has been decreased due to authigenic

minerals forming barriers and blocking the oil and gas flow. Micro-pore structures and overgrown grain surfaces have formed larger surfaces increasing the adhesion capacity of fluids. Small angle neutron scattering data indicate a mass fractal geometry of the pore space which spans over several orders of magnitude. In the next step the correlation between scattering data (bulk) and the microscopically measured roughness (surface) will be investigated. This correlation provides input for the assessment of the inner roughness of the rock.

The wetting experiments show that the same wetting phenomena (super-hydrophobicity) as known from atmospheric conditions also occur under reservoir conditions. Static and dynamic wetting properties, however, depend on the mass transfer on the phases and thus on the temperature and pressure. Further wetting experiments on model surfaces and on typical minerals like quartz, micas, calcite or feldspars shall provide further insight into the dynamic wetting behavior.

Our research and experiments aim to answer questions imposed by problems occurring in practical oil and gas exploitation activities. It is directed by theoretical petro-physical considerations and practical cases, as discussed with the RWE-Dea, Hamburg, the main oil and gas producer in Germany.

Acknowledgements
We thank the beamline scientists H. Lemmel (TU Wien, Atominstitut) and P. Lindner (ILL Grenoble) for their support in carrying out the neutron scattering experiments. We thank D. Spori and C. Cremmel (ETH Zürich, Laboratory for Surface Science and Technology) for the ceramic replicas.

References

Al-Futaisi, A., Qaboos U, S., Patzek, T.W. and U.C. Berkeley, 2003. Three-phase hydraulic conductances in angular capillaries. SPE J. 8 (3), 252-261.

Al-Futaisi, A., and T.W. Patzek, 2004. Secondary imbibition in NAPL-invaded mixed-wet sediments. J. Contam. Hydrol. 74: 61-81.

Altermann, W., Heckl, W.M., Stark, R.W., Strobel, J. and Ch. Wolkersdorfer, 2008. Nanostructure and wetting properties of sedimentary grains and pore-space surface (NanoPorO). Geotechnologien Science Report No. 12. Koordinierungsbüro Geotechnologien, Potsdam, ISSN 1619-7399, 58-69.

Anovitz, L.M., Lynn, G.W., Cole, D.R., Rother, G., Allard, L..F., Hamilton, W.A., Porcar L. and M.H. Kim, 2009. A new approach to quantification of metamorphism using ultra small and small angle neutron scattering. Geochimica Cosmochimica Acta, 73 (24), 7303-7324.

Barthlott, W. and C. Neinhuis, 1997. Purity of the sacred lotus, or escape from contamination in biological surfaces. Planta. 202, 1-8.

Broseta, D., Barre, L., Vizika, O., Shahidzadeh, N., Guilbaud, J. P. and S. Lyonnard, 2001. Capillary condensation in a fractal porous medium. Phys. Rev. Lett., 86 (23), 5313-5316.

Cassie, A.B.D. and S. Baxter, 1944. Wettability of porous surfaces. Transactions of the Faraday Society. 40: 0546-0550.

Erko, M., Wallacher, D., Brandt, A., and O. Paris, 2010. In-situ small-angle neutron scattering study of pore filling and pore emptying in ordered mesoporous silica. J. Appl. Crystallogr., 43, 1-7.

Fouillac, C., Sanjuan B., Gentier, S., and I. Czernichowski-Lauriol, 2004. Could sequestration of CO2 be combined with the development of enhanced geothermal systems? In: Third Annual Conference on Carbon Capture and Sequestration, Alexandria.

Hassenkam, T., Skovbjerg, L.L., and S.L.S. Stipp, 2009. Probing the intrinsically oil-wet surfaces of pores in north sea chalk at subpore resolution. Proceedings of the National Academy of Sciences (PNAS). 106: 6071-6076.

Jäger, P. and A. Pietsch. 2009. Characterization of reservoir systems at elevated pressure. J. Petrol. Eng. 64, 20-24.

Kremer, B., Bauer, M., Stark, R.W., Gast, N., Altermann, W., Gursky, H-J., Heckl, W.M. and J. Kazmierczak (in press). Raman and atomic force microscopy test for chlorococcalean affinities of problematic Silurian microfossils (»acritarchs«). Journal of Spectroscopy.

Neinhuis, C. and W. Barthlott, 1997. Characterization and distribution of water-repellent, self-cleaning plant surfaces. Annals of Botany. 79: 667-677.

Pape, H., Clauser, C. and J. Iffland, 1999. Permeability prediction based on fractal pore-space geometry. Geophysics, 64 (5), 1447-1460.

Pape, H. and C. Clauser, 2000. Variation of permeability with porosity in sandstone diagenesis interpreted with a fractal pore space model. Pure Appl. Geophys., 157 (4), 603-619.

Pruess, K., 2008. On production behavior of enhanced geothermal systems with CO_2 as working fluid. Energy Conversion and Management. 49, 1446-1454.

Pruess, K. and M. Azaroual, 2006. On the feasibility of using supercritical CO_2 as heat transmission fluid in an engineered hot dry rock geothermal system. In: 31st Workshop on Geothermal Reservoir Engineering, Stanford, CA. SGP-TR-179.

Radlinski, A.P., Ioannidis, M.A., Hinde, A.L. Hainbuchner, M. Baron, M., Rauch, H. and S.R. Kline, 2004. Angstrom-to-millimeter characterization of sedimentary rock microstructure. J. Colloid Interface Sci., 274 (2), 607-612.

Radlinski, A.P., 2006. Small-angle neutron scattering and the microstructure of rocks. Reviews in Mineralogy and Geochemistry, 63, 363-397.

Sen, D. Mazumder, S. and S. Tarafdar, 2002. Pore morphology and pore surface roughning in rocks: A small-angle neutron scattering investigation. J. Mater. Sci., 37 (5), 941-947.

Spori, D.M., T. Drobek, S. Zurcher, M. Ochsner, C. Sprecher, A. Muehlebach, and N.D. Spencer, 2008. Beyond the lotus effect: Roughness, influences on wetting over a wide surface-energy range. Langmuir. 24, 5411-5417.

Sutjiadi-Sia, Y., P. Jaeger and R. Eggers. 2008. Interfacial phenomena of aqueous systems in dense carbon dioxide. J. Supercrit. Fluid., 46, 272-279.

Triolo, F. Triolo, A. Agamalian, M.M. Lin, J.-S. Heenan, R.K. Lucido, G. and R. Triolo, 2000. Fractal approach in petrology: Combining ultra small angle, small angle and intermediate angle neutron scattering. J. Appl. Crystallogr. 33 (1), 863-866.

Wenzel, R.N., 1936. Resistance of solid surfaces to wetting by water. Ind. Eng. Chem. 28, 988-994.

Wong, P.Z. and A.J. Bray, 1988, Porod scattering from fractal surfaces. Phys. Rev. Lett., 60 (13), 1344-1344.

Wong, P.Z. and J. Howard, 1986. Surface roughening and the fractal nature of rocks. Phys. Rev. Lett., 57 (5), 637-640.

Reactivity of Calcite/Water-Interfaces (RECAWA): Molecular level process understanding for technical applications

Stelling J. (1), Neumann T.* (1), Kramar U. (1), Schäfer T. (2), Heberling F. (2), Winkler B. (3), Vinograd V. (3), Arbeck D. (3), Müller H.S. (4), Haist M. (4), Glowacky J. (4), Vucak M. (5), Fischer U. (6), Pust C. (6), Huber J. (7), Bosbach D. (8)

(1) Karlsruhe Institute of Technology (KIT), Institute of Mineralogy and Geochemistry (IMG), e-mail: stelling@kit.edu, neumann@kit.edu, utz.kramar@kit.edu

(2) Karlsruhe Institute of Technology (KIT), Institute for Nuclear Waste Disposal (INE), e-mail: thorsten.schaefer@kit.edu, frank.heberling@ine.fzk.de

(3) Goethe Universität Frankfurt (UF), Institut für Geowissenschaften (IfG), e-mail: b.winkler@kristall.uni-frankfurt.de, v.vinograd@kristall.uni-frankfurt.de, Arbeck@kristall.uni-frankfurt.de

(4) Karlsruhe Institute of Technology (KIT), Institute of Reinforced Concrete Structures and Building Materials (IfMB), e-mail: hsm@ifmb.uni-karlsruhe.de, haist@kit.edu, jens.glowacky@ifmb.uka.de

(5) Schaefer Kalk GmbH & Co. KG, e-mail: marijan.vucak@schaeferkalk.de

(6) Rheinkalk Akdolit GmbH & Co. KG, e-mail: uwe.fischer@rheinkalk.de, christopher.pust@rheinkalk.de

(7) Lafarge Zement Wössingen GmbH, e-mail: juergen.huber@lafarge-zement.lafarge.com

(8) Forschungszentrum Jülich GmbH, Institute of Energy Research (IEF), e-mail: d.bosbach@fz-juelich.de

*Coordinator of the project

Abstract

RECAWA intends to develop a fundamental understanding of the reactivity and dynamics of calcite surfaces during crystal growth in aquatic systems. Therefore, the calcite-water surface has been characterised at different hydrochemical conditions and surface diffraction measurements have been applied to probe if changes in zeta potential are accompanied by changes in the calcite-water interface structure. The interaction of calcite with Selenium is investigated in a mixed flow reactor (MFR) study which is accompanied by GI-EXAFS analyses to characterize the Se adsorption species.

The interaction of calcite surfaces with phosphate and phosphonates is the focus of two sub-projects. The sorption/precipitation mechanisms of PO_4^{3-} and HPO_3^{2+}, respectively, on different calcite powders (precipitated calcium carbonates and limestone powders) are investigated to determine sorption isotherms and phase transformations on the applied surfaces which is of great interest with regard to phosphate recycling and/or water treatment. Analytical work includes SEM, XRD and XAFS spectroscopy for a detailed characterisation of the calcite powders in different sections of the isotherms.

Experimental investigations on the interaction of limestone powder and two superplasticizers have been conducted with regard to concreting. These experiments were done at alkaline conditions and lead to massive reactions and changes in the zeta potential of the solutions and limestone powder when superplasticizers added.

Additional results of quantum-mechanical calculations and force-field modelling demonstrated that the Double Defect Method is able to quantitatively predict mixing properties of various iso-structural binary and ternary carbonate solid solutions. In particular, low equili-

brium retention levels of SO_4^{2-} and SeO_4^{2-} in carbonates imply that the reasonably large concentrations SO_4^{2-} and SeO_4^{2-} in carbonates reported in previous studies should be attributed to non-equilibrium entrapment effects.
Data obtained from atomistic modelling complement our data determined using lab methods. Further experimental and analytical, work including in-situ AFM studies using Iceland spar single crystals, is in progress and will help to interconnect the present results of the sub-projects.

1. Introduction

Carbonates are of high economic interest and represent an important resource for the chemical and pharmaceutical industry, glass and paper industry, construction material industry, for the production of fertilizers and for the quality of drinking water. Due to the abundance of carbonate rocks in the earth crust, carbonates are considered as a mineral mass product.
As the thermodynamically most stable and most abundant carbonate phase, calcite plays a prominent role for numerous natural processes in our environment. Calcite affects in various ways the global circulation of matter, regulates the pH and controls the chemical composition of natural aquatic systems, and has the ability to fix or structurally incorporate biologically active and, depending on the concentration, hazardous elements such as phosphorus, calcium, magnesium, iron, arsenic, selenium and other trace elements. Adsorption reactions are usually rather fast compared to co-precipitation reactions. In particular with respect to kinetic aspects of trace element sorption, the molecular level reactions at the mineral/water interface need to be understood in various fields of application to improve the effectiveness of industrial calcite mass products such as PCCs or filter material for water treatment. Atomistic models allow studying sorption of complexes and molecules at the mineral-water interface and the formation of solid solutions. These aspects of the interaction of calcite surfaces with dissolved reactants require different simulation approaches. Sorption processes are modelled using Molecular Dynamics, while solid solution formation is treated with statistical thermodynamic tools which combine quantum mechanical calculations and Monte Carlo simulations.
To achieve the goals of the joint research project, experimental and analytical work is divided in sub-projects which concentrate on different aspects of calcite surfaces.

2. The calcite-water surface and its interaction with Selenium

2.1. Structure and speciation of the calcite-water interface

To characterize the calcite surface potential as a function of the composition of the aqueous contact solution we measure calcite zeta potentials using two methods. (i) Electrokinetic measurements are performed in a Brookhaven Instruments zeta potential analyzer using phase analyses light scattering (PALS). For PALS measurements we use equilibrium solutions at three different CO_2 partial pressures, at atmospheric pressure. Suspensions are pre-equilibrated until the theoretically expected pH is reached. In equilibrium with pure CO_2 pH range is 5.8 to 6.8, in equilibrium with air (360 ppm CO_2) pH range is 7.5 to 9.6, and in equilibrium with N_2 (6 ppm CO_2) pH range is 8.4 to 10.3. We observe an increase in the iso-electric point (IEP) with decreasing CO_2 partial pressure. (ii) Streaming potential measurements are performed on an Anton Paar SurPASS electrokinetic analyzer. Streaming potential is measured as a function of pH performing pH titrations in a pH range from 5.5 to 11. As at these conditions solutions are undersaturated with respect to calcite, the calcite must be dissolving during the measurements. Solution analysis proofs, however, that this does not have a significant influence on the solution composition during the experiments. Hardly any pH dependence is observed in streaming potential measurements. Zeta potential increases with increasing Ca^{2+} concentration and decreases with increasing CO_3^{2-} concentration.

Table 2.1: Composition and chemical conditions in the contact solutions used for the surface diffraction study.

Dataset	1	2	3	4	5
solution state (eq. = equilibrium)	eq.: water - air - calcite	eq.: water - air - calcite	eq.: water - air - calcite	non- eq.	non- eq.
NaCl (mol/L)	-	0.097	0.03	0.01	0.01
additions (mol/L)	NaOH: 0.002	NaOH: 0.003	HCl 0.07	NaOH: 0.001 $CaCl_2$: 0.01	NaOH: 0.0005 Na_2CO_3: 0.01
$p(CO_2)$ (ppm)	360	360	360	-	-
zetapotential (mV)	~ 0	~ 0	~ 9	~ 8	~ -25
pH	8.6±0.1	8.6±0.1	7.5±0.1	10.9±0.1	11.1±0.1

Surface diffraction measurements are applied to probe if changes in zeta potential are accompanied by changes in the calcite-water interface structure. We perform in-situ surface diffraction measurements at the GSECARS undulator beamline at sector 13 of the Advanced Photon Source. Five crystal truncation rod datasets are recorded at the solution conditions listed in Table 2.1.

Main results of the interface structure analyses are:

- The part of the calcite(104)–water interface structure, to which surface diffraction measurements are mainly sensitive, does not change significantly, even for the investigated extreme differences in the composition of the contact solutions.
- No indication for calcium or carbonate inner–sphere complexes on the flat calcite(104)–face is observed.
- Two well ordered layers of water are identified at 2.35±0.10 Å and 3.24±0.12 Å above the calcite surface. Water molecules of the first layer are located above the surface calcium ions and those of the second layer are located above the surface carbonate ions.
- In contact with solution mainly surface carbonate ions relax slightly from their bulk position and tilt towards the surface by about 4°.
- A gradual increase in Debye–Waller factors from the bulk crystal to the solution is observed.
- Elevated Debye–Waller factors of water molecules in the second water layer in datasets 3 and 4 (high Ca^{2+} concentration in solution), as well as the drop in diffuse electron density at about 4.2 Å above the surface in dataset 5 (no Ca^{2+} in solution), might be indicative for calcium outer–sphere complexes.

A Basic Stern Surface complexation model is developed that, in accordance with the interface structure analyses, considers only outer-sphere adsorption of ions other than protons and hydroxide. The observed zeta potentials are well reproduced by the model. A major advantage compared to previous models (*van Cappellen et al., 1993; Pokrovsky et al., 2000; Wolthers et al., 2008*) is that a physically reasonable value for the Helmholtz-Capacitance (0.45 F/m^2) is obtained. Together with the Stern layer thickness, estimated from the surface diffraction results (~3.5 Å), this value can be used to estimate the relative permittivity of the interface water, to be about 18.

2.2. Selenite ($Se(IV)O_3^{2-}$) and Selenate ($Se(VI)O_4^{2-}$) interaction with calcite

The MFR study on selenite / selenate coprecipitation is ongoing. MFR experiments at pH 7.4 show that the pH has an influence on the incorporation. As expected anion adsorption and subsequent incorporation is increased at lower pH. Partition coefficients at pH 7.4 are ~10^{-3} for selenate and ~10^{-2} for selenite, which still shows that selenium incorporation into calcite is unfavorable, but the values are relatively large compared to the extremely low values measured at pH 10.3, which were below the detection limit of the method.
Comparison of the macroscopic calcite growth

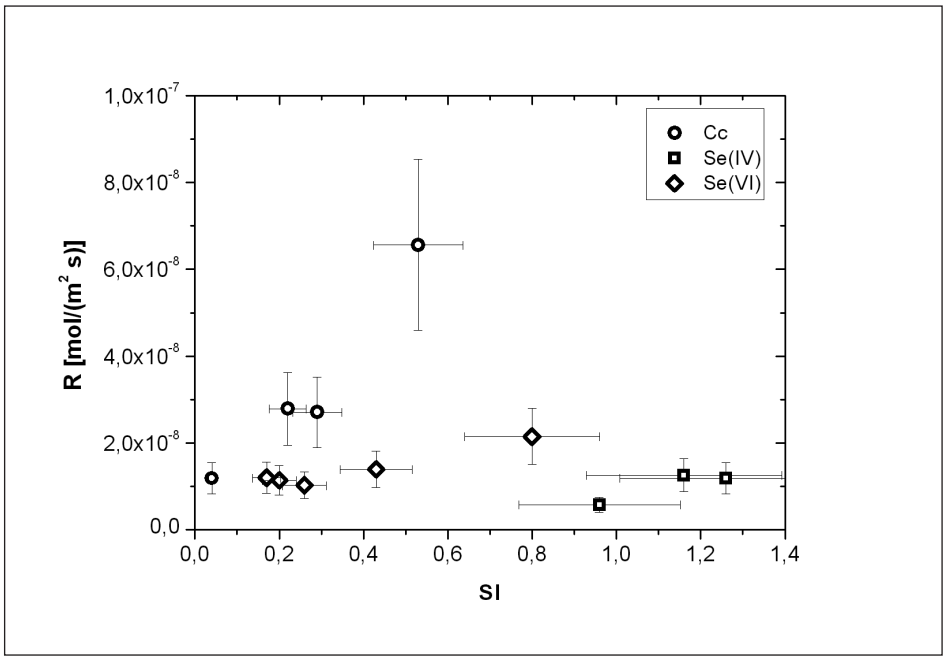

Figure 2.1: Macroscopic calcite growth rates obtained in MFR experiments on pure calcite (Cc, circles), in presence of selenite (Se(IV), squares), and selenate (Se(VI), diamonds).

rate obtained in MFR experiments in presence and absence of selenite / selenate (Fig. 2.1) shows the retarding effect, these anions have on calcite growth.

Selenium K-edge EXAFS is used to characterize the adsorption species of selenate at the calcite water interface. Adsorption samples are prepared in batch type adsorption experiments in pre-equilibrated calcite suspensions at pH 8.3 and 7.5 using calcite powder (Merck calcium carbonate suprapur) or freshly cleaved Iceland spar single crystal platelets as substrate. Initial SeO_4^{2-} concentration is 2×10^{-3} mol/L. EXAFS spectra measured on powder adsorption samples (black circles in Fig. 2.2) do, despite the lower signal to noise ratio, not deviate significantly from a reference EXAFS spectrum measured on a 0.1 mol/L $NaSeO_4$ solution (thick black line in Fig. 2.2). Therefore these spectra are considered inappropriate to characterize the adsorption species.

Only spectra measured on single crystal samples using grazing incidence to achieve surface sensitivity, show an additional contribution to the EXAFS most visible around k = 10.7 $Å^{-1}$ (dashed line in Fig. 2.2) that results in oscillations in the Fourier transform spectra between R = 2.7 Å and R = 3.7 Å. These are likely contributions to the adsorption species spectrum originating from the calcite surface. Detailed EXAFS data analysis is still in progress.

3. Fixation and phase transformation of phosphate at calcite surfaces

It is well known that phosphate is crucial for increased primary production, but its availability as a non-renewable resource is decreasing dramatically (*Gilbert, 2009; Driver et al., 1999*). On the other hand, severe environmental problems result through the discharge of nutrient rich waters from urban, agricultural and industrial sources. This leads to the eutrophication of water bodies and the enrichment of phosphate in sewage and wastewaters (*Smith, 2003*). Therefore, the immobilization of phosphate dissolved in eutrophic water bodies and wastewaters is a promising approach to solve this problem and to recycle phosphate.

In the past, calcite was used for the remediation of eutrophied water to immobilise dissolved phosphate (*Babin et al., 1994; Prepas et al, 1997; Hart et al., 2003*). Laboratory tests demonstrate the success of calcite application and show that a calcite barrier can reduce the

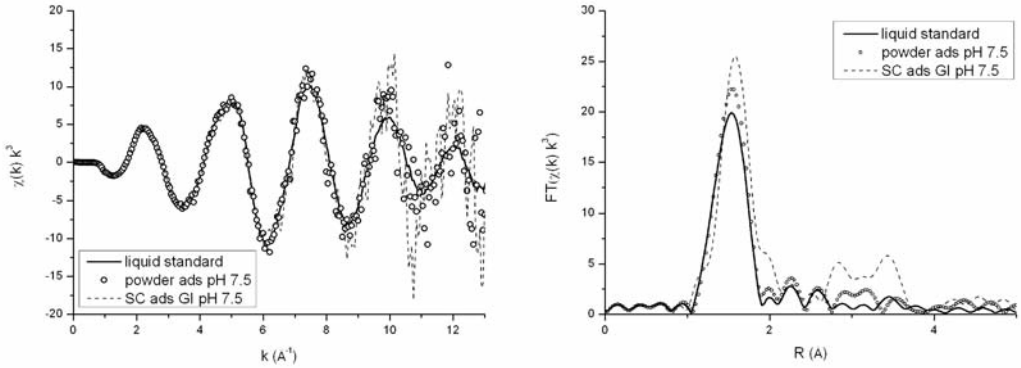

Figure 2.2: k3 weighted EXAFS (left) and Fourier Transform (right) spectra measured on: a liquid SeO_4^{2-} reference (thick black line), powder adsorption sample at pH 7.5 (circles), and single crystal adsorption sample measured at grazing incidence at pH 7.5 (dashed line).

phosphate flux from nutrient-rich sediments to the water. The mechanisms of phosphate fixation at the calcite surface are decisive for the efficiency and sustainability (*Babin et al., 1994; Berg et al., 2004*), but poorly understood at the atomic scale to date. Calcite has its point of zero charge between pH 8.0 and 9.5 (*Somasundaran & Agar, 1967*), while many other minerals have negative surfaces already at pH < 7. Hence, calcite exhibits a positive surface charge and can be used for anion adsorption.

A detailed explanation of the processes of phosphate fixation and phase transformation on calcite surfaces under varying hydrochemical conditions is investigated. The scientific and technical objectives cover:

i. the clarification of the mechanisms of phosphate fixation and phase transformations on calcite surfaces
ii. the characterisation of the hydrochemical conditions and crystallographic parameters for optimised and effective fixation of dissolved phosphate on calcite surfaces
iii. the identification and development of calcite products for the technical application

3.1. Experimental and analytical methods

The uptake of phosphate (PO_4^{3-}) by calcite from saturated calcite solutions has been examined using three types of calcite powders, (i) a powdered powder Devonian limestone (Sancy, FR) with a specific surface area of 1.76 m^2/g (SSA, estimated by N2-BET, sample A), (ii) precipitated $CaCO_3$ (*Merck p.a., 102066, 0.2 m^2/g; sample M), and (iii) a precipitated $CaCO_3$ delivered by Rheinkalk Akdolit (PCC, sample B, 37.45 m^2/g). Different amounts of calcite powder (0-50 g/L) were added to saturated calcite solutions (SI_{CaCO3} = 0.6 - 1.2, Ca^{2+} = 1.8 - 2.8 mmol/L, TA(HCO_3^-) = 4.0 - 8.0 mmol/L), produced from Merck p.a. chemicals ($CaCl_2$, $NaHCO_3$) and double-distilled H_2O (18.2 MΩ·cm) as described by Lin & Singer (2005). Phosphate was added in concentrations of 3 to 1000 µmol/L as H_3PO_4 or $Na_3PO_4 \times 6H_2O$. pH of the solutions was adjusted to 8.0 using HCl or NaOH. PO_4^{3-} concentrations of the calcite solutions are comparable to conditions of pore water and hypolimnion of eutrophic water bodies (*Belzile et al., 1996*). The batch solutions and the powders were shaken for 24 h (Fig. 3.1).

Afterwards the solutions and powders were separated by vacuum filtration. Residual concentrations of Ca^{2+} and PO_4^{3-} were analysed by AAS, ICP-OES and UV-VIS spectrophotometry, respectively. Total alkalinity (HCO_3^-) was chekked using an Aquamerck quick test (Merck 11109) and pH values were determined using a WTW SenTix 81 electrode attached to a WTW pH330 pH-meter. Changes in the morphology of the calcite sample powders were checked with REM. P concentrations and speciation of the powders were analysed by EDXRF and XANES spectroscopy, respectively.

3.2. Results

pH values remained stable at 8.10±0.15 during the experimental run. (Over)saturated calcite

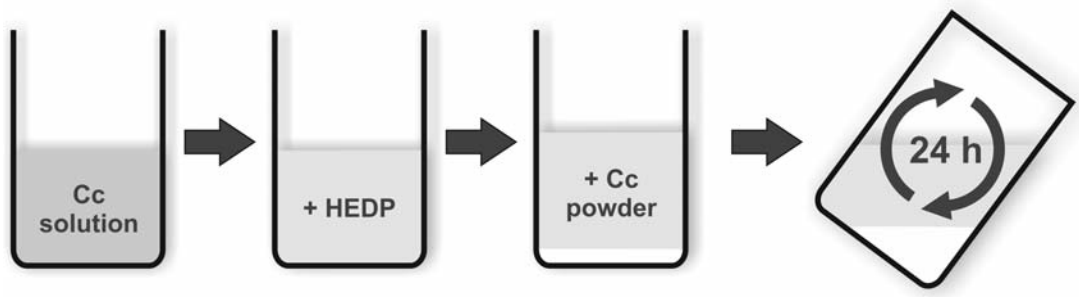

Figure 3.1: Scheme of a batch sorption experiments.

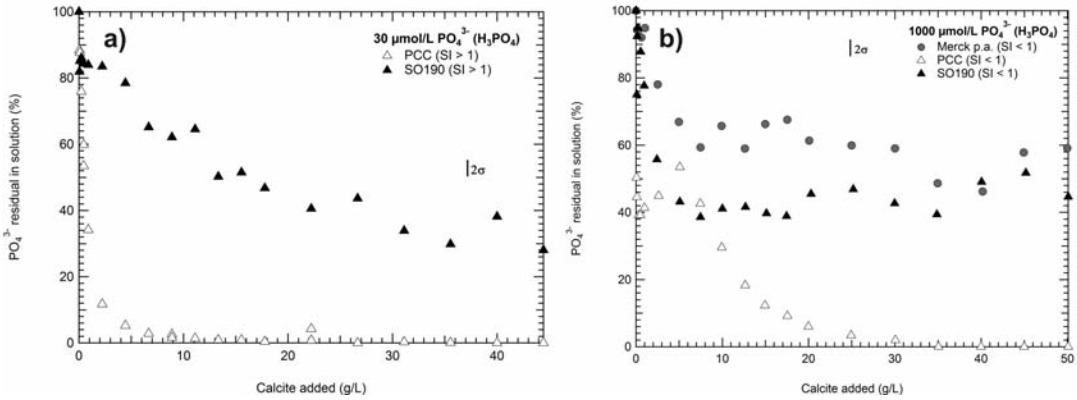

Figure 3.2: Normalized post-experimental PO_4^{3-} concentrations of experimental series starting with a) 30 µmol/L and 1000 µmol/L.

solutions show decreasing trends for Ca^{2+} and HCO_3^- and P concentrations in dependence of the SSA, respectively. Overall removal of phosphate from the batch solution ranges from 2 % to 100 %, dependent on the applied calcite powders. In contrast to experimental series of sample A and M, phosphate was eliminated from the batch solution of sample B series completely at all starting concentrations of 3 to 1000 µmol/L PO_4^{3-}. The addition of small amounts of calcite B (~10 g/L) results in a phosphate elimination of min. ~70 %, whereas calcite A and M result in a decrease of max. ~70 %. Adding high amounts of calcite powder to the batch solution (≥25 g/L) results in a complete phosphate elimination in the sample B experimental series, whereas the PO_4^{3-} concentration decreases by max. ~86 % for sample A and M. In the latter case, the residual PO_4^{3-} load of the solution is increasing with increasing starting concentration (see. Fig. 3.2 for details).

In general, phosphate concentration decreases with increasing amount of calcite powder added to the solution. Depending on the starting phosphate concentration of the batch solution, total phosphate uptake by calcite increases more rapidly in sample B series in comparison to sample A and M (Fig. 3.2 & 3.3). These results show that the ability of phosphate uptake can be considered as a function of the SSA which is crucial in terms of adsorption and precipitation mechanisms and phase transformations, respectively.

To evaluate these mechanisms, sorption isotherms have been determined. These isotherms are in good agreement with those of *Eiche et al. (2008). Van Cappellen (1991)* divided sorption isotherms for phosphate on calcite into four sub-sections (Fig. 3.3 a) Section (A) marks a range of concentration of calcite (Cc) and PO_4^{3-} in which only adsorption on the calcite surface occurs (high Cc/PO_4^{3-} values). (B) shows the precipitation of meta-stable Ca-P compounds, (C) the transformation into stable

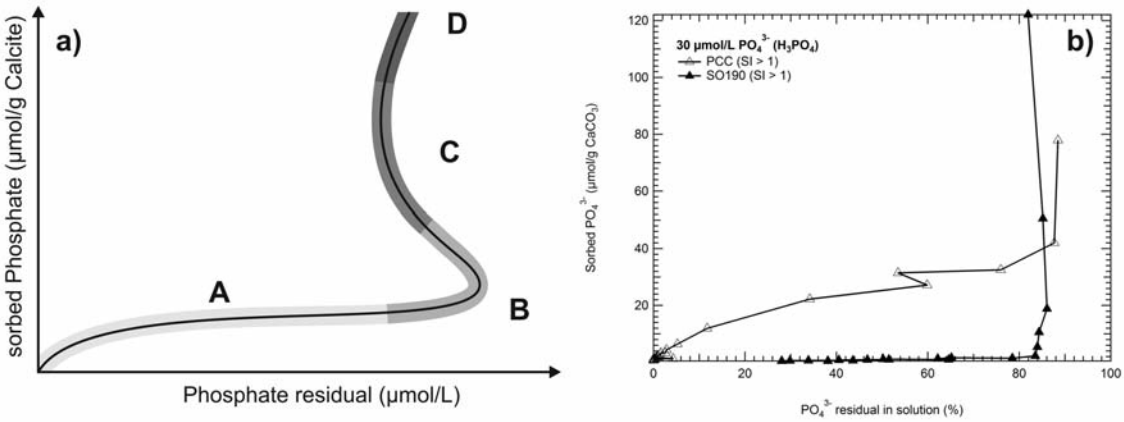

Figure 3.3: a) Schematic sorption isotherm for phosphate on calcite surfaces according to van Cappellen (1991), b) experimentally determined sorption isotherm for starting concentration of 30 µmol PO_4^{3-}/L.

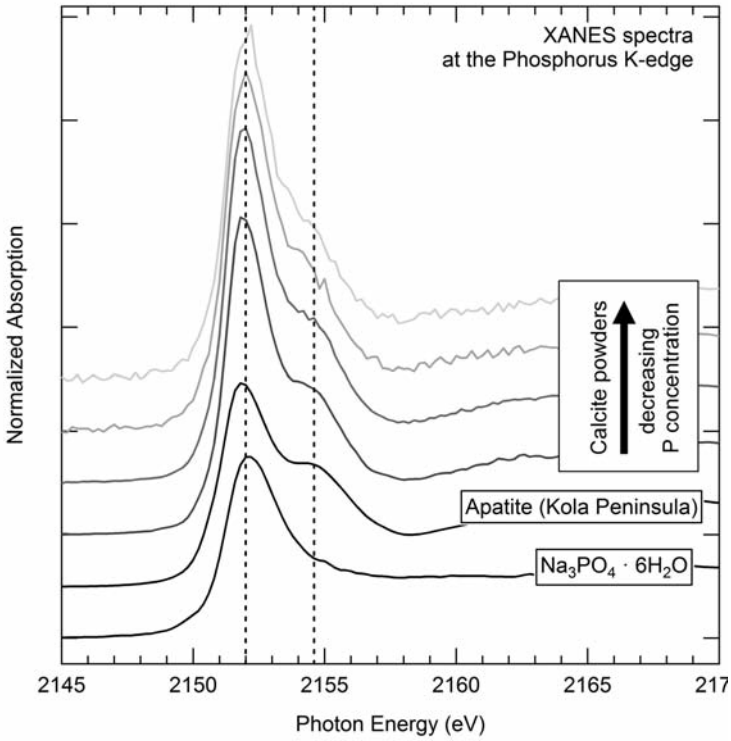

Figure 3.4: XANES spectra recorded at the P K-edge of phosphate-doped PCC powders and crystalline references materials, dashed lines mark energies at 2152.0 eV (phosphate »whiteline«) and 2154.6 eV. Analyses were conducted at the SUL-X and INE beamline at ANKA (KIT), respectively.

compounds and (D) the adsorption of phosphorus on the newly formed Ca-P surface (low Cc/PO_4^{3-}). These sections are different for the applied calcite powders of the experimental series. Figure 3.3 b) shows an example for experimentally determined sorption isotherms (30 µmol PO_4^{3-}/L) which can be divided in different sections. On the basis of these observations further analytical investigations will be carried out.

Processed calcite powders have been analysed using SEM imaging and, as a novel approach, XAFS spectroscopy (in particular XANES) is used to identify the speciation of phosphorus and phase transformations on the calcite surface. By applying these methods, a main goal is to understand the different phases of fixation and sorption and the transition zone (changeover from A to C in Fig. 3.3 a), respectively, on the calcite surface at the molecular scale.

First results show that XANES spectroscopy at the phosphorus K-edge is a suitable tool to identify the speciation of phosphorus on calcite (Fig. 3.4). Two characteristic features are observed at the P K-edge, the phosphate whi-

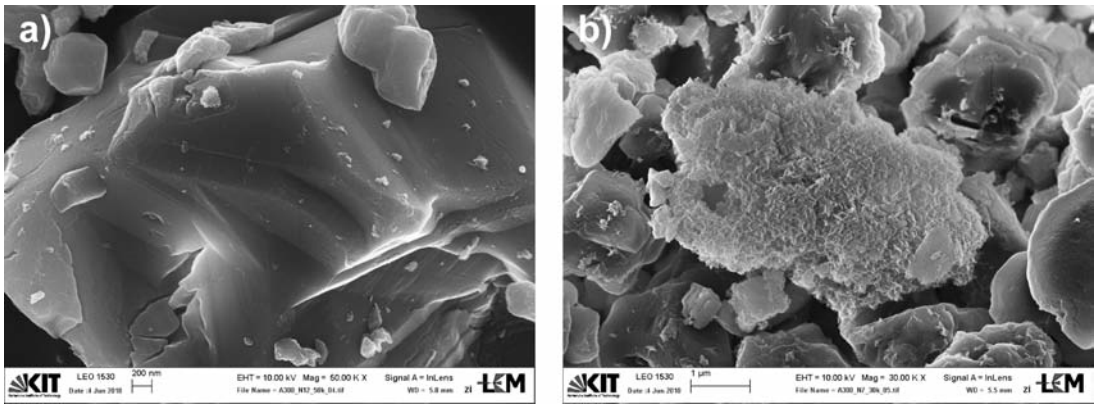

Figure 3.5: SEM images of processed limestone powders; a) section A, ~ 550 ppm P ≙ 6 at/nm2; b) section B, ~ 3600 ppm P ≙ 40 at/nm^2.

teline at 2152.0 eV and a shoulder at 2154.6 eV. The latter is characteristic for Ca-Phosphates and decreases with phosphorus concentration on the calcite powder, which shows a change in the coordination of phosphate. The analysed calcite samples are representative for parts (A) to (C) of the schematic sorption isotherm (see Fig. 3.3 a). SEM imaging has been perfomed for processed sample powders A and B. Only the limestone powder shows the occurrence of new phases in and therefore differences to the starting material. These phases have already been identified as Octa-Calcium-Phosphate (*Freeman and Rowell, 1981*).

3.3. Summary

Three calcite powders have been processed in batch sorption experiments. Based on the post-experimental solution chemistry, powders have been chosen for further analytical work. Merck $CaCO_3$, the limestone powder and the PCC powder show different shapes of the sorption isotherms. Phase transformations have been determined by SEM imaging for the limestone powder surfaces, but more detailed work including using SEM and EDX on all powders is necessary and in progress.

First XANES results at the P K-edge show two different spectral details and a change of the feature at 2154.6 eV with decreasing P concentration. Further XAFS spectroscopy (including XANES/EXAFS) at both the Ca K-edge (4038 eV) and the P K-edge (2146 eV) is planned. XPS and XRD analyses of the powders and AFM studies using Iceland spar single crystals, respectively, are in progress and will help to complete the characterisation of the atomic and molecular environment of phosphate at calcite surfaces.

4. Interactions of etidronic acid and PCC powders during the calcite crystal growth

Precipitated calcium carbonates (PCC), a purified, refined or synthetic calcium carbonate, are an industrial mass product commonly used during the production of pharmaceutical products, varnish and colours, paper, cosmetics and in the food processing industry (*e.g. Souto et al., 2008*). Moreover, organic additives such as etidronic acid (HEDP, HPO_3^{2+}), citric acid or tartaric acid are used in a wide field of industrial application of calcite chelating, dispersing or complexing agents in the production of paper, cosmetics and pharmaceutical products (*Dunn et al., 1994*). Our first experiments will focus on the interaction of HEDP during the calcite crystal growth.

First batch sorption experiments investigating the interaction of organic additives on the calcite crystal growth, especially of PCCs, were conducted in saturated and oversaturated calcite solutions and solution free of calcite. These solutions were produced as described in section 3.1. HEDP (etidronic acid, $C_2H_8O_7P_2$) was added in concentrations of 0 to 50 µmol/L (as organic agent) to the solution. For experiments 100 mg of calcite (Cc) powder (PCCs,

Merck p.a. $CaCO_3$, Iceland spar) varying in specific surface area (0.3 to 23.8 m^2/g) was added to 20 mL solution. Additionally, PCCs vary in crystal morphologies (scalenohedral, prismatic, rhombohedral). Afterwards, sample vials were closed and shaken for 24 h (Fig. 3.1). After the experiments, all solution were filtered and checked for alkalinity and pH. Ca^{2+} and P concentrations were determined AAS and/or ICP-OES. Phosphorus concentrations of the processed calcite powders were determined by EDXRF analyses.

pH values remained at 8.15 to 8.35 during the experimental run. (Over)saturated calcite solutions show decreasing trends for Ca^{2+} and HCO_3^- concentrations in dependence of the SSA. Differences can be observed in solutions where Cc powder with a max. SSA of ~2 m^2/g are used as crystal seeds. Here, the concentration of Ca^{2+} drops more efficiently when HEDP is available. Overall decrease of Ca^{2+} and HCO_3^- leads to a noticeable decrease of the calcite saturation, which was calculated using the PHREEQC software (*Parkhurst & Appelo, 1999*). Three experimental series with HEDP were conducted. Starting concentrations of 5 and 50 µmol/L were adjusted for (over)saturated calcite solutions and solutions without Ca^{2+} and HCO_3^- (Fig. 4.1). HEDP is eliminated from a pure etidronic acid solution by 80 to 90 %. Depending on the SSA of the applied Cc powder, up to 65 % of the starting HEDP is removed from the calcite solution. So far, no systematic interconnection of HEDP sorption and crystal morphology has been observed for SSA ~ 7 m^2/g. EDXRF analyses of Cc powders show P concentrations of 1000 to 1500 ppm.

First results show that the Ca^{2+} concentration of a calcite solution decreases stronger when HEDP is present. Differences in the decrease of HCO_3^- compared to solutions without HEDP have not been observed. From our experiments, this is valid for calcite powders with SSA ~ 2 m^2/g. This observation is supported by results reported by *Lin & Singer (2005)* or *Sawada et al. (2003)* and shows possible inhibition of calcite growth at these conditions due to precipitation Ca-P compounds. For HEDP a linear decrease dependent on the SSA of the Cc powder has been observed.

Changes in the calcite morphology and the P speciation and bonding at the calcite powder surfaces will be tracked using additional analytical methods (SEM, XRD, XPS, XAFS) and, furthermore, within in-situ AFM studies. Promi-

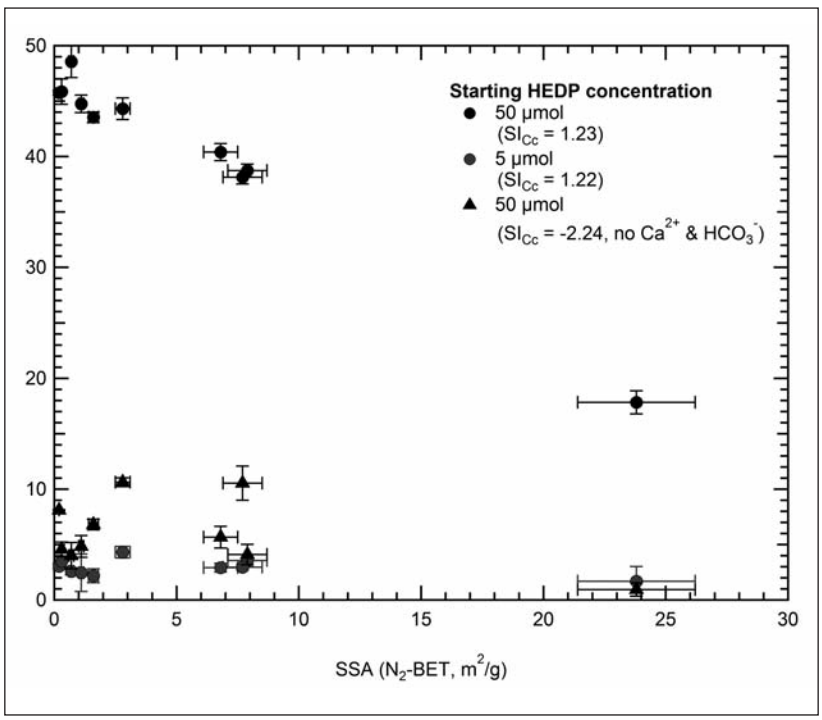

Figure 4.1: Remaining HEDP concentration in solution after experiment.

sing XANES measurements have been conducted at the P K-edge (Fig. 3.4), further analyses are planned.

5. Reactivity of calcite surfaces during concreting

Natural limestone plays a key role in the manufacturing of Portland cement and thus for the production of a broad bandwidth of building products, such as concrete. In order to reduce the ecological impact of modern cements, limestone is added to the cement as a filler material, thus reducing the cement clinker content. With increasing replacement rate, however, pronounced changes in the fresh and hardened concrete behaviour can be observed. At the fresh state, limestone strongly deteriorates the working mechanisms of modern concrete admixtures, such as superplasticizers, leading to pronounced problems in the placing and handling of the fresh concrete. This behaviour is normally attributed to the TOC content of the natural limestone, as this might interact with the organic matter of the superplasticizers. Systematic investigations regarding this important mechanism are not yet available. Further, limestone powder could be identified to trigger early hydration by acting as nucleus for the formation of calcium silicate hydrates, which are responsible for the strength of a hardened concrete (*Matschei et al., 2007*).

One of the primary goals of the research subproject described below, was to identify the interaction mechanisms of modern concrete superplasticizers with limestone powders (LSP) of different provenance and composition. On this basis, eluation tests investigating the dissolution behaviour of limestone in both an aqueous environment (carrier liquid water) and in an alkaline environment (pH 13, 1.0 mol/dm³ NaOH/KOH solution) were carried out. The volume fraction of solids in the solution was adjusted to be 5 vol.%, allowing for an undisturbed dissolution process far away from the saturation limit. Two types of superplasticizers, a polynaphtalene-sulphonate (PNS) which acts electrostatically and a polycarboxylate (PC) which acts sterically, were investigated. Each admixture was added to the carrier liquid at a dosage of 0.5 mass.% of the limestone. All investigations were carried out at 20 °C. The suspensions were continuously stirred during the investigation ensuring a homogeneous distribution of the particles in the carrier liquid. At certain time intervals, the pH value, conductivity and temperature of the solution were determined. Further, samples of 25 cm³ of the suspension were taken, filtrated and the filtrate was analyzed for its Ca, Mg and K ion content using the AAS method. Ca and Mg ions have been identified in earlier studies to have a significant influence on the rheological properties of the cement suspension (*Haist, 2009*).

As shown in Figure 5.1 (left), the Ca content in the carrier liquid strongly increases (background Ca content NaOH/KOH solution 0.14 g/dm³; NaOH/KOH + PC 0.41 g/dm³; NaOH/KOH+PNS 5.4 g/dm³) in the first minutes after addition of the solvent, indicating that pronounced quantities of limestone dissolve in the carrier liquid. This behaviour is independent of the presence of superplasticizer and the type of superplasticizer. After the first dissolution processes, the Ca content decreases again, indicating precipitation processes occurring in the solution. This process is identical for solutions with and without polynaphthalene-sulfonates. For suspensions containing the admixture on polycarboxylate basis, dissolution and precipitation processes seem to repeat several times, resulting in an oscillation of the total calcium content in the filtrate. The results further indicate, that the organic admixtures become chemically unstable over time and decompose after approx. 1400 min. (~24 h), resulting in a further decrease of the calcium content. Beyond this time, the precipitation process of calcium seems to continue, possibly accompanied by an oriented re-crystallization of calcium on the particle surface. However, from the logarithmic scaling of the time axis, no end-member could be identified from the measured data.

Plotting the calcium content in the filtrate eluated by the limestone normalized on calcium

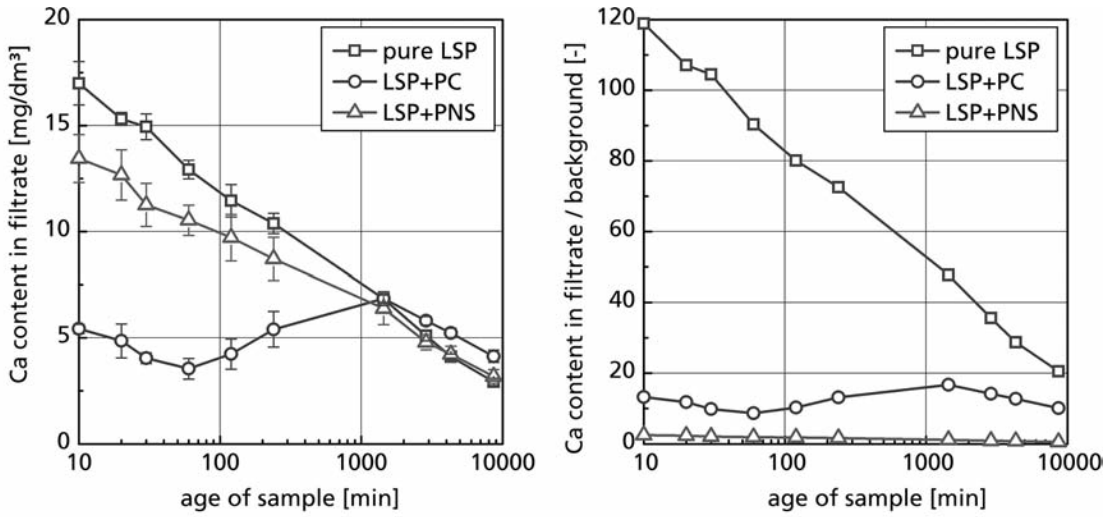

Figure 5.1: Calcium eluation of technical LSP in NaOH/KOH brine (pH 13, 1.0 mol/dm³) with and without superplasticizer based on polynaphthalin-sulfonate, PNS, or polycarboxylate, PC: absolute Ca content in filtrate (left) and content normalized by background (right).

content in the solution (with or without admixture), it becomes obvious, that the dissolution process of limestone and the release of calcium is strongly inhibited by the addition of both admixture types. The dissolution process itself is ascribed to the chemical instability of the limestone in the surrounding alkaline environment. Calcium dissolves from the surface of limestone powder and then precipitates again on the surface, possibly in a different crystal structure. At the same time there is an interaction of the superplasticizer with the calcite surface. This inhibits both the dissolution and the crystal growth, which could explain the time dependence of the calcium concentration in the normalized diagram (see Fig. 5.1, right). The eluation tests prove that limestone powder therefore interacts with both investigated superplasticizers, however in a different manor. In order to verify and characterise these processes in detail, surface sensitive analyses of the reactions between calcite and admixture will be carried out using AFM and ESEM methods. Additional eluation experiments are being carried out at the moment.

Based on the results of the eluation tests, combined rheological and electro-acoustical investigations on pure limestone powder suspensions and cement suspension with limestone powder fractions were carried out. The rheological behaviour of the suspension was determined using both oscillatory and rotational rheometer tests. First results of the rheological tests have been reported in (*Müller et al., 2009*). At the same time, the zeta potential of the particles and the medium agglomerate size in the suspension are determined in situ using electro-acoustical measurement techniques. Therefore, a defined AC voltage is applied to the sample, resulting in an electrical field in the suspension. In case the suspended particles are electrically charged with a charge of ζ (zeta potential in mV), the particles start to oscillate in the electrical field of amplitude E resulting in an oscillating pressure wave in the incompressible carrier liquid. This pressure signal is recorded using an ultrasound transducer. From the amplitude of the pressure signal p, the zeta potential ζ can be calculated using Eq. 5.1:

$$\zeta = \frac{p}{E} \cdot \frac{1}{(\rho_p - \rho_s) \cdot c \cdot \phi} \cdot \frac{3\eta_s}{2\varepsilon_0 \varepsilon_r} \cdot \frac{1}{G(\alpha) \cdot (1 + f(\lambda, \omega'))}$$

In Eq. 5.1 ρ_p and ρ_s denote the density of the particle and the carrier liquid, respectively. The parameter c denotes the speed of sound in the carrier liquid. The phase content ϕ in the tests was set to 0.44. η_s, ε_0 and ε_r describe the dynamic viscosity, the specific dielectrical constant and the permittivity of the carrier liquid. $G(\alpha)$ and $f(\lambda,\omega')$ are correction terms. For further details regarding this measurement technique see (*Haist et al., 2009*).

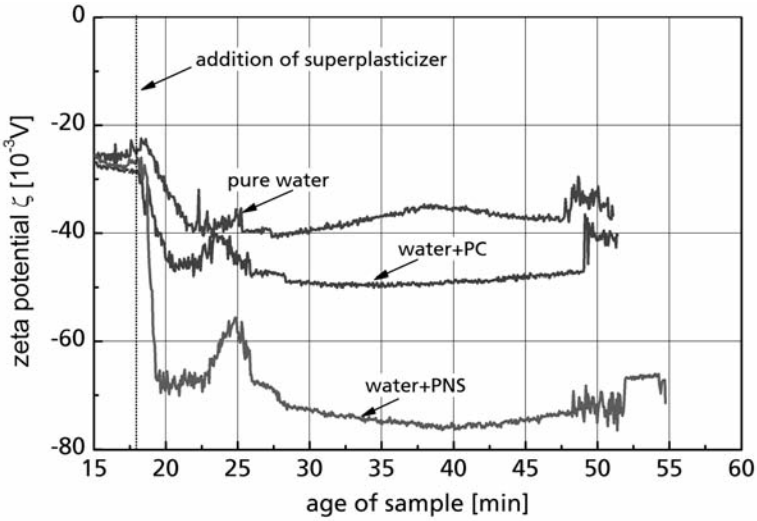

Figure 5.2: Temporal development of the zeta potential of limestone powder (LSP) in pure water, water and polycarboxylate (PC) and water and polynaphthalin-sulfonate (PNS).

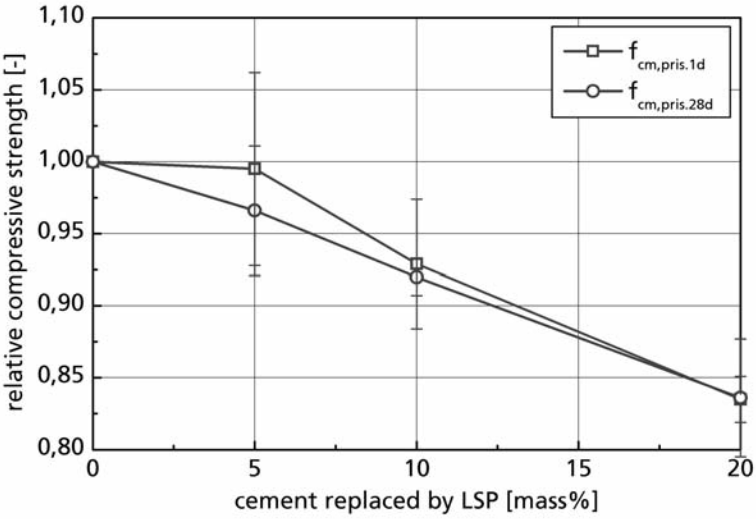

Figure 5.3: Influence of the cement replacement by limestone powder (LSP) on the compressive strength determined on prismatic specimens (40x40x160 mm³) normalized by the compressive strength of specimens with pure cement.

Figure 5.2 shows the influence of different types of superplasticizers on the zeta potential of limestone powder particles suspended in water. Both the addition of polycarboxylate (PC) as well as the addition of polynaphthalin-sulfonate (PNS) leads to a strong reduction of the zeta potential of the particles. For the admixture on PNS basis, this reduction is more pronounced than for the one on PC basis. However, also the suspension without superplasticizer addition shows significant changes in the zeta potential in a time frame between 17 and 25 min. after addition of water to the dry powder. The reasons for this reduction are assumed to be linked to the calcium eluation and re-precipitation observed in the eluation tests. However, the mechanisms for this process still have to be clarified by additional tests. The same is true for the pronounced peak in the zeta potential time curve at the age of approx. 23 to 25 min. This peak is observed independent of the presence and the type of superplasticizer and also has to be clarified.

The long-term influence of the cement replacement by limestone powder was studied using tests on hardened concrete. Therefore, prismatic specimens measuring 40 x 40 x 160 mm³ were casted from the different cement pastes, demolded after one day and stored in water until testing. On the specimens, the compressive and the bending tensile strength were determined according to DIN EN 196-1.

As shown in Figure 5.3, the replacement of cement by limestone powder leads to a systematic decrease in the compressive strength. The reduction of cement, however, is not identical to the reduction in strength. Despite the large scat-

ter, for cement replacements by LSP of up to 20 mass.%, a cement reduction by 1 % leads to a reduction of compressive strength of approximately 0.7 % for the investigated limestone powder. Further investigations are in progress.

6. Thermodynamics of mixing in carbonate solid solutions from atomistic simulations

In the past project period we have successfully modelled the thermodynamics of cationic, $(Ca/Mg)^{2+} = Cd^{2+}$ and anionic, $(CO_3)^{2-} = (SO_4/SeO_4)^{2-}$ substitutions in carbonates. The solid solutions have been modelled with two different atomistic simulation approaches, namely, the Double Defect Method (DDM) (*Vinograd et al., 2009*) and the Single Defect Method (SDM), which we have developed for iso-structural and non-iso-structural substitutions, respectively. The substitution $(Ca/Mg)^{2+}=Cd^{2+}$ has been studied within two binary sections of the ternary system $CaCO_3$-$MgCO_3$-$CdCO_3$. The description of the binary section $(Ca_{0.5}Mg_{0.5})CO_3$-$(Cd_{0.5}Mg_{0.5})CO_3$, dolomite-Cd-dolomite, required the development of a ternary version of the DDM (*Vinograd et al., 2010*), which was accomplished within the project. The modelling of the non-iso-structural solid solutions $CaCO_3$-$CaSO_4$ and $CaCO_3$-$CaSeO_4$ with calcite and aragonite structure types was performed using the SDM. The SDM provides an algorithm for the calculation of the thermodynamic properties of virtual end-members with the compositions of $CaSO_4$ and $CaSeO_4$, which involves simulation of supercell structures of the host phases ($CaCO_3$ calcite/aragonite) with one CO_3^{2-} unit replaced with a SO_4^{2-} or SeO_4^{2-} unit.

6.1. The system $CaCO_3$-$MgCO_3$-$CdCO_3$

The main aim of this study was to derive the mixing properties along the $CaCO_3$-$CdCO_3$ (calcite) and $(Ca_{0.5}Mg_{0.5})CO_3$-$(Cd_{0.5}Mg_{0.5})CO_3$ (dolomite) binaries and thus to be able to model the co-precipitation of Cd^{2+} with calcite and dolomite. The secondary aim was to provide an additional test for a new set of empirical pair potentials for Ca,Mg-carbonates developed by *Raiteri et al. (2010)*. The new force-field model has shown excellent performance in the description of relative stability of all known polymorphs of $CaCO_3$ and of hydration properties of calcite. The task was to test its accuracy in predicting the effects of mixing in the solid solutions. These aims essentially required us to model the mixing properties within the ternary system. The binary systems were modelled with the standard DDM (*Vinograd et al., 2009*). The simulation results are in the excellent agreement with the available experimental data. The mixing in the calcite-otavite binary is essentially ideal. This is in an agreement with the recent experimental data of *Katsikopoulos et al. (2008)*. The calcite-dolomite and otavite-dolomite binaries show the tendency to the formation of the ordered intermediate compounds with the dolomite structure. The predicted subsolidus phase relations are in good agreement with the experimental data of *Goldsmith and Heard (1961)* and *Goldsmith (1972)*. The temperature-composition diagrams are shown in Figure 6.1 a) & b). Here we wish to emphasize that this agreement did not required any adjustment of the force-field parameters of *Raiteri et al. (2010)*. The Cd-O potential was obtained by fitting to the formation energies of several ordered compounds in the otavite-magnesite system calculated quantum-mechanically by *Burton and van de Walle (2003)*. The obtained agreement with the experimental data within the binaries suggests that the model is sufficiently accurate for the compositions within the ternary system. Figure 6.2 shows the free energy of mixing in the ternary system at 873 K calculated with the ternary DDM. The miscibility gaps are shown in the projection of the free energy surface onto the ground plane. In Figure 6.3 the activities of the solid solutions with the calcite and dolomite structures are compared. Our results suggest that the mixing of Cd and Ca within the ordered dolomite structure is less ideal than within the calcite-otavite binary. This is the effect of the third component, $MgCO_3$. The increase in »non-ideality« is due the contraction of the dolomite lattice relative to the structure of calcite, which is caused by the presence of compact Mg-layers. The next step of our research will be

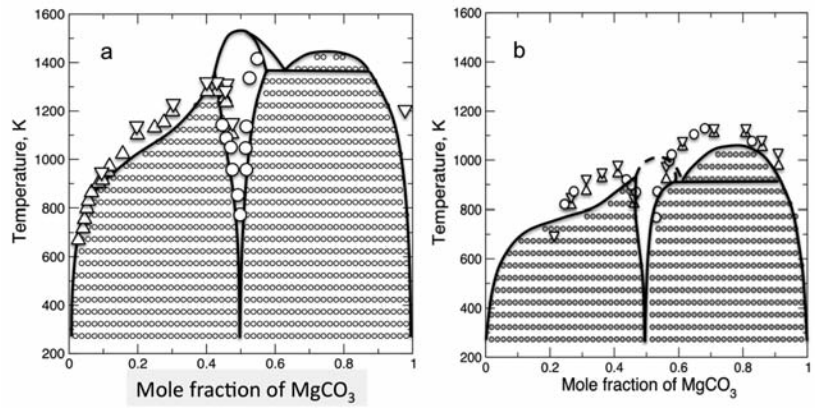

Figure 6.1: The subsolidus phase relations in calcite-magnesite (a) and otavite-magnesite (b) systems simulated with the Monte Carlo method using the pairwise interactions computed with the DDM. The symbols are the experimental data from *Goldsmith and Heard (1961)* (a) and *Goldsmith (1972)* (b), respectively.

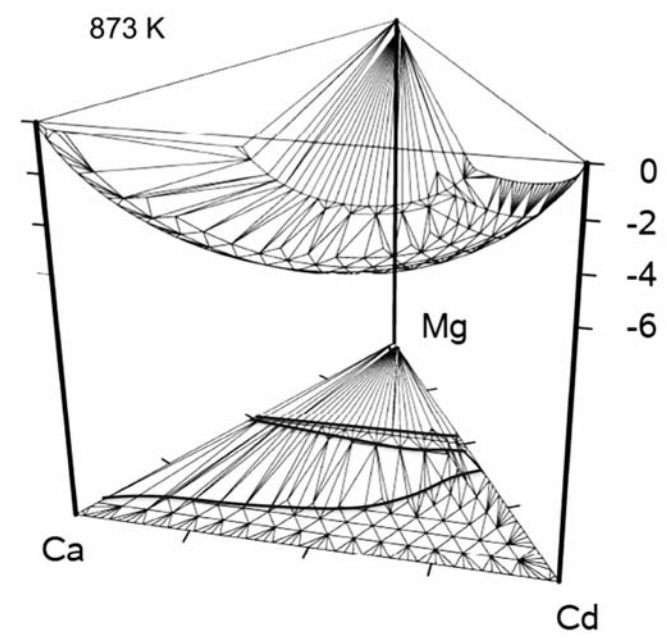

Figure 6.2: The Gibbs free energy of mixing in the calcite-magnesite-otavite, $CaCO_3$-$MgCO_3$-$CdCO_3$, system at 873 K simulated with the Monte Carlo method using the pairwise interactions computed with the ternary DDM. The solid curves outline the boundaries of the miscibility gaps.

to use the predicted activity-composition relations for the calculation of Lippmann diagrams and for the assessment of relative retention capacity of calcite and dolomite for Cd^{2+}.

6.2. The solid solutions of $CaCO_3$-$CaSO_4$ and $CaCO_3$-$CaSeO_4$ in calcite and aragonite

The thermodynamic description of these solid solutions is problematic. Indeed, all available solid solution theories including the DDM consider iso-structural solid solutions. The theory requires that the both end-members should belong to the same space group. This condition cannot be fulfilled, as it is not possible to build two iso-structural end-members due to the different geometry of CO_3^{2-} and SO_4^{2-}/SeO_4^{2-} groups. The fortunate circumstance is that due to the structural difference, these solid solutions are very dilute. Diluted solid solutions are typically very disordered and thus, the regular model description is adequate. Figure 6.4 shows the enthalpies of mixing of two hypothetical regular solid solutions with calcite and anhydrite structure types, for which complete sets of the end-members are unavailable. We are concerned with the description of mixing in the vicinity of pure calcite only. The enthalpy of mixing of a regular solid solution in the diluted range can be well modelled with a linear equation, which forms a tangent to the enthalpy of mixing curve. The white circle denotes the excess enthalpy of a supercell structure of calcite with a single defect of SO_4^{2-} substituting for CO_3^{2-}. The enthalpy of this

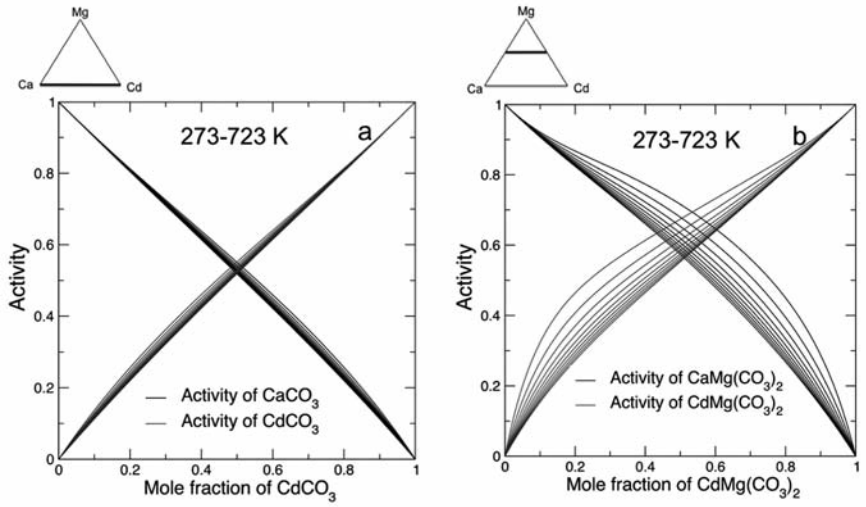

Figure 6.3: The activity-composition relations in calcite-otavite (a) and dolomite-Cd-dolomite (b) solid solutions computed with the Monte Carlo method.

Table 6.1: The total energies of the supercell structures and the total energies of the virtual end-members in eV calculated with SDM. The last column shows the energy of reference compounds, whose thermo- dynamic properties are assumed to be known.

Host phase	Single defect structure	Virtual end-member	Reference compound
$Ca_{16}(CO_3)_{16}$	$Ca_{16}(CO_3)_{15}SO_4$	$CaSO_4$ (in calcite)	$CaSO_4$ (anhydrite)
-39448.321	-40005.622	-3022.821	-3023.859
$Ca_{16}(CO_3)_{16}$	$Ca_{16}(CO_3)_{15}SO_4$	$CaSO_4$ (in aragonite)	$CaSO_4$ (anhydrite)
-39447.490	-40003.622	-3021.921	-3023.859
$Ca_{16}(CO_3)_{16}$	$Ca_{16}(CO_3)_{15}SeO_4$	$CaSeO_4$ (in calcite)	$CaSeO_4$ (anhydrite)
-39448.321	-39983.964	-3001.163	-3002.456
$Ca_{16}(CO_3)_{16}$	$Ca_{16}(CO_3)_{15}SeO_4$	$CaSeO_4$ (in aragonite)	$CaSeO_4$ (anhydrite)
-39447.490	-39982.142	-3000.120	-3002.466

The calculations are performed with CASTEP in DFT GGA approximation with PBESOL functional at 0 GPa

structure necessarily belongs to the enthalpy of mixing function of the disordered solid solution, because a structure with a single defect cannot have any ordering. The enthalpy of this structure also falls on the tangent, because the ratio of solute to host concentration is small. This implies that if it was possible to define a virtual end-member, which enthalpy falls on the tangent line, then such a solid solution would be strictly ideal. The single defect method is based on the notion that the enthalpy of the virtual end-member can be calculated knowing the absolute enthalpy of the single defect structure, the enthalpy of the host phase and the number of the exchangeable units in the supercell. Figure 6.5 shows the supercell structures of calcite and aragonite with a single defect of SO_4^{2-} used in the study. Table 6.1 shows the results of the calculation of the enthalpies of virtual compounds with $CaSO_4$ and $CaSeO_4$ composition, which form ideal solid solutions with calcite and aragonite. The standard enthalpies of the virtual compounds can be calculated knowing the standard enthalpy of a stable compound, which has the same composition as the virtual compound. Clearly, the enthalpy of this compound should be calculated with the same atomistic simulation approach, which was used to calculate the properties of the virtual end-member. In the case of the $CaCO_3$-$CaSO_4$ solid solution $CaSO_4$ anhydrite is a natural choice for the reference compound. In the case of the $CaCO_3$-$CaSeO_4$ system, a stable compound with $CaSeO_4$ composition does not exist. However, there is a possibility to estimate the standard properties of a compound iso-structural to anhydrite from the reaction (Eq.6.1.)

$$CaSeO_4 + CaSO_4{\times}2H_2O = CaSO_4 + CaSeO_4{\times}2H_2O$$

where $CaSeO_4{*}2H_2O$ is a well characterized compound iso-structural to gypsum. Our quantum-mechanical calculations suggest that the enthalpy change due to the reaction in Eq.

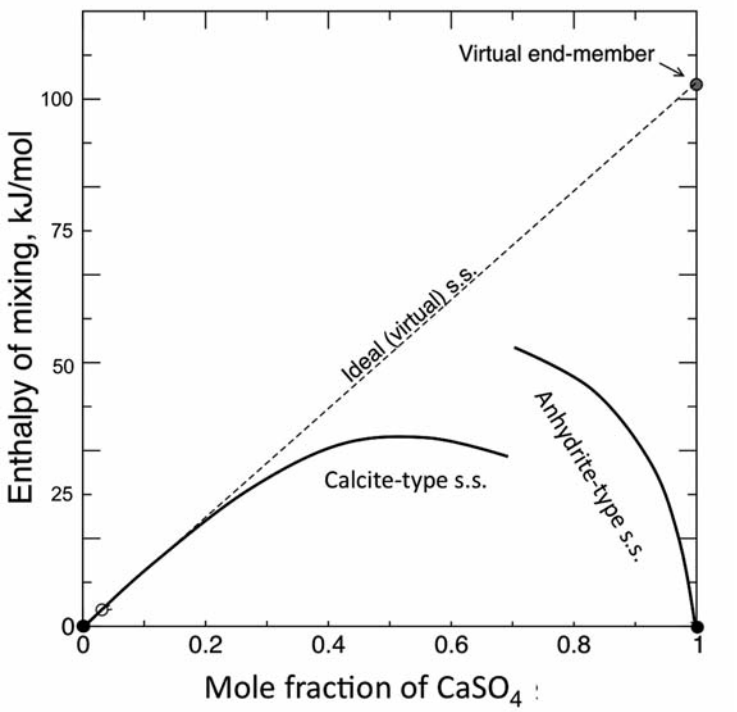

Figure 6.4: The virtual end-member construction for $CaCO_3$-$CaSO_4$ system. The solid circles are the stable host phases with calcite and anhydrite structures. The white circle is the excess energy of a supercell of calcite with one CO_3^{2-} group replaced with a SO_4^{2-} group. The grey circle is the enthalpy of the virtual $CaSO_4$ end-member, which corresponds to ideal calcite-type solid solution.

6.1 is -10.85 kJ/mole. Neglecting the entropy change in this reaction and using thermodynamic data for $CaSeO_4$*$2H_2O$, $CaSO_4$(anhydrite) and $CaSO_4$*$2H_2O$ (gypsum) from the Nagra-PSI data base (*Hummel et al., 2002*), we obtained -996.87 kJ/mol for the standard Gibbs free energy of $CaSeO_4$ (anhydrite). Our next concern was to estimate the standard entropies of the virtual end-members $CaSO_4$ (in calcite) and $CaSO_4$ (in aragonite) by calculating the phonon density of states of the relevant supercell structures. The lattice dynamics calculations were performed with the program GULP (*Gale and Rohl, 2003*). The force-field model was combined from the model of *Allan et al. (1993)* for sulphates and a new model of *Raiteri et al. (2010)* for carbonates. These calculations have shown that the standard entropies of the virtual compounds $CaSO_4$ (in calcite) and $CaSO_4$ (in aragonite) are 121.7 and 142.8 J/mol/K, respectively. Knowing the standard entropy of $CaSO_4$ (anhydrite) of 105.32 J/mol/K, and using the enthalpy values from Table 6.1, we obtained the values of -1226.41 and -1145.87 for the standard Gibbs free energies of $CaSO_4$ (in calcite) and $CaSO_4$ (in aragonite), respectively. Assuming that the entropy changes of the reactions

$$CaSeO_4 \text{ (in calcite)} = CaSeO_4 \text{ (anhydrite)}$$

(Eq. 6.2)

and

$$CaSeO_4 \text{ (in aragonite)} = CaSeO_4 \text{ (anhydrite)}$$

(Eq. 6.3)

are the same as in the analogous reactions for sulphates, we obtained the values of -877.11 and -781.81 kJ/mol for the standard Gibbs free energies of $CaSeO_4$ (in calcite) and $CaSeO_4$ (in aragonite), respectively.

The obtained values permit straightforward calculations of the retention levels of SO_4^{2-} and SeO_4^{2-} in carbonates equilibrated with aqueous solutions. Assuming that the maximum possible ion activity product $[Ca^{2+}][SO_4^{2-}]$ in aqueous solutions is limited by the equilibrium solubility product of $CaSO_4$*$2H_2O$ (gypsum), we can calculate the maximum retention levels of SO_4^{2-} in calcite and aragonite from the reactions:

$$CaSO_4 \text{ (in calcite)} = CaSO_4 \times 2H_2O \text{ (gypsum)} - 2H_2O$$

(Eq. 6.4)

$$CaSO_4 \text{ (in aragonite)} = CaSO_4 \times 2H_2O \text{ (gypsum)} - 2H_2O$$

(Eq. 6.5)

The maximum retention levels of SeO_4^{2-} can be obtained from the analogous reactions:

$$CaSeO_4 \text{ (in calcite)} = CaSeO_4 \times 2H_2O - 2H_2O$$

(Eq. 6.6)

$$CaSeO_4 \text{ (in aragonite)} = CaSeO_4 \times 2H_2O - 2H_2O$$

(Eq. 6.7)

The equilibrium concentration of SO_4^{2+} in calcite according to Eq. 6.4 is defined by the equation

$$RT \cdot \ln x\left(SO_4^{2-}\right) = \Delta G_f^0\left(CaSO_4 \cdot 2H_2O\right) - 2 \cdot \Delta G_f^0\left(CaSO_4(calcite)\right)$$
$$= -1797.24 + 474.26 + 1226.41 = -96.57 kJ / mol$$

(Eq. 6.8)

Therefore, the maximum equilibrium retention level of SO_4^{2-} in calcite at 298 K is $1.3*10^{-17}$. The analogous calculations for aragonite give an even smaller value of $8.3*10^{-32}$. The retention levels of SeO_4^{2-} in calcite and aragonite calculated using the reactions in Eq. 6.6 and Eq. 6.7 are $7.4*10^{-24}$ and $1.5*10^{-40}$, respectively. These small values are essentially determined by the predicted large enthalpies of the virtual compounds relative to the enthalpies of the anhydrite-type phases.

6.3. Summary

Our results show that quantum-mechanical calculations and force-field modelling provide useful tools for predicting equilibrium retention levels of hazardous components in carbonate minerals. Particularly, we have demonstrated that the DDM is able to quantitatively predict mixing properties of various iso-structural binary and ternary carbonate solid solutions. We have also demonstrated the possibility of a quantitative modelling of non-iso-structural solid solutions with the SDM.

The particularly interesting result is that the equilibrium retention levels of SO_4^{2-} and SeO_4^{2-} in carbonates are very low. This implies that the reasonably large concentrations SO_4^{2-} and SeO_4^{2-} in carbonates reported in literature (*Reeder et al., 1994; Pingitore et al., 1995*) should be attributed to non-equilibrium entrapment effects.

7. Conclusion and Outlook

In the past project period, promising and useful results with regard to industrial application have been achieved. The calcite(104)-water interface has been characterised by in-situ surface diffraction under varying hydrochemical conditions. Moreover, experimental results investigating the interaction of the calcite sur-

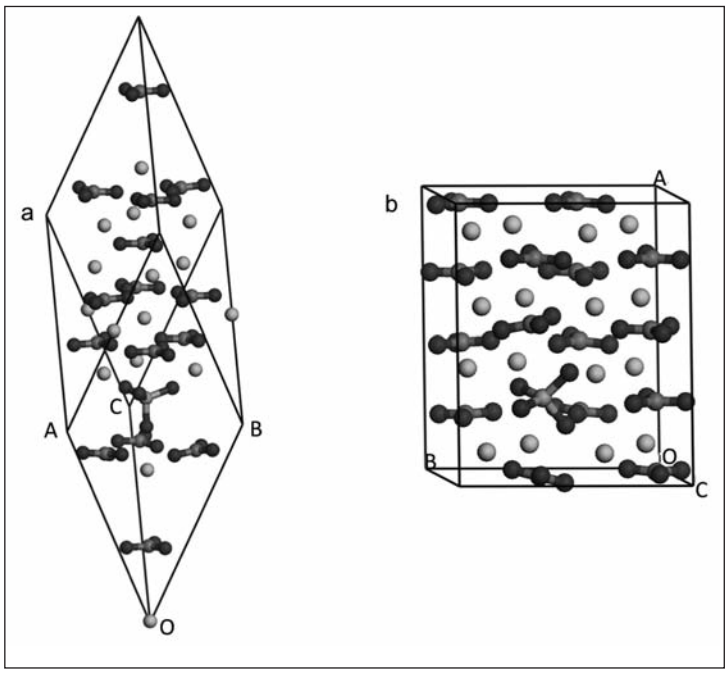

Figure 6.5: The relaxed 2x2x2 and 2x2x1 supercells of calcite (a) and aragonite (b) with one CO_3^{2-} unit replaced with SeO_4^{2-} unit. The geometry minimization calculations were performed with CASTEP in GGA-PBE approximation.

face and Se show that calcite is an efficient medium to immobilise oxianions and EXAFS studies characterized the adsorption species of Se, respectively.
Elimination of phosphate from calcite solutions by calcite powders shows that P fixation is predominantly a function of the specific surface area. Occurrence of sorption mechanisms, new Ca-P phases and phase transitions, respectively, is different for each applied calcite powder. Systematic SEM and EDX studies accompanied by further XRD and XAFS analyses will indicate points of changeover from sorption to precipitation. Additional AFM studies will help to understand inhibition and/or growth mechanisms on the calcite powder and single crystal surfaces. The results achieved to date provide a basis for forthcoming experimental and analytical work and are promising for advances in the application of calcite materials in water treatment and phosphate recycling, respectively.
Experiments investigating the interactions of limestone powder and superplasticizers, with regard to concreting, show uncommon dissolution and re-crystallisation pattern of calcite at alkaline conditions. Further analytical work is necessary to describe the observed behaviour of the admixtures during the experimental run-time.
Results of quantum-mechanical calculations and force-field modelling are useful to predict equilibrium retention levels calcite minerals. In the following project period, these methods will try to solve or support specific problems investigated with experimental methods in the lab.

Acknowledgements
We wish to thank Dr. Dmitrii Kulik, Dr. Enzo Curti (Paul Sherrer Institute, Switzerland), Prof. Julian D. Gale (Curtin University, Perth, Australia) for the help in this project. The atomistic calculations were performed at the Center for Scientific Computing at the University of Frankfurt.

The ANKA (KIT) beamline staff at SUL-X (Jörg Göttlicher, Ralph Steininger) and INE (Jörg Rothe, Kathy Dardenne) is greatly acknowledged for support during test analyses and beamtime measurements. Hartmut Gliemann is acknowledged for support during AFM analyses at the Institute of Functional Interfaces (KIT-IFG).

References

Austen, K., Wright, K., Slater, B. & Gale J.D. (2005) The interaction of dolomite surfaces with metal impurities: a computer simulation study. Phys. Chem. Chem. Phys. 7, 4150–4156.

Babin, J., Prepas, E.E., Murphy, T.P., Serediak, M., Curtis, P.J., Zhang, Y. & Chambers, P.A. (1994) Impact of lime on sediment phosphorus release in hardwater lakes: The case of hypereutrophic Halfmoon Lake, Alberta. Lake and Reservoir Management 8, 131-142.

Belzile, N., Pizarro, J., Filella, M. & Buffle, J. (1996) Sediment diffusive fluxes of Fe, Mn, and P in a eutrophic lake: Contribution from lateral vs. bottom sediments. Aquatic Sciences - Research Across Boundaries 58, 327-354.

Berg, U., Neumann, T., Donnert, D., Nüesch, R. & Stüben, D. (2004) Sediment capping in eutrophic lakes - efficiency of undisturbed calcite barriers to immobilize phosphorus. Appl. Geochem. 19, 1759-1771.

van Cappellen, P. (1991) The formation of marine apatit - A kinetic study. PhD thesis, Yale University, New Haven.

van Cappellen, P., Charlet, L., Stumm, W. & Wersin, P. (1993) A surface complexation model of the carbonate mineral-aqueous solution interface. Geochim. Cosmochim. Acta 57, 3505-3518.

Casey, W.H., Rock, P.A., Chung, J-B., Walling, E.M. & McBeath, M.K. (1996) Gibbs energies of formation of metal-carbonate solid solutions 2: the CaxSr1-xCO3 system at 298 K and 1 bar. Am. J. Sci. 296, 1–22.

Clark, S. J., Segall, M. D., Pickard, C. J., Hasnip, P. J., Probert, M. J., Refson, K. & Payne, M. C. (2005) First principles methods using CASTEP. Zeitschrift fuer Kristallographie 220, 567-570.
Driver, J., Lijmbach, D. & Steen, I. (1999) Why Recover Phosphorus for Recycling, and How?. Environ. Technol. 20, 651-662.

Dunn, C.J., Fitton, A. & Sorkin, E.M. (1994) Etidronic Acid - A Review of Its Pharmacological Properties and Therapeutic Efficacy In Resorptive Bone-disease. Drugs & Aging 5, 446-474.

Eiche, E.; Berg, U.; Song, Y. & Neumann, T. (2008) Fixation and Phase Transformation of Phosphate at Calcite Surfaces – Implications for Eutrophic Lake Restoration Australasian Institute of Mining and Metallurgy Bulletin, 292-302.

Freeman, J. S. & Rowell, D. L. (1981) The adsorption and precipitation of phosphate onto calcite. Europ. J. Soil Sci. 32, 75-84.

Gale, J.D. & Rohl, A.L. (2003) The General Utility Lattice Program (GULP). Molecular Simulations 29, 291-341.

Gilbert, N. (2009) Environment: The disappearing nutrient. Nature 461, 716-718.

Goldsmith, J.R. & Heard, H.C. (1961) Subsolidus phase relations in the system CaCO3-MgCO3. J. Geology 69, 45-74.

Goldsmith, J.R. (1972) Cadmium dolomite and the system CdCO3-MgCO3. J. Geology 80, 617-626.

Hummel, W., Berner, U.R., Curti, E., Pearson, F.J. & Thoenen, T. (2002) Nagra/PSI chemical thermodynamic data base 01/01. Radiochim. Acta 90, 805-813.

Haist, M. (2009) Zur Rheologie und den physikalischen Wechselwirkungen bei Zementsuspensionen. Dissertation Universität Karlsruhe (TH), Germany.

Hart, B., Roberts, S., James, R., Taylor, J., Donnert, D. & Furrer, R. (2003) Use of active barriers to reduce eutrophication problems in urban lakes. Water Sci. Technol. 47, 157-163.

Katsikopoulos, D., Fernandez-Gonzalez, Á. & Prieto, M. (2008) Crystallization of the (Cd,Ca) CO_3 solid solution in double diffusion systems: the partitioning behaviour of Cd^{2+} in calcite at different supersaturation rates. Min. Mag. 72, 433-436.

Kulik, D.A., Berner, U. & Curti, E. (2004) Modelling chemical equilibrium partitioning with the gems-psi code. In B. Smith and B. Gschwend, editors, PSI Scientific Report 2003. Nuclear Energy and Safety IV, Villigen. Paul Scherrer Institut.

Kulik, D.A., Vinograd, V.L., Paulsen, N. & Winkler, B. (2010) $(Ca,Sr)CO_3$ aqueous-solid solution systems: From atomistic simulations to thermodynamic modelling. Phys. Chem. Earth 35, 217-232.

Lin, Y.-P. & Singer, P. C. (2005) Inhibition of calcite crystal growth by polyphosphates. Water Res. 39, 4835-4843.

Matschei, Th., Lothenbach, B., Glasser, F. P. (2007) The role of calcium carbonate in cement hydration. In: Cement and Concrete Research 37, 551-558.

Müller, H. S., Haist, M., Glowacky, J. (2009) Reactivity of calcite surfaces during concreting. In: GEOTECHNOLOGIEN Statusbericht 2009, Universität Bayreuth, November 2009.

Parkhurst, D.L. & Appelo, C.A.J. (1999) User's Guide To PhreeqC (version 2) - A Computer Program For Speciation, Batch-reaction, One-dimensional Transport, And Inverse Geochemical Calculations. U.S. Geological Survey.

Perdew, J.P., Burke, K. & Ernzerhof, M. (1996) Generalized gradient approximation made simple. Phys. Rev. Lett. 77, 3865-3868.

Pingitore, N.E., Meitzner, G. & Love, K.M. (1995) Identification of sulfate in natural carbonates by X-ray absorption spectroscopy. Geochim. Cosmochim. Acta 59, 2477-2483.

Pokrovsky, O. S., Mielczarski, J. A., Barres, O. & Schott, J. (2000) Surface speciation models of calcite and dolomite/aqueous solution interfaces and their spectroscopic evaluation. Langmuir 16, 2677-2688.

Prepas, E.E., Murphy, T.P., Dinsmore, W.P., Burke, J.M., Chambers, P.A. & Reedyk, S. (1997) Lake Management Based on Lime Application and Hypolimnetic Oxygenation: the Experience in Eutrophic Hardwater Lakes in Alberta. Water Qual. Res. J. Can. 32, 273-293.

Raiteri, P., Gale, J.D., Vinograd, V.L. & Winkler, B. (2010) A computational investigation of the bulk and aqueous surface properties of calcite, magnesite and dolomite (in preparation)

Reeder, R.J., Lamble, G.M., Lee, J-F. & Staudt, W.F. (1994) Mechanism of SeO42-substitution in calcite: An XAFS study. Geochim. Cosmochim. Acta 58, 5639-5646.

Sawada, K., Abdel-Aal, N., Sekino, H. & Satoh, K. (2003) Adsorption of inorganic phosphates and organic polyphosphonate on calcite. Journal of the Chemical Society. Dalton Transactions, 342-347.

Smith, V.H. (2003) Eutrophication of freshwater and coastal marine ecosystems - A global problem. Environ. Sci. Poll. Res. 10, 126-139.
Somasundaran, P. & Agar, G.E. (1967) Zero Point of Charge of Calcite. J. Colloid Interface Sci. 24, 433-440.

Souto, E.C.S., Damasceno, J.J.R. & Hori, C.E. (2008) Study of Operational Conditions for the Precipitated Calcium Carbonate Production. Advanced Powder Technology VI 591-593, 526-530.

Vinograd, V.L., Sluiter, M.H.F. & Winkler, B. (2009) Subsolidus phase relations in the $CaCO_3$-$MgCO_3$ system predicted from the excess enthalpies of supercell structures with single and double defects. Phys. Rev. B 79,10420-104209.

Vinograd, V.L., Paulsen, N., Winkler, B. & van de Walle, A. (2010) Thermodynamics of mixing in the ternary rhombohedral carbonate solid solution (CaxMgyMn1–x–y)CO_3 from atomistic simulations. CALPHAD 34,113-119.

Wolthers, M., Charlet, L. & van Cappellen, P. (2008) The Surface Chemistry of Divalent Metal Carbonate Minerals; a critical Assessment of Surface Charge and Potential Data using the Charge Distribution Multi-Site Ion Complexation Model. Am. J. Sci. 308, 905-941.

Identification and modification of the surface properties of calcite fillers as a basis for new, highly filled adhesives

Diedel R. (1), Dörr H. (1), Geiß P. L.* (2), Presser M. (2), Roth E. (3), Wittwer W. (3)

(1) Forschungsinstitut für Anorganische Werkstoffe – Glas/Keramik – GmbH (FGK), Heinrich-Meister-Str. 2, 56203 Höhr-Grenzhausen

(2) University of Kaiserslautern, Department Mechanical and Process Engineering, Workgroup Materials and Surface Technologies (AWOK), Erwin-Schrödinger-Str., Building No. 58, 67663 Kaiserslautern

(3) Kömmerling Chemische Fabrik GmbH, Zweibrückerstr. 200, 66954 Pirmasens

* Coordinator of the project

Abstract

Powdered calcium carbonates from natural sources are being widely used as fillers in adhesive systems to improve processing and in service performance characteristics. The converting of limestone and marble to adhesive filler materials typically includes grinding and in some cases precipitation and coating to adjust particle size, processability and chemical reaction with the adhesive. It has been frequently observed that calcium carbonate powder batches with apparently similar particle-specific characteristics (e. g. density, chemical composition and particle size distribution) may exhibit significantly varying processing properties in terms of their effect on rheology, curing and adhesive performance of the adhesives formulation. This indicates that different calcium carbonates as raw materials for fillers obviously feature intrinsic characteristics which have not yet been identified and examined sufficiently and whose effect on the processing and product characteristics of highly filled reactive adhesive systems is essential to achieve a sufficient level of process stability, batch-to-batch reproducibility and last not least uniform product quality. The aim of this research project therefore is to reveal the structure-property-relationship between the manifold calcium carbonate particle characteristics on one hand and the physicochemical and technical properties of the resulting adhesives formulation on the other hand.

Introduction

Using leading edge analytical methods, the key particle characteristics and their influence on adhesive properties shall be identified to establish objectively measurable tolerance criteria. The resulting process window is intended to provide an optimum balance of technological target values related to the storage and application properties of the adhesive as well as its material properties after curing within application specific limits.

The variable parameters of the test matrix consider the following factors:

– geological source of raw materials
– grinding process and grinding aids
– grinding degree (entire spectrum of particle size distribution)
– modification state (uncoated, coated with stearates)

The corresponding resulting analytical effort in characterizing powdered calcium carbonate particle properties is the following:

– porosity (Hg pressure porosimetry)

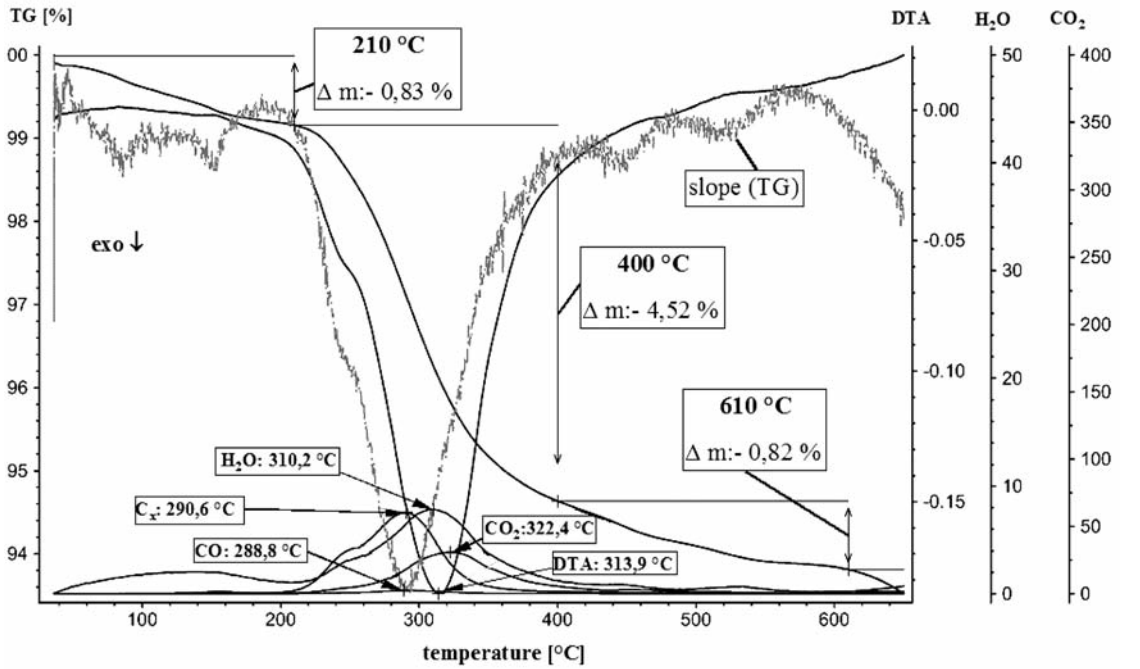

Figure 1: STA of PCC 6 with derivative of the TG curve

– mineral surface (BET nitrogen adsorption)
– chemical composition of the particle surface (Tof-SIMS, XPS)
– mineral composition and crystallinity (X-ray diffractometry)
– zeta potential in aqueous suspension (PCD measuring cell)

After dissolving the different calcium carbonate powders into representative adhesive formulations at a defined filler to prepolymer ratio the following adhesive properties are of major importance:
– curing kinetics (DSC measurements)
– viscosity depending on shear rate (plate-plate viscosimetry)
– sedimentation and phase segregation during storage over a period of 6 months
– change in viscosity during a storage period of 6 months
– thixotropy and sagging characteristics

Chemical and physical analysis of the calcite fillers

In the first year of the project the physical and chemical properties of 21 calcite samples have been analysed extensively. In general, the ground samples (GC and GCC) showed a higher amount of contamination by other mineral phases (mainly quartz), larger primary grains and a reduced agglomeration compared to precipitated products (PCC samples).

The uncoated filler products (GC) differ largely from the synthetic precipitated ones, the samples coated with stearic acid (GCC) having intermediate properties. Depending on the quality regarding crystalline quality and chemical purity these samples can be allocated to one group or the other.

Based upon revision and validation of the generated data, specific analytical methods where employed to investigate the surface properties of coated calcite. In particular the nature of the coating agent (mostly technical stearic acid) has been in the focus of attention.

Simultaneous Thermal Analysis STA (thermogravimetry and differential scanning calorimetry)

The decomposition of the coating agent has occured at temperatures far below the thermal decomposition temperature of carbonate (starting at 825 °C). Other components detected

Table 1: weight loss by decomposition of the coating agent

code	Δm [w%]	code	Δm [w%]
GC 1	0.08	GCC 1	0.97
GC 2	0.12	GCC 2	0.98
GC 3	0.08	GCC 3	1.11
GC 4	0.11	GCC 4	1.21
GC 5	0.10	GCC 5	1.30
PCC 1	2.95	GCC 6	1.76
PCC 2	7.29	GCC 7	1.87
PCC 3	4.82	GCC 8	0.39
PCC 4	2.86	GCC 9	1.09
PCC 5	2.64		
PCC 6	4.52		
PCC 7	2.40		

were physical and chemically bounded CO_2, (crystal-) water, early decomposing carbonates or hydroxides, and miscellaneous organic contaminants.

Fig. 1 shows the decomposition progress of a coated sample (PCC 6). The mass loss during the mean interval (here: 210 to 400 °C) is close – but not exactly – to the amount of the coating agent (compared to the weight loss of the uncoated samples, as specified in table 1). In addition to CO_2 and small amounts of water, due to the partial combustion of the organic compound, a component was detected, which could be assigned to a technical stearic acid composition (a mixture of stearic acid and palmitic acid) by infrared spectroscopy respectively its decarboxylated residue. Not all samples however exhibit a continuous gravimetric loss in weight. For some samples two or three different temperature ranges of decomposition could be observed.

For each sample the decomposition temperature range was determined individually on the basis of its gravimetric curve to minimize weight loss not attributed to the decomposition of the coating.
Table 1 shows the gravimetric change of the coated and uncoated samples in the decomposition range. The three groups of samples can be clearly distinguished according to their characteristic loss in weight. The significantly higher values of the coated precipitated calcites in comparison to the coated ground fillers indicate a higher amount of coating agent due to their smaller primary grain size.
The weight loss of the samples PCC 2, 3 and 6 is remarkably high and relates to the volume fracture of particles smaller than 2 µm, while the BET-values of these samples on a same level. Although GCC 7 and GCC 9 samples have similar specific surfaces compared to the PCCs, the mass loss rate is equal to those of other GCCs. The data suggest that only small amounts of the coating agent are chemically adhered to the particles surface area.

Zeta-Potential

The zeta potential generally depends on effects related to the particle surface. Hence this parameter should be able to give evidence of the surface occupancy. The potential was determined using the DT 1200 equipment from Quantachrome. The different calcite fillers have initially been measured in an aqueous suspension (8 g Powder to 72 ml water) in accordance with the usual procedure and titrated with 0.1 M sodium hydroxide to show the dependence of the potential with increasing pH. Fig. 2 shows the correlation for the GC samples. For samples GC1, GC2, GC3 and

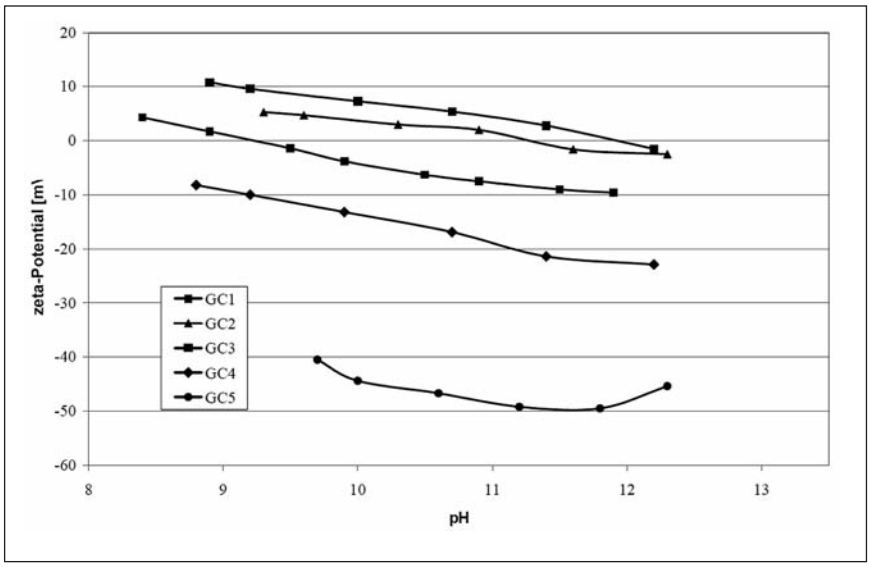

Figure 2: Zeta-potential as function of pH of uncoated calcites in an aqueous suspension

GC4 the potential decreases with increasing pH values.

While the zeta-potentials of these samples are located close to the isoelectric point sample GC 5, which has a much higher specific surface (BET) and a finer grain size distribution than the other fillers, shows a much lower potential. The observed strong variation of zeta-potential for different types of calcites has previously been reported in literature (P. Ney; Zeta-Potentiale und Flotierbarkeit von Mineralen; Springer-Verlag KG; 1973; 96-101.)

Coated Calcites have a tendency to bloat in water. Using pure ethanol in preparing the suspension however carries the risk of distorting the measurement by small amounts of water absorbed on different fillers due to their hygroscopic properties. To eliminate the influence filler humidity on the zeta-potential, GC, GCC and PCC samples were measured in a defined ethanol-water mixture containing10 w% of water. Table 2 gives an overview of the mean zeta-potential data obtained in this way and the corresponding standard deviation (SD). The values in column »Data 2« indicate results of validation experiments carried out to investigate the reproducibility of the described methodology.
Since a well-defined correlation of these results with other calcite properties could not yet be established, the data sets will be further extended to provide a basis for statistical correlation analysis, which is intended to reveal complex property-effect relations. For small values a higher degree of deviation in the results needs to be taken into account. The observed variations in the pH values of the samples (6.2 to 8) have been established after several hours of homogenisation. It should be noted that the ph-values were obtained using a standard pH sensor not being approved for use in alcoholic solution. Therefore the collected pH-values can be used for a qualitative comparison of the behaviour of different fillers and no statement can be made about the absolute accuracy of the pH-values. It could however bee observed that a change in pH has a significant effect on the zeta-potential.
Therefore in a next set of experiments the pH-value for all suspensions of fillers in a ethanol-water mixture was uniformly adjusted to a pH-value of 9.5 using an aqueous buffer solution (NH_3-solution 25 % (8 w%) / ammonia hydrogencarbonate (8 w%)). To avoid precipitation of the buffer the ethanol to water ratio had to be changed to 50:50. The results of the zeta-potential measurements at pH 9.5 according to this methodology are summarized in table 3.
In contrast to the measurements in table 2

Table 2: Zeta-potential in an ethanol-water-mixture (10 w%)

code	zeta-potential [mV]		SD [mV]		pH [-]		SD [-]	
	Data 1	Data 2	D1	D2	Data 1	Data 2	D1	D2
GC 1	28.1	26.5	0.6	0.9	7.1	7.2	0.2	0.1
GC 2	19.5		0.2		7.4		0.3	
GC 3	56.7	39.5	5.4	1.9	7.3	7	0	0.1
GC 4	20.7		0.6		7.1		0.2	
GC 5	20.6		0.2		6.2		0	
GCC 1	3.5		0.4		6.6		0	
GCC 2	6.2		0.2		6.7		0	
GCC 3	-8	-9.8	0.1	1.1	7.7	7.7	0.1	0.4
GCC 4	-9		0.3		7.8		0,1	
GCC 5	-16.5		0.1		8		0.1	
GCC 6	4.5		0.1		6.9		0.1	
GCC 7	6.8	9.4	0.1	0.1	6.5	6.4	0	0.1
GCC 8	1.4		0		6.9		0	
GCC 9	-13.5		0.1		8.2		0.1	
PCC 1	12.7		0.1		7.5		0.1	
PCC 2	8.7		0.2		7.1		0	
PCC 3	9.5		0.1		7.1		0	
PCC 4	16.9	17.9	0.3	0.1	7.3	7.1	0	0
PCC 5	9.3		0.1		6.3		0	
PCC 6	5.6		0.1		7.3		0	
PCC 7	3.8	3.5	0	0.2	7.6	7.4	0.1	0

Table 3: Zeta-potential in an ethanol/ aqueous based buffer (50 w%) system with a constant pH value (9.5 ±0.1)

code	zeta-potential [mV]		SD [mV]	
	Data 1	Data 2	D 1	D 2
GC 1	-7.6		0.3	
GC 2	-7.1	-3.9	0.1	0.2
GC 3	-7.6		0.1	
GC 4	-7.9	-6.5	0.2	0.3
GC 5	-13.6		0.2	
GCC 1	-13.7		0.6	
GCC 2	-14.8		2.0	
GCC 3	-16.6		1.4	
GCC 4	-17.3		1.5	
GCC 5	-17.9		0.5	
GCC 6	-15.3	-13.6	0.9	0.4
GCC 7	-17.8		0.3	
GCC 8	-17.5		0.4	
GCC 9	-15.2	-9.1	0.4	0.2
PCC 1	-12.8		0.2	
PCC 2	-3.5		0.2	
PCC 3	-6.1		0.1	
PCC 4	-16.0	-11.5	0.2	0.2
PCC 5	-22.9		0.6	
PCC 6	-15.7		0.2	
PCC 7	-11.4	-8.6	0.2	0.1

zeta-potentials at a uniform alkalinity of pH 9.5 using an ethanol-water-ratio of 50:50 are all located on a negative scale. The different results indicate that the chemical environment has a strong influence on the zeta-potential analysis and that measurements using different ethanol/water ratios should not be directly compared to each other.

Repeating seven measurements of the samples GC 2, GCC 9 and PCC 4 exhibited standard deviations of 23 %, 17 % and 11 %.

In practice the homogenisation of the coated samples in the solution containing the chemical buffer appeared to be difficult due to foaming and increasing viscosity of the suspension. These effects increased with an increa-

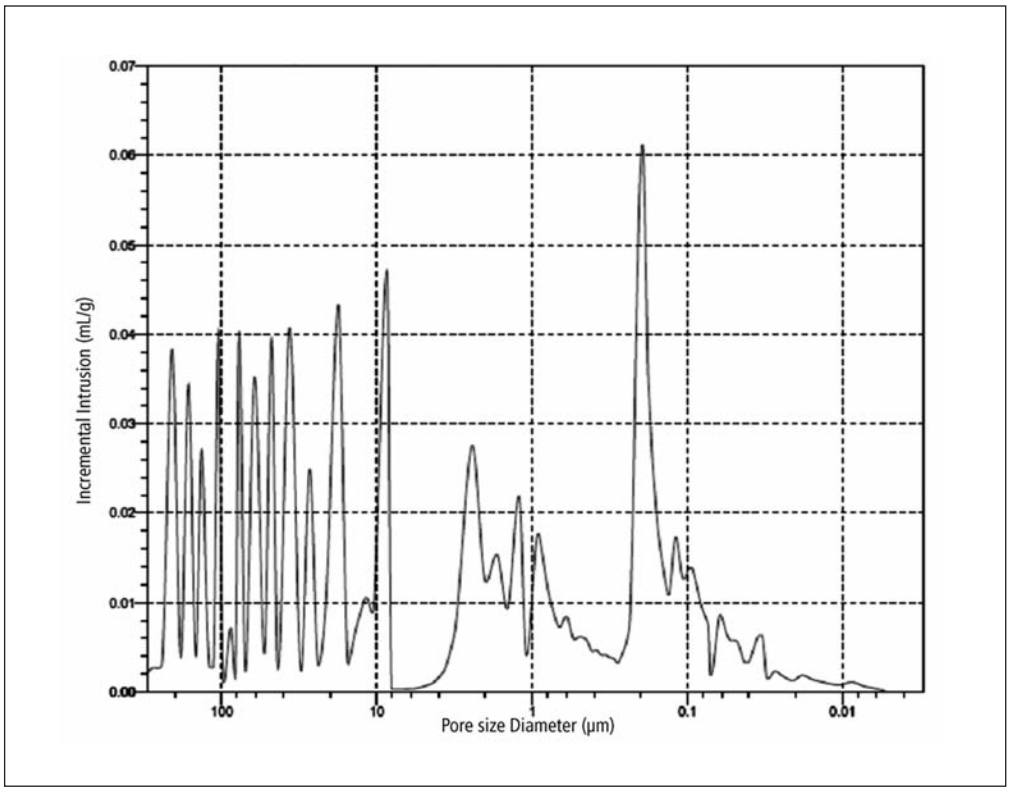

Figure 3: Pore size distribution of GCC 9 powder sample

sing amount of coating agent but accurate results still could be obtained.

Determination of porosity

The porosity was determined by Hg-porosimetry (with AutoPore IV 9520 from Micromeritics) using calcite powders as well as pellets, which were isostatically cold-pressed at 2000 bar.

Both types of experiments have been used to determine the open pore volume and the cavity. Compared to the results obtained using powder samples the porosity of the pellets generally has been shifted to lower values. This serves as an indication, that the porosity of the powder before compression can be characterized as a cavity type of porosity. Additional SEM imaging gave no indication of open porosity up to a detection limit of approximately 0.6 µm.

Density

For the full range of calcite fillers the density was measured using a helium pyknometer (table 4). An increased amount of coating agent causes a decrease of density. The difference between the measured density and the to the theoretical value for pure calcite (2.715 g/cm^3) can however not exactly be related to the amount of coating agent, because technical stearic acid used in the coating process typically contains undefined fractions of palmitic acid and inorganic contaminants like SiO_2 and $MgCO_3$.

Analysis of the surface interaction of coating agent and calcite

The chemical and physical analysis of the different coated and uncoated powdered calcite samples reveals how the variable parameters of the test matrix relate to the characteristic particle properties of the 21 types of fillers. To analyse the specific chemical and physical surface interaction between the coating agent and the calcite surface, calcite crystals were split and the reaction of the newly generated calcite cleavage planes with stearic acid investigated using FTIR-spectroscopy and ToF-SIMS.

In a first set of experiments reference FTIR-spectra of the virgin calcite surfaces were collected at different angles of rotation of the calcite crystal in relation to the diamond tip of the

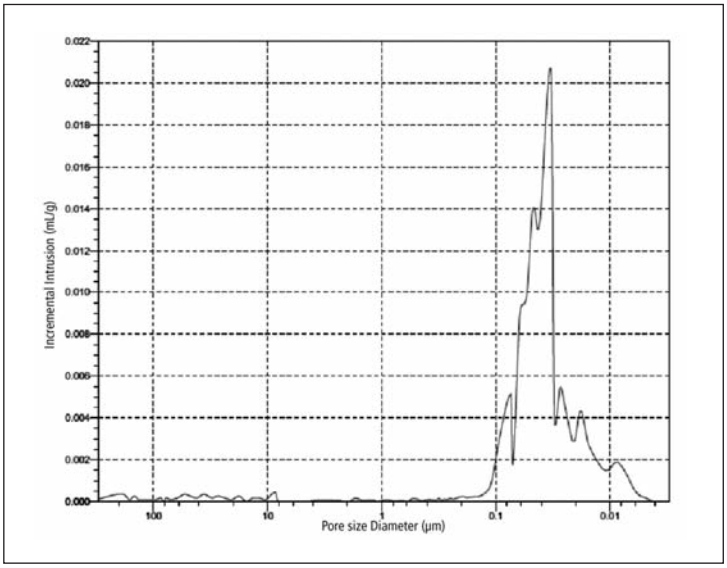

Figure 4: Pore size distribution of GCC 9 pellet sample

Table 4: Density (measured with He-pyknometer)

code	density[g/cm^3]	SD [g/cm^3]
GC1	2.738	0.003
GC2	2.729	0.005
GC3	2.732	0.006
GC4	2.737	0.003
GC5	2.723	0.007
GCC1	2.685	0.004
GCC2	2.675	0.005
GCC3	2.668	0.005
GCC4	2.659	0.006
GCC5	2.662	0.007
GCC6	2.637	0.004
GCC7	2.632	0.009
GCC8	2.707	0.003
GCC9	2.674	0.007
PCC1	2.544	0.006
PCC2	2.404	0.008
PCC3	2.493	0.009
PCC4	2.575	0.008
PCC5	2.574	0.008
PCC6	2.491	0.008
PCC7	2.598	0.009

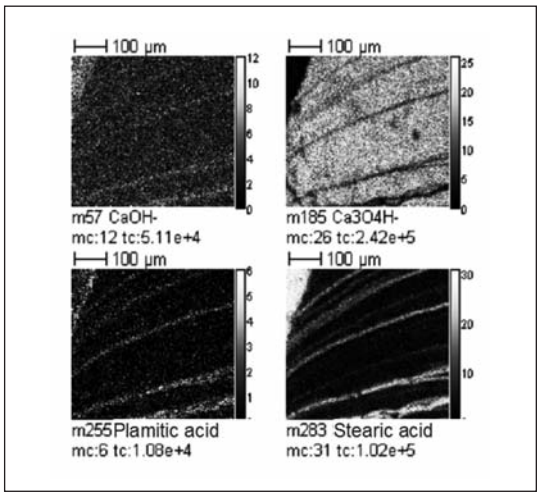

Figure 5: ToF-SIMS mapping of the distribution of stearic acid on the surface of calcite crystals after desorption in isopropanol (negative polarity)

FTIR-spectrometer. Due to the optical anisotropy of the calcite crystal a constant angle of rotation needs to be maintained in comparative measurements. The virgin calcite surface was then coated with stearic acid at 70 °C which is to a large degree similar to the industrial coating process of the powdered calcite fillers. The presence of stearic acid on the calcite surface could afterwards be easily detected by FTIR-spectroscopy.

To find out whether the nature of the surface adhesion between stearic acid and calcite is dominated by physical or chemical interaction, it was attempted desorption of excessive stearic acid was carried out in isopropanol at ambient temperature. Surprisingly 30 seconds of immersion in isopropanol at ambient temperature were sufficient to completely remove the stearic acid from the calcite surface, at least beyond the threshold of sensitivity of the FTIR-analysis. Compared to the spectra of the virgin calcite surface immediately after splitting, the IR-spectra of the desorbed calcite surfaces show characteristic peaks indicating the presence of CO_3^{2-} which could not be observed before the coating and desorbing procedure.

To take advantage of a higher resolution and sensitivity, additional analyses were conducted using ToF-SIMS at the Institut für Oberflächen und Schichtanalytik (ifos) in Kaiserslautern. The ToF-SIMS measurements confirmed the results of the FTIR-experiments in so far, as most of the stearic acid seemed to have been removed after desorption in isopropanol. However at the edge of fracture planes a higher amount of residual stearic acid had collected which obviously resisted desorption due to a strong surface interaction. The total amount of this stearic acid residue found by ToF-SIMS analysis however is below the detection threshold of the FTIR-spectrometer.

The results above suggest, that a strong surface interaction between calcite and stearic acid occurs predominantly at dislocations like edges and fracture planes. Transferred to the case of coated powdered calcite fillers this observation could lead to an explanation of the difference in filler properties due to parameters related to the geological origin and parameters of the grinding and coating process. Further experiments and analyses including defined coating and desorption of stearic acid in combination with calcite crystals and calcite powders are planned to gain further insight and understanding of the calcite-coating and calcite-polymer interaction in highly filled adhesives.

Technical adhesive product validation

Various application-specific test methods have been established to characterize the uncured adhesive material In terms of e.g. storage stability, extrudability, sagging behaviour, spreading and wetting. The difference in curing characteristics, which have been previously investigated by Dynamic Scanning Calorimetry (DSC), in practice determine the pot life and the increase of shore hardness as a measure for the curing adhesives cohesive strength.

In this part of the project the correlation between the chemical-physical properties of the different calcite fillers (published in the first science report of this project) and the technical product properties of a polyurethane adhesive formulation including these fillers, have been investigated.

Sedimentation behaviour after storage

Sedimentation during storage is an undesired phaenomenon because segregation of the adhesive formulation leads to non-uniform

Figure 6: Sedimentation after different storage times at 50 °C (1, 4, 8, 12 weeks)

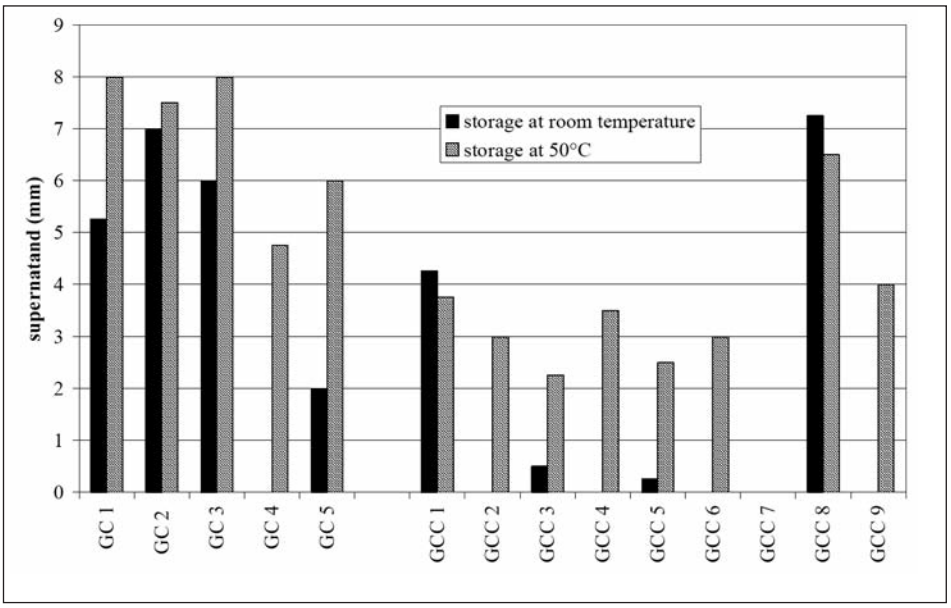

Figure 7: Sedimentation behaviour of polyurethane adhesive with different calcites

product properties (Fig. 6). If segregation occurs during storage, the liquid and solid phases have to be remixed and homogenised before application which causes increased effort and expenses.

After preparing adhesive formulations using the different types of uncoated and coated fillers the amount of supernatant was measured after a storage period of six months at room temperature and at 50 °C (Fig. 7).

Especially after storage at 50 °C a correlation between the used calcite filler and the sedimentation in the polyurethane adhesives A component becomes obvious. The GC types with low BET values generally tend to segregate more than the GCC calcites with larger BET values. GCC 8 represents in so far an exception, as its level of sedimentation characteristic is more similar to the GC types of fillers. Because of their small particle size causing high adhesive viscosities, all PCC fillers exhibit no sedimentation at all.

Extrusion behaviour

The extrusion behaviour is an important feature directly related to the dispensing of an adhesive. In hand operated dispensing tools the extrusion behaviour relates to the effort necessary to squeeze a certain amount of adhesives through the dispensing tip. The extrusion rate was determined using a pneumatic cartridge dispenser at an operating pressure of 5000 hPa and measuring the amount of adhesive dispen-

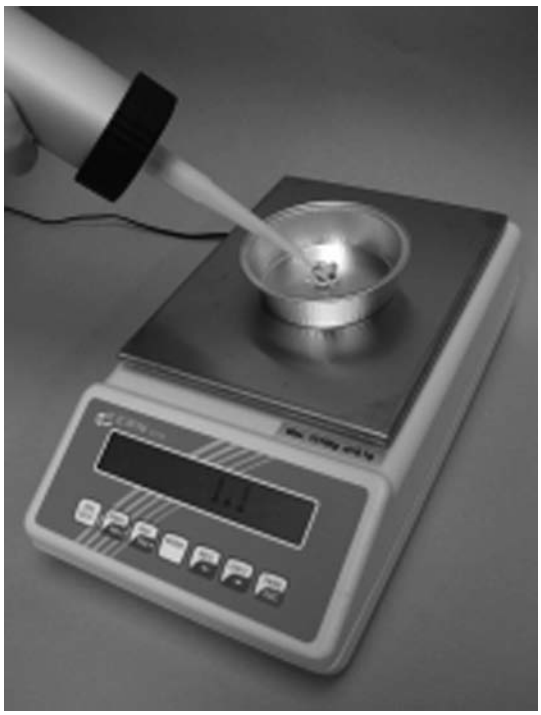

Figure 8: Measuring the cartridge extrudability of an adhesive-filler-formulation

sed in a defined period of time (Figure 8). Results in Figure 9 are expressed in g/s units.

Similar to the results shown in the chapter before the extrusion rate depends on the physical characteristic of the calcite filler. The GC formulations with a low viscosity, based on the low BET of the filler, have a higher extrusion rate in opposition to the GCC and PCC types. The same exceptions as in Figure 7 are visible, GCC 7 is similar to the PCC group and GCC 8 looks like a GC calcite.

Sagging

Sagging relates to flow of an adhesive rope under the effect of gravity (Figure 10). To determinate sagging according to EN ISO 14678, an adhesive rope with a certain diameter is applied to a vertical metal plate and the distance of flow after one minute is measured (Figure 11).

Figure 11 illustrates, that sagging predominantly occurs when uncoated GC fillers are being used. GCC8 and GCC1 however also exhibit a significant amount of sagging. The sagging characteristic of the GC types of fillers relates to their BET value and particle size.
Sagging does generally not occur when PCC types of fillers are being used in the adhesives formulation.

Curing characteristics

Curing of the reactive adhesive starts after mixing the A and B component. The term »pot life« relates to the period of time during which the mixed adhesive can be handled and applied without the risk of loss of adhesive performance due to an advanced level of curing leading to a higher viscosity of the adhesive and poor wetting properties. Once the transition from the viscous to the solid state of the adhesive is accomplished, the shore hardness gives an indication of the attained level of cohesive strength until the curing reaction is completed.

Pot life

The pot life was determined by measuring the increase in viscosity after mixing both reactive components. The pot life is considered to have expired, once the viscosity has doubled its initial value (Fig. 12).

It should be assumed, that the chemical reaction between the coating agent (stearic acid) and the adhesives formulation causes a reduction in pot life. The exception represented by GCC2, PCC4 and PCC7 however suggest, that inverse effects related to other particle properties can cause prolonged pot life even in the presence of coated fillers.

Shore A hardness

The progression of the shore hardness in time relates to the speed of cure of a certain adhesive formulation. This parameter is especially important to determine the time, when an adhesively bonded structure has developed a sufficient initial load capacity and can be handled for further manufacturing steps. To access this characteristic a specimen with defined thickness (5 mm) is cured under normal climate at 23 °C and 50 % r. h. and the shore A hardness is measured (Fig. 13).
As in the case of the pot life, the results of the shore A hardness after 6 hours of curing show

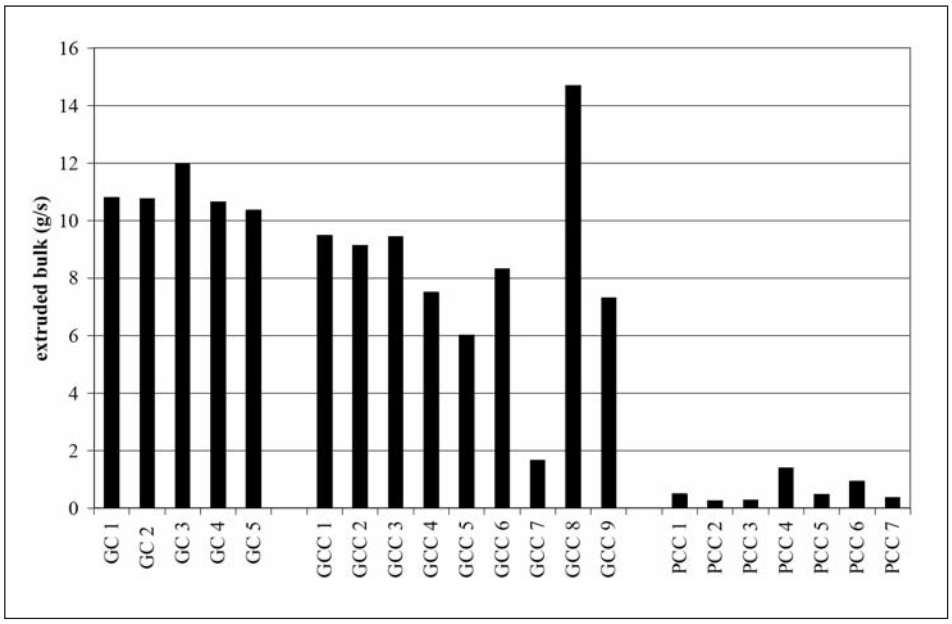

Figure 9: Extrusion rate at 5000 hPa and 23°C with a polyurethane A component including different fillers

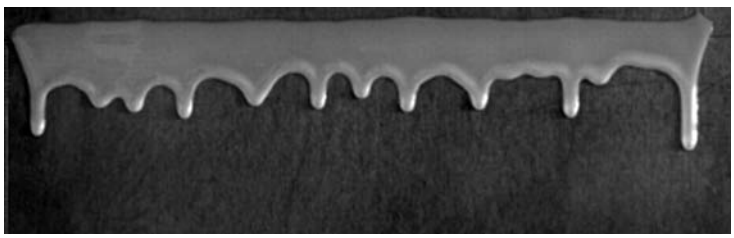

Figure 10: Sagging of an adhesive rope on a vertical adherent surface

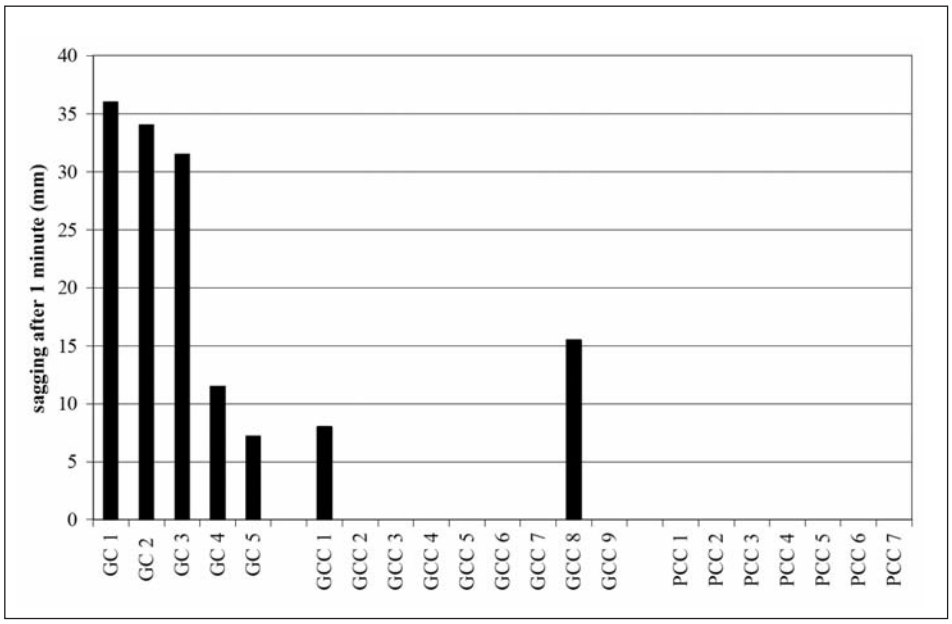

Figure 11: Flow behaviour of polyurethane A-component with different calcite fillers

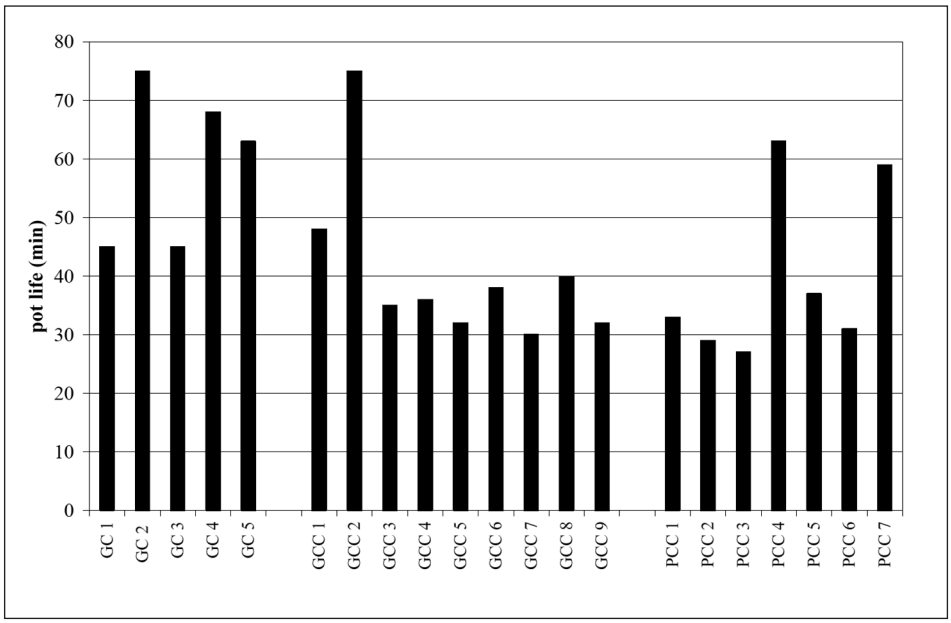

Figure 12: Pot life of 2 component polyurethane mixture with different fillers at 23 °C

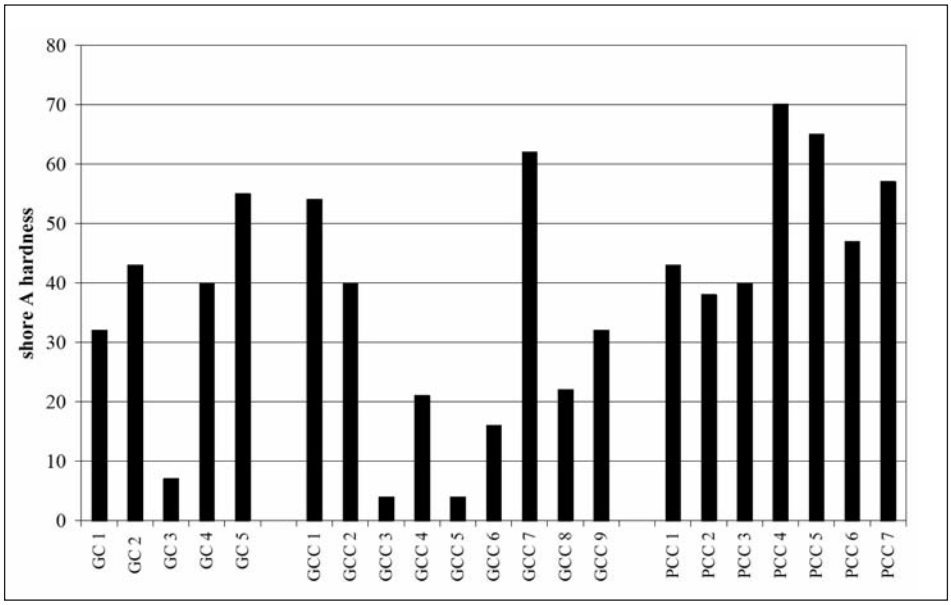

Figure 13: Shore A hardness of a polyurethane mixture with different fillers after different curing time

a non-uniform characteristic. To identify multi-dimensional property-effect-relations sophisticated mathematical methods of regression analysis have been applied in the course of the project taking advantage of the generated database now comprising sets of analytical particle characteristics, chemical and physical adhesives properties as well as technical product features.

Analysis of property-effect-relations of calcitic fillers in adhesives

The data based mathematical analysis is focused on gaining insight into the influence of intrinsic properties of calcitic fillers on the chemical/physical as well as on the technical properties of the corresponding formulated adhesives. For this purpose data from validated measurements were provided for 21 different calcitic fillers, each of them belonging to one of the three groups GC, GCC or PCC.

For the basic characterization of the different fillers various parameters concerning for example the chemical composition, the zeta potential, the specific surface and the distribution of particle sizes were chosen. In order to keep the number of potential influence parameters as small as possible, the shapes of the particle distributions were analyzed in such a way that they can well be approximated via 5 parametric bimodal densities. A further analysis of the so-defined input parameter space was carried out to detect and eliminate multicollinearities. As a first result it could be confirmed that 6 of the input variables can be explained on a 95%-level via linear combinations of the remaining independent ones.

In the next step of this subproject mappings between the set of remaining influence parameters and the set of the corresponding adhesive properties, the so-called output parameters, will be identified via the estimation of mathematical regression models. In order to account for the unbalance between the numbers of model parameters to be estimated and the available measurements, a further reduction of the input space via principal component analysis, respectively factor analysis will be performed previously. As models for regression purely linear models as well as models that are non-linear in their parameters will be considered. In parallel a partial least squares regression (PLS) approach, that simultaneously considers the structure of the output space, will be investigated. Finally the best model for each of the adhesive properties will be identified via cross validation techniques. A study of the corresponding relevance diagrams that are computed from the identified models then is expected to reveal the impact of the individual calcitic filler properties on the chemical/physical as well as on the technical properties of the corresponding formulated adhesives.

OAP process optimization

Based on classical quality management tools according to Ishikawa, FMEA and R&R, the FGK has developed a method of process capability analysis (OAP method: Output Accepted Process), with which natural mineral raw materials (clays, kaolins, feldspars, carbonates) are tested for their influence and their stability in manufacturing processes. To identify the dominant process parameters and their range, to control the coating process in an industrial environment, a first inventory of the processing steps, the critical parameters and the actual process control was performed according to the OAP® procedure in cooperation with the industrial partner. In this inventory the actual process and product flow as well as the status of the process control (including the handling of non-conformities) »as is« was taken into account, indicating a high degree of process capability and closed loop controls. On the basis of the chemical and physical analysis of the calcite fillers additional parameters have been identified, which may be used e. g. in the filler coating process as a basis for raw materials and process control. Due to the lack of sufficient detection and measurement possibilities these parameters can however only be assessed as sum-parameters, which impedes their specific use and integration in the actual process control.

Therefore during the upcoming phase of the project additional effort will be taken to qualify methods like e.g. the measurement of the zeta-potential of a filler suspension and to implement them into an enhanced process control, as described in the phase model presentation of the adhesive production (Fig. 14).

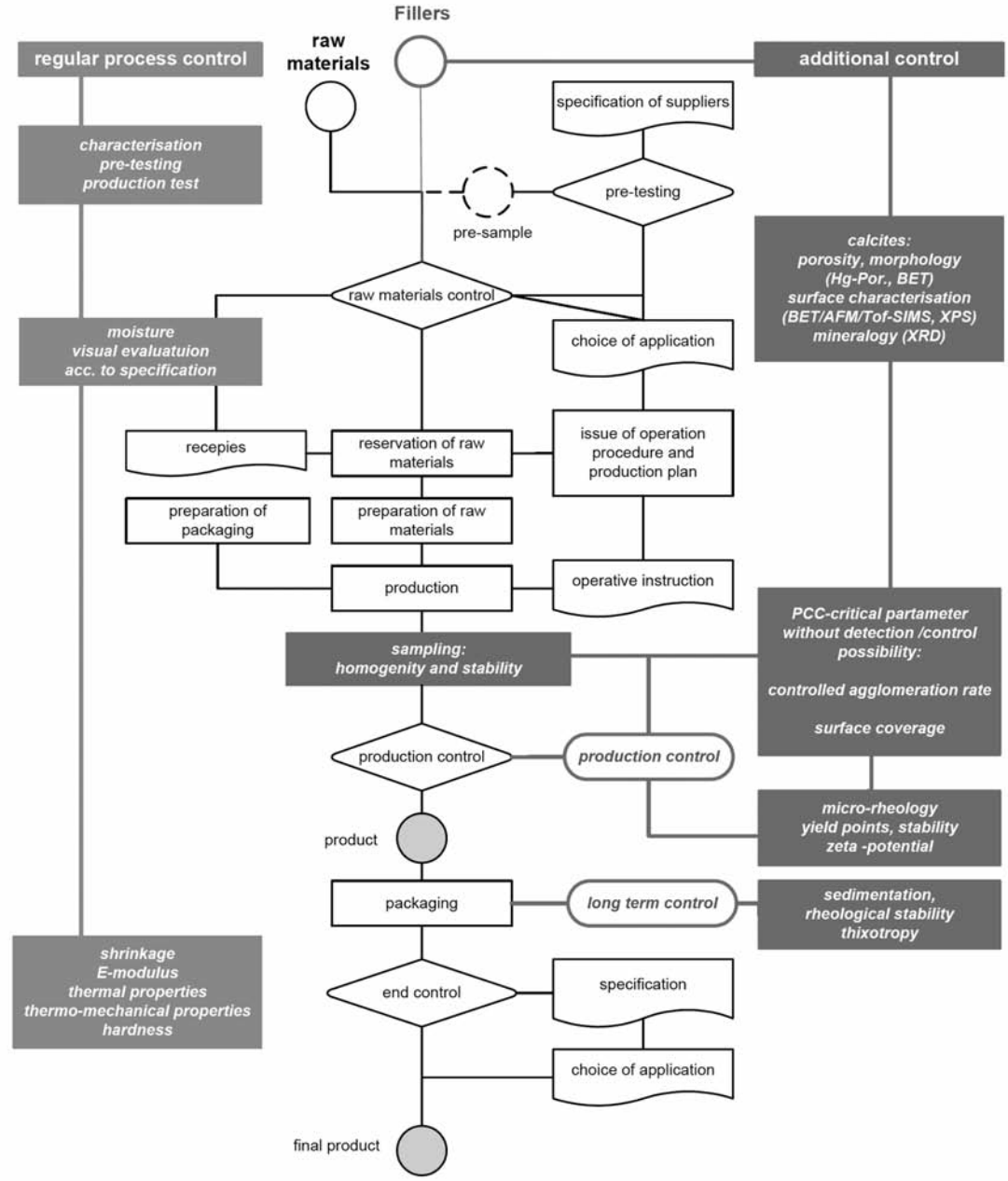

Figure 14: Simplified phase model presentation of the adhesive production process using calcite fillers, including the additional control factors specified for the coating process

Summary

In the current stage of the project the identification of the intrinsic, chemical-physical material characteristics of the filler particles to a large degree has been accomplished. The influence of various types of fillers on the flow behaviour and curing reaction of adhesives was previously investigated by means of rheology and analysis. Technical test methods, which are specific to the use of adhesives, have now been applied adjacent to the analytical techniques of the objective chemical and physical property characterization. The technical product validation comprises aspects related to storage stability and processing properties (before curing), and »material properties« (after the curing process).

The acquired experimental data are being correlated and evaluated by means of advanced regression analysis. As a first result it could be confirmed that six of the filler property input variables can be explained on a 95 %-level via

linear combinations of the remaining independent ones. In the next step mappings between the set of remaining influence parameters and the set of the corresponding adhesive properties, the so-called output parameters, are identified via the estimation of mathematical regression models. In order to account for the unbalance between the numbers of model parameters to be estimated and the available measurements, a further reduction of the input space via principal component analysis, respectively factor analysis will be performed.

To analyse the specific chemical and physical surface interaction between the coating agent and the calcite surface, calcite crystals were split and the reaction of the newly generated calcite cleavage planes with stearic acid investigated using FTIR-spectroscopy and ToF-SIMS. The ToF-SIMS measurements and the results of the FTIR-experiments reveal that a large amount of coated stearic acid can easily be removed from the calcite surface by desorption in isopropanol. However at the edge of fracture planes a higher amount of residual staric acid had collected which obviously resisted desorption due to a strong surface interaction. Projected to the case of coated powdered calcite fillers this observation could lead to an explanation of the difference in filler properties due to parameters related to the geological origin and parameters of the grinding and coating process. Further experiments and analyses including defined coating and desorption of stearic acid in combination with calcite crystals and calcite powders are planned to gain further insight and understanding of the calcite-coating and calcite-polymer interaction.

To identify the dominant process parameters and their range, to control the coating process in an industrial environment, a first inventory of the processing steps, the critical parameters and the actual process control was performed according to the OAP® procedure in cooperation with the industrial partner. On the basis of the chemical and physical analysis of the calcite fillers additional parameters have been identified, which may be used e.g. in the filler coating process as a basis for raw materials and process control once the corresponding analytical methods have been sufficiently qualified for their application in an industrial environment.

In the future the knowledge of the technically relevant characteristics of the calcite filled adhesives provides the basis for avoiding the risk of deviating batches due to fluctuations in the supply of raw materials and the potential to reduce the effort in selecting new cost-optimised sources of raw materials. As a result the development cycles of new adhesive products with improved application characteristics are shortened and new adhesive products with improved characteristics will be available to e.g. the transportation or the building and construction industry.

InProTunnel: Interfacial Processes between Mineral and Tool Surfaces - Causes, Problems and Solutions in Mechanical Tunnel Driving

Feinendegen M. (1), Spagnoli G. (2), Stanjek H. (3), Neher H.P. (4), Ernst R. (5), Weh M. (6), Fernández-Steeger T. M. (2)*, Ziegler M. (1), Azzam R. (2)

(1) Chair of Geotechnical Engineering and Institute of Foundation Engineering, Soil Mechanics, Rock Mechanics and Waterways Construction, RWTH Aachen University

(2) Chair of Engineering Geology and Hydrogeology, RWTH Aachen University

(3) Clay and Interface Mineralogy, RWTH Aachen University

(4) Ed. Züblin AG, Stuttgart

(5) Herrenknecht AG, Schwanau

(6) Marti Tunnelbau AG, Bern, CH

* Coordinator of the project

Abstract

During mechanical tunnel driving in fine grained soil or rock the excavated material often sticks to the cutting tools or conveying system, which may cause great difficulties in its excavation and transport. In the InProTunnel project this problem is faced on different scales particularly for the method of Earth Pressure Balanced (EPB) shield tunnelling. Major influences from tunnel boring machine (TBM) operation are identified by project data analyses, clogging propensity is evaluated by a new laboratory test, alternative manipulation techniques are developed based on modifications of the physico-chemical and electroosmotic behaviour of clay minerals and will be tested in an especially designed clogging test system.

1. Introduction

In the course of the joint research project »Interfacial Processes between Mineral and Tool Surfaces - Causes, Problems and Solutions in Mechanical Tunnel Driving« (InProTunnel) the problem of clogging during tunnel driving in fine grained soil or rock is investigated particularly for the method of EPB shield tunnelling. Three university institutes and four industrial partners are working on new techniques to identify the relevant effects and interactions on different scales. Furthermore, new manipulation methods for the avoidance or reduction of adhesion-caused impacts are investigated. The resulting proposals for solution will have a positive effect on the efficiency, sustainability and profitability of tunnelling projects.

In a first step, data deriving from TBM operation, geological and environmental parameters are analysed (cf. ch. 2). Detected correlations are used to identify positive or negative effects with respect to the sticking of excavated material to the cutting tools or transportation equipment.

Secondly, new laboratory tests to investigate and classify different soils and rocks are developed as until now no suitable test procedure or classification scheme for the clogging potential is available (cf. ch. 3). The adhesion of clays or clayey soft rocks in mechanical tunnel driving has already been investigated in several research projects (*Jancsecz 1991, Wilms 1995, Thewes 1999, Burbaum 2009*); nevertheless, no generally accepted (standardized) test cur-

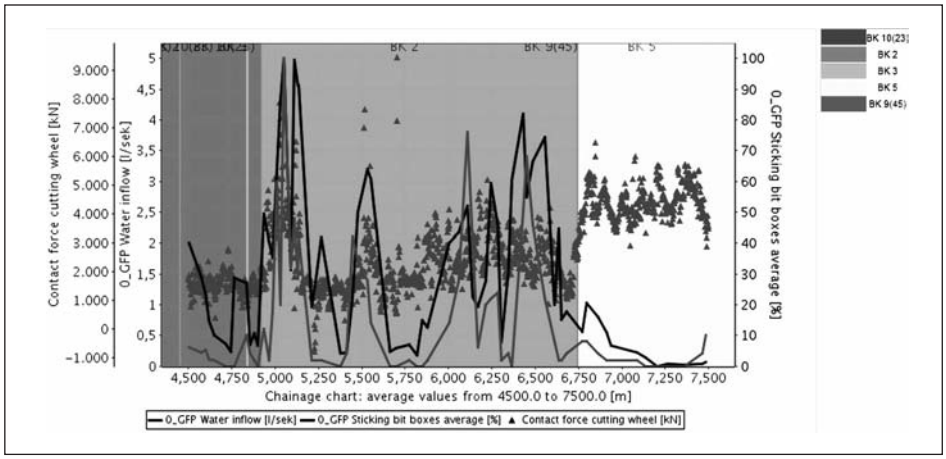

Figure 1: Graphical multi-axes evaluation of TBM and geological/geotechnical data

rently exists to determine the clogging behaviour from a practical (tunnel) construction point of view.

Clay minerals show a mechanical behaviour which cannot simply be extrapolated from classical soil mechanics. The mechanical properties of fine-grained soils like clays are intimately related to the chemical properties of the respective minerals and pore fluids. Additionally, it is well known, that electric fields strongly affect the mechanical behaviour of soft soils. Since these processes are of great importance for the occurrence of adhesion and/or clogging as well as for the development of methods for their reduction the acting mechanisms are investigated on the micro scale in a third part of the project (cf. ch. 4).

Finally, new manipulation techniques based on chemical modifications as well as electroosmotic methods will be tested in a realistic test setup. These tests are presently in the design state (cf. ch. 5).

2. Data Analysis from TBM tunnelling projects

2.2. Project Database

The data generated by tunnel driving with TBM (penetration, thrust forces, pressures of annular grouting etc.) are crucial information for the interpretation and prediction of advance rates and potential troubles. The same applies for survey data and geological or geotechnical information.

Based on a powerful SQL database an application to collect, store, process and analyse the data of tunnel projects has been developed. Project partners have direct access to the database by means of a web-based graphical user interface (GUI). The application is designed as a socalled »thin-client« based on a central server database. Thus the application is independent from operating system and can be accessed from anywhere via internet. Only an internet browser is needed to run the application.

The basic function of the database is the storage of TBM data. Moreover, survey and geological/geotechnical data or any other type of process data referenced to chainage or time can be incorporated. All kinds of data can be processed and analyzed in graphical or tabular format regarding chainage or time. Standardized charts and tables as well as individual ones can be generated. Even a multiaxes evaluation of the data is feasible. Thus, the system is capable to interconnect all data of a project to become aware of existing correlations. Detected correlations can be used to identify positive or negative effects from different parameters with respect to e.g. the degree of sticking of excavated material.

In the framework of the InProTunnel project data from one tunnel project in southern Germany,

where clogging problems were encountered, are available in the database. In figure 1 values for the local water inflow at the face, the relative amount of sticking of excavated material to the cutting wheel as well as the contact force of the cutter head are given for an approximately 3 km long tunnel part. Moreover, the respective geology is plotted in the background. The chart shows, that the clogging of the cutter head is strongly related to the water inflow at the face which is directly linked to the respective geology. Another fact is, that the sticking of excavated material to the cutting tools leads to an increasing contact force of the cutter head, when regarding the respective geology. The needed energy and the corresponding construction costs increase.

2.2. Influences on clogging from geology and TBM operation

When regarding the processes that lead to clogging problems in a TBM drive one has to distinguish between primary and secondary causes. Primary causes are mainly the following geotechnical conditions:

– The composition of the subsoil, especially the type and amount of clay minerals,
– The slaking durability,
– The water content of the soil prone to clogging and/or the availability of free water in the adjacent soil.

In this connection not only one layer or type of soil has to be regarded, but all materials that will be excavated at the same time have to be taken into consideration.

The secondary causes of clogging result from the interaction between cutting technology and subsoil. During the excavation and transport of the material the mechanical wear causes a loss of strength which may even lead to a complete disintegration of the composite structure. The varying consistency of the fine grain fraction and its percentage with respect to the total soil mass are major influences on the clogging propensity. In several TBM drives it could be observed, that a higher sand fraction in the excavated material led to considerably lower adherences.
Adherences may occur at all surfaces that are in contact with the excavated material during excavation, transport or disposal. The material first sticks to the tool surfaces due to adhesion forces. Clogging problems will follow when the amount of adhering soil leads to a narrowing in the transportation ways:

– The material is compacted and pressed to the tool surfaces or already adhering soil. By this, also material that normally shows no clogging propensity often tends to stick.
– Because of the possibly high pressure the adhesive forces may be considerably higher as well.
– If the inner strength of the soil (cohesion) is higher than the forces acting during excavation and (unpressurised) transport soil agglomerations can persist. When pressed through narrowings these aggregates may be squeezed or sheared. This leads to an exposure of their inner parts, where the water content and the clogging tendency is often much higher than in the rest of the excavated material.

If the adhering soil has no lateral support, high adhesive forces and/or cohesion is needed to prevent it from breaking of. Usually clogging is observed much less on moving parts, where not only gravitational forces like on stationary parts, but also rotational or shear forces are acting. However, the mechanical wear of the material in connection with the machinery working on the TBM leads to a massive rise of the temperature, which again results in very tough and permanent adherences. This can be very unfavourable, when these hard adherences act as a kind of support for softer material. For example, during a TBM drive the roller bit boxes are often filled with fairly wet soil. On the frontside and the backside this material is sliding (rotating) over the material in the excavation chamber or at the tunnel face, which frequently leads to the described effects. Such kind of adherences can be very long-lasting and can be carried far beyond the areas of subsoil that is originally prone to clogging.

As already seen before (cf. Fig. 1) the occurrence of clogging is very much dependent on

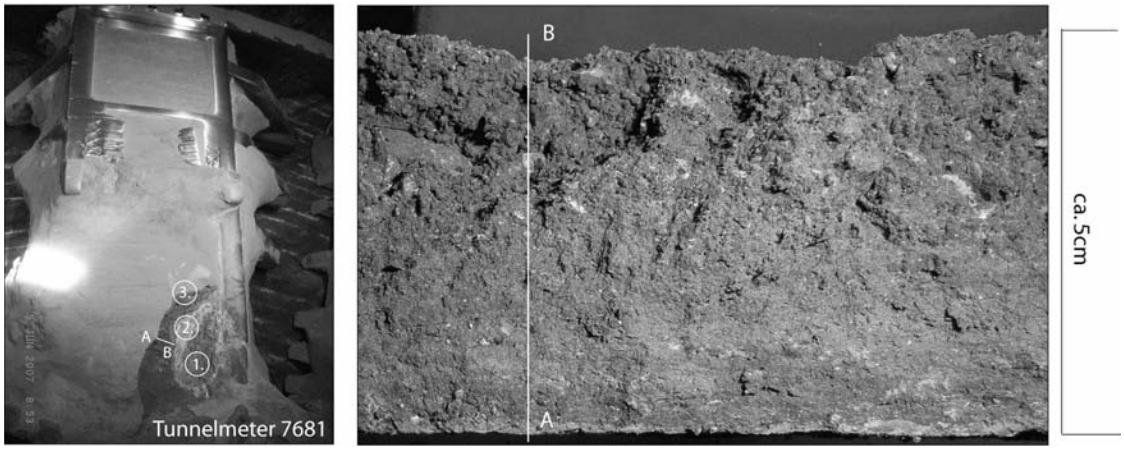

Figure 2: Adherences in the roller bit box of an EPB-TBM

the availability of water and the resulting consistency of the excavated material. When the original subsoil is relatively dry and only the tunnel driving operations cause a contact with water, then sometimes layered adherences are formed. In figure 2 heavily protracted adherences with such a layered structure are shown. The original colours are grey in the inner part (1), brown (2), grey (3) and light grey on the surface. When the picture was taken, the outer cutting wheel openings were almost free from clogging. Only the roller bit boxes showed the protracted adherences from earlier occurrences of water inflow. In the cross section A-B it can be seen how the adhering soil has been pulverized in the (rotating) contact surface to the material in the excavation chamber, has lost water due to the high temperature and changed its colour from a dark to a lighter grey. This very hard layer acts as a kind of protection for the softer soil within the roller bit box, which had to be removed by hand in the end.

3. Laboratory testing of the clogging behaviour

3.1. Cone pull-out test

For a better identification and quantification of the mechanisms affecting the clogging behaviour on a laboratory scale, the so called »cone pull-out test« has been developed (*Feinendegen et al. 2010*). The equipment and the test procedure are shown in figure 3.

The sample material is compacted in a standard proctor device, a steel cone is inserted into a pre-drilled coneshaped cavity and loaded for 10 minutes with the magnitude of the applied load between 3.8kN/m² and 189kN/m² depending on the consistency. The load is then taken off and the specimen is placed in a test stand where the cone is pulled out with a velocity of 5 mm/min. The tensile forces and the displacements are recorded.

Different clay types with varying mineralogy and plasticity have been tested up to now in a number of test series with different cones and soil consistencies. Table 1 shows the relevant properties of some selected clays.

3.2. Preliminary tests

In the following, some exemplary results of preliminary tests on the so called »clay 3«, a medium plastic clay from a quarry in the Westerwald (Germany) are illustrated. One important difference -amongst others- was, that the test cones in the later main experiments (cf. ch. 3.3) consisted of stainless steel, which has different surface characteristics than the constructional (black) steel that was used in the preliminary tests. The results thus cannot be compared directly.

It should be mentioned, that all curves shown in the following normally represent the mean values of four tests. Only when the deviation is too large, the respective data are neglected.
Figure 4 shows the progress of the vertical ten-

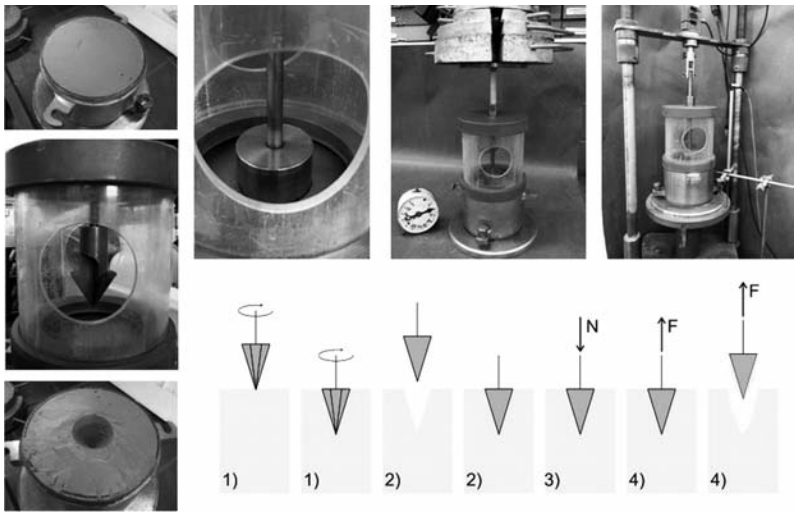

Figure 3: Cone pull-out test

Table1: Tested clays

Clay		3	13	14	15	16
Plasticity I_P	%	27.6	21 1	129	50.7	385
Liquid Lim. w_L	%	47	49.3	159 7	72.3	455
Plastic Lim. w_P	%	19.4	28.2	30.7	21.6	70
Loss on ign.	%	4.1	3.9	2.6	4.9	n.d.
Calcium cont.	%	0.1	0.1	0.2	16.4	n.d.
<0.063	%	88.0	88.0	97.0	95.0	96.0
<0.0002	%	72.0	59.0	33.0	49.0	86.0
Smectite	%	-	2.0	35.0	17.5	100
Kaolinite	%	29.5	65.2	36.0	39.5	-
Illite	%	23.5	12.5	7.0	20.0	-
Calcite	%	-	-	-	4.0	-
Chlorite	%	-	-	1,0	-	-
Quarzite	%	47	20.3	15.0	16.2	-

sile stresses for clay 3 tested with different cone inclinations at a consistency of I_C = 0.70. It can be seen, that with the »nearly flat« cone 0 (10°) tensile forces can only be measured for displacements less than 3mm, while with the »steep« cone 4 (72.6°) they are acting over a quite large range up to 11mm. After several comparative tests, only cone 3 (58°) was used furthermore, since it provided the most characteristic results for all analysed soils.

In figure 5 the respective results for different consistencies tested with cone 3 are shown. Here the stiff material (I_C = 0.85) shows quite high tensile stresses at very short displacement ways whereas for the softer material the maximum decreases with tensile forces still acting over large ways. An integration of these tensile stress-displacement curves delivers the »Pull Energy« which represents the energy that is needed to pull the cone out of the soil.

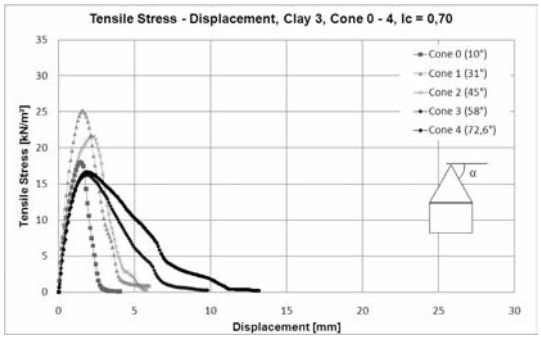

Figure 4: Tensile stress - displacement curves for different cone inclinations

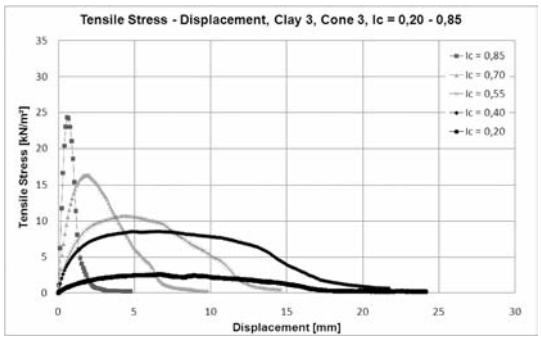

Figure 5: Tensile stress - displacement curves for different consistencies

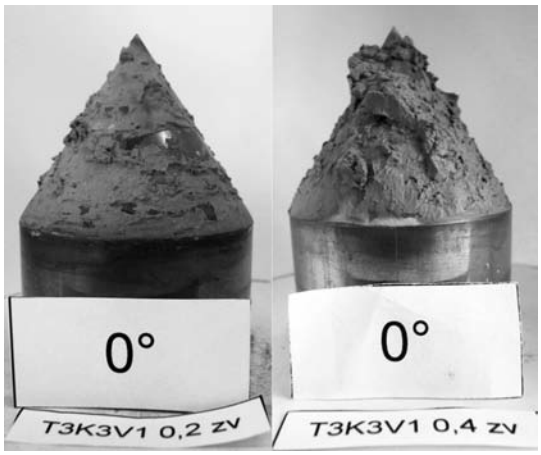

Figure 6: Adhering soil for IC = 0.20 and IC = 0.4 (0° = viewing direction)

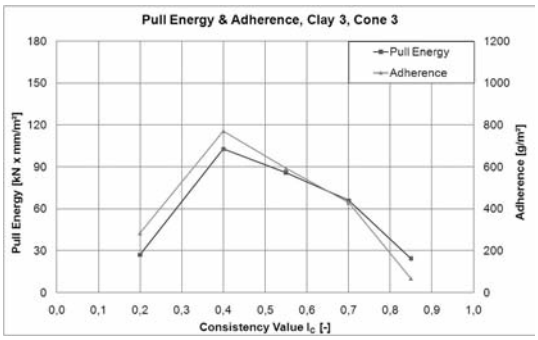

Figure 7: Pull energy and adherence over consistency

In addition to the tensile stress measurements, after each test the mass of adhering soil (cf. fig. 6) was determined by weighing. This parameter is defined as »adherence« in the following.

When plotting the pull energy, which was derived from the tensile (= bond) stresses, over the consistency and comparing it to the measured adherences, a good correlation could be observed from the first tests series (fig. 7). Both the clogging potential as well as the adherence show relatively high values in a soft to stiff consistency and a decrease towards the »wet« and the »dry« side. This corresponds quite well with the experiences from practice (*Weh et al. 2009a*, b). Clogging problems mainly occur, when the material in the excavation chamber is in or gets into a plastic state. They are usually much smaller when the soil is very dry or near liquid.

3.3. Main experiments

In the main experiments four different clays were examined: clay 13, like clay 3 from the Westerwald; clay 14, the extremly plastic so called »Ypresian Clay« (= »London Clay«); clay 15, the again well-known »Boomse Klei« and clay 16, which represents a pure smectite.
In figure 8 the curves of the pull energy over the consistency are shown for these four clays, whereas in figure 9 the corresponding adherences are plotted. It can easily be seen, that the (quantitative) correlation of these curves is not always as good as in the preliminary tests, but the (qualitative) shape is still somehow similar.
Nevertheless, from figure 9 a direct comparison of the four soils can be drawn. Clay 14, the »Ypresian Clay«, shows a characteristic steep developing with a very high maximum of adherence (1150 g/m²) at a consistency of I_C = 0.54. The curves for clay 15, the »Boomse

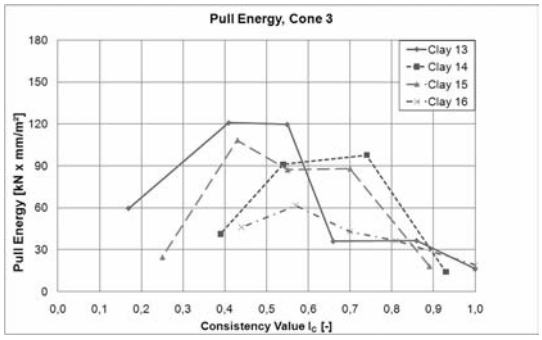

Figure 8: Pull energy over consistency

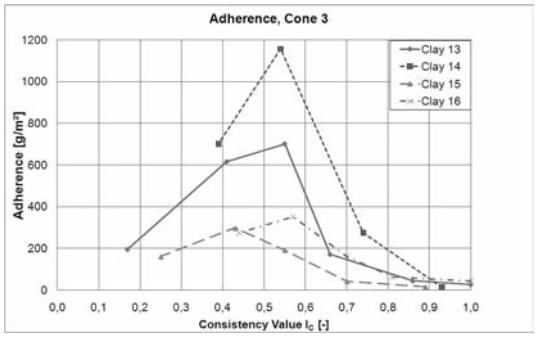

Figure 9: Adherence over consistency

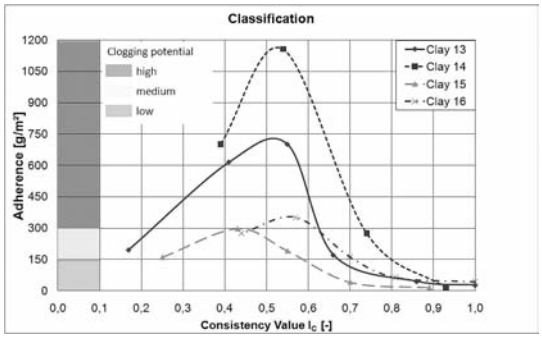

Figure 10: Draft of a classification scheme

Klei« and the pure smectite (clay 16) are more even with considerably lower adherences of 275 g/m² and 350 g/m² respectively. Finally, for Clay 13 from the Westerwald the maximum value of 700 g/m² lies in between, but the curve is a bit irregular.

3.4. Evaluation of the clogging potential

Based on the results obtained so far, a draft of a classification scheme to quantify the clogging potential of different fine-grained soils has been developed (fig. 10). Classes of high, medium and low clogging potential are assigned to the diagram with the adherences derived from the cone pull-out tests plotted over the consistency.

One can directly identify the very high risk of clogging for clay 14. In particular, the sharp increase of the curve up to the maximum of 1150 g/m² is a strong indication for problems to be expected. Also Clay 13 with a maximum adherence of 700 g/m² will lead to extensive clogging. But also for the two other clays noteworthy adherences have to be reckoned with.

In this connection it should be mentioned, that all clays presented here were deliberately chosen as »sticky« clays. Other samples were examined that showed adherences of less than 100 g/m² and can thus be defined as »not prone to clogging«. Anyhow, the ranges of high, medium and low clogging potential are up to now defined arbitrarily. There is still a strong need for a verification by the EPB tunnelling praxis!

4. New manipulation techniques

4.1. Theoretical background of the chemo-mechanical coupling of clays

Clay minerals are characterized by strong electrical attractive and repulsive forces that vary significantly in magnitude depending on mineralogical composition and the charge on their surface as well as on their edges. Thus the clay mineralogy becomes important in geotechnical engineering with fine-grained soils. The region in the particles size vs. stress field where chemo-mechanical coupling may take place reflects the relevance of double layer phenomena as well as the relative balance between local contract-level electrical forces and boundary-skeletal forces resulting from Terzaghi's effective stress (*Santamarina et al. 2002*).
The chemo-mechanical coupling plays an important role for the engineering response of the material. Numerous authors have already

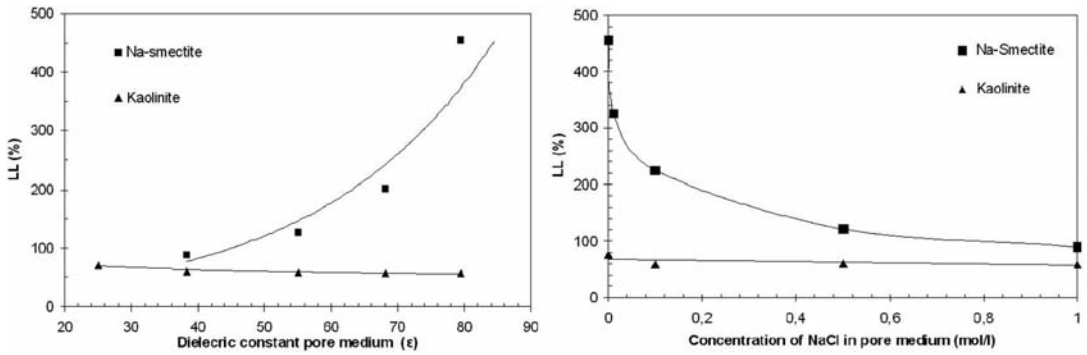

Figure 11: Variation of the liquid limit of Smectite and Kaolinite for different dielectric constant (left) or electrolyte concentration (right) of pore fluids (*after Spagnoli et al. 2010b*)

investigated the problem (*Mesri and Olson 1970; Anandarajah and Zhao 2000; Spagnoli et al. 2010a*). Dielectric constant and electrolyte concentration of the pore fluids are important controlling parameters, particularly in the case of 2:1 expanding clays such as Smectite. Kaolinite (1:1 non-expanding clay) and Illite (2:1 non-expanding clay) do not respond in the same way. In fact, they have a very thin diffuse double layer (DDL) expansion (*Gajo and Maines 2007*) due to the negligible isomorphic substitution. With increasing salt concentration the DDL thickness decreases leading to smaller specimen volume. For the following discussion, it will be assumed that the DDL theory is applicable.

Clay particle systems are frequently described as a series of parallel clay particles. The Poisson-Boltzmann equation (*Mitchell and Soga 2005*) for a single particle can be used to obtain the midplane electrolyte concentration and potential between two particles. An approximate indication of the influences of particle spacing and pore fluids chemistry can be seen in terms of thickness of the DDL. However, the variation of liquid limit for Kaolinite with fluids of different dielectric constant or electrolyte concentration is almost negligible compared to the variation which occurs for Smectite (Fig. 11). The difference in chemo-mechanical behaviour of Kaolinite and Smectite is probably due to the existence of two different mechanisms governing the liquid limit. One mechanism might be controlled by the thickness of the DDL which governs the liquid limit. *Sridharan and Venkatappa Rao (1975)* stated that the liquid limit of soils is mainly controlled by the amount of DDL held water. The most important conclusions, concerning the structure of the double layer as function of the electrolyte concentration (and / or dielectric constant) of the fluid is, that the extension of the double layer in solution decreases with increasing electrolyte concentration (or decreasing dielectric constant).

This can be seen from the fact that the liquid limit for Smectite is 455 % with water and 89% with a non polar fluid. Since liquid limit is the amount of fluid which must be added to a soil to allow the layers most distant from the soil particle to acquire the properties of free water (*Sridharan et al. 1988*), it can be stated that the fluid content at the liquid limit is contributed also by the fluid content due to the diffuse double layer. Therefore, the liquid limit is a measure for water (or fluid) held as double layer water (held with rigidity) plus water (or fluid) in the liquid state. For this reason, the decrease in liquid limit for Na-Smectite with non-polar fluids can be explained by a suppressed or thin double layer which is in accordance to equation (1).

$$\frac{1}{\kappa} = \left(\frac{\varepsilon_0 \varepsilon R T}{2 n_0 e^2 \nu^2} \right)^{\frac{1}{2}} \qquad (1)$$

where $1/\kappa$ is the DDL thickness (in nm), T is the absolute temperature given in K, n_0 the ionic concentration in the bulk solution in mol/l, ε_0

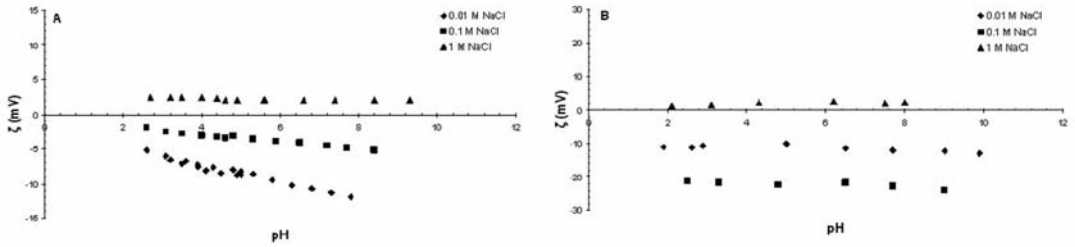

Figure 12: ζ - potential measurements for Kaolinite (left) and Na-Smectite (right)

and ε are the electric permittivity of vacuum and the relative dielectric constant of the pore fluid, respectively, whereas υ^2 is the valence of the prevailing cation. The constants are the elementary charge (e = $1.602 \cdot 10^{-19}$ C) and the gas constant (R = 8.3145 J/mol·K) (*Israelachvili 1991*).
For Kaolinite a change in the fluids dielectric constant (or electrolyte concentration) does not lead to any appreciable change in double layer thickness. In addition, it could be stated that the DDL for non-swelling clays is very small or not existing. Hence, the diffuse double layer approach does not apply for such clays.

4.2. ζ-potential measurements

The electrokinetic behaviour of clay suspensions was investigated using an electroacoustic technique (DT1200 ζ-potential analyzer, Dispersion Technology, Inc., USA), which is based on the determination of the dynamic mobility obtained from the electrokinetic sonic amplitude signal (ESA) of the charged particles in non-dilute suspensions (*Galassi et al. 2001*). Simultaneously the electrophoretic mobility μ is calculated using the following equation (*Dukhin and Goetz 2002*):

$$\mu = \frac{2\varepsilon\varepsilon_0\zeta(\rho_p - \rho_s)\rho_m}{3\eta(\rho_p - \rho_m)\rho_s} G(s,\varphi)(1 + F(Du,\omega,\varphi)) \qquad (2)$$

where ε is the dielectric constant of pore fluids, ε_0 the dielectric constant of the vacuum, ρ_p the density of the particles, ρ_s the density of the dispersion, ρ_m the density of the medium, G is a function, Du the Dukhin number, ω the frequency and φ the volume fraction (*Dukhin and Goetz 2002*). The advantage of this technique is the ability of propagating ultrasound through samples that are not transparent for light and therefore this technique offers a unique opportunity to characterize concentrated dispersions (*Dohnalová et al. 2008*).

In figure 12 the variation of the ζ-potential for dispersions of Kaolinite and Na-Smectite with different ionic strength and pH is shown. It can be observed that for Na-Smectite, the ζ-potential is negative for the whole pH interval. It is essentially independent of pH. In contrast, the ζ-potential of Kaolinite becomes more negative with increasing pH. Increasing the ionic strength the values of ζ-potential become less negative. With a 1M electrolyte concentration for both materials, the ζ-potential is slightly positive (between 2 and 3 mV). Experimental results show that the ζ-potential is in general more negative at high pH, low ionic concentration and low ion valence (*Santamarina et al. 2002*). The increasing negative ζ-potential of Kaolinite in case of pH rise can be attributed to the deprotonation of the aluminol group on the edges of the Kaolinite, forming a complexed anion which contributes to the rise of the negative surface charge and subsequently to an increase of the repulsive forces among particles. The different electrokinetic behaviour of the tested clays results from the fact that Kaolinite has OH^- termination sites on the gibbsite face as well as on the edges, while Smectite has OH^- sites only on the edges which play a negligible role in determining the electrokinetic parameters (dominated by the constant negative charge of faces) of Smectites (*Benna et al. 1999*). Others have found that the ζ-potential of Smectite, though relatively constant at - 30 mV between 10^{-5} and 10^{-2} M, did fluctuate up to 10 mV with changes in the

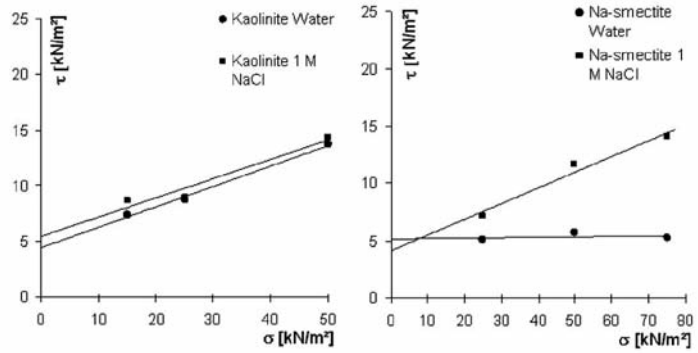

Figure 13: Modified shear test on Kaolinite (left) and Na-Smectite (right) for water and 1 M NaCl (after *Spagnoli et al.* 2010c)

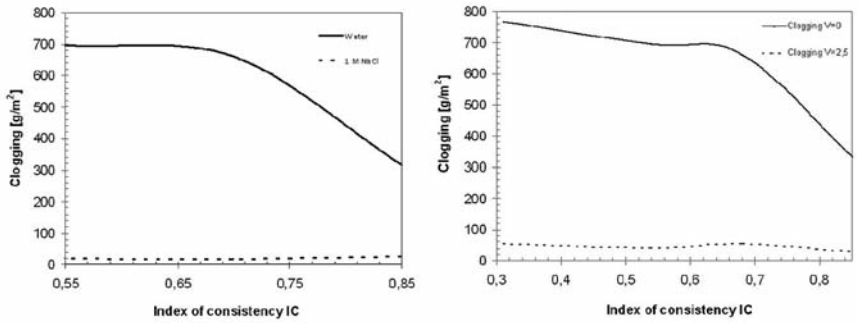

Figure 14: Variation of the clogging for Na-Smectite mixed with water or 1 mol/l NaCl (left) and with additional application of an electrical field (right)

concentration of indifferent electrolyte (*Hunter 1981*). As only 5% of the negative charge of the 2:1 clay minerals is controlled by the pH value, whereas 50% or more of the surface charge of 1:1 minerals are controlled by the pH value (*Das 2008*), it can be stated, that the ζ-potential of swellable clays is less sensitive to pH variations than that of 1:1 minerals. Regarding the positive values of the ζ- potential for 1M NaCl, we are not sure whether this is due to the rapid sedimentation in the measuring chamber or due to the higher ionic strength.

4.3. Variation of the clogging of clays

Several modified direct shear tests were performed for Kaolinite and Na-Smectite mixed with water and 1 M NaCl to reach a consistency of 0.5. The sample was gently places at a metal surface, loaded with very low pressure (15-75 kPa) for 10 minutes and then sheared with a shear rate of 0.5 mm/min. With this test the shear resistance of the interface between clay and metal may be described by the Coulomb criterion. It has two components: the adhesion (resistance at zero normal stress and a frictional component (adhesive friction; described by the angle δ). In this case, the adhesive shear strength of clay on metal is less than the applied shear stress and also less than the internal shear strength of the clay (*Kooistra et al. 1998*). *Spagnoli et al.* (2010c) described the strong variation of adhesive shear strength for Na-Smectite for different pore fluids while for Kaolinite no variation occurred. It is interesting that for Na-Smectite with water as pore fluid, the shear resistance is independent of the normal stress. The results (fig. 13) show for Na-Smectite a slight decrease of adhesion strength but a general increase in internal shear strength. From a pure mechanical point of view, clogging occurs during modified shear tests if:

$$\sigma_n < \frac{a - c}{\tan\varphi - \tan\delta} \qquad (3)$$

It is theoretically possible to predict if sticking will occur when the adhesion (a), the cohesion (c), the adhesive friction angle (δ), the internal friction angle (φ) and the normal

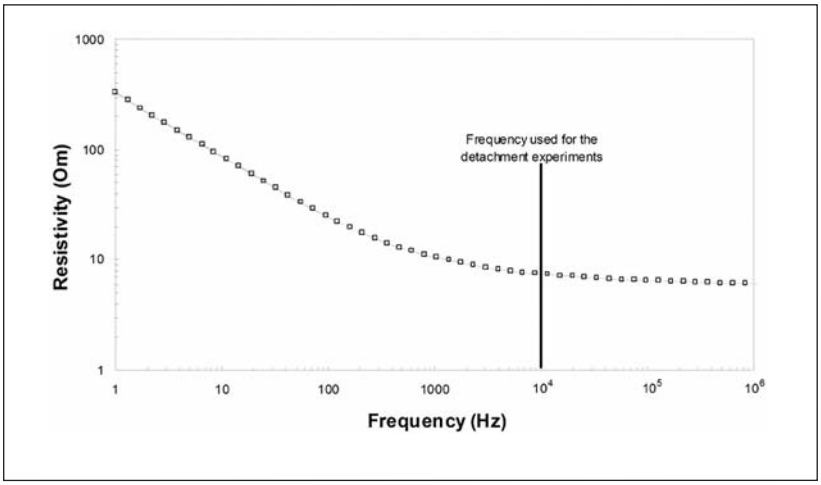

Figure 15: Resistivity of the electrode-soil system versus frequency obtained by IS measurements for Smectite

stress (σ_n) are known.

Starting from the assumption stated by the DDL theory the clogging of Na-Smectite mixed with water and 1 mol/l NaCl, adjusted to different consistencies (0.55, 0.65, 0.7, and 0.85) was investigated using the cone-pull out test. Figure 14 (left) shows that the clay mixed with the 1 mol/l NaCl fluid does not stick any more to the cone. In fact, the increased internal shear strength of the clay due to the mixing with a fluid with higher electrolyte concentration, leads to a general drop of the stickiness of the material.

Geotechnical engineers have investigated and applied electroosmosis to consolidate and strengthen clayey soils and mine tailings since the 1940s (*Casagrande 1947*). Other successful field applications of electroosmotic consolidation included *Bjerrum et al.* (1967) and *Lo et al.* (1991). *Davis and Poulos* (1980) studied the use of electroosmosis to aid pile driving in clayey soil. However, electroosmosis could also be used to reduce the clogging of the material. Therefore, experiments with the cone pull-out test were performed. The procedure is the same as explained before. In this case the cone was used as cathode while the proctor pot was the anode. A potential of 2.5 V was used in all tests by applying DC for 10 minutes. After this time the cone was pulled out. Fig. 14 (right) shows the results.

The drop in clogging for both clays is clearly visible. By applying an electric charge to the steel parts, water can be transported through the clay by electroosmosis to the interface between the clay and the steel. This creates a film of water at the clay-steel interface and therefore reduces the adherence. However, the use of DC could be a disadvantage. Extended electrical laboratory investigation was performed by using AC. Not only current intensity but also water flow depend on the electric impedance of the electrode-soil system (ERS impedance), i. e., the current intensity depends on the soil resistivity and on the electrode-soil contact (ERC) impedance. It has been shown that for DC measurements the contact impedance is often crucial for the system impedance whereas for high frequencies (e. g. 10 kHz) the influence of the contact impedance is of minor importance. Electrical impedance spectroscopy (IS) measurements were carried out (two electrodes) to study the properties of the electrode-soil system (ERS) and especially the influence of the contact impedance on the ERS impedance. IS measurements on clay samples were performed in the frequency range from 1 Hz to 1 MHz using the IAI impedance analyzer PSM1735. Fig. 15 shows that AC signals are more effective in reducing adherence than DC signals due to the lower resistivity. Therefore, with AC generally lower field strengths are needed to reduce the adherence time.

However, application of electroosmosis during operational tunnel heading could lead to problems in the tunneling practice. By applying a negative charge to the steel surface of the

TBM, this steel surface is protected from corrosion. However the anode will corrode faster compared to an uncharged surface. The anode will not only wear out faster; a rusted anode will also have a lower conductivity and as a result the amount of water transported by electroosmosis will be lower. Furthermore, the voltages used to generate an electroosmotic flow will electrolyze the water. Therefore hydrogen and oxygen gas will develop due to the following half reactions for water electrolysis:
at the anode: $2H_2O - 4e^- \rightarrow O_2\,(g) + 4H^+$
at the cathode: $2H_2O + 2e^- \rightarrow H_2\,(g) + 2OH^-$

The oxygen developed at the anode will probably not cause problems. However the hydrogen gas is flammable, and if mixed with oxygen at the right concentration it can explode. When an electric current passes through a clay specimen, the clay is heated and the temperature will rise. As the specific resistance of clay is many times larger than that of steel, the heat development in the clay is many times larger than in the steel electrodes. Also the influence of the electrical current and magnetic fields on computers and electrical machines inside the TBM is difficult to predict.

5. Clogging test system

To transfer and prove the results of the new standardized adhesion laboratory test and to verify new manipulation techniques, a Clogging Test System (CloggTS) will be developed. It is designed to support the geotechnical cohesice soft ground evaluation and conditioning related to clogging affinity in early project phases. The test also aims at coming closer to some geological-geotechnical aspects and to the reality of TBM layout with respect to material excavation and conveying processes in EPB-TBM. Some major demands on the test procedure are:

- To construct a robust, effective and economic clogging test system adapted to multiple use.
- To log those operational TBM data relevant for detecting clogging. Among those are visual notes, advance rate, face contact force of the cutting tool, torque of cutting and conveying tools, cutting tool revolution (rpm), temperature, and if so, the amount of additives given into the system. It is planned to vary operational data during testing.
- To avoid or control unwanted processes and other effects on operational data. Among these are face support managing (including material conditioning, excavation mode variation), not well documented geological changes and TBM technical adaptations. Empirically, these effects may complicate the assessment of the clogging affinity of the subsoil in TBM drives.
- To enable a systematic and complex investigation of clogging and soft ground material conditioning. This includes the detection of index properties and other characteristics of the ground and additives. Besides classical parameters also parameters relevant to clogging like ground water saturation, slake durability, adhesion stress, ζ-potential, clay mineralogy, void ratio, swelling potential or cation exchange capacity (CEC) are involved.
- To test geomaterial samples taken undisturbed if possible. High quality samples (bore cores) are preferred. By this, further geological/geotechnical ground characteristics that may be of importance for the adhesion/clogging propensity can be involved. Among those are low-scale geological interbedding and fissuring (e. g. fissured clays), ground water saturation, anisotropic ground properties and mixed tunnel face conditions.
- A complex approach with well defined testing conditions may contribute to a better understanding of the sometimes puzzling situation with respect to stickiness of soft ground materials.
- To assess the transferability of medium-scale test results to TBM projects.
- To evaluate the efficiency and applicability of chemical or physical conditioning (clay surface manipulation) of soft ground materials regarding technical, operational and environmental aspects as well as the reuse of the excavated material.

The clogging test ground samples in bore cores (diameter approx. 100mm, length approx. 0.5

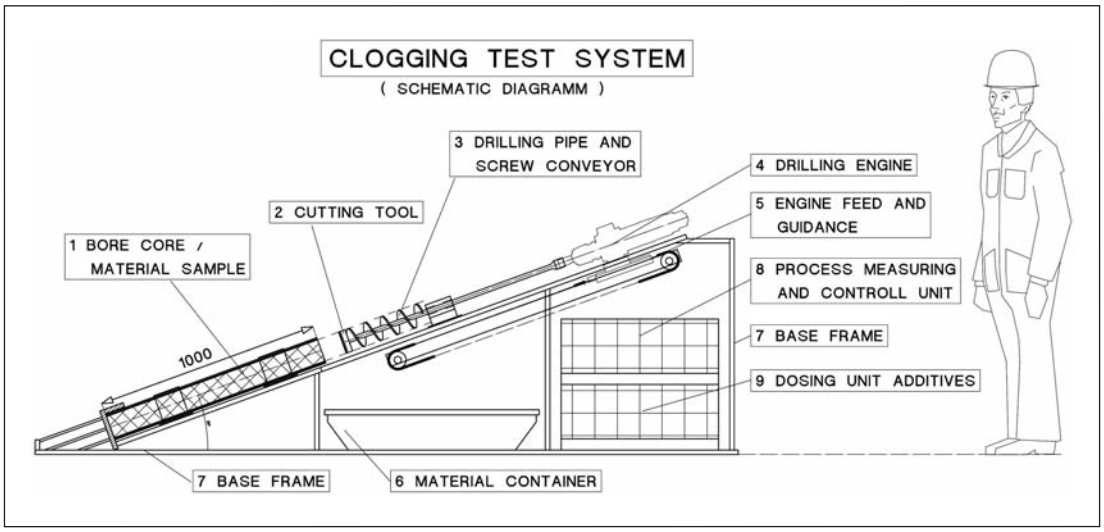

Figure 16: Clogging test system (prototype)

- 1.0 m) are cut using open steel cutting tools. The opening ratio and the design of these tools will be varied. Driving and rotation of the cutting tool assembled on a drill pipe is realized by a linear rotary drive on a guidance. The bore cores to be cut are fixed to prevent them from sliding and extruding. The material transport is realized with a screw conveying system which is affixed to a drill pipe. The test system is inclined as for the screw conveyor position in EPB drives. A simplified plan of the clogging testing system is shown in figure 16.

The process measuring and control units are used to set and vary testing parameters. Advance rate, face contact force and possibly revolution of the cutting wheel are planned to be varied during tests. These parameters shall simulate a range of operational data typical for TBM drives in clays, clay soils and clayey soft rocks.

For a conditioning the of material an adapted dosage unit is used. Water, electrolyte solutions, slurries or foam can be added to the system in front or behind the cutting tool using a channel inside the drill pipe. For possible electrokinetic tests the cutting tool could be used as cathode. For foam conditioning an adapted foam generator can be used.

6. Summary

In the joint research project InProTunnel the problem of clogging during EPB tunnel driving in fine grained soil or rock is investigated on different scales.

From the analyses of project data, amongst others based on a SQL database, some factors of prime importance for the occurrence of clogging problems were determined. In addition to the evident parameters (clay) mineralogy and particle size of the excavated material, in particular the significant influence of the water content and/or water inflow and the resulting (change of) consistency of the material could be identified.

With the cone pull-out test a practical laboratory test to investigate different soils with respect to their clogging behaviour could be designed and put into practice. Based on the newly defined parameter »adherence« a draft for a classification scheme for the clogging potential has been developed. Anyhow, the new tests still needs to be verified by the EPB tunnelling praxis.

In the context of a comprehensive examination of the chemomechanical coupling of clays the influence of different pore fluids and their impact on the mechanical behaviour has been investigated. Shear tests and cone pull-out

tests show the effectiveness of modified electrolyte concentrations as well as the application of an electric charge to the steel parts with respect to a reduction of the adhesion.

Finally, the different factors affecting the clogging propensity, that have been identified so far, will be studied in a TBM-like medium-scale test. The respective test setup is currently in the concept state.

References

Anandarajah, A. and Zhao D. (2000). Triaxial behavior of kaolinite in different pore fluids, Journal of the Geotechnical Engineering Division, ASCE, 126, 2, 148-155.

Benna, M., Kbir-Ariguib, N., Magnin A. and Bergaya, F. (1999). Effect of pH on rheological properties of purified sodium bentonite suspensions. Journal of Colloid and Interface Science, 218, 442-455

Bjerrum, L., Moum, J. and Eide, O. (1967). Application of electroosmosis to a foundation problem in a Norwegian quick clay. Geotechnique, 17, 3, 214-235.

Burbaum, U. (2009). Adhäsion bindiger Böden an Werkstoffoberflächen von Tunnelvortriebsmaschinen. Institut für Angewandte Geowissenschaften. Technische Universität Darmstadt.
Casagrande, L. (1949), Electroosmosis in soil. Geotechnique, 1, 3, 159-177.

Das, M.B. (2008). Advanced Soil Mechanics, Taylor and Francis

Davis, E.H. and Poulos, H.G. (1980). The relief of negative skin friction on piles by electroosmosis. Research report R-367, School of Civil Engineering, University of Sidney, Australia.

Dohnalová, Ž, Svoboda, L. and Šulcová, P. (2008). Characterization of kaolin dispersion using acoustic and electroacoustic spectroscopy. Journal of Mining and Metallurgy, 44, 63-72

Dukhin, A. S. and Goetz, P. J. (2002). Ultrasound for characterizing colloids. Particle size, zeta potential, rheology, Elsevier

Feinendegen, M., Ziegler, M., Spagnoli, G., Fernández-Steeger, T., Stanjek, H. (2010). A new laboratory test to evaluate the problem of clogging in mechanical tunnel driving with EPB-shields. In: Proc. EUROCK 2010, Lausanne, Switzerland, Taylor & Francis Group, London.
Gajo, A. and Maines, M. (2007). Mechanical effects of aqueous solutions in organic acids and bases on a natural active clay, Géotechnique, 57, 8, 687-699

Galassi, C., Costa, A.L. and Pozzi, P. (2001). Influence of ionic environment and pH on the electrokinetic properties of ball clays, Clays and Clay Minerals, 49, 263-269

Hunter, R. J. (1981). Zeta Potential in Colloid Science. Academic Press, London

Israelachvili, J. (1991). Intermolecular and surface forces, Academic Press

Jancsecz, S. (1991). Definition geotechnischer Parameter für den Einsatz von Schildvortriebsmaschinen mit suspensionsgestützter Ortsbrust. In: STUVA-Tagung 1991, Düsseldorf. Alba-Fachverlag.

Kooistra, A., Verhoef, P.N.W., Broere, W., Ngan-Tillard, J.M.. and van Tol, A.F. (1998). Appraisal of stickiness of natural clays from laboratory tests. In R. Rijkers and M. van Staveren, (eds.), Engineering Geology and Infrastructure, 101-113

Lo, K. Y., Ho, K. S. and Inculet, I. I. (1991). Field test of electroosmotic strengthening of soft sensitive clay. Canadian Geotechnical Journal, 28, 1, 74-83.

Mesri, G. and Olson, R.E. (1970). Shear strength of montmorillonite. Géotechnique 20(3), 261-270.

Mitchell, J.K. and Soga, K. (2005). Fundamentals of Soil Behavior. John Wiley and Sons Santamarina, J.C., Klein, K.A., Palomino, A. and Guimaraes, M.S. (2002). Microscale aspects of chemical-mechanical coupling: interparticle forces and fabric. chemomechanical coupling in clays; from nanoscale to engineering applications, Di Maio, Hueckel and Loret editors, 47-63

Spagnoli, G., Fernández-Steeger, T., Feinendegen, M., Stanjek, H. and Azzam R. (2010a). The influence of the dielectric constant and electrolyte concentration of the pore fluids on the undrained shear strength of smectite. Soils and Foundations, 50, 5 (accepted)

Spagnoli, G., Feinendegen, M., Neher H., Fernández-Steeger, T. and Azzam R. (2010b). Verklebungsproblematik zwischen Tonen und TBM. Veröffentlichungen des Grundbauinstitutes der Technischen Universität Berlin, 7th October 2010, 50 (accepted)

Spagnoli, G., Fernández-Steeger, T., Azzam, R., Feinendegen, M. and Stanjek, H. (2010c). The influence of different pore fluids compositions on the shearing behaviour of clays. 11th Congress of the International Association for Engineering Geology and the Environment, IAEG, 5-10 September 2010, Auckland, New Zealand (ac-cepted)

Sridharan, A. and Venkatappa, Rao G. (1975). Mechanism controlling the liquid limit of clays, Proc. Istanbul Con-ference on Soil Mechanics and Foundation Engineering, 1, 75-87.

Sridharan, A., Rao, S. M. and Murthy, N. S. (1988). Liquid limit of kaolinitic soils, Geotechnique, 38, 2 191-198

Thewes, M. (1999). Adhäsion von Tonböden beim Tunnelvortrieb mit Flüssigkeitsschilden. Institut für Bodenmechanik und Grundbau, Nr. 21. Gesamthochschule Wuppertal.

Weh, M., Ziegler, M., Zwick, O. (2009a). Verklebungen bei EPB-Vortrieben in wechselndem Baugrund: Eintritts-bedingungen und Gegenmaßnahmen. In: STUVA-Tagung 2009, Hamburg. Gütersloh: Bauverlag.

Weh, M., Zwick, O., Ziegler, M. (2009b). Maschinenvortrieb in verklebungsanfälligem Baugrund, Teil 1: Tunnel 28(1), 25-36 und Teil 2: Tunnel 28(2), 18-28.

Wilms, J. (1995). Zum Einfluß der Eigenschaften des Stützmediums auf das Verschleißverhalten eines Erddruckschildes. Fachgebiet Baubetrieb und Bauwirtschaft, Nr. 12. Universität-Gesamthochschule Essen.

Zimnik, A.R., van Baalen, L.R., Verhoef, P.N.W., Ngan-Tillgard, D.J.M. (2000). The adherence of clay to steel surfaces. In: GeoEng 2000: An International Conference on Geotechnical and Geological Engineering. Melbourne, Australia., Lancaster, Technomic Publ. Basel.

SIMSAN - Simulation-supported development of process-stable raw material components and suspensions for the production of ceramic sanitary ware on the basis of modified mineral surfaces

Engels M. (1)*, Agné T. (2), Bayard E. (2), Diedel R. (1), Emmerich H. (6), Emmerich K. (3), Haas S. (5), Latief O. (4), Peuker M. (1), Steudel A. (3), Vuin A. (5), Yang H. (6)

(1) Forschungsinstitut für Anorganische Werkstoffe – Glas/Keramik – GmbH (FGK), Höhr-Grenzhausen

(2) Villeroy & Boch AG, Mettlach/Saar

(3) Karlsruhe Institute of Technology (KIT), Centre of Competence for Material Moisture (CMM), Eggenstein-Leopoldshafen

(4) Stephan Schmidt KG (SSKG), Dornburg

(5) Zschimmer & Schwarz GmbH & Co. KG (Z&S), Lahnstein

(6) Materials and Process Simulation (MPS), Fakultät für Angewandte Naturwissenschaften, Universität Bayreuth**, Bayreuth

* Coordinator of the Project

** Former allocated at the CME Center for Computational Engineering Science of RWTH Aachen

Abstract

The article focuses on the status of the research after the second project year. In addition to the basic characterisation of the chosen reference material mixture for sanitary slip casting, as presented in previous publications for the Geotechnologien Science Reports, it focuses especially on the characterisation results of the basic raw material components, which in the second year of the project were investigated. These are the basis for the funtional characterisation of novel body concepts and reference systems for the experimental validation of the simulation model. The development of first body concepts, derived from the mineralogical characterisation of the raw materials, is supported using a principal FMEA-based assesment of influences on the functional behaviour of the body as casting slip. Parameter analysis and statistical design of experiment techniques are being implemented to experimentally evaluate basic mineralogical influences within the context of a slip composition including differerent additive contributions. Significant interactions have to be specified and and to parameters effects ranked for further development. These insights will be the basis for laboratory pilot scale tests, which will in the next project phase focus on identifying and validating processing parameter influences.

The characterisation results have furthermore been used to develop simplified reference systems for the experimental validation of the simulation. After a short standstill in the modell development, caused by the relocation of the simulation expertise provided by CME from RWTH Aachen to the Materials and Process Simulation Group in Bayreuth, the results are being transferred into a binary, up to ternary model approach, based upon a simplified composition and particle system. The simplifica-

tion, performed in varying degrees, is based on the translation of the identified mineralogy of the components into particle systems with particle size and ratio aspects, charge specifications of identified surfaces and surface potential effects in different settings and environments. As the experimental validation is ambiguous due to the limitations of the experimental techniques for the basic systems, recommended literature as well as first approach validation experiments are used to generate basic input. The status of the development of the hybrid model algorithm, first implementation of parameter settings so far, resulting input requirements and the next steps to be taken are discussed. In this regard the importance of the working procedure for rheological slip characterisation, developed within the project for functional characterisation of the systems is highlighted.

Introduction

This article highlights the status of the interdisciplinary project, in which the impact of chemical and physical characteristics of the mineralogical surfaces of the mineral raw materials on the process will be exemplary clarified for highly automated sanitary ceramic pressure-casting systems. The primary goal of this project is to enable the raw material suppliers and the ceramics industry to develop adapted stable raw material mixtures and casting slurries and establishing stable and robust processes by way of quantitative predictions from simulation calculations. These are validated by statistical experiments including the effectiveness of additives and process-defining parameters. It provides a novel approach for extracting and processing technology of the raw materials, engineering of performance characteristics during the production by additive modification of the surfaces, and adequate process control during pressure-casting in the ceramic production. Due to the high complexity of the subject, the project relies on a strong interaction between the different partners from the processing chain, represented by the partner from sanitary ware industry, a raw materials supplier, a supplier of additives for the ceramic industry, expertise in the field of colloid chemistry and analytical characterisation and modelling competence. This cooperation already resulted in the specification of a working procedure for a for unambiguous capable and transferable rheological slip characterisation, useable for the whole process chain, which has already been presented to the relevant ceramic industry at the 2010 annual Meeting of the German Ceramic Society [1].

Experimental results

The fact that common techniques used to control the raw materials fail to detect differences in raw materials characteristics which correlate to known process variations requires the investigation of important intrinsic material characteristics as well as their influences on the rheology and the process ability. The composition of the joint project group offers a unique basis to perform the conventional ceramic product and process characterisation as well as measurement of colloidal parameters (rheology, cation exchange capacity zeta potential, flow potential), state of the art mineralogical analysis and submicron particle size measurement, which cannot be achieved by regular production laboratory equipment, but constitute the essential basis for the input in the numeric calculations as well as process and product development. The results presented here build upon the results previously presented in preceding GEOTECHNOLGIEN Science Reports No. 12.

Characterisation of the aplied raw materials

Based upon the knowledge of sanitary pressure casting bodies present in the consortium, a specified mixture of plastic clay components, feldspars, kaolin, quartz as well as alternative kaolin and clay components for a production-relevant casting slip have been specified, using the relevant bandwidth of mineralogical and particle size composition in regard to functional characteristics. In the preceding publications the initial characterisation of the body

composition as sum of the components by chemical analysis, particle size measurement using sieve analysis, sedimentation and laser light scattering, specific surface measurement using BET, as well as thermal analysis has been presented. Zeta potential measurements at different pH settings of the system, supported by the measurement of eluted cation and anionic components using ICP, have been performed. This composition has been used as reference basis for the development of a sodium silicate-based deflocculant system by Z&S, aimed at optimal deflocculation and stabilisation of the slip. In the following the results of the separate raw materials characterisation, essential as basis for the development of novel body formulations, additional deflocculant systems and reference systems for experimental validation of the numeric calculations are presented.

As described in the prececding articles patricle size analysis plays a significant role in the definition of the specification of the particle model for simulation. The results from the chemical, mineralogical and colloidal charactersiation of the different patricle size fractions of the body composition (0.63 µm, 0.63 – 2 µm, 2 – 6.3 µm, and 6.3 – 63 µm), which had to be obtained using a special fractioning technique conceived by KIT/CMM, due to the high amount of the fine fraction of the clay mixture as specified by sedigraph analysis (50 % < 0.63 µm), were used for first assessment of the particle charge distribution for the clay fraction. Particle size and morphology data, eminent for the description of rheological characteristics and microstructural development of the body during slip casting formulation, have been derived from a comparison and evaluation of the available particle size analysis techniques. For the submicron range alternative measurements to sedimentation and laser light scattering like acoustic spectrometry, dynamic light scattering techniques as well as new laser scattering equipment using different light beam settings (and using Mie theory based evaluation) for edge diffraction effects have been implemented by the project partners.To generate a fist assessment of the morphology and an »actual« size distribution of the fractions, samples were freeze-dried for electron microscopy image analysis. Most important conclusion from this previous investigation is that in the chosen composition there is a noticeable transition at the 2 µm fraction: the lower fractions, mainly below 0.63 µm, consist of mainly plate-like particles with a general average length about 300 nm and a stack thickness of 50 – 70 nm (with aspect ratio 1:6.8) with a clay-based chemical composition, whereas above 2 micron a grain type size with high SiO_2 contents, indicating quartz and feldspar to be main components, prevails. This implies a different validity of different measurement techniques for different fractions, the new laser scattering techniques and acoustic spectrometry providing also a validated possibility for the measurement of the fraction below 2 µm, as this fraction, in this case mainly below 0,63 µm, cannot adequatly be measured by regular light scattering and sedigraph These results have been presented at the annual meeting of the German Ceramic Society to support further implementation for the essential focus on the submicron fraction characterisation in clay minerals [2]. Regarding the raw materials characterisation as presented here laser light scattering results have been used for the general classification of the particle size distribution of the raw materials, whereas for the specification of the particles for the fractions reference is made to the previous results of the fractioned composition.

In Table 1 the characterisation results of the clay raw materials, including chemical analysis by X-ray fluorescence, mineralogical phase analysis by X-Ray diffraction using the Autoquan software for Rietveld analysis [3], CEC measurements and the amount of soluble salts, also a strongly influence the behaviour of the raw material, due to surface interactions and influences in the ionic concentration, are summarized. For a simplified description of the surface and edge charge and the charge distribution of the particles the previously implemented estimation, based upon pH dependent CEC measurement after Dohrmann [4], is used.

Table 1. Characterisation results for the raw materials components.

Raw Materials: clay mixture		Mixture 1001	Clay D	Clay E	Clay G	Clay H	Clay L	Kaolin A	Kaolin B
Chemical Analysis									
SiO_2	[wt%]	70.69	56.95	55.78	68.07	79.31	71.40	54.42	55.00
Al_2O_3	[wt%]	23.37	35.28	37.04	24.90	16.31	22.50	41.13	40.80
TiO_2	[wt%]	1.57	1.69	2.10	1.34	1.31	1.63	0.09	0.52
Fe_2O_3	[wt%]	1.17	1.51	1.79	1.47	0.87	1.07	1.38	1.23
CaO	[wt%]	0.19	0.22	0.25	0.25	0.16	0.18	0.09	0.10
K_2O	[wt%]	2.28	3.45	2.16	2.61	1.48	2.32	2.36	1.94
MgO	[wt%]	0.45	0.56	0.48	0.36	0.34	0.51	0.28	0.25
Na_2O	[wt%]	0.09	0.17	0.13	0.17	< 0,05	0.20	0.07	0.04
SO_3	[wt%]	0.07	0.06	0.17	0.22	0.05	0.07		0.08
L.o.i.	[wt%]	6.89	13.34	11.30	8.47	5.00	7.40	11.94	12.40
Density	[g/cm³]	2.65	2.54	2.65	2.64	2.66	2.66	2.68	2.64
Specific Surface									
BET	[m²/g]	20.6	30.83	37.41	23.08	15.5	22.3	9.5	8.84
Sieve Analysis (wet sieving)									
> 63	[wt%]	2.16	6.97	0.14	0.99	8.53	0.94	0.02	0.27
< 63	[wt%]	97.84	93.03	99.86	99.01	91.47	99.06	99.98	99.73
PSD By laser light scattering using Malvern Mastersizer Typ S with ultrasonic sample treatment[1,2]									
< 8 µm	[vol%]	77.1	90.8	97.2	77.7	62.1	81.0	52.4	46.0
< 2 µm	[vol%]	29.8	48.5	51.9	33.8	24.5	30.5	13.9	9.1
d10	[µm]	0.9	0.5	0.5	0.7	0.9	0.8	1.6	2.2
d50	[µm]	3.6	2.1	1.9	3.3	5.1	3.3	7.7	8.9
d90	[µm]	14.6	7.6	5.2	13.9	39.0	11.9	22.8	28.0
Soluble Salts[4]									
Al	[mg/kg]	n.b.	159.7	< 0,5	792.6	5.7	n.b.	0.4	n.d.
Ca	[mg/kg]	37.3	20.4	105.4	92.7	35.4	49.0	6.7	106.0
K	[mg/kg]	38.9	24.7	20.4	113.3	11.6	116.0	17.3	13.0
Mg	[mg/kg]	24.3	6.4	58.2	48.1	16.9	43.0	3.4	22.0
Na	[mg/kg]	39.5	11.3	6.8	125.3	5.5	16.0	13.5	15.0
Chlorid	[mg/kg]	19.4	46.6	13.9	23.2	12.5	91.0	25.1	12.0
Sulfat	[mg/kg]	63.8	109.0	524.4	48.2	158.7	131.0	137.9	128.0
Nitrat	[mg/kg]	n.d.	< 4,8	< 4,8	8.1	< 4,8	n.d.	6.1	n.d.
Phosphat	[mg/kg]	n.d.	n.d.	n.d.	n.d.	n.d.	n.d.	n.d.	n.d.
Conductivity [3,5]	[µs/cm]		51.2	179.0	126.5	69.6	50.0	60.1	-
pH-Value[3,5]	-		4.8	5.8	8.0	6.6	7.4	5.9	-
CEC	meq/100g	8.1	12.1	10.3	8.3	4.3	8.6	2.7	1.4
pH[6]		8.7	6.2	8.3	8.8	9.3	7.5	7.9	7.5
Mineralogical phase Analysis by X-ray Diffraction[7]									
Quartz	[%]	35.3	7.4	6.1	31.8	54.2	36.2	4.0	
Na-Ca-Feldspars	[%]	2.6	3.9	1.0	3.2	0.4	2.7	1.0	
K-Feldspar	[%]	1.4	1.3	1.7	1.1	1.9	-		
Rutile	[%]	1.6	1.9	1.6	1.3	1.2	1.4		
Kaolinite	[%]	28.2	36.5	55.6	25.8	21.1	26.6	75.4	
Muscovite	[%]	11.7	17.5	9.1	15.4	7.6	13.1	19.6	
Illite	[%]	7.4	13.7	9.1	11.7	5.3	5.8		
Swellable phases	[%]	11.8	17.8	15.8	9.7	8.3	12.7		
Sum of clay minerals	[%]	59.1	85.5	89.6	62.6	42.3	58.2		
CEC	meq/100g	8.0	12.0	10.0	10.0	5.0			
Estimation swellable conten	[%]	10.0	15.0	12.0	12.0	6.0			
Swellable content (autoquan	[%]	12.0	18.0	16.0	10.0	8.0			

[1] For PSD measurement the material was dispersed in an aqueous solution of 0,1 wt% $Na_4P_2O_7$.
[2] Measurements performed by FGK, evaluated using Fraunhofer Approximation.
[3] Measured during the determination of soluble salts
[4] Average value from duplo measurement
[5] Average value from triple measurement
[6] Measured during CEC determination
[7] Data from KIT/CME
n.d. = not determined

Table 2. pH dependence of the particle size measurement using acoustic spectrometry for the fraction < 0.63 µm of the mixture.

PSD-measurements as f(pH) for Ffraction < 0,63 µm by acoustic spectrometry using DT 1200[1]					
		pH 2,1	pH 3,4	pH 5,8	pH 8,9
d10	[µm]	0.62	0.11	0.09	0.20
d50	[µm]	0.63	0.84	0.53	0.89
d90	[µm]	0.65	6.17	5.37	4.07
mean	[µm]	0.63	2.68	12.51	1.89
std.dev.		0.01	0.31	0.31	0.55
Fit		unimodal	bimodal	bimodal	unimodal
Fit-error	[%]	**34.00**	5.31	3.46	**23.00**

[1] For PSD measurement the material was dispersed in demin. water, pH-adjustment with NaOH and HCl

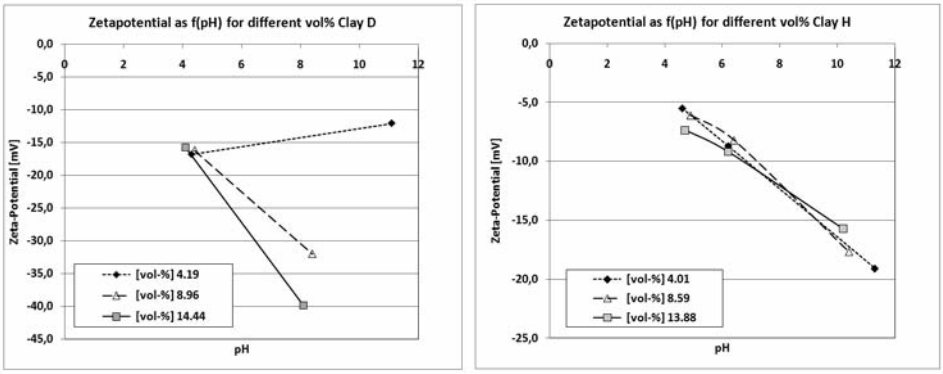

Figure 1: pH dependent zeta potential measurement for Clay D and H.

Regarding the possible meta-stable character of the material within the pH range investigated (pH 4 to pH 8) a comparison with reference data from literature [5] is being implemented as orientation for the validation experiments and the numerical calculations. For the estimation of surface potentials, necessary for the simulation approach, the influence of pH, ionic strength and volume concentration for selected clays is being investigated and as far as possible experimentally validated. First results are presented in the chapter on the reference systems for the experimental validation. To investigate the possible influence of delamination effects within the pH range the pH dependence of particle size measurement of the fraction < 0,63 µm was investigated using acoustic spectrometry (Quantachrome DT1200 Zeta Potential, Table 2). Within the pH range used no significant effects could be detrmined, lower and higher pH values however indicate larger deviations, due to the measurement limitations (see fit error, Table 2).

Development of reference systems for experimental validation of the simulation

As a basic reference system for the validation experiments different approaches have been investigated. A first approach, based upon using a well-defined Ca-bentonite with a high montmorrillonite content (up to 96 %, d_{50} around 3 µm) to provide a defined amount of swellable material in a basis reference system, had to be abandoned due to the strong gelation of the material, impeding initial characterisation as well as experimental implementation.

Based upon the characterisation results of the clay raw material and the kaolin (Table 1), feldspar and quartz components the choice was made to convert to the specified clay raw materials and their mixtures with specific differences in the amount kaolinite, quartz and amount of swellable material. For a first approach the clays D (37 % kaolinite - 7 % quartz - 18 % swellable material - total clay content 86 %), E (56 % kaolinite, the content of quartz,

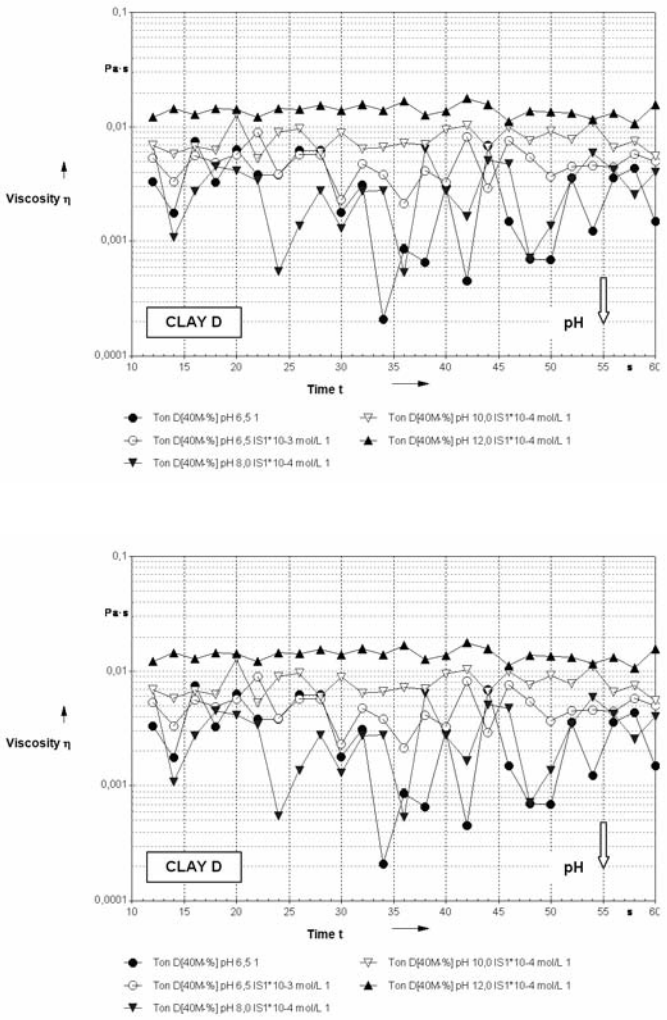

Figure 2: Rheological characterisation of Clay D and H at different pH values and ionic concentrations.

swellable material and total clay content being comparable to clay D) and H (21% kaolinite - 54 % quartz, 8 % swellable material and total clay content comparable of 42 %) have been chosen. Clay D and E should indicate how the amount of kaolinite and other clay components (illite, muscovite) could be treated in the modelling; clay H introduces the dilution effetct by the quartz influence.

For each these clays corresponding deflocculation curves have been measured by Z&S using the developed additive systems. For later implementation first assessments of the ionic concentration due to the additive dissociation, influencing the electrolyte environment of the particle system, have been established. In this regard the possible approach of the description of the permittivity, which in the context of the project cannot be unambiguously defined, is under investigation [6]. For the estimation of the surface potentials, necessary for the simulation approach, the influence of pH, ionic strength and volume concentration for these selected clays is being investigated. In figure 1 the difference between the zeta potential of clay D (high amount of swellable metarial) and H (high amount of quartz) is displayed. Measurement limitations however are reached measuring the clay materials without the use of additives at higher volume fractions and at the specified pH values.

Implementation of different ionic concentrations by using KCl did not generate reliable results by exeedingly high zeta potential readings. Especially the determination of a reliable particle size by acoustic spectrometry proves to be difficult in these settings. Further literature research regarding measurement settings

and validation of the results is therefore being performed. For the experimental validation of the functional behaviour of the systems under these settings rotational viscosimetry measurements are being performed. Figure 2 presents first results. Clay D seems to stabilise at a higher viscosity at pH increase. Clay H works in an opposite direction, however at a higher viscosity level than clay D. Mixture sequences are being experimentally processed and will be adapted to the progress in model development.

Development of body compositions for laboratory scale pilot testing

A first investigation into the effect of the plastic clay components in the body formulation by standard characterisation of the rheological and physical characteristics (like cast formation, dry bending strength, deflection and dry shrinkage) of a mixture sequence by succesive replacement of the plastic content by kaolin confirmed the significant influence of the plastic components, especially by significant shifts in rheology (figure 3.). As the exchange of kaolin might not be a feasible route for production slip compositions, alternative systems have to be investigated.

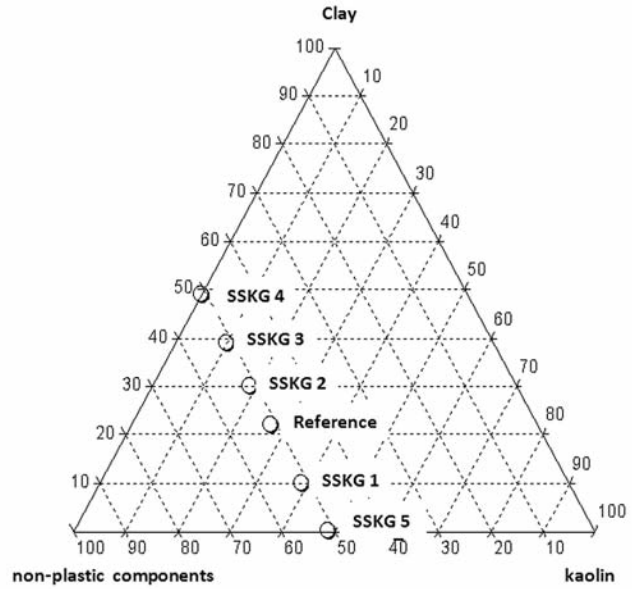

		Physical-technical characteristics					
		Reference	SSKG_1	SSKG_2	SSKG_3	SSKG_4	SSKG_5
slip direct	specific density [g/L]	1783	1806	1767	1763	1762	1799
	Fordcup [s]	32.59	60.86	27.48	24.98	26.45	196
	1. Gallenkamp [°Gal]	336	335	337	335	327	298
	2. Gallenkamp [°Gal] 5min	333	334	335	327	313	273
	thixotropy acc. to Gallenkamp	3	1	2	8	14	25
rheology	viscosity @ 100s^{-1}	0.23	0.38	0.17	0.14	0.16	1.13
	viscosity @ 0.01s^{-1}	2.82	2.18	6.3	56	116.8	28.03
	thixotropy [%] n. SV	33.45	38.74	26.86	13.99	14.49	23.08
slip after 24h	specific density [g/L]	1799	1806	1804	1797	1794	1808
	Fordcup [s]	39.51	74.11	30.61	37.49	92.42	273
	1. Gallenkamp [°Gal]	331	327	333	322	255	270
	2. Gallenkamp [°Gal] 5min	317	312	315	257	65	184
	thixotropy acc. to Gallenkamp	14	15	18	65	190	86
rheology after 24 h	viscosity @ 100s^{-1}	0.25	0.42	0.19	0.23	0.58	1.21
	viscosity @ 0.01s^{-1}	42.57	33.01	92.58	349.3	933.3	131.9
	thixotropy [%] n. SV	15.59	18.14	12.19	22.8	68.89	19.87
cast samples after 24	cake formation [mm/h]	9.5	14.7	8	7.3	9.2	n.m.
	dry bending strength [N/mm²]	1.74	0.9	2.18	2.66	3.03	0.54
	deflection [mm]	77/71	78/76	76/72	76/73	73/68	91/94
	dry shrinkage [%]	2.01	2.01	2.68	3.36	4.03	2.35
	total shrinkage [%]	10.58	11.07	10.47	10.37	10.1	13.75
	firing shrinkage [%]	8.75	9.25	8	7.25	6.33	11.67

Figure 3: Body development and characterisation by succesive replacement of the plastic clay fraction by kaolin content.

	Raw material	Reference	M1	M2	M3
	Clay D	15%	0%	0%	15%
	Clay E	5%	0%	5%	0%
	Clay G	5%	12%	15%	15%
	Clay H	13%	19%	15%	15%
	Clay L	63%	69%	65%	55%
		Physical-technical characteristics			
slip direct	specific density [g/L]	1783	1762	1770	1775
	Fordcup [s]	41	34	37	37
	1. Gallenkamp [°Gal]	324	336	332	335
	2. Gallenkamp [°Gal] 5min	236	331	328	316
	thixotropy acc. to Gallenkamp	88	5	4	19
slip after 24h	specific density [g/L]	1798	1800	1803	1801
	Fordcup [s]	67	35	38	44
	1. Gallenkamp [°Gal]	271	336	330	325
	2. Gallenkamp [°Gal] 5min	130	320	309	248
	thixotropy acc. to Gallenkamp	141	16	21	77
cast samples after 24h	cake formation [mm/h]	11.81	9.94	9.12	11.44
	dry bending strength [N/mm²]	1.77	1.72	1.81	1.65
	deflection [mm]	94/87	91/84	82/80	78/77

Figure 4: Body development by succesive replacement of the clay fraction with swellable material content and initial functional characterisation

Based upon these results a second approach was conceived, based on modification of the amount of swellable material within the plastic fraction by clay exchange. For this reason the clays D and E, identified as main contributants of swellable minerals, have succesively been replaced by the other clay components. Figure 4 specifies these mixture compositions and identifies quantitatively the significant influence of the swellable metarials. From this mixture range the composition without clay D and E (M1) is chosen as first basis for the statistical experiments to identify the key parameters and their interactions in comparison to the reference system. In figure 5 the significant differences in rheological behaviour of both mixtures at different practicable specific densities, as derived from the developped rheology measurement routine, are presented. Especially at lower specific densities a significant viscosity increase in the case of the mixture M1 - without swellable material- is detected, confirming the necessity of these components for adequate pressure casting slips. The next step is to quantify these influences within the context of production slip compositions, to be tested on a laboratory scale.

Statistical Design of Experiments fort he development of laboratory scale casting slip

To support de development of the laboratory scale casting slips, a screening of the relevant influencing factors, the magnitude and significance of their influence and their interactions is of importance, especially in regard to the project goal of developing and maintaining robust processes based upon improvement of relevant material and definition of process parameters with adequate control possibilities. In this regard the use of statistical design of experiment techniques [7], as implemented by V&B to support the development of the rheology measurement routine, is perceived as a necessary mean of screening these interactions within a manageable effort.

For this purpose the previously performed FMEA-based parameter analysis was used to specify dependent and independent variables or factors, background variables to be considered and levels settings for the relevant factors. As target value a stable rheological behaviour in time is specified, measured by the key data from the rheology measurement routine developed within the project. This routine, including a defined sample preparation, has proven to provide an essential basis for measurement comparabilty within the consortium. For this purpose the jump test routine with succesive changes in shear rates from 0.5 s^{-1} to 100 s^{-1} and back is chosen for rheology measurements at specified time intervals. The proven comparability renders a unique possibility to split the

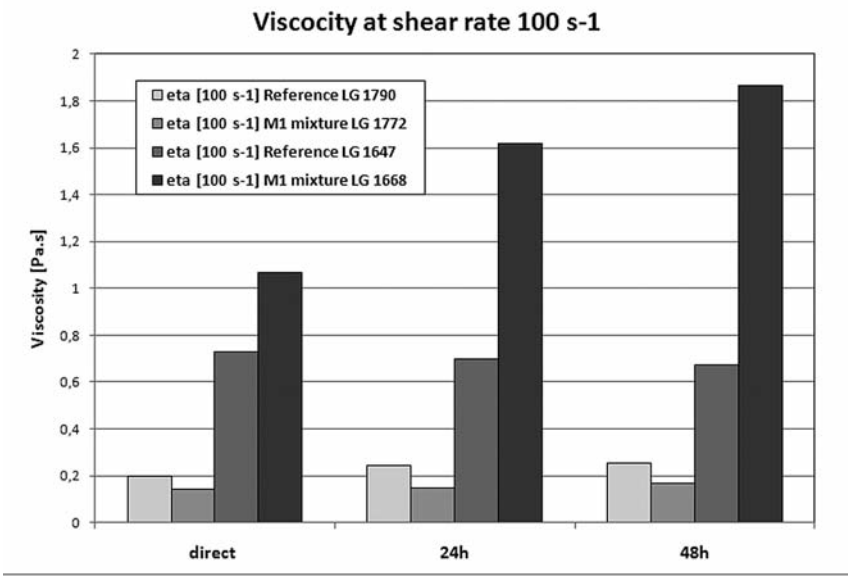

Figure 5: Rotational viscosimetry at shear rate 100 s^{-1} for the reference and the M1 mixture at different specific densities of the slip (LG = specific density in g/L)

efforts for the designed experiments within the consortium, thus providing the possibility use the available capacity to expand the amount of measurements and so enhance the reliability of interpretation of the results, inherent to statistical experimental design.

From the FMEA analysis of parameters influencing the rheology, a total of 13 influencing factors was defined, from which 5 were identified as main factors to be adressed for the identification of the interaction of the mineralogical surfaces with additives on rheology on a laboratory scale (see table 3). The factor mineralogy (specified by the measured mineralogical phases including the amount of swellable materials) is introduced by the forementioned body compositions. As main factor also the kaolin quality is specified, based upon the practical experience that different amounts of soluble salts, inherent to the kaolin quality, may influence the rheology and its stability. Therefore an alternative kaolin quality is introduced (see »kaolin B« in table 1).

For the specification of the additive combination as well as the specification of the levels, like the amount added, the developed additives, also including polyacrylates and phosphonates, which addtionaly to the electrostatic functionality implement sterical stabilisation, were pre-tested using the chosen body compositions. In this case for each additive type the qualitative levels for the dosage are quantitatively specified for experimental implementation. Regarding the use of filtration aids at this stage 2 alternatives are defined. Specific density of the slip as well as temperature and water quality have been defined as background variables, here to be controlled but kept constant within specified tolerances. The other factors derived from the assessment, mainly processing parameters derived from production practice, adressing recycling of casting slip, ageing in production and upscaling influences on mixing and slip transport, will be adressed in subsequent test plans.

For the screening of the identified main parameters at first a so called 2^{5-1} screening plan is being implemented, developed using the statistical software »statistica«, already sucessfully implemented at V&B. This plan is builds upon a base design of 5 experimental factors with each 2 levels, leading to 16 combinations to be tested, which are randomized and divided over the participating project partners. Each partner will prepare and measure one specified additional combination in duplo from his selection for reproducability and repeatability control, as well as 1 combination, specified to be measured by each of the partners separately to validate the anticipated comparabilty of results. The experimental design takes into account that 2 factor interactions can be adressed, but 3 factor interactions are neglected in this

Table 3: The statistical experimental setup for the evaluation from basic mineralogical interactions to processing influences on laboratory scale in the development of body composition concepts

factors	Basic Plan	Expanded Plan	Laboratory-scale	Pilot scale
mineralogy	2-level (swellable)	2-level (swellable)		
bactericide		2-level (with-without)		
kaolin quality	2-level (2 qualities)	2-level (2 qualities)		
amount of additive	2-level (low-high)	3-level (non-linear)		
additive type	2-level	3-level		
filtration support-additive	2-level	2-level		
water quality			X	
recycle slip quality			X	
amount recycle slip			X	X
slip temperature			X	X
slip processing			(X)	X
ageing time			X	X
processing parameters				X
Experimental design	Half 2^{5-1} Plan 16 combinations 4+2 comb./Partner	½ experimental plan, 72 combinations 18+3 combin./Partner	2^{5-1} Plan 16 combinations	2^{5-1} Plan 16 combinations

stage. Furthermore mixed interactions of dependent variables might not be detected, which is inherent to the statistical experimental design. To increase the resolution of the results this plan can be »folded« to 32 combinations, adding a second »block« of measurements to adress possible differences by repetition. As a next step a plan based upon 6 factors, with an increased number of additives and amounts of additive by a 3 level approach (adressing the non-linear deflocculation behaviour more realistically) has been designed, leading to a total of 72 combinations to be evaluated by expansion of the original set of experimental data.

The results as generated by rheological analysis will be evaluated within the tolerances as specified by the industrial partners. Based upon these results, which are supported by additional measurements by the partners (additional oscillation measurements, conductivity, pH development, casting performance) additional influences and their interactions to create optimal and stable casting performance will be specified to be included in following experiments. The results of the experimental validation will be presented and discussed in following publications.

Modelling

The performed model development so far has been based upon the simulation of a colloidal system, consisting of spherical particles in an electrolyte, motivated by previous studies [8, 9] on aluminum oxide particles, and showing repoducible results. To exemplify the capabilities of this approach the phase diagram was ampled as defined by two parameters: pH value and ionic strength. Varying these parameters enabled the simulation of the transition from a stable suspension to a state of agglomeration, by increasing ionic strength and pH value, as presented in the previous publications. Based upon the results the single component spheric particle model has been extended to a binary version, where the two components can have different material nature, sizes, densities etc. The algorithm now simulates two main components, derived from the raw material characterisation: small clay particles below 2 µm to be further specified and large particles (> 5 µm), specified as quartz patricles. The description of the particles regarding charge distribution and surface potential is, as mentioned before, based on assumptions from experimental validation where possible, otherwise from reference values from literature [5, 10].The simplified binary model already allows a study of the influence of the chemical/minerlogical nature and the size of colloidal

Table 4: The 2^{5-1} screening plan for the specification of the mineralogical composition effects and the interaction of the mineralogical surfaces with additives on rheology

Combination	Partner	mineralogy (composition)	kaolin quality	additive type	amount of additive	filtration support additive
2	FGK	M1	kaolin A	S1A1	low	Castmate
7	FGK	reference	kaolin B	S1PT2	low	FH1
15	FGK	reference	kaolin B	S1PT2	high	Castmate
10	FGK	M1	kaolin A	S1A1	high	FH1
17	FGK	reference	kaolin B	S1PT2	low	FH1
18	FGK	reference	kaolin A	S1A1	high	Castmate
12	SSKG	M1	kaolin B	S1A1	high	Castmate
4	SSKG	M1	kaolin B	S1A1	low	FH1
12	SSKG	reference	kaolin A	S1PT2	high	FH1
5	SSKG	reference	kaolin A	S1PT2	low	Castmate
19	SSKG	reference	kaolin A	S1PT2	high	FH1
20	SSKG	reference	kaolin A	S1A1	high	Castmate
11	V&B	reference	kaolin B	S1A1	high	FH1
6	V&B	M1	kaolin A	S1PT2	low	FH1
14	V&B	M1	kaolin A	S1PT2	high	Castmate
3	V&B	reference	kaolin B	S1A1	low	Castmate
21	V&B	M1	kaolin A	S1PT2	low	FH1
22	V&B	reference	kaolin A	S1A1	high	Castmate
8	Z&S	M1	kaolin B	S1PT2	low	Castmate
1	Z&S	reference	kaolin A	S1A1	low	FH1
16	Z&S	M1	kaolin B	S1PT2	high	FH1
9	Z&S	reference	kaolin A	S1A1	high	Castmate
23	Z&S	M1	kaolin B	S1PT2	high	FH1
24	Z&S	reference	kaolin A	S1A1	high	Castmate

particles on the rheological properties of the investigated system, being an essential parameter for the production process. At the least basic trends in behaviour will be derived from the simplified description, guiding further explorations of more complex and realistic models (like the transition to a ternary system).

For the simulations, a combination of two different techniques has been used: Molecular Dynamics (MD) [11] and Stochastic Rotational Dynamics (SRD) [12] (also known as Multiparticle Collision Dynamics). These techniques allow various thermodynamic and rheological properties of a system, with the use of statistical mechanics, starting with the microscopic and mesoscopic components, which in this case are the fluid and the colloidal particles respectively to be modelled. With the MD technique, the following interactions between colloidal particles are included in the simulation: screened Coulomb repulsion, van der Waals attraction, contact repulsion and short-range lubrication forces. The SRD, on the other hand, is used in combination with MD in a hybrid manner, in order to include the long-range hydrodynamic interactions between colloids and thermal fluctuations due to random collision between fluid particles and colloids.

To incorporate the dependence of the stability of colloidal systems on pH value now the so-called charge regulation model [14] is implemented in the program. It manages to model the adsorption-desorption reaction of electrolyte ions on the surface of colloidal particles. An expression of the effective surface potential of colloidal particles is worked out as the function of the pH value and the ionic strength of electrolytes. Experimental data therefore are needed to calibrate the model to adjust its parameters to the used material.

To show the tendency of the behavior of the binary component model including this regulation model a small system cell of the size 8.88 µm by 4.44 µm by 4.44 µm is modelled. The volume fraction of colloidal particles is 40% (as specified from industrial partice) and the temperature is 303K. 1182 Alumina particles of the radius 0.185 µm and 591 quartz particles of the radius 0.25 µm are considered. The colloidal dispersions are now sheared with the rate 100 s^{-1}, comparable to the testing procedure implemented for the clay characterisation. Ionic strength and pH value have been varied to investigate the stability of the colloidal dispersions and transitions between different states. In Figure 6 snapshots of three states with pH value 6.5 and different ionic

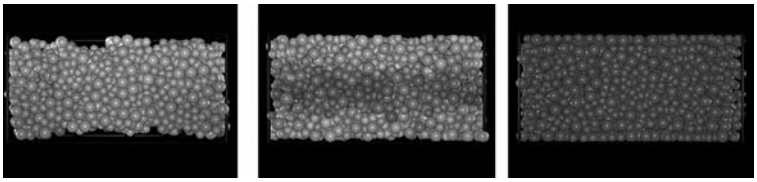

Figure 6: Snapshots of a cluster state (left), a stable colloidal suspension (middle) and a repulsive state (right) with the pH value 6.5 and the ionic strength $1*10^{-2}$, $1*10^{-3}$ and $1*10^{-4}$ mol per liter respectively. Lighter color indicates higher speed than darker color.

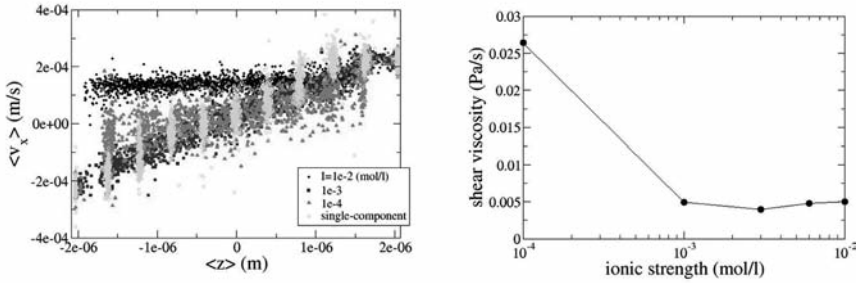

Figure 7: Velocity profiles of colloidal particles in direction perpendicular to the shear flow for the states shown in Fig.6. (left) and shear viscosity versus the ionic strength with the pH value 6.5. (right).

strengths are presented. At a high ionic strength corresponding to salt concentration of $1*10^{-2}$ mol per liter, the repulsive coulomb interaction is strongly screened. The colloidal particles agglomerate to form clusters due to the domination of the van der Waals attraction, which under shear attach themselves to one of the boundary planes and change shape with time due to the motion of the surrounding fluids. With decreasing ionic strength to $1*10^{-3}$ mol per liter a stable suspension is observed in result from the balance of the screened Coulomb repulsion and the van der Waals attraction, with a nearly linear velocity profile of colloidal particles (see Fig. 7), like a Newtonian fluid.

Further decrease of ionic strength to $1*10^{-4}$ mol per liter leads to a repulsive state where the colloidal particles rearrange their configurations under shear. Except in the boundary layers colloidal particles can move in both directions irrespective the velocity of the surrounding fluid. The particle velocity profiles in the direction perpendicular to the shear flow as presented in Fig. 7 show the different nature of these states. The variation of the shear viscosity with the ionic strength as shown in the left diagram in Fig. 7 can be used to further explore the difference between these states. As can be seen from the plot, the shear viscosity of the repulsive state is much higher than for the stable suspension state and the cluster state. The strong increase of the viscosity would originate from the increase of the effective particle size in the repulsive state. Similar transitions are observed as varying the pH value from 8, 10 to 12 with a fixed ionic strength $1*10^{-4}$ mol per liter. It has to be kept in mind that the parameters used in above simulations are up to now simple modifications of the single component system [8, 9] to include the second component of quartz particles, the system kaolinite/quartz at the moment being regarded as more suitable for the modelling.

The difficulty in the definition of the particle for the binary and ternary system originates from the description of the surface types, which can be allocated due to the mineralogical characterisation:

Kaolinite as 1:1 layer silicate contains three types of surfaces: siloxanplanes (Q4), gibbsitic planes (Al-OH bonds) and edges (broken bonds from silanol and aluminol groups). Here no permanent surface charge can be determined and edge charges are variable by adsorption and desorption of protons at the edges.

Illite/Muscovite as 2:1 layer silicates contains two siloxanplanes and edges. In this case the particles are specified with high permanent negative surface charge (0.26 to 0.34 Cm^{-2}) due to substitution in the 2:1 layers. Strong specific sorption of counter ions (K^+) might cause much lower zeta potentials compared to

swellable clay minerals like smectites in general or montmorillonite in special. Edge charges vary by adsorption and desorption of protons at the edges.

Smectites like montmorillonite as 2:1 layer silicate also contain siloxanplanes and edges, showing intermediate permanent negative surface charges (0.10 to 0.14 Cm^{-2}) due to substitution in the 2:1 layers, subject to specific sorption of large mono valent (e.g. Cs^{+}, which are not common ceramic clays) or »common sized« tri and quadro valent cations (Fe^{3+}, Al^{3+}, Si^{4+}) due to oxidation and/or dissolution of soluble salts in the clay material, with variable edge charges by adsorption and desorption of protons at the edges.

On this basis the following assumptions are discussed for modelling: the siloxan surface of kaolinite can be treated similar to quartz, the edge charge being estimated as most important. Quartz and feldspars could be regarded as similar for modeling. For the approximation of a binary system the raw clay materials selected could be treated simply as a binary mixture of quartz and kaolinite resulting in a mass ratio 90:10 for Clay D and 60:40 for Clay H. For the transition to a ternary system the edge zeta-potential of the different silicate systems can be modeled as the linear combination of those of quartz and alumina. The ternary modelling will be based upon kaolonite, quartz and swellable minerals, using different edge zeta-potential settings. The effect of the soluble salt ions (like Al^{3+}) ands the liquefier interactions can be included later on in the modelling by the charge regulation model to model the adsorption-desorption reaction of electrolyte ions on the surface of colloidal particles, influencing the zeta potential. For the first steps these factors are neglected. To derive necessary input for the effective surface potential and the isolelectric point of the used material the experimantal results and reference data [10] are investigated, the literature however delivering distinctly different values within a partially unspecified context for the mineralogical components.

An important task in the next step towards the simulation of clays is the introduction of platelike particles into the system. The main challenge to be overcome for this task results from the fact that –in contrast to the case of spherical particles, where symmetry allows great simplification of the problem– the theoretical and computational framework needed to obtain the inter-particle interactions are not yet fully developed [15]. As mentioned in prevoius publications two different, likely complementary, approaches have been defined. The first option, »glueing« of point-like particles (or spheres) to a plate-like structure [15, 16], obtaining the interaction between platelets by adding the interaction between the corresponding point-like particles, can only be achieved at relatively high computational cost, arising from the many interactions between pointlike particles that need to be taken into account in order to obtain the total force and torque on each platelet at each step of the simulation. The second approach is to obtain the solution to the Poisson-Boltzmann equation of a disc immersed in an electrolyte [17]. This method has the advantage of computational economy, but must be treated carefully regarding the constraints on the charge distribution on the platelet. In the spirit of the charge renormalization theory it is expected that suitable parameterizations of the model would extend the validity of the used approximations beyond their original theoretical constraints. In the next project period the plate-like clay particles will be implemented in the program by using this approach.

Outlook

The research during the next project phase will concentrate on development of the numerical simulation of binary and ternary systems and the development of the numerical computation of platelike particles. The development will be based upon characterisation and experimental validation using the selected clay materials and their mixtures, as well as literature evaluation regarding reference data on surface potential dependency on pH, ionic

concentration and volume fraction. The statistically designed experimentation will be evaluated and expanded to provide the basis for new material mixture concepts to be tested on a laboratory pilot scale, based upon the developed rheological evaluation method. From the evaluation of the interactions of the mineralogical composition with the developed additives new additive concepts will be optimized and developed.

References

[1] Prüfmittelfähigkeit der rheologischen Charakterisierung keramischer Schlicker mit Hilfe moderner Rheometer, Engels M. (2010), presentation at the Annual Meeting of the German Ceramic Society 2010, Hermsdorf/-Thüringen, 23.03.2010

[2] Vergleich der Korngrößenanalyse – Sedigraph, Laserbeugung, Zetasizer und REM bei Tonmineralen, Latief O. (2010), presentation at the Annual Meeting of the German Ceramic Society 2010, Hermsdorf/Thüringen, 23.03.2010

[3] Quantitative phase analysis using the Rietveld method and a fundamental parameter approach, Kleeberg R., Bergmann J. (2002), Proceedings of the II International School on Powder Diffraction, pp. 63-76.

[4] Kationenaustauschkapazität von Tonen - Bewertung bisheriger Analysenverfahren und Vorstellung einer neuen und exakten Silber-Thioharnstoff-Methode, Dohrmann R. (11997), Diss. RWTH Aachen, AGB-Verlag Nr. 26, 234 S. ISBN: 3-86073-605-1

[5] Surface Charging and Points of zero Charge, Kosmulski, M. (2009), Surfactant Science series Volume 145,CRC Press

[6] Characterization of water in bacterial cellulose using dielectric spectroscopy and electron microscopy, Gelin K et al. (2007), Polymer 48, pp. 7623 – 7631

[7] Taschenbuch Versuchsplanung, Kleppmann W. (2003), Carl Hanser Verlag Wien, ISBN: 3-446-22319-3

[8] Simulation of claylike colloids, Hecht M. et al. (2005), Phys. Rev. E 72, 011408.

[9] Shear viscosity of claylike colloids in computer simulations and experiments. Hecht et al. (2006), Phys. Rev. E 74 021403

[10] On the zeta potential and surface charge ofmontmorillonite in aqueous electrolyte solutions, Delgado A. et al. (1986), J. of Colloid and Interface Science Vol 113 p.,203-211.

[11] Computer Simulations of Liquids, Allen M. P. and Tildesley D. J. (1987) Oxford Science Publications, ISBN: 0 19 855 645 4 (Pbk)

[12] Mesoscopic model for solvent dynamics, Malevanets A. and Kapral R. (1999), J. Chem. Phys. 110, 8605

[13] Solute molecular dynamics in a mesoscale solvent, Malevanets A. and Kapral R., (2000), J. Chem. Phys. 112, 7260

[14] Electrical double layer interactions under regulation by surface ionization equilibria---dissimilar amphoteric surfaces,. Chan D.Y.C et al. (1976), J. Chem. Soc. Furuduy Trans. 1, 72, 2844

[15] Interaction of Nanometric Clay Platelets, Jonsson B. et al. (2008) Langmuir, 24 (20).

[16] Aging in a Laponite colloidal suspension: A Brownian dynamics simulation study, Mossa S. et al. (2007), J. Chem. Phys. 126, 014905

[17] Electrostatic Properties of Membranes: The Poisson-Boltzmann Theory, Andelman D. (1995), Handbook of Biological Physics. Volume 1. Elsevier Science.

Control mechanisms of clays and their specific surface area in growing media – assessment of clay properties and their parametrization for the optimization of plant quality

Dultz S. (1)*, Schellhorn M. (2), Schmilewski G. (3), Schenk M.K. (4), Dombrowski, I., (4), Schmidt, E. (2), Walsch, J. (1), Below, M. (1)

(1) Institute of Soil Science, Leibniz University Hanover, e-mail: dultz@ifbk.uni-hannover.de, walsch@ifbk.uni-hannover.de

(2) Stephan Schmidt KG, Langendernbach, e-mail: Matthias.Schellhorn@schmidt-tone.de, Eva.Schmidt@schmidt-tone.de

(3) Klasmann-Deilmann GmbH, Geeste-Groß Hesepe, e-mail: schmilewski@klasmann-deilmann.de

(4) Institute of Plant Nutrition, Leibniz University Hanover, e-mail: schenk@pflern.uni-hannover.de, dombrowski@pflern.uni-hannover.de

*Coordinator of the project

Summary

The addition of clay to growing media aims at constant supply of potassium, phosphorus and micro nutrients, pH-buffering, improvement of rewettability, and cohesion of growing media. The identification of suitable clays and their classification is a prerequisite for product and cultivation safety. A range of different clays highly variable in their mineral parameters were selected for experiments on nutrient buffering (P) and Mn toxicity, their ability to improve the rewettability and binding capacity of growing media. From batch experiments and growth trials it was derived that a threshold value for the sum of exchangeable and easy reducible Mn in clays for growing media is not justified, as even very high Mn contents in clay were not phytotoxic. The P binding capacity of clays was strongly correlated with the oxalate extractable Fe and Al content. A newly developed capillary rise method (WOK) was used to characterize the rewettability of growing media. The speed of rewetting mainly depends on the fineness of the amended clay. Surface free energy (SFE) data of the growing media indicate that those with a good rewettability show also high values for SFE. Compared to the kaolinitic and illitic clay amendments, bentonites show no significant increase in the SFE. Surfaces of clay minerals exhibiting originally polar and hydrophilic surfaces, can render hydrophobic when coated with weakly or non-polar organic matter moieties. Dissolved organic carbon (DOC) sorption was found to be positively correlated with the specific surface area (SSA), cation exchange capacity (CEC) and amount of dithionite extractable Al and Fe. Clays containing expandable clay minerals with high CEC and SSA (e.g. smectites) and those rich in Al- and Fe-oxides seem to be less effective for improving rewettability, whereas an addition of non-expandable clays with lower SSA, CEC (e. g. kaolinitic and illitic clays) and amorphous oxide content appears more promising. New insights on the adsorption of DOM on clay mineral`s surfaces will be obtained in the third year by chemical analysis of the surface with X-ray photoelectron spectroscopy (XPS), surface topography analysis and contact angle measurements. A new method for the determination

Table 1: Properties of growing media and their constituents that pertain to »quality« (adapted from *Schmilewski, 2008*).

Chemical	Physical	Biological	Economic
pH	structure and stability	pathogens	availability
nutrient content	water and air capacity	weeds	price
buffering capacity	bulk density	microbial activity	consistency of quality
noxious substances	wettability	storage life	cultivation technique

of the binding capacity of clays in blocking media is currently being tested and will be studied together with determinations on K-dynamics.

Introduction

Concept on function und effect of clays in growing media related to practice

A suitable rooting medium is fundamental for plant growth. Horticultural crops have certain requirements which the grower needs to fulfil with the help of individually tailored growing techniques and cultivation measures. For the selection of growing media constituents each should possess optimum characteristics for the specific culture. Modern horticulture with computer-controlled irrigation and fertilisation programmes, potting machines, pricking robots, climate-controlled greenhouses and just-in-time production requires dependable, quality-assured growing media. Specialist companies rely on ready-made growing media which are either part of the manufacturer's standard range or special mixtures produced at the grower's request. For the development of formulations and the production of growing media suitable for this market a large number of chemical, physical, biological and economic characteristics of the constituents must be taken into account (Table 1).

Due to its characteristics Sphagnum peat has been the most important constituent of organic growing media for several decades. A high water and air capacity in combination with other favourable features make peat ideal for this purpose. After fertilising and liming, peat is the sole constituent of many growing media. Nonetheless, peat has also some drawbacks arising from the relatively poor wettability when dry, limited nutrient buffering capacity, and structural stability. Mineral amendments, especially those rich in clays, are commonly incorporated into the organic media in order to improve physical and chemical conditions.

In horticultural practice, clays are amended to peat in amounts of 10-80 kg/m³. The amendment aims mainly to improve the following three different properties of the growing media:

1. Buffering of nutrients. Clay amendment shall ensure that optimum conditions adjusted at start of the crop remain constant during cultivation. Relative large amounts of clay are needed.
2. Rewettability during irrigation. Due to the large specific surface area and charged surface sites, hydrophilic mineral surfaces of clay minerals coating the surfaces of peat should have a positive effect on the wettability of inherently water repellent growing media and the amount of plant available water. Relative low amounts of clay are needed.
3. Binding capacity. For the use of pricking robots when transplanting young plants and also for the production of peat blocks (e.g. 4 x 4 x 4 cm) for mechanical sowing the cohesion of the growing media shall be improved by the amendment of a suitable clay. Relative low amounts of clay are needed.

As a certain clay can hardly support all of the required properties, also blends of different clays are used in growing media industry. Clays available show great differences in their mineral parameters, e. g. texture, mineralogical composition, layer charge, and oxide content. Chemical as well as physical characteristics of the growing media strongly depend on the kind of clay amendment. Currently no proven

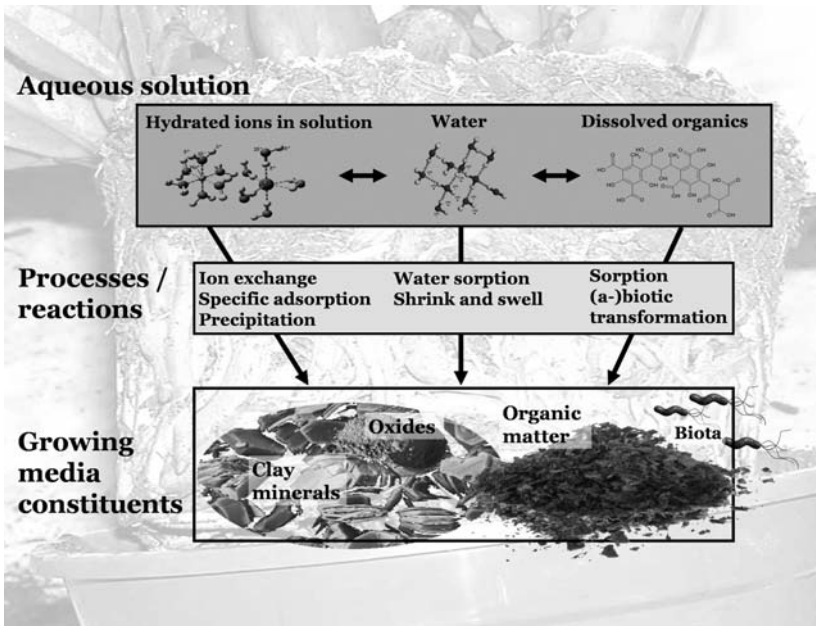

Figure 1: Scheme for the interactions growing media constituents with solution.

standards are available for evaluation of clay for use in growing media and to design growing media perfectly for specific crops and production methods. Here improved knowledge of the mechanisms and processes of these clays in growing media helps to identify suitable clays and to make the prognosis of clay properties more reliable.

Surface chemistry of growing media constituents

The amendment of clays or clay blends to peat together with the addition of fertilizers and lime in a growing medium has a strong effect on the surface chemistry of its constituents. Clay and peat stem from very different environments and a distinct number of exchange reactions can be assumed. E. g. the clays used in this project from Mesozoic-Tertiary weathering mantle of the Rhenish Massif are undersaturated for the binding of dissolved organic matter (DOM), whereas peat is known to be a source for DOM. For this reason the external surfaces of clay minerals might act as a sink for DOM, whereby in turn the adsorption of DOM can modify the surface properties of the clay minerals. Here the interaction of water with peat and clay minerals defines the physical and chemical properties of the growing medium, as virtually all chemical and biological reactions take place at the solid-water interface. A scheme of the interactions of water with the growing media constituents is shown in Fig. 1.

The solid-water interface is important because it controls the retention and transport of nutrients and pollutants and provides physical support for plants. Also contained in the pore solution besides inorganic solutes is DOM, its fate and transport highly depending on interactions of the solid-water interface. On addition, many chemical species in the growing media solution can interact with each other. Solute behaviour is controlled by multiple solid phases, different clay minerals, oxides and organic matter, which have a complex and heterogeneous nature. The type of surface reaction has a decisive role for the potential of the solid phase for the desired properties listed above.

Water repellent surfaces of growing media

Water repellent (hydrophobic) growing media can cause problems as, after drying out, they require a long time to rewet (*Michel et al., 2001*). For that reason the rewettability could become a property with major repercussions for plant growth (*Doerr et al., 2000*). Organic material in peats used for growing media comprises many substances which are only weakly or non-polar. As a consequence they are not able to form hydrogen bonds with water mole-

cules and hence exhibit often distinct water repellence (hydrophobicity). On the other hand, charged mineral surfaces are usually hydrophilic as they are capable of forming hydrogen-bonds. Thus, when incorporated into a water repellent sandy soil or a growing medium, it is expected that charged clay minerals show a positive influence on the wettability, by increasing the surface area, masking hydrophobic organic surfaces and exposing hydrophilic clay surfaces *(McKissock et al., 2002; Lichner et al., 2006*). The effect of mineral amendments on the wettability of soils was subject to several studies. Nevertheless, the results were somewhat inconsistent. Indication was obtained that the variations observed depend to a great extent on the formation of organic coatings on mineral surfaces. The adsorption of weakly or non-polar organic matter moieties can render a hydrophilic mineral surface hydrophobic (*Chenu et al., 2000; Doerr et al., 2000*). The hydrophilic reactivity of mineral surfaces and accordingly their positive influence on wettability can be reduced or even lost, when the minerals tend to accumulate hydrophobic organic compounds derived from soil organic matter or peat on their external surfaces.

For soils sorption of dissolved organic matter onto mineral surfaces was found to be affected by the parameters CEC, SSA and content of amorphous oxides (*e. g. Kaiser and Guggenberger, 2000; Kahle et al., 2004*). The stability of organic coatings depends on the type of bond, which is not only dependent on the chemical composition of DOM, but also on mineral surface properties. Basically it has to be assumed that wettability is largely influenced by the sorption of DOM and, as the wettability is a dynamic property, also desorption processes.

In the study on rewettability of growing media, the effect of certain clay amendments, highly different in their mineral parameters (mineralogical composition, specific surface area, oxalate and dithionite soluble Fe- and Al-oxides, texture) was determined. Processes and reactions responsible for the variations in growing media wettability are assessed and used to rate the effectiveness of the amendment. The results will be used to find reliable criteria for the selection of suitable clays for improving wettability.

Clays for improving P buffering capacity

The amendment of clay to peat-based growing media is supposed to improve both physical and chemical properties of growing media. Pure white peat is nearly non-buffered and the buffering capacity for the nutrients potassium and phosphorus can be increased by the addition of clay. A buffered growing media can absorb nutrients in large amounts by binding them and is able to release them again in the solution of the growing media when plants deplete the nutrient concentration. By this, fluctuations of plant demand or fertigation can be balanced and optimal growing conditions can be maintained.

The buffering capacity of a clay in growing media is mainly caused by its contents of amorphous Fe- and Al-oxides. Therefore P fixation varies widely between clay minerals and the choice of the »right« clay is very important. In horticultural practice the basic fertilization of a growing media is generally not sufficient to supply the plants over the whole vegetation period with nutrients and subsequent fertigation is necessary. The nutrient concentration in the fertigation solution should reflect the nutrient demand of plants. Growth rate and nutrient uptake of plants differs widely between species and cultivars and is dependent on environmental conditions. Therefore optimum fertigation concentration can be determined only with uncertainties.

Thus, i) clay characteristics affecting P buffering capacity were determined and ii) the influence of the buffering capacity of peat/clay-growing media on the safety of plant cultivation at varied concentrations of P fertigation was investigated.

Progress within the project

The work in the first two years focused on the two sections »Buffering of nutrients« (1) and »Rewettability during irrigation« (2). In preliminary studies in the section »Binding capacity« (3) different methods were tried out and extensive experiments on blocked growing me-

Table 1: Physical, chemical and mineralogical properties of seven clay samples from the Westerwald area, representing saprolithic clay (S), bentonite (B), translocated clays (U) and blends (M).

Sample	sand/silt/clay (wt%)	CEC ($mmol_c/kg$)	SSA (m^2/g)	Al_{ox} (g/kg)	Fe_{ox} (g/kg)	***Mineralogical composition <2 µm fraction*** (d = dominant, t = traces)
01S	42 / 45 / 13	287	11	0.34	0.61	illite, kaolinite (d); chlorite, quartz (t)
06B	41 / 38 / 21	840	106	2.24	2.96	smectite (d); illite, kaolinite (t)
07B	46 / 41 / 13	881	92	1.77	1.53	smectite (d); illite, kaolinite (t)
27U	2 / 52 / 46	223	20	0.09	0.02	kaolinite, quartz (d)
28U	2 / 18 / 80	435	44	0.26	0.11	kaolinite, illite (d)
36M	2 / 35 / 63	256	30	0.16	0.33	kaolinite (high crystallinity), illite (d)
38M	25 / 40 / 35	572	62	1.06	0.87	kaolinite, illite (d)

dia by mechanical agitation will be carried out in the third year.

Determinations on Manganese toxicity (section 1) on clays with different contents of active Mn (sum of exchangeable and easy reducable Mn) reveal that a threshold value for Mn in clays for growing media is not justified (*Dombrowski and Schenk, 2010*). Even very high Mn contents in clays only resulted in small increase of Mn concentration in the solution of the growing medium. Additionally plants tolerated high Mn-concentrations in the growing media solution because, i) Mn was complexed by DOM and thus is less phytotoxic ii) silicic acid dissolved in growing media solution alleviated the harmful Mn effects. Results on the P binding capacity of clays, strongly correlated with the oxalate extractable Fe and Al content of clays, are described in detail in the result section.

For the determination of the rewettability of growing media the capillary rise method was used. For this purpose a WOK-apparatus allowing 8 simultaneous measurements was installed at Klasmann-Deilmann GmbH. The effectiveness in improving the wettability of growing media was found to depend on the surface properties of the clay minerals amended which govern the binding of DOM. Amendments with non-expandable clay minerals with low SSA, CEC (e.g. kaolinite and illite) and clays with a low amorphous oxide content appear most promising (*Walsch and Dultz, 2010*). The fineness of the clay was observed to be a decisive factor for improving the rewettability.

Material and Methods

Rewettability

Seven clay samples with distinct differences in mineral parameters (Tab. 1) and a blend of different Sphagnum peats with a moderate degree of decomposition were used.

The growing media was limed (6.0 kg/m^3) and fertilized (1.1 kg NPK 14-16-18 standard fertilizer per m^3 growing media. The rewettability of the growing media mixtures was assessed in terms of capillary water uptake (WOK, Dutch RHP foundation) and contact angle (CA) measurements (OCA 20, Data Physics). In the WOK apparatus dry samples are placed in cylindrical rings (500 cm^3) on a layer of water and the increase in water content is logged over time for 24 h (Fig. 2).

Hydration of particles in the growing media was determined in an environmental scanning electron microscope (ESEM; Quanta 200, Fei). As peat surfaces consisting mainly of C are covered with clay minerals rich in Si, the degree of coverage of the peat surface can be described by the C/Si ratio. By energy dispersive X-ray spectroscopy five different sections each of 6 mm^2 size were determined.

The adsorption of peat derived DOM on mineral surfaces was determined in batch adsorption experiments. DOM solutions for adsorption experiments were extracted from limed and fertilized peat. Batch adsorption experiments were carried out for 24 h at 20 °C in the dark. DOC concentrations were measured with a total organic carbon analyser (liquiTOC, elementar). Aromaticity of the adsorbed DOC and DOM-fractionation phenomena due to adsorption

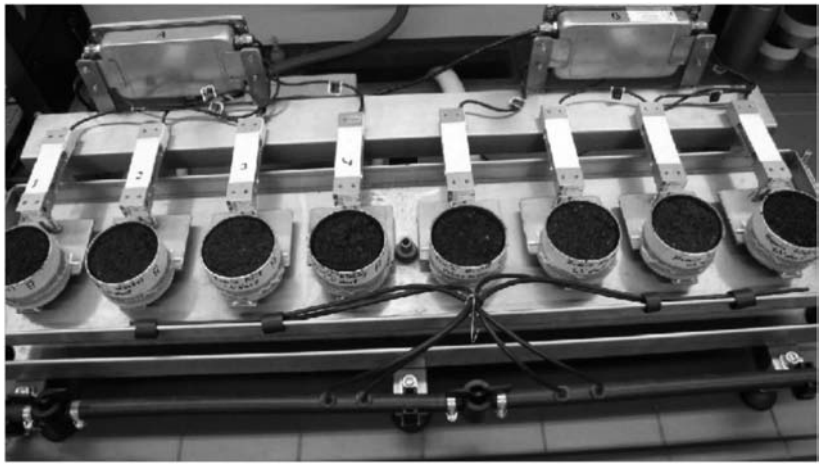

Figure 2: WOK apparatus used for the determination of the time dependent water uptake capacity.

were determined with a Cary 50 UV-Vis spectrometer (Varian). According to *Chin et al. (1994)* absorbance values were recorded at a wavelength of 280 nm, where electron transitions occur for a number of aromatic substances.

P buffering capacity

The influence of P buffering of peat/clay growing media on the safety of plant cultivation was characterized in a plant experiment. At first nine clays with different P fixation capacity were selected for the determination of plant availability of P in peat/clay growing media. To assess the P fixation clays and growing media were shaken in a P solution (1000 mg P L^{-1}) at a ratio of 1:10 for 24h. Oxalate soluble Fe and Al were extracted using 0.2 M oxalate solution. Based on these data two clays with a low P fixation (04S and 01S) and two with a high P fixation (06B and 39W) were selected for the plant experiment and mixed with peat (80 vol-% peat, 20 vol-% clay).

For each growing media a calibration curve was established to determine the amount of P needed to obtain a CAT extractable P concentration of 25 mg P/L growing media, which is usually adjusted in horticultural practice. CAT (0.01 M $CaCl_2$ + 0.002 M DTPA) is commonly used for the extraction of potentially plant available P in horticultural growing media (*Alt & Peters, 1992*). The growing media were equilibrated in an oven at 50°C for 48 h, then at room temperature for another 48 h prior to determining the CAT extractable P concentration. Previous work showed that this incubation procedure is highly correlated with CAT soluble P after 9 weeks of storage.

Seedlings of Impatiens walleriana F1 »Candy ® Coral Bee« were planted in 600 ml plastic pots (∅ 12 cm) filled with the different growing media and pure white peat as control. Volume weight of growing media was determined according to standard method of VDLUFA (1991). All growing media were fertilized with 1.5 g L-1 of a P free compound fertilizer (Ferti 8® – N : P_2O_5 : K_2O = 20 : 0 : 16 + micronutrients) and pH was adjusted with $CaCO_3$ to pH 6 (0.01 M $CaCl_2$). The CAT soluble P content of 25 mg P/L growing media was obtained by addition of $Ca(H_2PO_4)_2$ according to the calibration curves. The fertigation solution contained in mg/L solution: 120 N as KNO_3 and NH_4NO_3, 130 K as KNO_3, K_2SO_4 and KH_2PO_4, 10 Mg as $MgSO_4$*7 H_2O and 200 Flori® 10. The P concentration of the fertigation solution was varied (in mg P/L solution): 0 (= *no P*), 17 (= *sufficient P*) and 35 (= *excess P*). Plants were harvested after 10 weeks cultivation after measuring plant height and diameter and length of internodes. The P concentration in plant d.m. was measured after wet digestion and the P concentration in the solutions was determined with the ammonium-vanadate-molybdate method. Treatments were replicated five times (each replicate consisted of 5 plants) in a completely randomized design and statistical analysis was performed with the program R 2.8.1. Means were compared between treatments at α = 0.05 using Tukey-Test.

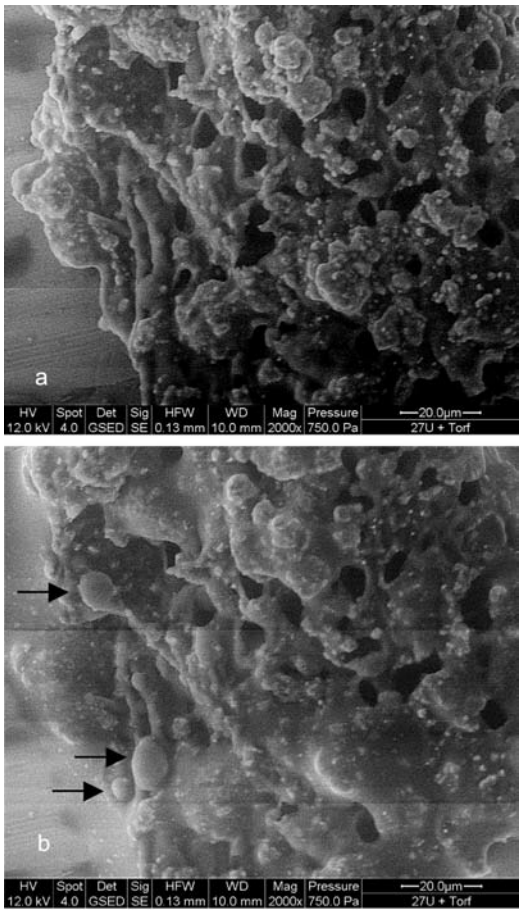

Figure 3a, b: Environmental scanning electron microscope (ESEM) observation of a peat-based growing media amended with a translocated clay (27 U) submitted to hydration conditions. The image shows a leave of Sphagnum moss peat covered with clay platelets in the dry state (a) and directly after beginning of condensation (b). Note that condensation starts at sites where clay minerals coat the peat´s surface. Water droplets are marked with arrows.

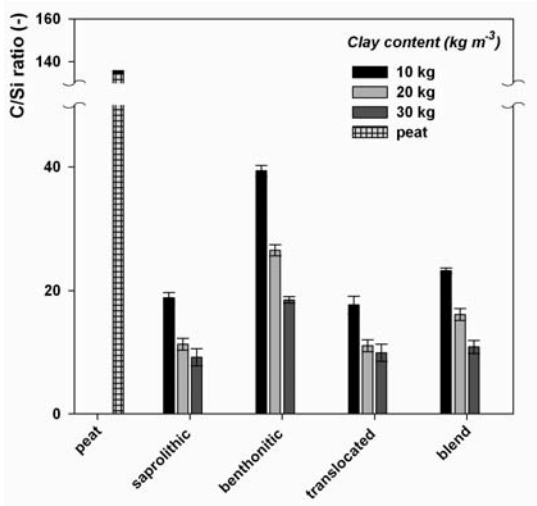

Figure 4: Coverage degree of peat surfaces with clay minerals expressed by the C/Si ratio (n=5). Low values indicate highly covered surfaces.

Results

Rewettability

ESEM observations

Growing media submitted to hydration show clearly that the condensation of water starts on the hydrophilic clay particles coating the external surfaces of the peat compounds (Fig. 3a, b). The formation of water drops on the surface of peat indicates high contact angels and strongly hydrophobic properties.

Saprolithic and translocated clays have the strongest effect on surface coverage of peat compounds with clay minerals (Fig. 4). Here already 20 kg/m³ are sufficient to reach lowest C/Si ratios indicating maximum coverage degree. Bentonites and clay blends still increase the coverage degree of the peat`s surface by the addition of 30 kg/m³. Bentonites show small effects even at the largest amended amount. Here C/Si-ratios are comparable with growing media amended with saprolithic and translocated clays in amounts of 10 kg/m³.

Water uptake is improved for all samples by the amendment of clay (Fig. 5), strongly depending on the clay parameters. Clays consisting mainly of illite and kaolinite (saprolithic and translocated clays) show fastest water uptake (50 vol.% within 10 min).

At C/Si ratios <20, where the surfaces of peat are most completely coated with clay minerals, all clay-peat systems show the highest water uptake rate. Highest variability is observed for a saprolitic clay rich in illite and kaolinite, where the water uptake rate ranges from 2.6 to 15.5 (%v/v)/min. Bentonites show only minor effects, water uptake ranges from 1.47 to 3.63 (%v/v)/min. The translocated clay is most effective to improve water uptake rate with small amended amounts. Larger added amounts show only slight improvements. For the clay blend and bentonite, the absolute amount of amended clay showed minor effects, but water uptake rate is quite higher than that of original peat (1.3 (%v/v)/min). The results show a good

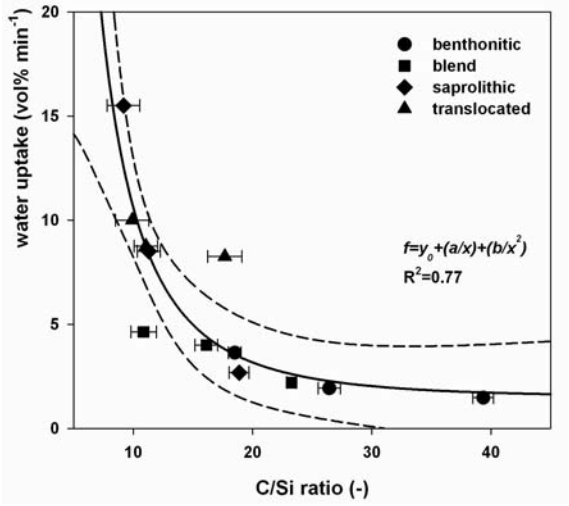

Figure 5: Effect of four different clays on the water uptake rate. Growing media are amended in amounts of 10, 20 and 30 kg/m³ clay. Water uptake rate is determined by the time (min) needed to 50% saturation. The dashed line is the 95% confidence interval of the linear regression (solid line).

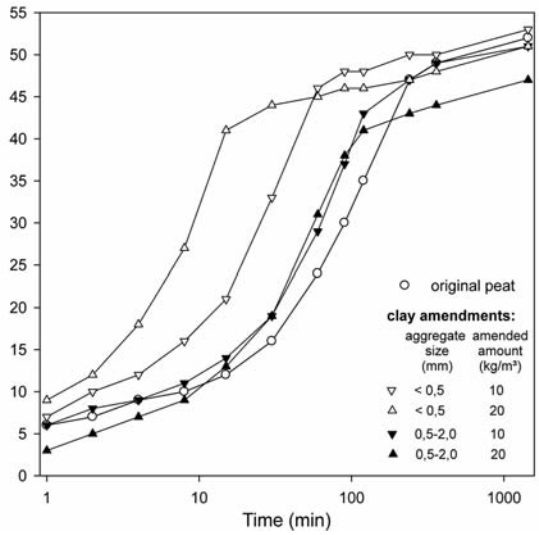

Figure 6: Time dependent water uptake of a growing media (fineness of peat: 0-10 mm) to which translocated clay 36M was added in two different amounts (10 and 20 kg/m³) und two particle size fractions (<0.5 and 0.5-2.0 mm).

correlation of the surface coverage degree expressed by the C/Si ratio and rewettability determined by the capillary rise »WOK« method. The determination of the C/Si ratio in a relatively short procedure is a suitable method to identify suitable clays and the amount of clay needed.

Effect of clay particle size on water uptake characteristics

Time dependent water uptake measurements on growing media with clays of different particle size fractions reveal that the initial particle size of the amended clay has a strong influence on the water uptake rate. For fine aggregate sizes <0.5 mm the fastest water uptake was observed (Fig. 6). Note that in horticultural practice irrigation is often performed in the ebb and flow mode. If the uptake rate is high the time needed for irrigation can be shortened. After the total duration of the experiment of 1440 min (24 h) in the WOK apparatus the differences in water uptake rate are low. This is not relelevant for horticultural practice, where the differences at the beginning of irrigation are most important. Here the growing media where the smallest aggregate size (< 0,5 mm) and the highest amount of amended clay (20 kg/m³) shows the fastest water uptake rate in the time period up to 15 min.

Effect of different clays on water uptake characteristics

From the water uptake curves, it becomes evident that the growing media differ significantly in their rewetting behaviour (Fig. 7). Pure peat showed the slowest water uptake, whereas the increase in the volumetric water content of mineral amended growing media was generally faster. Up to 50 % water saturation, also marked variations in the rewetting behaviour among the different mineral amendments were observed. Amendments of smectite rich clays (06B and 07B) caused only a minor increase in water uptake velocity, while kaolinitic and illitic mineral amendments notably enhanced the rewetting. It can be concluded that the wettability of a growing media is a dynamic property, which is to a great extent influenced by the clay mineralogy and also other mineral parameters.

Formation of hydrophobic coatings on clay mineral surfaces

Mineral surfaces provide a variety of reactive functional groups on their surface, which allows strong interaction with dissolved organic and inorganic substances. Consequently, batch adsorption experiments with peat derived DOM revealed that both, the bulk samples

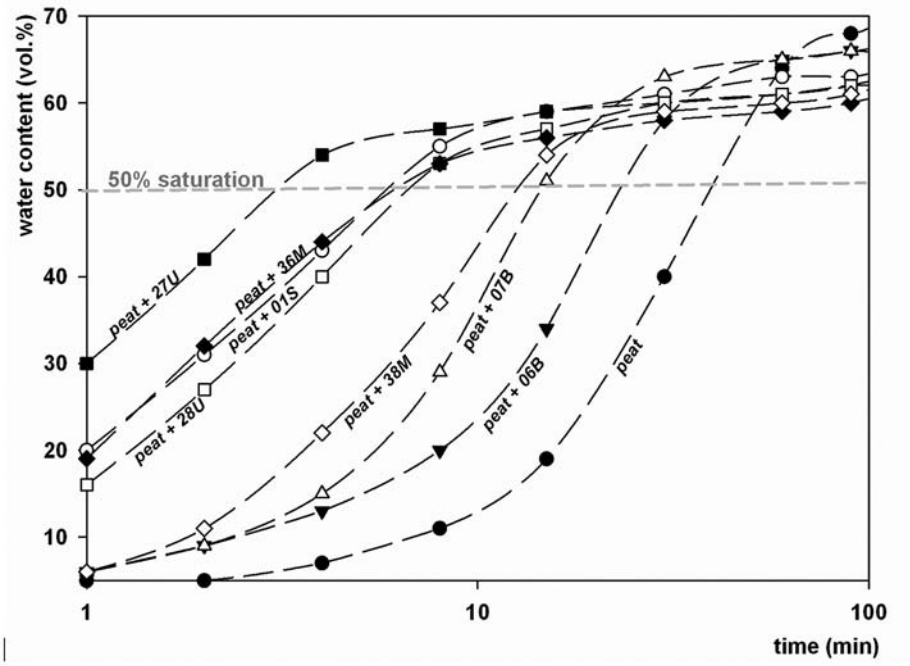

Figure 7: Time dependent water uptake of peat-based growing media amended with different clays in an amount of 30 kg/m3. For comparison, the water uptake of the pure peat is shown.

as well as the clay fractions adsorb relatively high amounts of dissolved organic substances (Fig. 8). For the samples under investigation, the adsorbed C content varies between 20 and 180 mmol C kg^{-1}, with the highest amount being adsorbed by the samples rich in smectite (06B and 07B).

The composition of the organic coatings on the mineral phase was determined by UV-Vis analyses of the equilibrium solutions after the batch adsorption experiments (Fig. 9). Here, a decrease in light absorbance values (Abs_{280}) indicates a high removal of aromatic organic substances from the solution due to the sorption onto mineral surfaces.

The extent of sorption was found to be dependent on the mineral parameters of the samples (Fig. 9, a, b, c). Linear regression analysis showed that sorption of aromatic compounds correlates well with the SSA, CEC and amount of oxalate soluble Al and Fe, which is consistent with findings reported elsewhere (*e.g. Kaiser and Guggenberger, 2000; Kahle et al., 2004*). *Abs*orption at 280 nm shows strongest correlation to the SSA (r^2 = 0.86), which is most likely due to the higher surface area available for DOC sorption. Considering liming and fertilization, it can be suggested that DOM sorption is most likely also mediated by the solution chemistry. For instance *Feng et al. (2005)* found that sorption of peat derived humic acid onto kaolinite and montmorillonite increased with increasing ionic strength and decreasing pH, and that the presence of Ca^{2+} largely enhanced the sorption. Subsequently, DOC linkage to negatively charged mineral surfaces via cation-bridges appears to be an important binding mechanism, which is also indicated by the positive correlation (r^2 = 0.66) between adsorbed DOC and the CEC of the clay amendment. The correlation with the sum of oxalate extractable Al and Fe (r^2 = 0.71) is indicative for DOC binding onto poorly crystalline Fe and Al minerals (*Mikutta et al., 2005*). It can be assumed that the amount and composition of adsorbed DOM as well as the mineral parameters are the key to explain the observed variations in wettability and accordingly the differences in the effectiveness of the mineral amendments.

Effect of hydrophobic mineral coatings on water uptake rate

Adsorption of peat derived DOM onto mineral

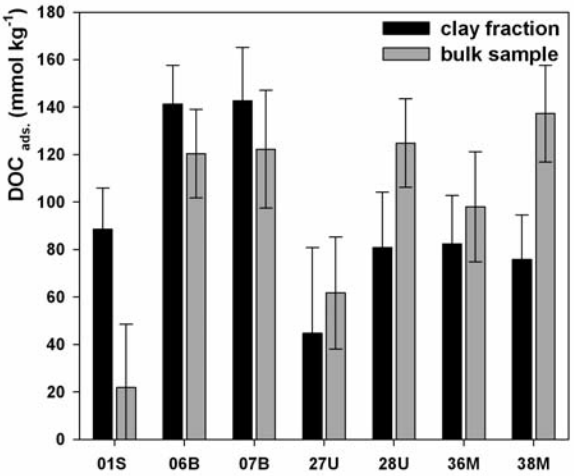

Figure 8: Sorption of peat derived DOM on bulk clay samples and the clay fractions.

surfaces influences the wettability of the growing media in a negative way (Fig. 10). From the non-linear regression it becomes evident that variations in wettability of the growing media can be attributed to a high extent to differences in the affinities of the mineral surfaces for aromatic DOM compounds. Most probably the hydrophilic behaviour of the mineral surfaces is affected by the adsorbed organic compounds forming hydrophobic surface coatings, diminishing their positive effect on the wettability.

Conclusions on rewettability

It was shown that the absorption of aromatic organic compounds changes the hydrophilicity of clay mineral surfaces. The intermolecular interactions involved in the formation of hydrophobic coatings can be very complex. However, significant effects can be expected if specific properties of the dissolved organic matter is varied (molecular size, configuration and polarity or hydrophobicity) and also specific surface properties of the adsorbents (texture, mineralogical composition and the distribution of reactive functional groups). Additionally, the properties of the organic and inorganic reactants can be affected by aqueous phase processes (e. g. hydrolysis, hydration, dissolution, and precipitation). Here the composition and properties of the aqueous solution (e. g. pH, ionic strength, presence of bridging-cations or competitive anions) have to be considered as well.

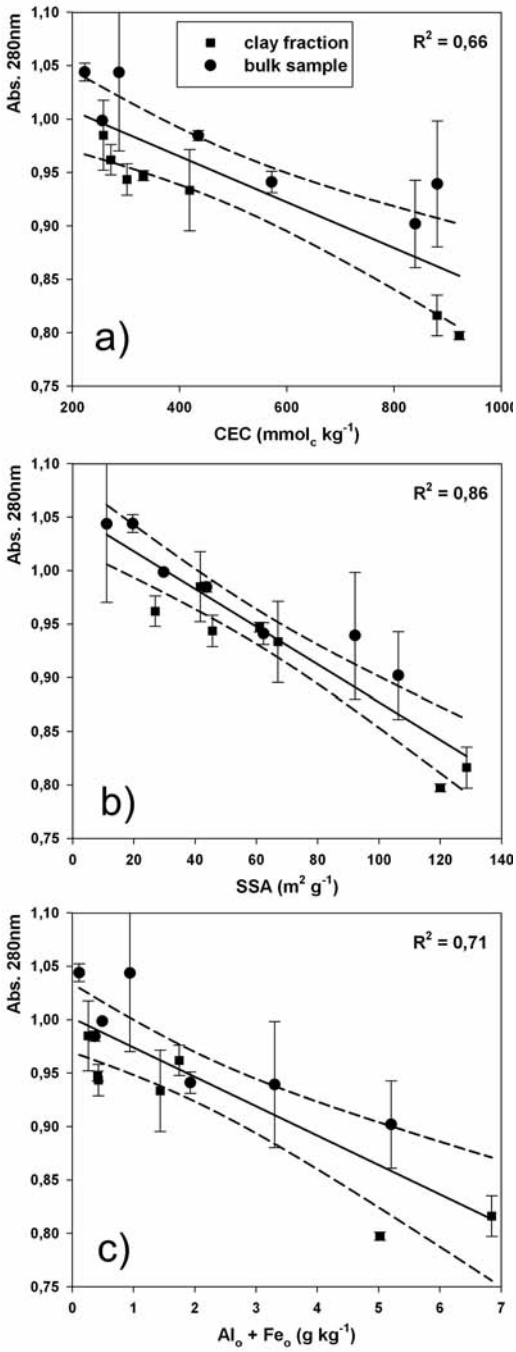

Figure 9: UV-Vis light absorbance values of the equilibrium solutions after batch adsorption experiment. Note, a decrease in the Abs_{280}-values indicates a high removal of peat derived aromatic organic substances due to sorption onto mineral surfaces. Abs_{280}-values are shown in relation to mineral properties a) CEC, b) SSA and c) oxalate soluble Fe and Al. The dashed line is the 95% confidence interval of the linear regression (solid line).

For instance, *Tarchitzky et al.* (2000) explained the role of polyvalent cations for water repellency with the enhanced formation of coatings on mineral surfaces, resulting in a reduction of the hydrophilic reactivity. Additionally it has

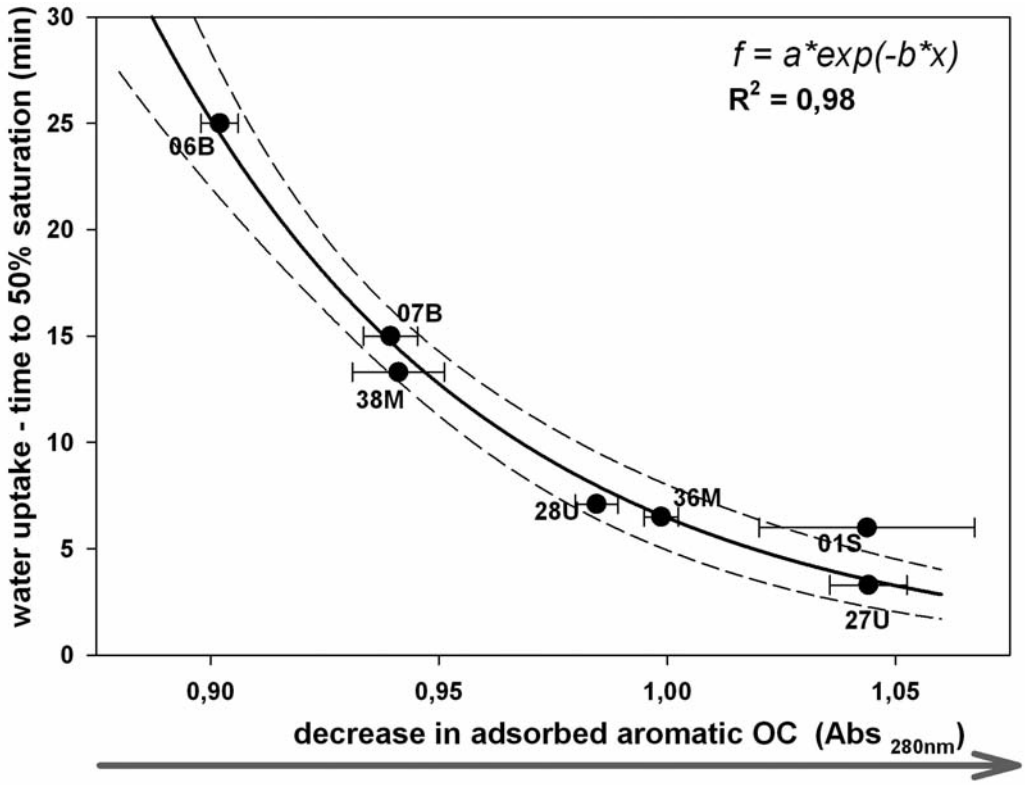

Figure 10: Water uptake of growing media amended with different clays in relation to the adsorption of aromatic compounds from peat derived DOM. The measure for the absorption of aromatic organic compounds from the equilibrium solution is the absorbance at 280 nm.

been suggested by *Hurraß and Schaumann (2006)* that bridges by polyvalent cations may cause an aggregation of the humic substances tht would also result in a lower wettability.

The results of our study show that the observed differences in rewettability can be mainly attributed to the extent and kind of organic coatings on the mineral surfaces. Obviously the formation of these coatings relies on differences in the sorption properties of the minerals and, in turn on distinct mineral properties. Mineral amendments containing expandable clay minerals with high CEC and SSA (e. g. smectites) and amendments rich in amorphous Fe and Al compounds seem to be less effective, due to their high affinity for peat derived DOM, especially for hydrophobic DOM constituents (Fig. 11). Accordingly, an addition of non-expandable clays with lower SSA, CEC and amorphous oxide content (e.g. kaolinite and illite) seems more promising.

P buffering capacity

The nine selected clays differed clearly in their P binding capacity and content of $\sum Fe_{ox}+Al_{ox}$ (Fig. 12). The P binding of the clays correlated positively with the $\sum Fe_{ox}+Al_{ox}$, but could not fully explain the whole variation in P fixation. It is assumed that the surface of the oxides differs widely, which will be investigated in further experiments.

After ten weeks cultivation the varied P fertigation resulted in clear differences in plant growth and quality among the treatments and growing media.

Without P fertigation the elongation of shoots was reduced in pure white peat and the two clays with low P binding capacity 04S and 01S, compared to peat/clay blends containing clay 06B and 39W. Also P fertigation increased internode length in these blends (Fig. 13). The same trend was observed in plant diameter and height (data not shown).

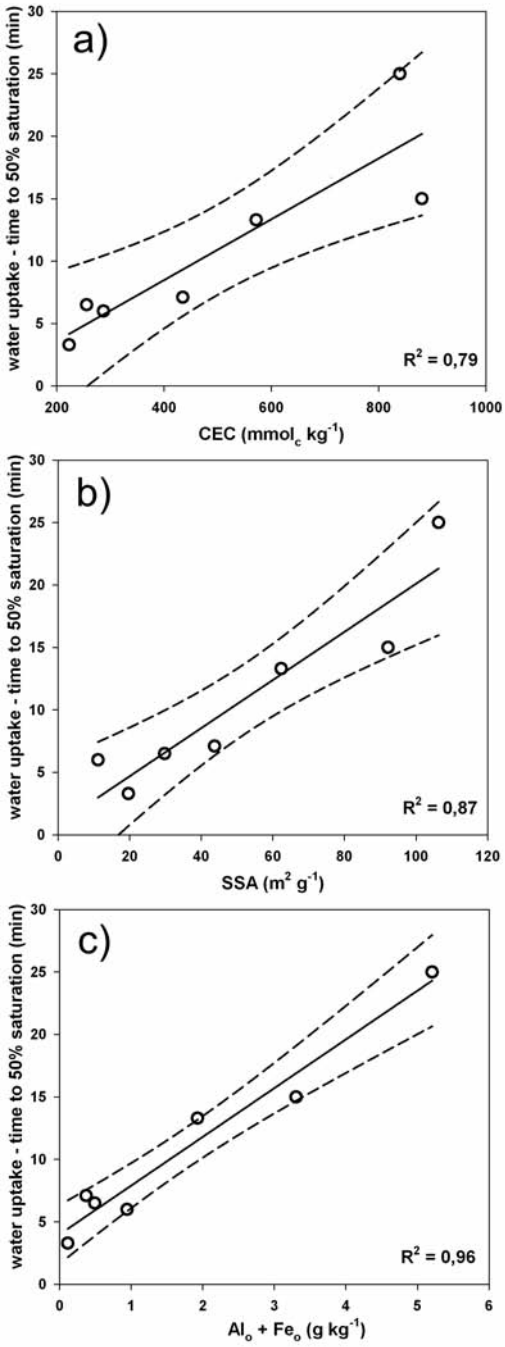

Figure 11: Water uptake of peat-based growing media mixtures amended with different clays with an amount of 30 kg m^{-3} and its relation to mineral properties a) CEC, b) SSA and c) oxalate soluble Fe and Al. Dashed line is the 95% confidence interval of the linear regression (solid line).

In all growing media the dry matter yield of the plants not fertigated with P was reduced compared to those receiving P. Without P fertigation yield of treatments in pure white peat and in the peat /clay blend 04S was lower than in the other three peat/clay mixtures (Fig. 14).

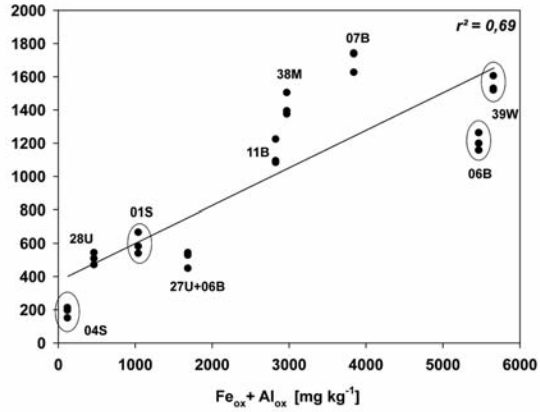

Figure 12: Relationship between the content of oxalate soluble Fe and Al and the P binding of nine different clays in a batch experiment with a P supply of 10000 mg kg^{-1}. Marked clays were used in the plant experiment.

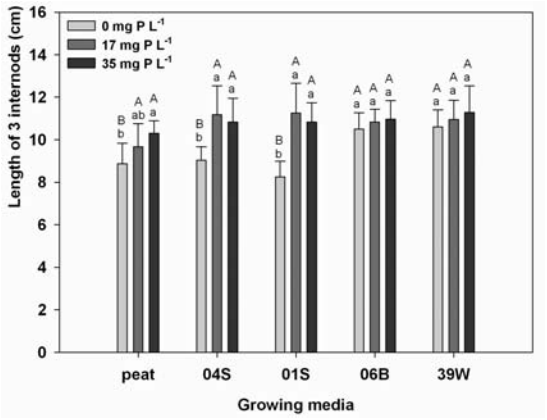

Figure 13: Length of internodes of Impatiens walleriana depending on growing media type and P conc. in fertigation solution. Different capital letters indicate significant differences between growing media at the same P fertigation level and different small letters indicate significant differences between fertigation treatments (p<0.05).

The increasing P supply via fertigation resulted in increased P conc. in plant d.m. in all growing media. Without P fertigation, P concentration in shoot d.m. was the lowest in treatment pure white peat and the peat/clay blend 04S and the highest P concentration was obtained in the treatment 06B. The same differences between growing media were observed with fertigation concentration 17 mg P L^{-1} solution, but no longer at the highest P fertigation level (Fig. 15).

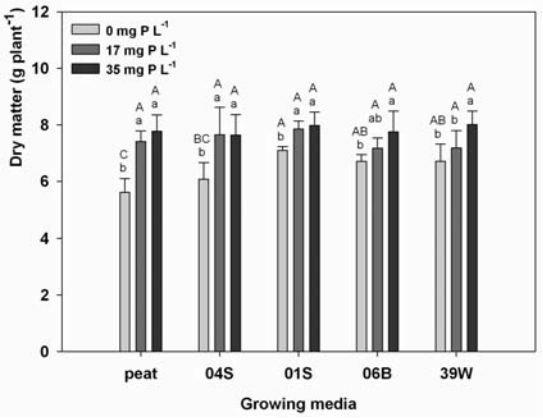

Figure 14: Dry matter of Impatiens walleriana depending on growing media type and P conc. in fertigation solution. Different capital letters indicate significant differences between growing media at the same P fertigation level and different small letters indicate significant differences between fertigation treatments ($p<0.05$).

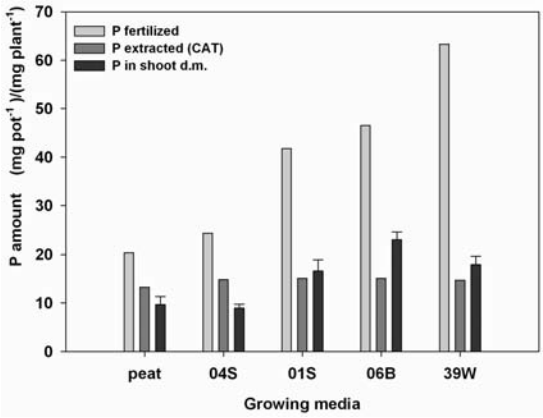

Figure 16: Amounts of fertilized and CAT-extractable P per plant container (0.6 L growing media) and P contained in shoot d.m. of Impatiens walleriana depending on growing media type.

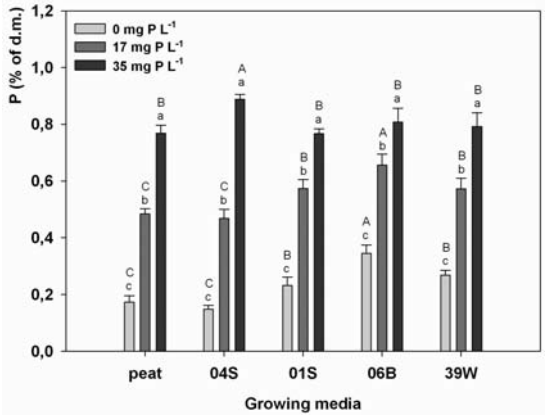

Figure 15: Phosphorus conc. in d.m. of Impatiens walleriana depending on growing media type and P conc. in fertigation solution. Different capital letters indicate significant differences between growing media at the same P fertigation level and different small letters indicate significant differences between fertigation treatments ($p<0.05$).

To characterize the capacity of different clays to supply P to plants the P amount contained in shoot d.m. was calculated for the treatment without P fertigation (Fig. 16). The clays 01S, 06B and 39W supplied about twice as much P to plants compared to pure peat and peat/clay blend 04S. In the latter treatments plants did not exhaust the P amount determined by CAT extraction whereas in the other treatments even more P was taken up than characterized as plant available by the extraction. In all growing media more P was fertilized than determined as plant available or taken up in shoot d.m., which was more pronounced in blends with clays having a high binding capacity (01S, 06B and 39W). At the same CAT level, in this case 25 mg/L growing medium, peat/clay blends containing clay with a high P binding capacity supplied more P to plants indicating the capacity to buffer fluctuating P supply. In horticultural practice P availability in growing media is characterized by CAT extraction procedure.

Conclusions on P buffering capacity

The P binding capacity of clays was strongly correlated with the oxalate extractable Fe and Al content. However, this factor did not fully explain the observed variability. Low availability of P reduced internode length and supported compaction of plants. But at the same time d.m. production was decreased indicating that shortage of P is not a successful strategy to produce more compact and better shaped plants. Peat-clay blends containing clay with a high P binding capacity provided up to twice as much P to plants than those with a lower binding capacity, thus buffering fluctuations in P uptake and P fertigation. The common extraction procedure for horticultural growing media tended to underestimate the plant available P in peat-clay blends with high binding capacity. To improve the understanding of P binding of clays specific surface of oxides will be investigated.

References

Alt, D. & Peters, I. (1992) Die $CaCl_2$/DTPA- Methode zur Untersuchung gärtnerischer Erden auf Mengen- und Spurenelemente. Agribiol. Res. 45, 204-214.

Chenu, C., Le Bissonnais, Y. & Arrouays, D. (2000) Organic matter influence on clay wettability and soil aggregate stability. Soil Sci. Soc. Am. J. 64, 1479-1486.

Chin, Y.P., Aiken, G. & O'Loughlin E. (1994) Molecular weight, polydispersity, and spectroscopic properties of aquatic humic substances. Environ. Sci.Technol. 28, 1853-1858.

Doerr, S.H., Shakesby, R.A. & Walsh, R.P.D. (2000) Soil water repellency: its causes, characteristics and hydro-geomorphological significance. Earth-Science Reviews 51, 33-65.

Dombrowski, I. & Schenk, M.K. (2010) Manganese toxicity in peat/clay blends used as growing media? Conf. »Genetics of Plant Mineral Nutrition«, Deutsche Gesellschaft für Pflanzenernährung, Abstract Book p. 62.

Feng, X., Simpson, A.J. & Simpson, M.J. (2005) Chemical and mineralogical controls on humic acid sorption to clay mineral surfaces. Organic Geochemistry 36, 1553–1566.

Hurraß, J. & Schaumann, G.E. (2006) Properties of soil organic matter and aqueous extracts of actually water repellent and wettable soil samples. Geoderma 132, 222-139.

Kahle, M., Kleber, M. & Jahn, R. (2004) Retention of dissolved organic matter by phyllosilicate and soil clay fractions in relation to mineral properties. Organic Geochemistry 35, 269-276.

Kaiser, K. & Guggenberger, G. (2000) The role of DOM sorption to mineral surfaces in the preservation or organic matter in soils. Organic Geochemistry 31, 711-725.

Lichner, L., Dlapa, P., Doerr, S.H. & Mataix-Solera, J. (2006) Evaluation of different clay minerals as additives for soil water repellency alleviation. Appl. Clay Sci. 31, 238-248.

Marschner, H. (1995) Mineral nutrition of higher plants. 2nd ed. Academic Press, London, UK.

McKissock, I., Gilkes, R.J. & Walker E.L. (2002) The reduction of water repellency by added clay is influenced by clay and soil properties. Appl. Clay Sci. 20, 225-241.

Michel, J.C., Riviere, L.M. & Bellon-Fontaine, M.N. (2001) Measurement of the wettability of organic materials in relation to water content by the capillary rise method. European Journal of Soil Science 52, 459-467.

Mikutta, R., Kleber, M. & Jahn, R. (2005) Poorly crystalline minerals protect organic carbon in clay subfractions from acid subsoil horizons. Geoderma 128, 106-115.

Schmilewski, G. (2008) The role of peat in assuring the quality of growing media. Mires and Peat 3, 1-8.

Tarchitzky, J., Hatcher, P.G. & Chen, Y. (2000) Properties and distribution of humic substances and inorganic structure-stabilizing components in particle-size fractions of cultivated Mediterranean soils. Soil Sci. 165, 328– 342.

VDLUFA, 1991. Bestimmung der Rohdichte (Volumengewicht) von gärtnerischen Erden und Substraten ohne sperrige Komponenten. VDLUFA Methodenbuch, Band 1. Die Untersuchung von Böden. 4. Auflage, VDLUFA Verlag, Darmstadt.

Verhagen, J.B.G.M. (2004) Effectiveness of clay in peat based growing media. Acta Hort. 644, 115-122.

Walsch, J.& Dultz, S. (2010) Improving the wettability of peat based growing media by the amendment of clay. Acta Mineralogica-Petrographica Abstract Series 6, 5th Mid-European Clay Conference, Budapest, Hungary, p. 85.

SURFTRAP - Development and Optimisation of a Process to Biosynthesize Reactive Iron Mineral Surfaces for Water Treatment Purposes

Peiffer S.*, Paikaray S., Damian Ch. (1), Janneck E., Ehinger S., Martin M. (2), Schlömann M., Wiacek C., Kipry J., (3), Schmahl W., Pentcheva R., Otte K., Götz A., Wang Z., Hsieh K. (4), Meyer J., Schöne G. (5), Koch T. (6), Ziegler A. (7), Burghardt D. (8)

(1) Department of Hydrology, University of Bayreuth, Universitätsstraße 30, D-95440 Bayreuth

(2) GEOS Ingenieurgesellschaft mbH, Gewerbepark »Schwarze Kiefern«, D-09633 Halsbrücke

(3) Department of Environmental Microbiology, Tech. University of Freiberg, Leipziger Str. 29, D-09599 Freiberg

(4) Department of Earth and Environmental Science, Section Crystallography, University of Munich, D-80333 Munich

(5) Wismut GmbH, 09117 Chemnitz

(6) Vattenfall Europe Mining AG, 03050 Cottbus

(7) Central Facility for Electron Microscopy, University of Ulm, 89069 Ulm, Germany

(8) Institute for Groundwater Management, Technical University of Dresden, 01062 Dresden

*Coordinator of the project

1. Introduction

In this project we aim to develop a low-cost technology to remove ionic constituents from raw waters such as arsenic species. The proposed technology is based on the reactivity of schwertmannite, an oxyhydroxosulfate of the mean stochiometry $Fe_8O_8(OH)_6SO_4$ (molar mass 772.89 g/mol). This mineral typically forms in acidic and sulfate rich mine waters as a secondary mineral upon oxidation of Fe(II) in a biologically mediated process. Schwertmannite can be generated in a biotechnological process after aeration of mining process waters. It forms surface-rich aggregates of needle-like nanocrystals. It rapidly transforms into ferric hydroxides of high specific surface area once exposed to water containing at least some alkalinity. Our rationale follows the concept to make use of this transformation reaction by adding biosynthesized schwertmannite to contaminated raw waters where it generates a large sorption capacity to remove the pollutants (*Peiffer et al., 2008*).

2. Materials and Methods

2.1. Microbial Investigations

2.1.1. Depth profile of activity of microorganisms in schwertmannite

A Schwertmannite core from the carrier material of the pilot plant was collected with a hollow drill and cutted into 0.5 cm layers (volume of each layer=1.7 cm^3). The mineral was dissolved with 0.2 M oxalic acid and the cells

Table1: 16S rRNA probes used for FISH analyses

Probe	Target	Probe sequence (5'-3')	Reference
BSC0459_deg	*Ferrovum myxofaciens*	TCCAGRTTATTCGCCTGA	modified by Hallberg et al., 2006
GALTS0084	*Gallionella* TrefC4	CCACTAACCTGGGAGCAA	Hallberg et al., 2006
Helper 1	Upstream of GALTS0084	GATATATTACTCACCCGTTCG	Hallberg et al., 2006
Helper 2	Downstream of GALTS0084	GCCCCCAGGCCCGTTCGA	Hallberg et al., 2006

were washed with 1x PBS buffer. The resuspended cells were analysed with the LIVE/DEAD® BacLight™ Bacterial Viability Kit (Invitrogen, L13152) and FISH (fluorescence in situ hybridisation). The FISH analyses were performed after *Hallberg et al.* (2006) with probes for Ferrovum myxofaciens and Gallionella TrefC4 (tab. 1).

2.1.2 Biologic Analysis / Interface Bacteria – Mineral

We investigated samples from cultures of the species *Leptospirillum ferrooxidans*. To investigate the interface between mineral and organic matter the organic matter had to be fixated. This was done by physical (high pressure cryo-fixation) and chemical methods (2.5 % glutardialdehyde/2.0 % paraformaldehyde mixture in 0.2 M cacodylate butter (pH 4.5)). Several steps for drying and contrasting followed. The fixated samples were embedded in Epon and cut into 70 nm thick sections with a DIATOM diamond knife on a microtome for the TEM. For the SEM work, the samples were critical point dried and coated with platinum. Samples were taken from two positions: from the sediment and from a bioactive TERMINOX foil.

2.2 Schwertmannit generation

The designed pilot plant consists of an oxidation basin with removable growth carriers as well as an aeration and a precipitation tank. The overall volume is about 10.5 m³ and the oxidation basin has a capacity of 8.14 m³. Due to the high flow rate of the circulation pump (approximately 30 m³/h) low gradients of process parameters can be guaranteed. The water inflow is intensively aerated. A chain cleaner assembled at the bottom of the oxidation basin removes dropping schwertmannite to the sludge colllecting channel. From there the sludge is pumped to a storage tank where the sludge can sediment and thicken. The thickened sludge can be recycled to the oxidation basin or pumped into big bags for dewatering by gravity.

From the chemical engineering point of view, the designed pilot plant is a hybrid type of bioreactor. It has physical characteristics of a fixed-bed reactor in parallel with a circulation reactor. The advantages of this special reactor design are avoiding plugs in the fixed-bed (growth carrier) and a free circulation inside the oxidation basin.

The pilot plant was operated continuously since the start of the project.

2.3. Mineralogical and Structural Analysis

2.3.1. Mineral analysis

The crystal structure of the prepared precipitates (see below) was examined by XRD. XRD measurements were performed on a Stoe powder diffractometer and on an Oxford Diffraction area detector diffractometer, both using Mo-kα_1 radiation. Scanning electron microscope (SEM) analyses of the biologic samples were performed with a Hitachi S-5200 field emission scanning electron microscope equipped with an EDX and a STEM detector. For the SE-pictures an accelerating voltage of 4kV was used and for the EDX and STEM analyses 20kV was employed. SEM pictures of the mineral samples were taken on a JEOL 6500 F SEM with 5kV accelerating voltage.

Specific surface areas were measured by Brunauer-Emmett-Teller (BET) method (*Brunauer et al., 1938*) using a FlowSorb II 2300 (Fa. Micromeritics) and N_2/Ar (80 %/20 %) as adsorbate.

Different methods from literature to produce schwertmannite were compared. The first method was published by *Bigham et al. 1990*: 2L of MilliQ water were heated to 60 °C and 10.8 g of $FeCl_3$*$6H_2O$ and 3 g of Na_2SO_4 were added. The solution was kept at 60 °C for 12 minutes. The orange suspension was then placed in a dialysis bag and dialyzed against MilliQ water. The water was changed daily during a period of 33 days. The precipitate was then filtered and vacuum dried. This sample will be referred to as dialyzed schwertmannite. A second recipe originates from Pentinghouse and was first published by *Regenspurg et al. 2004*: 5 g of $FeSO_4$ was dissolved in 1L of distilled water. Then 5 mL of H_2O_2 (32 %) were added. The solution became brown-red, and after only few minutes, a rust-colored precipitate could be observed. After 24 h of ripening in solution at 25 °C the obtained material was vacuum-

dried. We will refer to that material as fast-H_2O_2-schwertmannite. The method of Pentinghouse was also applied in a modified way. H_2O_2 (0.03%) was pumped over 24 h continuously (flow rate: 5 mL/h) to 100 mL culture media iFe containing 25 mM ferrous iron (*Johnson and Hallberg, 2007*). The synthesis was performed at 30 °C. After the ferrous iron oxidation and the precipitation the precipitate was harvested by centrifugation (6000 g, 15 min) and freeze dried. The samples will be called slow H_2O_2-schwertmannite. A third recipe was described by *Loan et al.* (2004) and samples were synthesized in a slightly modified way with 2.5 g of $Fe_2(SO_4)_3 \bullet xH_2O$ that was dissolved in 500 ml of MilliQ water in glass bottle and stored at 85 °C for 24 hours. The precipitate was vacuum dried and this sample will be referred to as 85 °C-schwertmannite.

2.3.2. XAS

XAS experiments were conducted at the SUL-X beamline at ANKA synchrotron facility in Karlsruhe, Germany. The investigated samples were synthesized by the dialyses bag method described above but initial solutions were modified by addition of arsenate, chromate or vanadate to replace sulfate. Samples were prepared with concentrations of 1.65 mmol (16.5 %), 2.5 mmol (25 %), 5 mmol (50 %) and 10 mmol (100 %), respectively, the percentage indicates the ratio of heavy metal to sulfate. Goethite and lepidocrocite samples were synthesized as references and exposed to solutions of arsenate, chromate or vanadate respectively. The solutions for the chromate standards contained 0.7 mM, 2 mM and 10 mM chromate, 1 mM and 5 mM arsenate and 1 mM vanadate, respectively.

2.3.3. Density functional theory (DFT) calculations

Using systematic density functional theory (DFT) calculations we study the structural, energetic, and sorption properties of schwertmannite as well as goethite(101), akaganeite(100), and lepidocrocite(010) surfaces with different terminations. The exchange and correlation potential is treated within the LDA/GGA+U approach which is explicitly suitable for the strongly correlated FeOOH system.

2.4. Schwertmannite Transformation and Arsenic Adsorption

2.4.1. SchwertmanniteTranformation tests

Stability experiments were carried out for four months using 5 g/L (equivalent to 7.75 mmol/L SO_4^{2-}) sediment load in milli-Q water using polypropylene reactor vials with regular shaking (4-5 times per day) at room temperature and atmospheric pressure. The system was investigated at four different pH conditions, i.e., 5.0, 6.0, 7.0 and 8.0. The pH adjustments were done with NaOH/HCl prior to addition of schwertmannite samples. Due to release of protons in the course of ageing processes (equation 2), additional pH adjustments were done daily using 1.0 N NaOH and the amount of NaOH consumed was noted. Samples were collected at regular intervals for four months. Similar stabilization experiments were conducted at pH 3.0, i.e., within the stability range of schwertmannite (pH 3-4.5) to distinguish the role of higher pH on the fate of sulfate. The solid phase was separated by filtration and oven dried at 60 °C.

2.4.2. As(III)-Schwertmannite interactions

Three different schwertmannite (SHM) specimens produced through chemical and biological processes were used in the current study. SHM_MS was synthesized in a mine water treatment plant (GEOS, Freiberg, Germany) by microbial oxidation of Fe(II) between pH 2.9-3.2 (*Glombitza et al., 2007*) from SO_4^{2-} rich mine waters. One schwertmannite sample was synthesized by fast synthesis method called »oxidative synthesis« as described by *Regenspurg and Peiffer* (2005). 10 g of $FeSO_4.*7H_2O$ was dissolved in deionized water and ~ 5 ml of 32% H_2O_2 was added drop wise to accelerate the oxidation of Fe^{2+} to Fe^{3+}. The reaction was preceded for 24 hours and the pH remained stable at 2.4. The precipitated orange coloured solids were filtered and oven dried at 35-40 °C. The samples were used directly for further experimental purposes without any treatment, cal-

led here after SHM_FS. Schwertmannite was also synthesised as described by *Bigham et al.* (1990) The specimen is called SHM_DS.

The sorption studies were conducted as batch experiments. The suspension was allowed to equilibrate for 5 days with a sediment load of 0.25 g/25 ml at pH 3.0 and initial As(III) concentrations ranging from 0.13 to 1.33 mmol/L. Preliminary kinetic experiments demonstrated that equilibrium is achieved after this time. The suspension was continuously stirred during the whole reaction time. The pH of the As(III) containing solutions were adjusted to pH 3.0±0.05 before addition of schwertmannite to avoid possible transformation of SHM at changing pH conditions (*Jönsson et al., 2005*). The ionic strength was maintained at 0.01 mol/L by $NaNO_3$. Experiments were performed in the dark in the presence of oxygen in polypropylene reactor vials that were preconditioned by 10 % nitric acid overnight. After the equilibration time samples were filtered through < 0.45 µm cellulose filter papers and the aqueous phase was analyzed for pH, Fe(II), Fe(t), SO_4^{2-} and As(t) concentrations. Solid phase was characterized by XRD, FTIR, SEM and XANES techniques. Solid phase arsenic loading was determined by mass balance ($CS=(C_i-C_{eq})*V/M$), where C_i and C^{eq} are initial and equilibrium As concentrations (mol/L), M is mass of sorbent (g), L is volume of solution (L). SHM samples were stored in crimp sealed serum vials in O_2 free glove box to eliminate the effect of atmospheric O_2 in As(III) oxidation during storage for As species measurement by XANES.

Two commonly used statistical isotherm models were fitted with experimental data using IsoFit v1.2 (*Matott and Rabideau, 2008*) to evaluate the sorption behavior. Langmuir model (Eq. 1) demonstrates a monolayer sorption mechanism with homogeneous sorption energies, while Freundlich model is an empirical model demonstrating multilayer sorption sites and heterogeneous sorption energies (Eq. 2) (*Weber and DiGiano, 1996*).

2.4.3. Dumping Experiments with Arsenic-loaded Schwertmannite/Transformation products

Long-term experiments were set up to study the development of the chemical bonding between the species and schwertmannite or schwertmannite transformation products upon ageing in order to test their deposition properties. Periodically, the desorption of arsenic by synthetic rainwater (pH 5, elution 1d/month, B-tests) or groundwater (pH 7, continuous elution, C-tests) was analysed. The »groundwater« was effluent water (< 0.1 mg As/L, <0.2 mg U/L) of the water treatment plant in Schlema-Alberoda (table 2). As summarized in table 5, five different »dumping sceniaros« were investigated. Each test contains 9g mineral precipitate and was eluted periodically or continuously by 10 mL water. The experiments will be accompanied by XAS (X-Ray-Absorption-Spectroscopy) and EXAFS studies, results were already open.

2.4.4. Laboratory experiments for pilot test preparation

Following to SHM transformation and As-Adsorption experiments from the last year, a other test was performed in duplicate. Therein, brown coal filter ash (FA) (co. the neutralization was used instead of the conventional dosage of lime milk. 1 L influent water from the water treatment plant in Schlema-Alberoda (average composition see table 2) was acidified by 0.1M HCl and air-stripped for 30 minutes in order to eliminate inorganic carbon. After filtration (0,2 µm cellulose acetate), FA (about 0.15 g/L as 0.5% FA-water suspension) and SHM (42.6 mg/L according to 20 mg Fe/L as 2 % SHM-water suspension) was added subsequently in order to distinguish between arsenic, uranium and radium immobilization to FA

$$c_s = c(s_{tot})\frac{K_{Ads}c_{eq}}{(1+K_{Ads}c_{eq})} \quad \text{(Eq.1)}$$

$$c_s = K_F \cdot C_{eq}^{\ n} \quad \text{(Eq.2)}$$

c_s = concentration of As(III) adsorbed at the solid phase (mol/g)
c_{eq} = equilibrium concentration of As(III) in the aqueous phase (mol/L)
$c(s_{tot})$ = total concentration of surface sites (mol/g)
K_{Ads} = Langmuir sorption coefficient (L/mol)
n = Freundlich exponent (≤ 1)
K_F = Freundlich adsorption coefficient (Ln/(moln-1 g))

Table 2: Selected parameters of the Schlema-Alberoda treatment plant's inflow (*May 2010*)

pH	redox potential	electric conductivity	Cl	SO_4	HCO_3	Fe(tot)	As	U	^{226}Ra
[-]	[mV]	[µS/cm]	[mg/L]						[mBq/L]
6,95	+/-0	2300	55	760	630	5	1.0	2.0	1700

Table 3: Overview of previously performed pilot test campaigns

Cam-paign	date	flow rate	schwermannite			pH-buffering agent
		m^3/h	sample	pre-conditioning	dosage (mg Fe/L)	
1	21.-23.10.09	0.5-0.75	S2-013	neutralized with lime milk	48	lime milk
2	10.-13.11.09	0.94-0.91	S2-013	neutralized with lime milk	25	lime milk
3	23.-26.11.09	0.93-0.88	S2-013	untreated	21	lime milk
4	09.-12.02.09	0.93	S2-015	untreated	(1.4)-36	lime milk
5	10.-19.03.10	0.90 – 0.70	S2-015	untreated	2.7 -25	lime milk
6a	06.-07.04.10	0.95	-	-	0 (blank)	lime milk
6b	07.-16.04.10	0.95 – 0.80	S2-001	untreated	9.8 - 22	lime milk
7	11.-20.08.10	1.00	S2-013	untreated	17-26	brown coal filter ash

and SHM. Samples were filtered by 0,2 µm cellulose acetate and acidified before AAS, ICP-OES as well as γ-spectrometry analysis.

2.5. Pilot test for removal of arsenic from mine water

The schwertmannite produced in the pilot plant Tzschelln was used to enhance the arsenic removal from mine water in the abandoned uranium mine of Schlema-Alberoda (East Germany). The uranium mine water has to be purified from iron, arsenic, uranium and radium, iron and manganese. The installed treatment technology is described by *Meyer, et al. (2009)*. The average composition of mine water inflow is shown in table 2.

The required limit of arsenic for discharging into the river Mulde is ≤ 0.1-0.3 mg/L (dependent on flow rate of the Zwickauer Mulde river). The naturally occurring iron concentration is not sufficient for complete arsenic removal or to meet the prescribed maximum value. Thus it was investigated, whether it is possible to enhance the arsenic removal by dosing SHM as a diluted aqueous suspension.
The pilot plant was constructed in a building of the mine water treatment plant of the Wismut at Schlema and consists of a precipitation tank, a flocculation tank and an inclined clarifier. A flow chart of the pilot plant is shown in figure 1. A data logger records the pH in the precipitation tank and enables adjustment of pH by controlling a peristaltic pump to dose lime milk. Table 3 summarized main parameters of the last seven pilot campaigns.

The water to be treated in the pilot plant is taken from the inflow of the mine water treatment plant after the acidification and CO_2 stripping stage.
Until now three schwertmannite samples were applied: two wet filtered aggregate samples and one dried sample from the pilot plant at Tzschelln. The schwertmannite is suspended in process water and stored in a tank with agita-

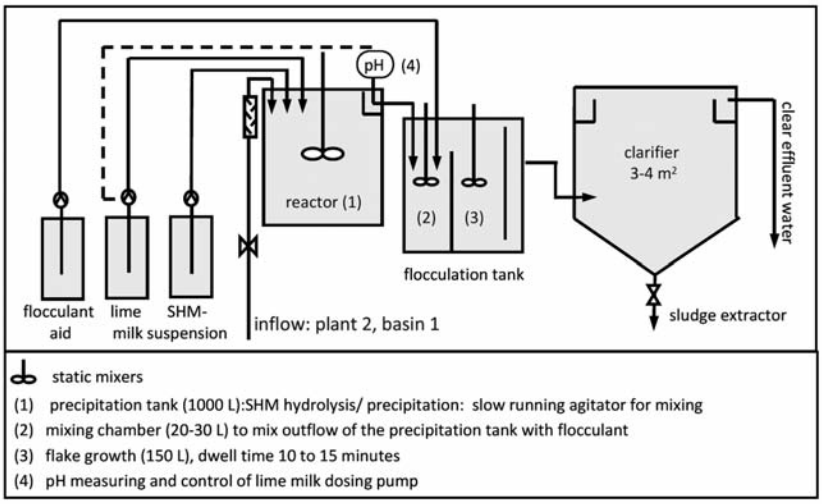

Figure 1: Flow chart of the mine water treatment pilot plant

tor. In the first pilot experiments the schwertmannite was pre-hydrolysized by adding lime milk to the storage tank until pH 8. Schwertmannite suspension with 5 wt% of solids led to plugging of the dosing tube. Dilution to 1 wt% solved the problem.

Lime milk and a flocculant are taken from the storage tanks of the mine water treatment plant. With a peristaltic pump the schwertmannite suspension is dosed into the precipitation tank. Lime milk is dosed simultanously to adjust pH to 7.5. Subsequently the water flows to the flocculation tank where the polymer flocculant is dosed. In this tank precipitates are transformed to flocks. In the following inclined clarifier these flocks are sedimented. The overflow of the clarifier goes back into the main treatment plant.

To monitor the treatment process inflow and outflow of the pilot plant were analyzed for total arsenic, iron and uranium. In the outflow, dissolved concentrations were determined, too. The sludge from the clarifier was analysed for uranium and arsenic and investigated by a sedimentation test.

3. Results and Discussion

3.1. Microbial Investigations

3.1.1. Bacterial activity and diversity in the schwertmannite deposits

For a stable process of schwertmannite generation the number and activity of iron oxidizing bacteria play a key role in the pilot plant. Because bacteria are present in the water as well as in the schwertmannite that is deposited on the carrier material a recirculation of precipitated schwertmannite could stabilize the process and increase the oxidation rate if the bacterial cell numbers are high in the mineral phase.

To obtain detailed information about the activity and diversity of bacteria in the schwertmannite a depth profile was prepared and the microbial cells were analysed with a Bacterial Viability Kit and FISH analyses. A 4-week old 2 cm thick sample core was cut into 4 layers, where layer 0-0.5 cm represented the youngest (water facing) layer.

The first data indicate a decreasing total cell number with increasing depth (Fig.2). $3x10^6$ cells were detected in the first layer (0-0.5 cm) and $1.4x10^6$ cells in the deepest layer (1.5-2.0 cm). More than 40 % of the cells in the first centimetre were found to be viable. In the deepest layer more than 30 % of the cells were still alive. This trend could be observed in material from different water depth.

To obtain information about the microbial community structure in the different layers the samples were investigated with FISH probes for *Ferrovum myxofaciens* and *Gallionella* TrefC4. Figure 3 shows the dominance of *Ferrovum myxofaciens* which reaches 25 to 36 % of the

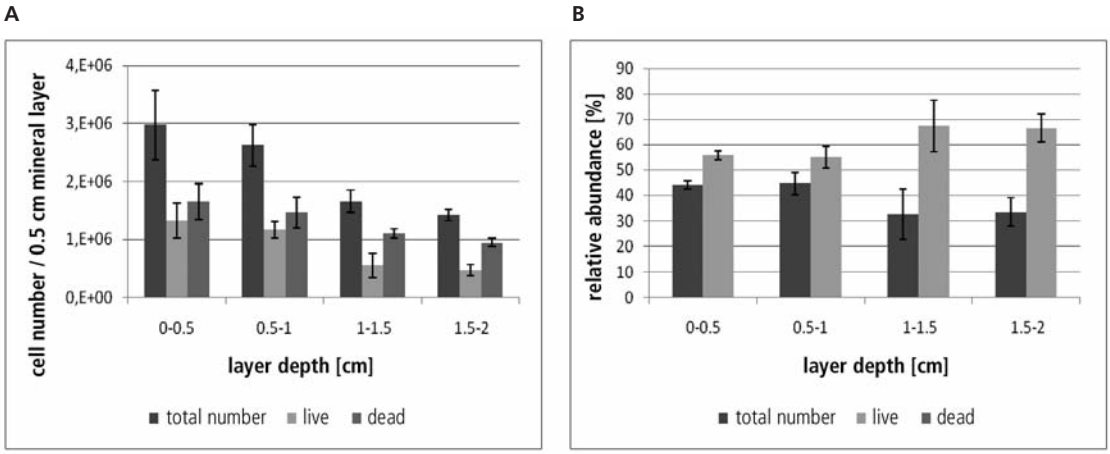

Figure 2: **A** cell number of total, living and dead cell per mineral layer, **B** relative abundance of living and dead cells in correlation to the depth of schwertmannite deposit on carrier material

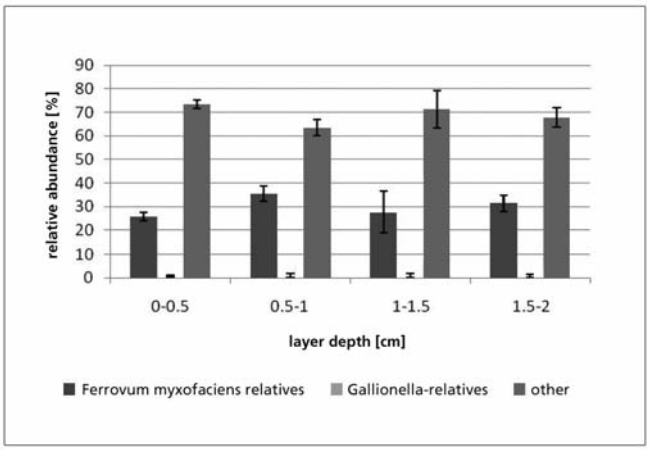

Figure 3: relative abundance of *Ferrovum myxofaciens* and *Gallionella* TrefC4 in correlation to the depth of schwertmannite deposit on carrier material

microbial community. In contrast to this approximately only 1% of the microbial cells were detected as *Gallionella* TrefC4 cells.

Previous investigations of the microbial community from water of the pilot plant demonstrated, that relatives of *Ferrovum myxofaciens* and *Gallionella* are the main species with a percentage of the total microbial community up to 90% (*Heinzel et al. 2009*).The differences may be due to the use of different methods for the analyses. For example T-RFLP, used by *Heinzel et al.* (2009), analyses the relative composition of PCR-amplified 16S rRNA gene fragments. In contrast to this, the microscopic FISH approach to quantify cells by fluorescent DNA probe is a direct method that avoids the PCR amplification. PCR amplification has been shown to produce artifacts in microbial diversity (*Acinas et al. 2005*).

This problem of comparison between FISH-based and PCR-based analyses is also supported by our initial results from first TRFLP analyses of the same samples that indicate that *Ferrovum myxofaciens* comprises up to 90% of the total bacterial cells (data not shown). More analyses have to been done to quantify the microbial diversity and activity and to give a suggestion which part of the schwertmannite deposit should recirculate.

3.1.2 Biologic Analysis / Interface Bacteria – Mineral

Ferris et al. (2004) put forward the theory that schwertmannite hedge hogs (globular aggregates with concentrically surrounded by schwertmannite whiskers) are overgrown bacteria. Our TEM analyses of microtome sections showed that these hedge hogs are in fact massive and that no sign of overgrown cells are in inside these aggregations (Fig. 4). Furthermore no direct connection of bacteria and mineral could be found. Instead traces of EPS (extra-

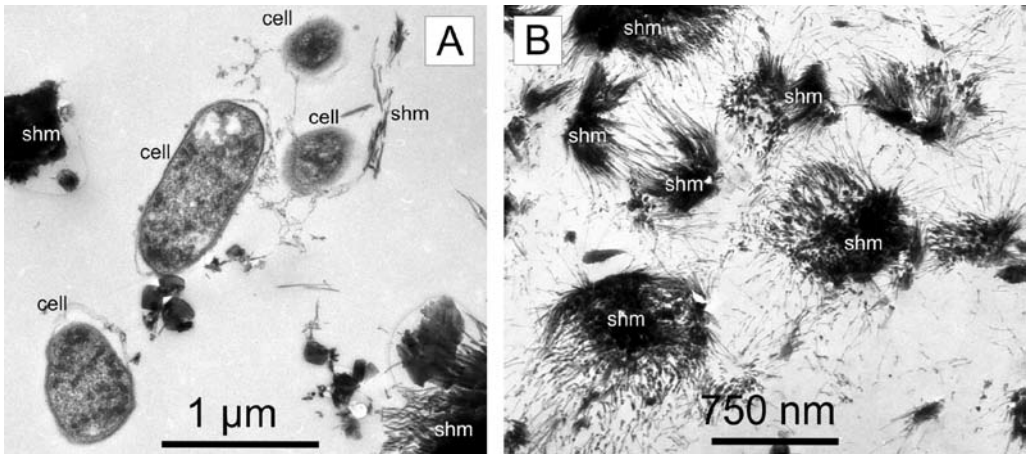

Figure 4: TEM images from cultures of *Leptospirillum ferrooxidans*. **A** Two cells that are surrounded by EPS. The schwertmannite whiskers in that sample are not connected directly to the cell but to the EPS. **B** Sections through schwertmannite hedge hogs. They are of massive nature and no signs of an overgrown cell can be found in the center

cellular polymeric substance) are present in the samples that connect mineral and cell. We assume that the EPS is a seed for the precipitation of schwertmannite to prevent lethal cell overgrowth. This hypothesis is underlined by the results of section 3.3.2. where we show that schwertmannite whiskers form if the oxidation of iron happens slowly, irrespective of a biotic or abiotic environment.

3.2. Schwertmannite Generation: Estimation of the oxidation capacity

The microbially enhanced oxidation process in the pilot plant occurs both on the surface of the biofilm carriers and in the free volume of the oxidation basin. The oxidation rate is influenced by various parameters, e.g. oxygen supply, pH, temperature, sludge circulation, composition of the inflowing mine water and surface area of the biofilm carrier. At technical scale only the sludge circulation and the amounts of carriers can be used to accelerate the oxidation rate. So in a first step the oxidation rate was determined in the pilot plant at different surface areas of the growth carrier. In these experiments the oxidation rate was calculated according to Eq. (3) from the total amount of ferric iron (Fe(III)ges) formed during microbial oxidation and the residence time τ. The results are presented in figure 5. By drawing the oxidation rate as a function of A_F/V_R ratio it was possible to distinguish $\nu_{Ox\text{-}F}$ and $\nu_{Ox\text{-}V}$ and to estimate these values.

Fig. 6 shows the oxidation rate of the pilot plant according eq. (1). Oxidation rates in the range of 10 – 40 g/(m³h) were achieved. The overall value was in the range of 20 – 25 g/(m³h).

$$\nu_{ox} = \frac{Fe(III)_{ges}}{\tau} = \frac{Fe(III)_{ges}}{v_R} \cdot Q_{zu} = \nu_{ox-F} \cdot \frac{A_F}{V_R} + \nu_{ox-V} \quad \left[\frac{g}{m^3 \cdot h}\right] \qquad \text{(Eq.3)}$$

(Eq.3)

A_F	Surface of the growth carriers and all other surfaces inside the reactor	[m²]
$Fe(III)_{ges}$	Total amount of ferric iron formed by microbial oxidation	[g/m³]
Q_{Zu}	Inflow	[m³/h]
V_R	Reactor volume	[m³]
ν_{Ox}	Total (overall) oxidation rate	[g/(m³·h)]
$\nu_{Ox\text{-}F}$	Oxidation rate caused by oxidation at the carrier	[g/(m²·h)]
$\nu_{Ox\text{-}V}$	Oxidation rate caused by oxidation in free reactor volume	[g/(m³·h)]

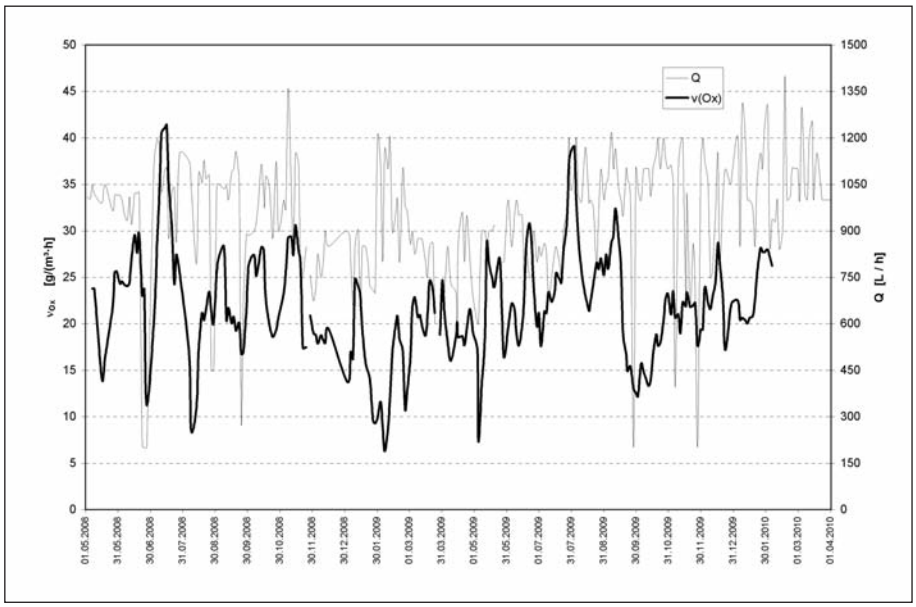

Figure 6: Oxidation rate and throughput of the pilot plant at Tzschelln until April 2010

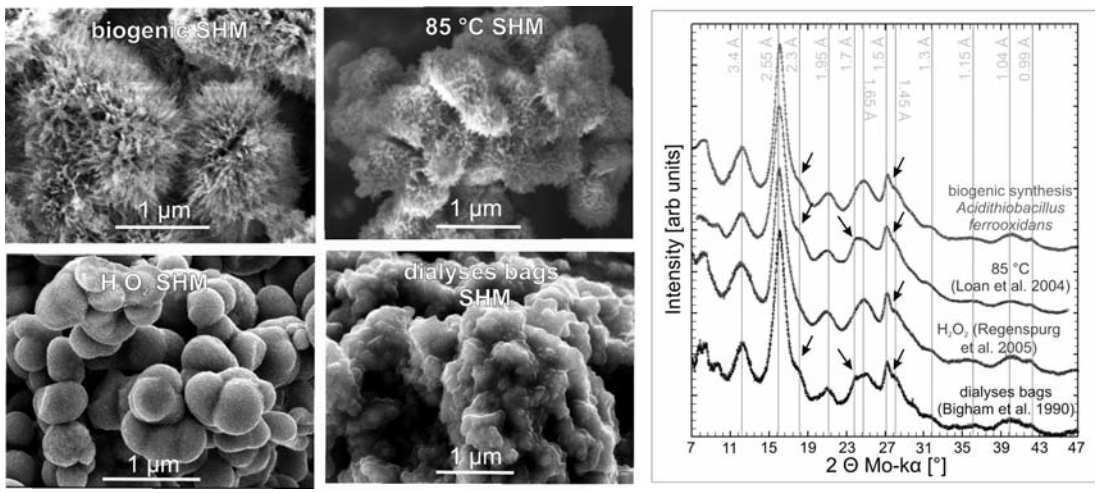

Figure 7: Left: Exemplary SEM pictures of schwertmannite precipitated by different methods. The typical schwertmannite hedge hog morphology is present in the biogenic schwertmannite (produced in the pilot plant) and the schwertmannite synthesized abiotically at 85 °C. Right: diffractograms of synthesized samples. All show the typical schwertmannite reflections, however, the products differ regarding the intensity ratio between several peaks (e.g. 1.5 Å vs. 1.45 Å, intensity of shoulder at 2.3 Å) as well as regarding the peak width.

The influence of the flow-rate on the oxidation performance of the pilot plant was discussed in detail in the Science Report 2009 (*Peiffer et al., 2009*).

3.3. Mineralogical and Structural Analysis

3.3.1. Schwertmannite structure

The morphology of the schwertmannite depends on the way of synthesis. Samples that were synthesized with H_2O_2 consist of round spheres whereas samples that were produced by bacterial oxidation showed the characteristic whiskers. Samples synthesized in an inorganic but slow way showed a third variety. Exemplary SEM pictures are shown in Fig. 7. Samples synthetised by a slow oxidation with diluted H_2O_2 also showed whiskers indicating that the whiskers form in environments with slower oxidation processes and not specifically

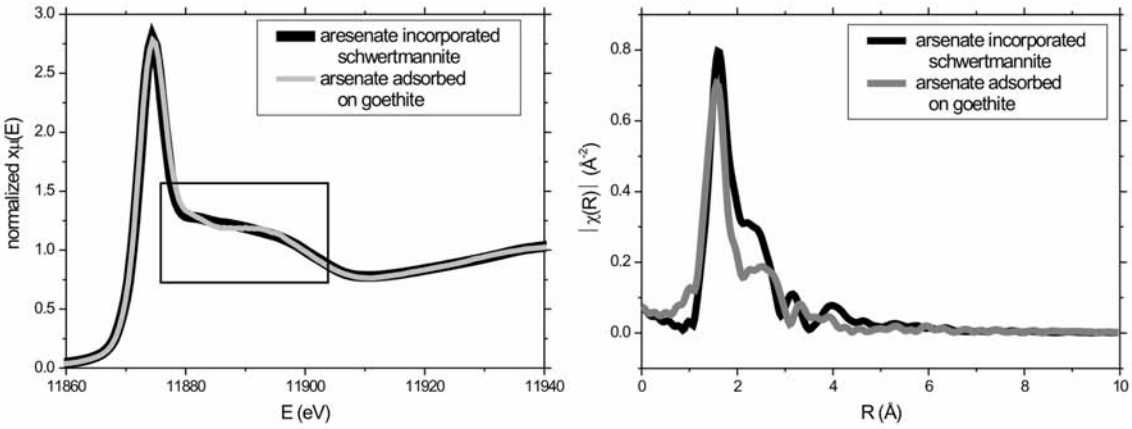

Figure 8: Representative examples of As K-edge EXAFS spectra of representative examples of aresenate adsorbed on goethite (grey) and incorporated in schwertmannite (black). The left graph shows a magnification of the XANES region. Please note the differences between goethite and schwertmannite in the marked box. The graphs on the right show the radial distribution function. Whereas the first coordination sphere (As-O) is the same in both samples the second (shoulder between 2 and 3 Å) and third (between 3 and 4 Å) coordination sphere is closer to the central atom indicating a stronger bond.

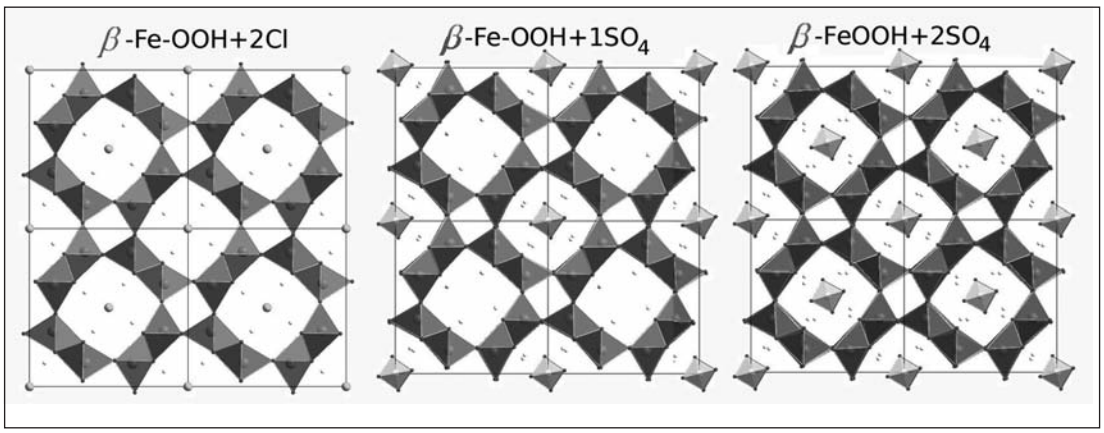

Figure 9: Akaganeite with interstitial ions

due to biotic/organic influence. The XRD measurement on the 2D detector allowed precise analyses of the different synthesized schwertmannites in finite time. Even though the specimens show similar diffraction patterns there are distinct variations in intensity and peak width. Also additional reflections appear in some samples (Fig. 1). This indicates that the »schwertmannites« are not one homogeneous phase but a mixture. This raises the demand for a reproducible method to synthesize pure schwertmannite.

3.3.2. XAS

The evaluation of XAS data is ongoing work. Preliminary results on the As K-edge spectra of arsenic adsorbed to lepidocrocite and goethite are essentially identical independent of As concentration and of the adsorbant. Also the As K-edge spectra of schwertmannite are identical for different concentrations of As. Anyhow, a comparison of the spectra and the radial distribution function of both materials, the standards and the co-precipitated schwertmannites, shows that arsenate absorbed in schwertmannite is bonded more closely, and therefore more strongly, to the iron than the arsenate adsorbed on goethite and lepidocrocite surfaces (Fig. 8).

3.3.3. Results DFT: Bulk FeOOH polymorphs and bulk schwertmannite

Our work on the bulk properties of the FeOOH polymorphs goethite (α), akaganeite (β), lepi-

docrocite (γ), and the high pressure phase (ε) was recently published in Physical Review B (*Otte 2009*). The energetic relations among the phases reveal that the framework structures (α, β, ε) are more favorable than the layered one (γ). The schwertmannite structure is considered akin to akaganeite where additional interstitial sulfate ions are added in the channels, see Fig. 9. Because schwertmannite is synthesized in Cl- containing solution, we consider as a starting point Cl atoms in the akaganeite channels. We find that the Cl-ions widen the channels. As Cl is singly negatively charged, we have explored the role of introducing a background charge of the whole simulation cell to model correctly the electronic properties.

Table 4:

β-FeOOH+	**1SO_4**	**2Cl**	**2SO_4**
V_0 [Å^3/f.u.]	42.54 [+1%]	42.33 [+0.5%]	42.96 [+2%]
$E_{sorption}$[eV]	-0.195	-0.265	-0.092

Furthermore, we explore the bonding mechanisms of SO_4^{2-}. We find that the channels adapt to the ions in the middle of the channels. However, this adjustment of the framework is connected with a high energy cost. The sorption energy of the system can be determined per formula unit and unit cell (f.u./u.c.) as

$$E_{Sorption}=E_{System}-E_{\beta\text{-}FeOOH}-E_{Ion} \quad \text{(Equ.4)}$$

where negative values correspond to an exothermic reaction. The absolute value sorption energy decreases with increasing sulfate concentration: The lowest absolute value of $E_{Sorption}$ =-0.092 eV is obtained fort the highest sulfate concentration (every akaganeite channel is occupied by sulfate ions) where the strongest distortion of the akaganeite framework occurs (table 4). The sum formula of schwertmannite Fe16O16(OH)16-2n(SO4)n (n=1-3) according to (Bigham 1994) allows for an even higher sulfate concentration in exchange with hydroxyl groups. Therefore, further bonding mechanisms (mono- and bidentate) are currently under investigation.
A further task under investigation is the sorption of As(V). As an even larger molecule, it is found to cause a stronger distortion of the framework. The sulfate-arsenate exchange is a further aspect we are currently working on.

Sorption on the FeOOH surfaces

The FeOOH polymorphs have high surface areas and high sorption affinities for aqueous solutes (*Cornell 2001*). The transformation product after arsenate incorporation in schwertmannite is expected to be a FeOOH polymorph. Various terminations of the most prominent and relevant surfaces in sorption reactions, goethite(101), akaganeite(100), and lepidocrocite (010), are modeled. Prior to studying adsorp-

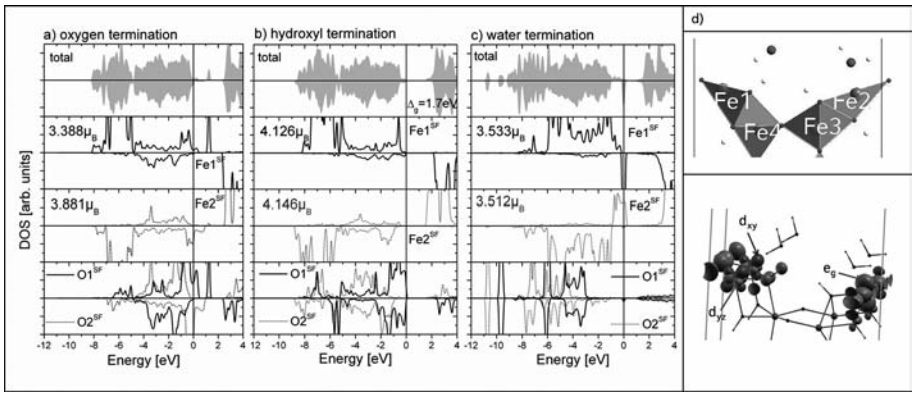

Figure 10: Density of states (a-c) and spin density plot (d) of β-FeOOH (100)-surface

tion processes it is important to understand the properties of the clean surfaces. Oxygen, hydroxyl and water terminations are considered to model different pH conditions.

Indeed, we find that the surface termination impacts strongly the oxidation state of the Fe at the surface as displayed in Fig. 10 for akaganeite(100). The deprotonated oxygen termination (basic condition, Fig. 10a) leads to a reduction of the surface iron, Fe^{SF}, and the respective magnetic moments, MFe, are reduced. The hydroxyl termination with all iron in Fe^{3+} and a band gap of 1.7eV (Fig. 10b) is closest to bulk behavior. For a water termination which represents an acid environment, (Fig. 10c), the Fe^{SF} are reduced to Fe^{2+} and a breaking of FeO_6 octahedra at the surface occurs.

The spin density plot (Fig. 10d) integrated around the Fermi level for the water termination reveals that the $Fe1^{SF}$ is reduced with a 6^{th} partially occupied d_{xy} orbital, while for $Fe2^{SF}$ the one spin channel is fully and a 6^{th} electron appears in the opposite spin channel with partially filled e_g-states at the Fermi level. Similar properties are obtained for goethite(101) and lepidocrocite(010), but are not displayed here. Ongoing work focuses on the adsorption of arsenate on these relaxed surface terminations.

3.4. Schwertmannite Transformation and Arsenic Adsorption

3.4.1. Transformation of schwertmannite

Long term exposure of schwertmannite to pH values between 5 and 8 for 4 months at normal atmospheric condition leads a sulfate release, which increased with time and pH up to roughly 1.40 mmol/g solid phase, corresponding to 90 % of total initial sulfate, after 4 months of exposure at pH 8 (Fig.11). The higher SO_4^{2-} release at elevated pH is probably due to the direct exchange of OH^- for the SO_4^{2-} ion at the schwertmannite surface, while faster SO_4^{2-} release during initial days may be due to release of surface-adsorbed SO_4^{2-}.

3.4.2. As(III)-schwertmannite interactions

A detailed understanding on As(III)-schwertmannite interaction in acidic medium which will foster attempts to remove As(III) with this mineral was obtained. Schwertmannites turned out to be able to remove significant fractions of As(III) (> 97 %) from contaminated water, the efficiency of which strongly depends on surface area and synthesis pathway. The different synthesis products, produced through biotical and abiotical synthesis pathways differ in their physical and chemical properties including morphology, dissolution rate, surface area and crystallinity which strongly affects the

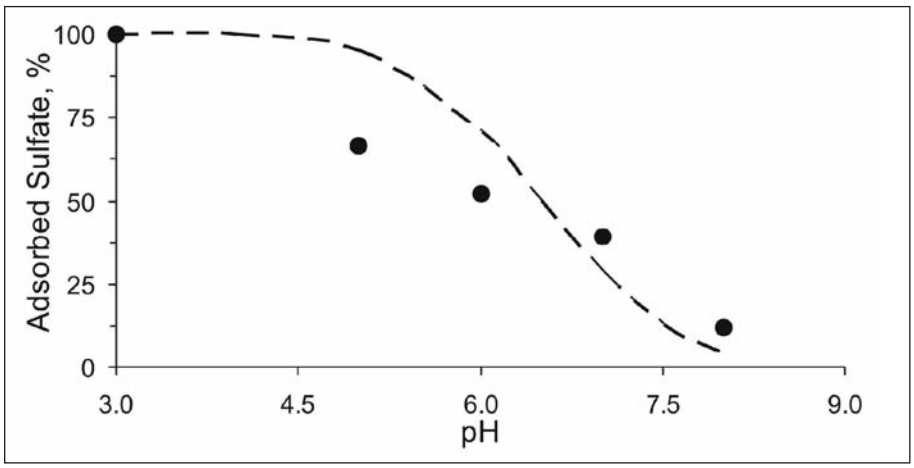

Figure 11: PHREEQC modelled (lines) SO_4^{2-} adsorption profile by schwertmannite at different pH values. The experimentally observed values at pH 5, 6, 7 and 8 after 120 days are shown as filled circles.

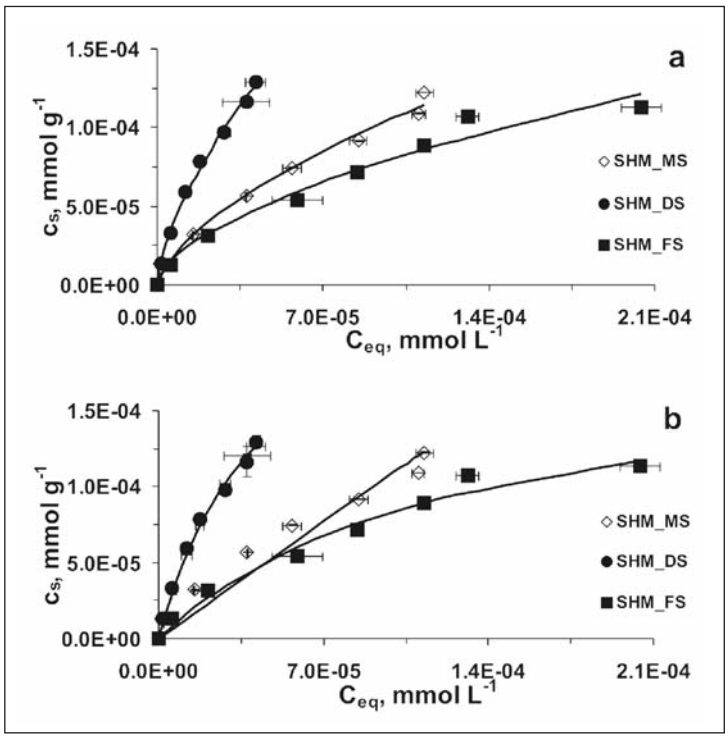

Figure12: Freundlich (a) and Langmuir (b) sorption model fits to the experimental data. Solid lines repre-sent model predicted sorbed As(III), while experimental data are shown by filled and open symbols.

Table 5: Arsenic mobilization under different dumping scenarios

Scenario	1 (blank)		2 (blank)		3		4		5	
	dumping of uncontamined SHM		dumping of un-contamined SHM-transformation product		dumping of **As** loaded **SHM**		dumping of **As** loaded **SHM transformation product**		dumping of **As** and **U** loaded **SHM transformation product**	
As adsorbed (mol As/ mol SHM)	0.00016		0.00016		0.02535		0.02557		0.02250	
test	**1B**	**1C**	**2B**	**2C**	**3B**	**3C**	**4B**	**4C**	**5B**	**5C**
arsenic elution by / time	rainwater (pH 5) 1d/month	ground-water (pH 7)	rainwater (pH 5) 1d/month	ground-water (pH 7)	rainwater (pH 5) 1d/month	ground-water (pH 7)	rainwater (pH 5) 1d/month	ground-water (pH 7)	rainwater (pH 5) 1d/month	ground-water (pH 7)
49 d	0.24%	0,00%	0,17%		**1.38%**	0.07%	0,02%	0,00%	0,00%	0,00%
78 d	0,17%	0,00%	0,00%	0,00%	**1.00%**	0,05%	0,02%	0,00%	0,00%	0,00%
106 d	0,00%	0,00%	0,07%	0,00%	**1.22%**	0,04%	0,02%	0,00%	0,00%	0,00%
140 d	0,09%	0,00%	0,06%	0,00%	**1,44%**	0,02%	0,02%	0,00%	0,00%	0,00%

sorption behaviour of As(III) (Fig.12).

Our findings suggests the occurrence of two removal mechanisms: 1) ligand exchange with surface adsorbed SO_4^{2-} which appears to be of minor relevance as indicated by the absence of any particular trend in SO_4^{2-} release in case of SHM_FS, and the weak SO_4^{2-} release in case of SHM_DS inspite the highest As(III) uptake and SSA of the three specimens and 2) formation of amorphous As(III)-Fe(III)-SO_4^{2-} precipitates at higher aqueous As concentrations as indicated by increased diffraction intensity proportionally with the As(III) loading and the appearance of new IR bands. These amorphous surface precipitates may stabilize sorbed As(III) towards surface oxidation. Most of the aqueous As(III) appeared to sorb through the second mechanism.

3.4.3. Dumping experiments with As-loaded SHM – samples

The relative amounts (%) of mobilized arsenic by periodical eluation with rain water (pH 5, B-

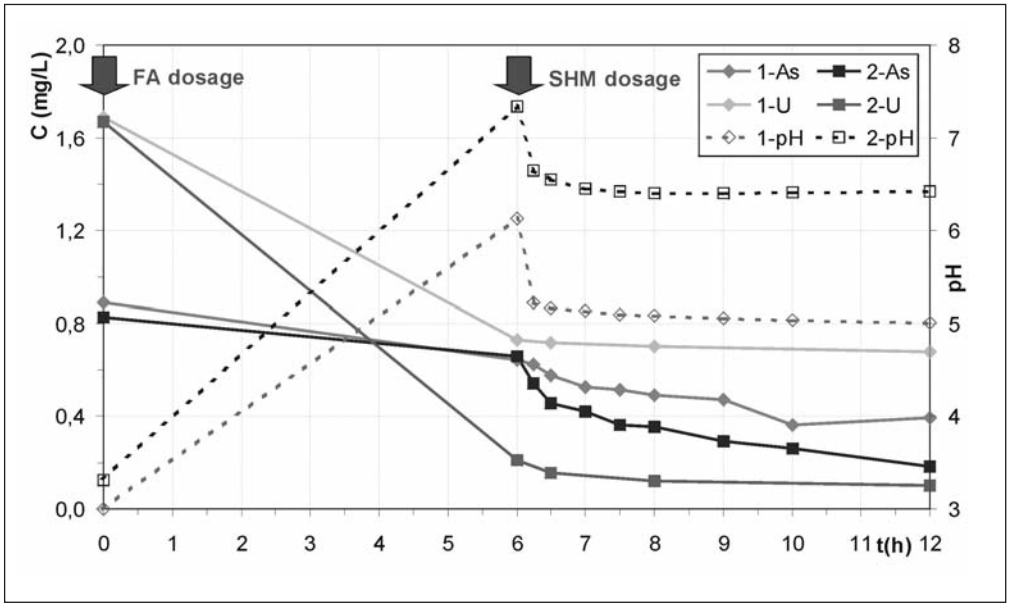

Figure 13: Arsenic and uranium elimination in batch tests, where FA was used as neutralizing agent

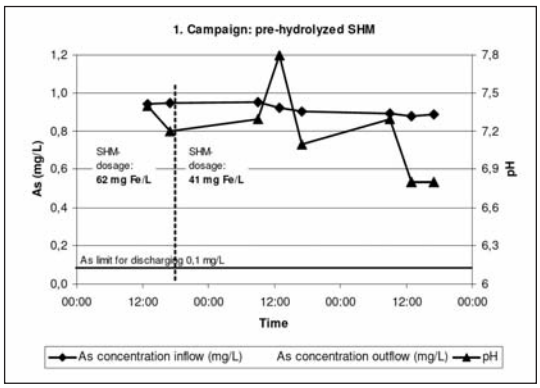

Figure 14: Comparison of As concentration of inflow and outflow (pre-hydrolyzed SHM, 62 and 41 mg Fe/L)

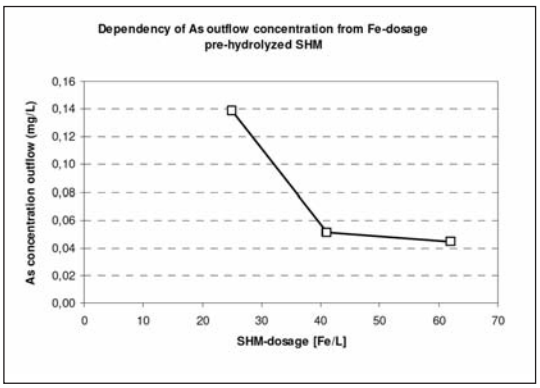

Figure 15: Residual As concentration depending from SHM dosage (pre-hydrolyzed SHM)

tets) or continuous elution with groundwater (pH 7) were summarized in table 5. Actually (after 140 days), a significant arsenic mobilization was only detectable in test 3B, a periodical elution of As-loaded Schwertmannit with rain water.

3.4.4. Laboratory experiments for pilot test preparation

Fig. 13 shows the promising results of the first batch tests, where brown coal filter ash (FA) was used instead of lime milk for the neutralisation of the acidic process water of the water treatment plant in Schlema-Alberoda. Six hours after the addition of 0.21 g/L (test 1) and 0.16 g/L (test 2) FA addition, 0.22 mg As/L and 0.96 mg U/L could be immobilized in test 1 (pH6,13), 0.17 mg As/L and 1.46 mg U/L in SHM/L (20 mg Fe/L) was added to each test. Six hours later, a total of 0.49 mg As/L, 1.01 mg U/L and about 1000 mBq ^{226}Ra/L were eliminated in test 1 (pH 5.01), a total of 0.64 mg As/L, 1.57 mg U/L and about 930 mBq ^{226}Ra/L in test 2 (pH 6.42).

3.5. Pilot test for removal of arsenic from mine water

As mentioned above the required limit of As for discharging into the river Mulde is $\leq$ 0.1 0.3 mg/L (dependent on flow rate of the Zwickauer Mulde river). The naturally occurring iron concentration is not sufficient for complete arsenic removal or to meet the prescribed maximum

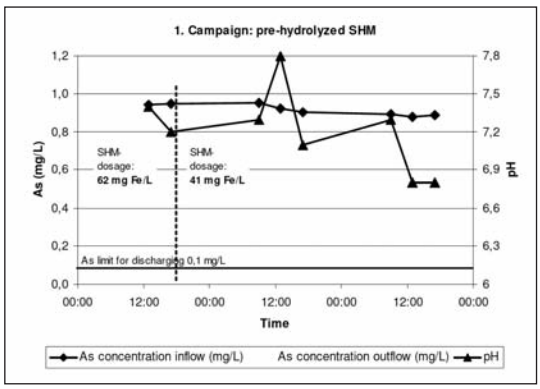

Figure 16: Comparison of As concentration of inflow and outflow (untreated SHM, 21 mg Fe/L)

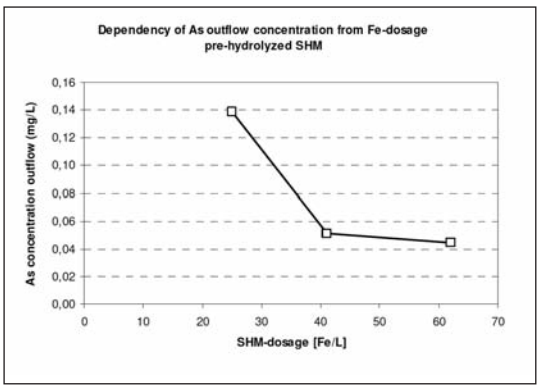

Figure 17: Enhancement of arsenic removal by dosage of schwertmannite suspension

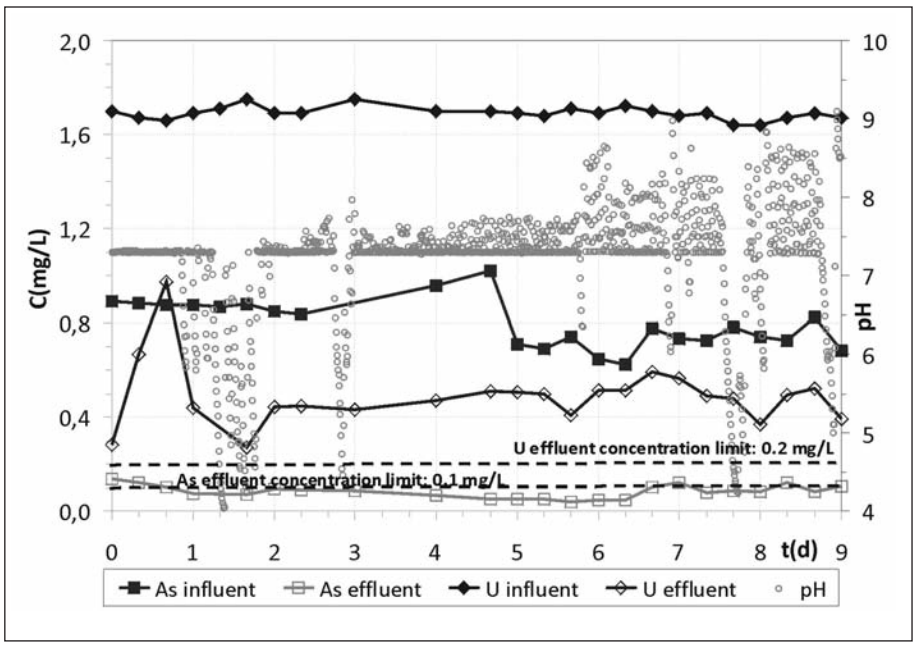

Figure 18: Arsenic and Uranium elimination during the pilot test campaign 7

value. The main results of the pilot tests are shown in fig. 14 to 17. Fig. 14 shows the results of the first pilot experiment with pre-hydrolyzed SHM. Pre-hydrolysis was applied because lab scale investigations of the revealed that the SHM transformation at high sulfate concentrations, as in the Schlema-Alberoda mine water, is delayed. In order to directly compare the performance of the two SHM varieties in the third pilot experiment untreated SHM was applied (fig. 16).

Surprisingly in the campaign with untreated SHM at comparable dosage a better As elimination was obtained. A dosage >30 mg Fe/L pre-hydrolyzed SHM was necessary to reach the limit for discharge of 0.1 mg As/L (Fig.15). With untreated SHM dosage of 21mg Fe/L was sufficient to reach this concentration. Fig 17 shows that, compared to As removal by the iron content of the mine water alone, it was possible to improve the arsenic removal from 60 % to nearly 90 % by dosing 20-40 mg/L Fe, and 35-70 mg/L SHM (dry mass) respectively.

Following to the promising results of the first batch tests with brown coal filter ash (FA) as neutralizing agent (chapter 3.4.4),pilot test campaign 7 was performed with FA dosage instead of lime milk. A suspension of 5 % FA and water of the river Mulde was used. This leads to an average, effective dosage of 0,15 g FA/L process water. The SHM-addition was

comparable with the foregoing campaigns (17-26 mg Fe/L). As shown in Fig.18, the required limit for discharging into the river Mulde could always be hold for arsenic. The averaged uranium elimination was 1,2 mg/L, probably due to a precipitation of Calciumuranate together with eluated Calcium from the FA.

4. References

Acinas, S. G., Sarma-Rupavtarm, R., Klepac-Ceraj, V. and Martin F. Polz (2005): PCR-Induced Sequence Artifacts and Bias: Insights from Comparison of Two 16S rRNA Clone Libraries Constructed from the Same Sample. Appl. Environ. Mircobiol 71:8966-8969.

Bigham et al., (1994) Mineral. Mag. 58: 641
Bigham, J. M., Schwertmann, U., Carlson, L., Murad, E. (1990): A poorly crystallized oxyhydroxysulfate of iron formed by bacterial oxidation of Fe(II) in acid mine water. Geochimica et Cosmochimica Acta, 54, 2743-2758.

Brunauer, S., P.H. Emmett and E. Teller (1938): Adsorption of gases in multimolecular layers. J. Am. Chem. Soc. 60: 309-19

Cornell and Schwertmann, (2001): Wiley-VCH GmBH & Co. KGaA, Weinheim, ISBN 3-527-30274-3

Ferris F. G., Hallbeck, L., Kennedy, C.B., Pedersen, K. (2004): Geochemistry of acidic Rio Tinto headwaters and role of bacteria in solid phase metal partitioning. Chemical Geology, 212, 291-300.

Glombitza, F., Janneck, E., Arnold, I., Rolland, W., Uhlmann, W.(2007): Eisenhydroxisulfate aus der Bergbauwasserbehandlung als Rohstoff. In: Heft 110 der Schriftenreihe der GDMB, S.31-40 ISBN 3-935797-35-4

Hallberg, K.B., K. Coupland, S. Kimura and D.B. Johnson (2006): Macroscopic streamer growths in acidic, metal-rich mine waters in north Wales consist of novel and remarkably simple bacterial communities. Appl. Environ. Mircobiol. 72(3): 2022-2030

Heinzel, E., E. Janneck, F. Glombitza, M. Schlömann and J. Seifert (2009): Population dynamics of iron-oxidizing communities in pilot plants for the treatment of acid mine waters. Environ. Sci. Technol. 43(16): 6138-6144

Janneck, E., (2008) Abschlussbericht FKZ: 01 RI05013; Teilprojekt 1: Koordination sowie Anlagenbetrieb und Produktherstellung

Loan, M., Cowley, J. M., Hart, R., Parkinson, G. M. (2004): Evidence on the structure of synthetic schwertmannite. American Mineralogist, 89, 1735-1742.

Otte, K., Pentcheva, R., Schmahl, W. W. and Rustad, J. R.; (2009): Pressure induced structural and electronic transitions in FeOOH from first principles, Phys. Rev. B 85, 205116

Peiffer, S., Burghardt, D., Janneck, E., Pinka, J., Schlömann, M., Wiacek, C., Seifert, J., Schmahl, W., Pentcheva, R., Meyer, J., Rolland, W. (2008) in: Geotechnologien Science Report No. 12, pp. 34-45; ISSN 1619-7399

Regenspurg, S., Peifer, S. (2005): Arsenate and chromate incorporation in schwertmannite. Applied Geochemistry, 20, 1226-1339.

MicroActiv - Optimization of water purification technology for arsenic and antimony scavenging by microbially-activated Fe-oxide minerals

Kersten M. (1)*, Bahr C. (5), Daus B. (4), Driehaus W. (5), Kappler A. (2), Karabacheva S. (1), Kolbe F. (4), Posth N. (2), Reich T.Y. (1), Schurk K. (3), Stanjek H. (3), Wennrich R. (4)

(1) Geosciences Institute, Johannes Gutenberg-University Mainz, kersten@uni-mainz.de

(2) Center for Applied Geosciences, University of Tübingen, andreas.kappler@uni-tuebingen.de

(3) Ton- und Grenzflächenmineralogie, RWTH Aachen, stanjek@iml.rwth-aachen.de

(4) Helmholtz Centre for Environmental Research – UFZ Leipzig, birgit.daus@ufz.de

(5) GEH Wasserchemie GmbH & Co. KG, Osnabrück, info@geh-wasserchemie.de

* Coordinator of the project

Abstract

The main research activity of this collaborative research effort is the optimization of water treatment technology on basis of granulated Fe hydroxides (= GFH, or in German GEH). GEH® is applied by the SME-Partner, the GEH Wasserchemie GmbH & Co. KG established in 1997 and now one of the leading providers of iron-based high-capacity adsorbents for use in fixed bed filter process. Over 2000 plants have yet been delivered into more than 20 countries worldwide. Main purpose is treatment of As- and Sb-tainted waters, providing e.g. in India more than half million people with treated tap water. GEH® is based on pure synthetic iron hydroxide (β-FeOOH, akaganeite) with a large effective surface area (>250 m²/g) and an adsorption capacity of up to 50 g/kg As if applied on waters containing only As. This enables a simple, low maintenance removal procedure with capacities of up to 300,000 bed volumes over years without producing hazardous As-loaded sludge to be costly deposited. The main practical problem is the yet less well understood efficiency degradation with different groundwater milieus; with more or less reduced bed volume capacity. Our experiments revealed that these effects are mainly due to competing inorganic oxyanion species (e.g., silicate). An open question to be solved for the SME partner was whether a specific biogenic functionalization of the surface may help in optimizing towards a more versatile and smooth filter technology, but our preliminary experiment results were not thus promising towards this task. Instead, we found a severe inhomogeneity in adsorption efficiency and competing effects by inorganic oxyanion species on an individual grain scale which may become unexpected and new key information how to improve on the GEH production process.

Introduction

Access to safe drinking water is now a basic human right and a critical component of effective policy for health protection. Due to its high toxicity at even low concentrations (in the µg/L range), arsenic is a cause for concern in many regions of the world. Millions of people in Southeast Asia are severely suffering from drinking As-tainted tap water which has become a national health disaster in some of these countries. Recently, arsenic contamination of shallow aquifers have been reported, e.g., for the northwestern Hetao Plain of Inner Mongolia, China, an arid region with slow groundwater flow and arsenic concentration up to 1000 µg/L.

This is particularly important as the risk of contamination to human health will increase because of increasing groundwater demand upon decreasing quality and availability of surface water in such arid regions. According to the World Health Organization the maximum concentration of arsenic allowed in drinking water is 10 µg/L. This is because long term exposure to arsenic can affect human health and mental development of children, among other possible adverse effects. The skin seems to be quite susceptible to the effects of chronic exposure of As via drinking water. Arsenic-induced skin lesions seem to be the most common and initial symptoms of arsenicosis (»blackfood disease«). Other manifestations include neurological effects, obstetric problems, high blood pressure, diabetes mellitus, diseases of the respiratory system and of blood vessels including cardiovascular, and cancers typically involving the skin, lung, and bladder (*Rahman et al. 2009*). If the contaminated groundwater is also used for irrigation, a second health risk via the food chain may be present. The global impact now makes it a top priority water quality issue, second in order to microbiological contamination. In SE Asia and China, many tube wells have been drilled into aquifers to avoid for the latter hazard, but as realized later at the price of the former problem. The magnitude of this human tragedy increasingly encountered will depend on the rate at which monitoring and mitigation programs can be implemented in the affected regions.

There are multiple factors that need to be accessed before choosing a solution for a suitable mitigation strategy once arsenic contaminated groundwater are found. Two categories of processes largely control arsenic mobility in aquifers: (1) solid-phase oxidation and dissolution reactions, and (2) adsorption and desorption reactions, mainly governed by the aquifer physicochemical conditions. For an option to mitigate safe drinking water in case of already installed tubewells, a variety of methods have been developed in the last years. Existing technologies for the removal of arsenic from contaminated water such as oxidation/precipitation, coagulation/coprecipitation, ion exchange, adsorption, etc. are well established, and have their merits and limitations. Efficient options are activated carbon and in particular iron oxide coated media (*Schmidt et al. 2008, Kersten and Vlasova 2009a*). Oxidation/adsorption reactions are influenced by physicochemical milieu conditions such as pH and redox state, but also presence of competing anions such as silicate and phosphate, and solid phase structural changes at the atomic level. An understanding of factors controlling the arsenic mobility and remediation options requires knowledge of the natural groundwater characteristics as well as abiotic and biotic surface reactions on a molecular or species scale. Any option has then to be evaluated and adopted to the physicochemical characteristics of the local groundwater sources in order to enhance their efficiency in field practice and to build trust for their wider acceptance and use. This has to be done for arsenic, but also other emerging oxyanion contaminants like antimonate and vanadate (Figure 1).

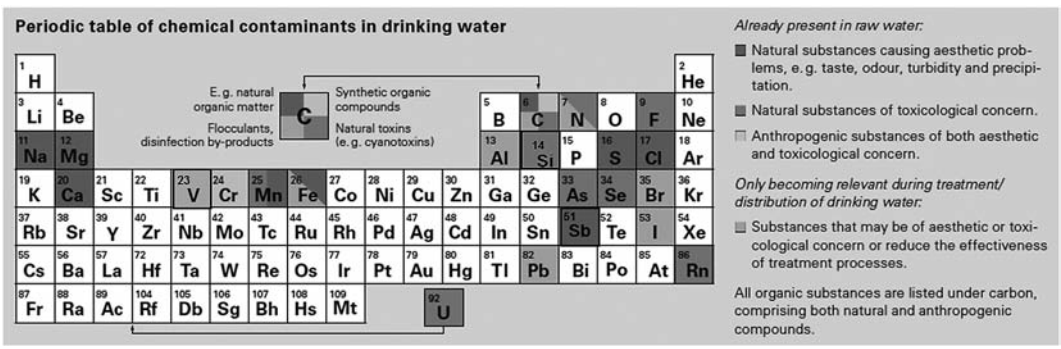

Figure 1: Major contaminants in groundwater used for producing tap water (modified after *Von Gunten 2008*).

Materials and Hypotheses

The groundwater treatment by various iron oxide media filter techniques achieve capacities which in practice depend on varying operation conditions, e.g. intermittent operation, but also if not predominantly on quality variations in the water treated. Breakthrough may occur much earlier than predicted, presumably as an effect of interfering water constituents. During a long-lasting practice with natural groundwater, the SME partner GEH Wasserchemie GmbH has observed complex competition relationships, such as even an antagonistic effect by Ca which may significantly mitigate the competing effect by silicate (*Smith and Edwards, 2005; Sperlich and Werner, 2005*). In principle, the adsorber columns are capable to provide for very long service lives - up to 300,000 bed volumes - before the maximum permissible arsenic concentration of 10 µg/L is reached in the effluent stream. Evaluation of laboratory and field monitoring data reveals, however, that actual live cycles can be as short as 50,000 bed volumes at some locations without immediately evident causes. In most cases this appears to be the result of a combination of numerous factors detrimental to the As adsorption process (e.g. pH, silicate, water hardness, inappropriate operating conditions, Ca concentration, etc.) which are not yet understood in detail.

It is of particular importance to clarify the dynamic behavior of silica species and their depositional behavior on the adsorbent media. Silica undergoes polymerization, precipitation, dissolution or adsorption depending on the pH and/or temperature (*Kersten and Vlasova 2009b*), which becomes greatly complicated in the presence of other ions. A general paradigm is that the addition of electrolytes to a supersaturated solution accelerates the aggregation and precipitation of polymeric species. However, experimental results recently showed that polysilicic acid in the presence of Ca ions (1 mM/L) is apparently stable in solution over extended time, compared with that under a Ca-free condition (*Chida et al. 2007*). On the other hand, the concentration of soluble monomeric silicate in the presence of Ca ions immediately became metastable, that is, slightly higher than the solubility of silica. Its dynamic behavior was similar to that in the Ca-free condition. One of our hypotheses is therefore, that the antagonistic behavior of increased Ca concentrations is based on its stabilization of the Si polymer in groundwater. Dissolved polymeric Si is much less adsorbed and thus competitive than monomer silicic acid with respect to arsenate and other toxic oxyanions (*Swedlund and Webster 1999, Swedlund et al. 2009*). The SME partner expects a major breakthrough by the scientific deliverables of this collaborative project with potential for optimizing their water treatment technology. The project is therefore aimed at resolving these open questions and hypotheses by a collaborative activity according to the complementary methodology and expertise of the participants. These activities are namely concentrating on experiments with water purification units based on Fe oxide phases in laboratory columns and on a field scale with different ground

Table 1: Trace metal contents of used GEH adsorbent samples taken from the top of the filter bed (XRF measurements)

	Units*	fresh GEH (average of 10 samples)	used GEH from different waterworks sites				
			Boss.	Neud.	Schö.	Ober.	Trög.
Arsenic (As)	g/kg	< 0.002	5.0	13.3	7.1	6.1	2.6
Phosphate (PO_4)	g/kg	< 0.3	7.6	14.9	20.4	20.7	10.5
Silicate (SiO_2)	g/kg	1.5	67.9	55.6	43.2	60.5	65.0
Vanadium (V)	g/kg	0.1	1.8	0.7	0.5	1.2	0.4
Antimony (Sb)	g/kg	< 0.002	0.002	0.006	0.013	0.003	0.003

*Metal concentrations given relative to solids content

water regimes (WP 1, GEH Wasserchemie GmbH), spectroscopy of the oxyanion sorbates involved in the surface reactions on a molecular scale (WP 2, Geoscience Institute of Univ. Mainz), characterization of adsorption reactions on microbiologically activated iron mineral surfaces (WP 3, ZAG at Univ. Tübingen), characterization of the GEH sorbent structures on a nanoscale by applying X-ray techniques (WP 4, RWTH Aachen), and adsorption batch experiments and analytical characterization of potentially formed organic metalloid species (WP 5, UFZ-Helmholtz Leipzig).

For the investigations, both fresh and used GEH adsorbent samples from several waterworks were collected and analyzed. The trace metal contents determined in the used GEH samples were compared with those of fresh GEH adsorbent taken from current production. The results from five German waterworks are summarized in Table 1. They show high arsenic loading in the used GEH adsorbent materials, ranging from approx. 3 g/kg up to over 13 g/kg. These arsenic levels correlate with the As concentrations in the inlet raw water (12 - 40 µg/L As) and with the duration of operation of the adsorber system. The analyses also revealed high loading levels of phosphate and vanadium along with high silicate loading, the latter up to 6 wt.-%. The inlet raw water entering these waterworks typically contains 0.1 - 0.2 mg/L PO_4 and approx. 5 - 10 mg/L Si. Inlet concentrations of both vanadium and antimony are typically below 10 µg/L, e.g. 1.6 µg/L Sb and 1.7 µg/L V at the »Boss« water works. Since only negligible antimony loading was found in the used adsorbents, it can be concluded that vanadium is much better adsorbed by the GEH adsorbent than is antimony. The high vanadium loading found confirms the high adsorption capacity for this element onto iron hydroxides as reported in literature (*e.g. Naeem et al. 2007*).

The following further findings can be summarized from the used GEH bulk chemical analysis:

– During operation, chloride and sulfate were eluted by the raw water from the GEH materials. The content of both anions in the adsorbent thereby decreased to approx. 0.5 % chloride and 0.1 % sulfate. New GEH adsorbent contains approx. 2 % chloride and 0.6 % sulfate resulting from the manufacturing process. The chloride ion is an important constituent of the akaganeite crystal structure.
– An increase in alkaline earth metal content was found in the used adsorbent, presumably due to co-sorption of cations (Mg, Ca, Sr) or precipitation of insoluble compounds (Ba).
– Enrichment with other trace metals (e.g. Cu and Zn) in the used adsorbent was also found but only in some water works.
– The filter bed shows an inhomogeneous contaminant loading distribution: At the top of the filter, the GEH material is found to be highly loaded whereas at the bottom of the filter, the GEH adsorbent is less loaded.

Preliminary Results of the Laboratory Experiments

While at room temperature, Mössbauer spectra indicate akaganeite as the major phase of the active GEH filter medium, a deviation in fit at 4.9 K revealed a more complex composition. Quantitative analysis of the spectra suggests equal proportions in ferrihydrite (Fh) and akaganeite (β-FeOOH) composition. Therefore the research project partner from RWTH Aachen performed a thorough investigation with help of X-ray diffraction analysis (XRD). To optimize the XRD analysis of the GEH material, the potential ferrihydrite content had to be quantified with a Rietveld program due to its low crystallinity. For this task, a synthetic 2-line ferrihydrite was prepared as a standard and analyzed by XRD. After subtracting the background of the diffractometer, the net intensities of the ferrihydrite were converted into observed structure factors by using a hexagonal cell with a primitive space group. The peaks were refined with isotropic peak widths. With this new structure a better detection of 2-line ferrihydrite was possible. In five known mixtures of this ferrihydrite with hematite an excellent correlation of $r^2 = 1$ was obtained (Figure 2). While in previous investigations the akag-

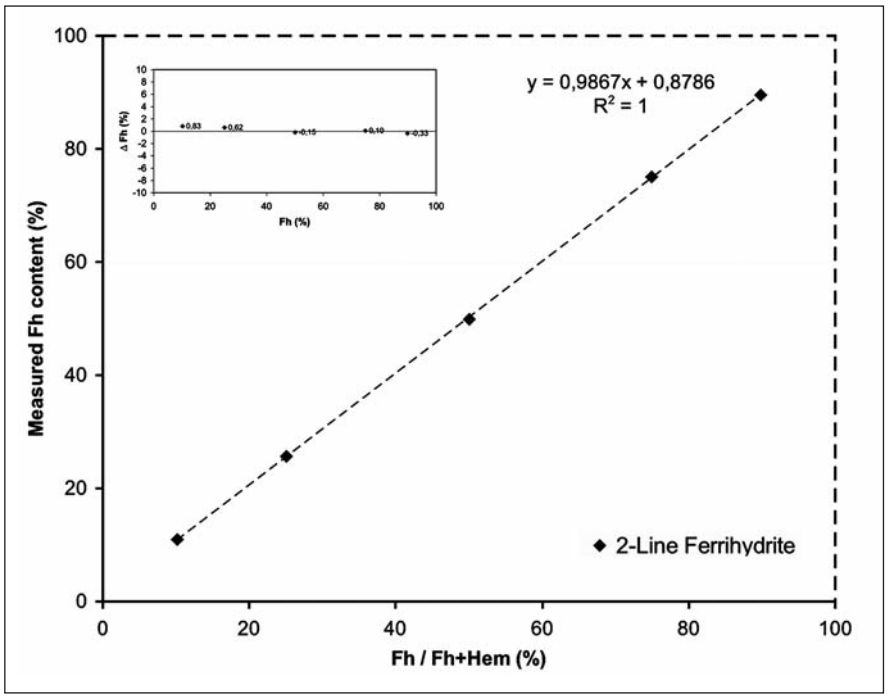

Figure 2: Comparing weighted-in with BGMN fitted Fh content. The deviations from the regression line are less than 1% absolute.

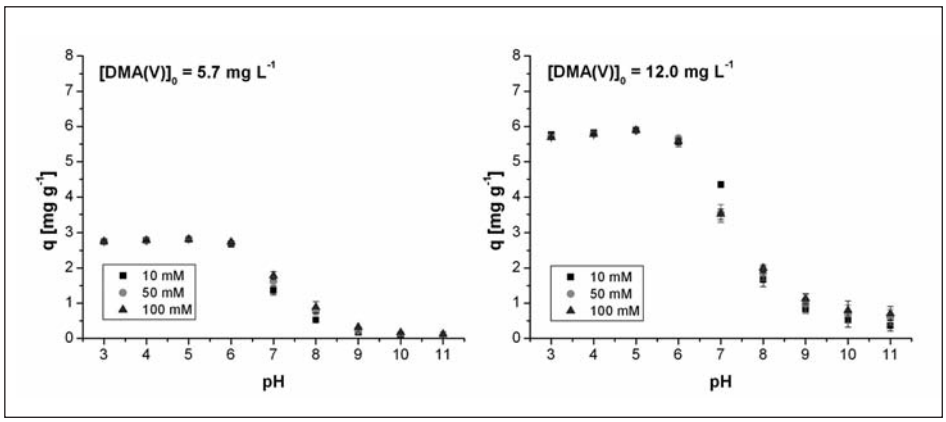

Figure 3: Sorption loadings of DMA(V) onto GEH material; variation of initial concentrations (5.7 and 12.0 mg/L), ionic strengths (10, 50, and 100 mM) and pH.

aneite seemed to be a major phase of the bulk GEH, the new ferrihydrite structure resulted now in a higher content of as much as 37 - 47 wt.-% of Fh in fresh GEH. These amounts correspond better to the Mössbauer data provided by the research partner ZAG Tübingen. Moreover, the ferrihydrite in GEH seems to differ from the synthetic 2-line ferrihydrite. It appears to be an even poorer crystallized Fe-oxihydroxide phase because the significant two lines of ferrihydrite are not clearly visible in the XRD patterns. Further investigations on this issue are in progress to refine the quantitative XRD analysis.

The fresh GEH material was tested for the removal of inorganic and methylated arsenic and antimony species from water by the project partner UFZ Leipzig. Batch experiments with GEH suspensions (2 g/L) were done with arsenate (As(V)), arsenite (As(III)), dimethyl arsenic acid (DMA(V)), antimonate (Sb(V)), and trimethyl antimonate (TMSb(V)). The ionic strength was adjusted with sodium nitrate to final concentrations of 10 mM, 50 mM, and 100 mM, respectively. The samples were shaken for 24 h at 150 rpm at room temperature, which was found previously to be sufficient for equilibration (*Daus et al., 2004*). The total con-

centrations of antimony and arsenic in the supernatant liquids were analysed by ICP-MS. As an example, the results of DMA(V) are summarized in Figure 3.

The adsorption efficiency for DMA(V) decreases at pH values higher than 6. This effect was observed for the adsorption on both goethite and ferrihydrite in other studies (*Lafferty et al., 2005*). The influence of the ionic strength is negligible. These experimental data are provided by the UFZ group for modelling to be done by the University of Mainz partner. Another important factor influencing the performance of the water treatment filters are competitive adsorption reactions by other water constituents. This effect is well known for phosphate which can compete for sorption sites during the adsorption process as well as remobilize already adsorbed arsenate (*Zhang et al. 2007*). The used water works material contains not only arsenic but also vanadium (Table 1). Moreover, recent literature data indicate effects of vanadium on As adsorption efficiency by GEH adsorber (*Speitel et al. 2010*). Therefore, vanadium was included in competition experiments besides phosphate, antimonate, arsenite, and arsenate. For the competition experiments, the concentration of arsenate, antimonite, and vanadate as primary oxyanion was chosen to be 10 mg/L. The correspondent sorption capacity for arsenate at this initial concentration is approximately 5 g/kg, which is a typical loading in water works material after 2 years in use. The concentrations of the competing oxyanions (arsenate, arsenite, antimonate, phosphate, or vanadate) were varied from 1 - 100 mg/L. A volume of 50 mL of the mixed solution was added to 0.1 g GEH material (2 g/L suspension). The material was shaken under identical conditions such as pH = 7. In the supernatant after centrifugation (3000 rpm, 10 min), arsenic, antimony, and vanadium concentrations were analysed.

The results shown in Figure 4 revealed that the sorption of antimonate onto GEH was most affected by the other oxyanions. Its sorption capacity decreased in presence of vanadate (about 9 %) and even more in the presence of phosphate, arsenite, and arsenate (up to 30 %) for a ratio of competitive oxyanion/antimonate of 10:1. This ratio is quite realistic for raw waters of water works as found at the test site. Therefore, antimonate is apparently most sensitive for sorption disturbance by other water constituents. Vanadate as primary oxyanion seems to be relative robust to competitive reactions in the investigated concentration ratios. The sorption of arsenate was less sensitive than the sorption of antimonate, but vanadate can decrease the capacity by 23 % at a surplus of factor 10. The adsorption affinity towards GEH therefore increases in the order antimonate – arsenate – vanadate. Therefore, not only silicate but also vanadate concentration in the raw water should be taken into account to predict a premature break-through of arsenate.

Additional experiments on adsorption kinetics of silicate onto GEH were performed in a

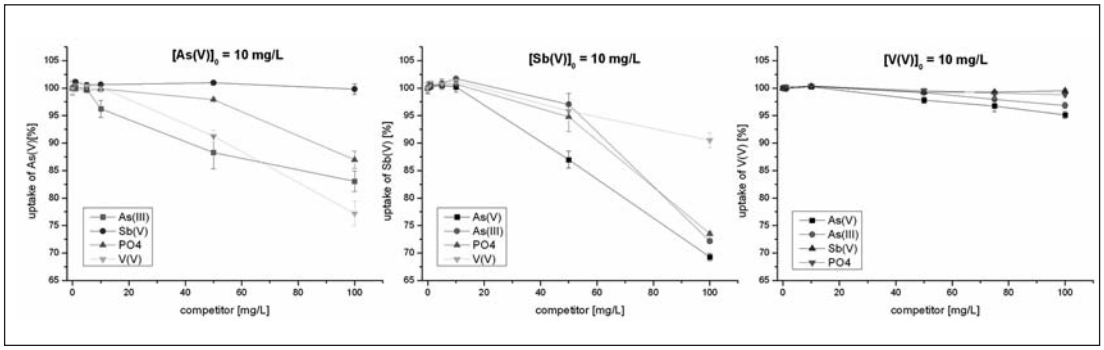

Figure 4: Overview of competition experiments performed at pH 7 and 24 h shaking.

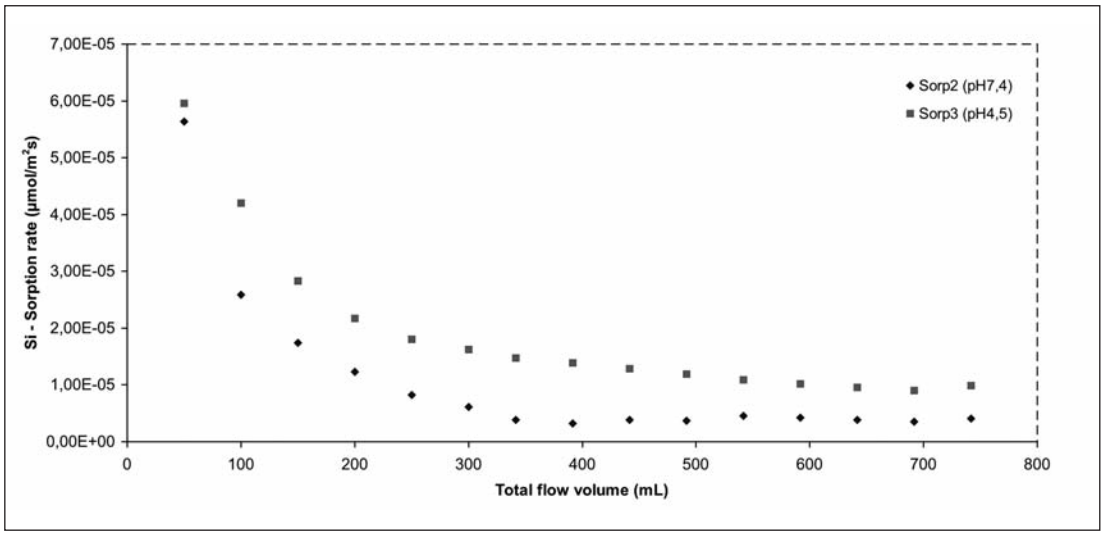

Figure 5: Sorption rates of Si onto GEH by variation of pH.

mixed-flow reactor (MFR) by the project partner at RWTH Aachen. The material in the reactor was flushed by a 0.05 M KCl solution. The pH was adjusted to different values in various sorption cycles to observe the influence of pH onto the sorption behaviour. After equilibration, solutions with selected inlet concentrations of silicate were pumped through the MFR by a HPLC pump which ensured exact flow rates. Silicate was measured photometrically as monomeric Si with the molybdenum-blue method after *Köster* (1979). From the balance of silicate in the input output solutions, sorption rates were calculated (Figure 5). Higher sorption rates were observed at lower the pH value.

Rapid small scale column tests (RSSCT method: *Westerhoff et al.* 2005) were carried out to investigate the breakthrough behavior of the competing anions As, V, phosphate and silicate at ambient concentrations. Unlike the competitive adsorption in batch experiments described above, these tests aimed at investigation of the dynamic adsorption properties in filter columns. The RSSCT breakthrough curves show concentration in the effluent as a function of water throughput expressed in bed volumes. Ideally, the RSSCT results are directly applicable to the corresponding full-scale GEH adsorber beds at the water works. An artificially formulated ground water was used, containing As, V, phosphate, and silicate in a typical background water matrix (pH 6.8; I = 270 µS/cm). GEH adsorbent (grain size: 63-75 µm) was filled into the filter column, providing a bed volume of 5.3 cm^3. The RSSCT data indicates an arsenic breakthrough at 80,000 BV relative to the threshold value of 10 µg/L As (Figure 6). The arsenic adsorption capacity for this particular water is significantly lower than those determined from typical breakthrough curves for water without competing anions. Vanadium shows a similar breakthrough behavior, although the breakthrough curve is shifted significantly to higher BV. Here, the effluent V concentration exceeds the 10 µg/L value at approx. 140,000 BV. Considering the fact that the V concentration in the influent is approx. half of the As concentration, it can be concluded that adsorption capacity of GEH adsorbent is similar for both elements. Analyses showed loading levels in the used GEH adsorbent of 2.8 g/kg As and 2.0 g/kg V (dry weight). Moreover, the breakthrough curves show several peaks which correlate with temporary pH value variations in the inlet raw water (increases from pH 6.8 up to 7.2). This reflects the strong influence of pH on arsenic adsorption by GEH absorbent. The same effect is also observed for the vanadium curve, albeit less pronounced.

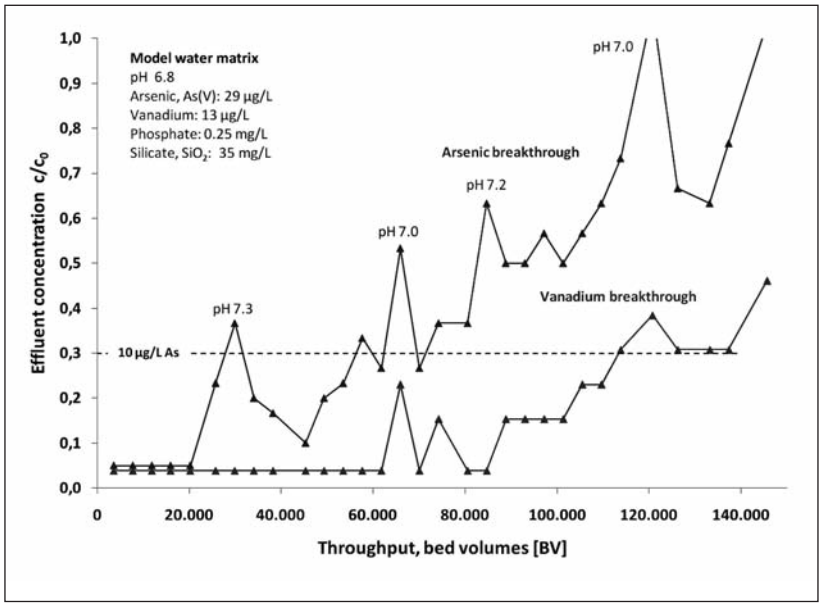

Figure 6: Arsenic and vanadium breakthrough curves, determined in rapid small scale column testing (RSSCT) using a model ground water matrix

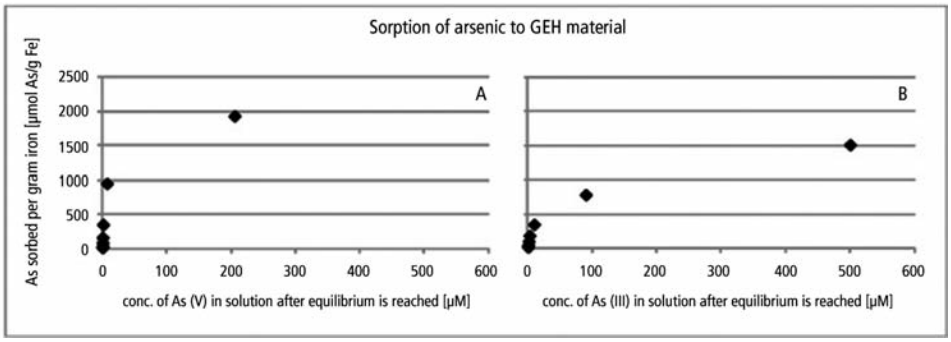

Figure 7: Sorption of arsenic to GEH material, with (A) sorption of As(V), and (B) sorption of As(III).

As detailed already in the last report (*Kersten et al. 2009*), Fe(II)-oxidizing bacteria were found on the 2-year old GEH filter material. Initial experiments with the related bacteria stem Acidovorax sp. BoFeN1 showed efficient removal of As(V) and As(III) by co-precipitation of the arsenic with biogenic Fe(III) hydroxides formed by these bacteria (*Hohmann et al. 2010*). For this reason, laboratory experiments were carried out to first determine which minerals and cell-mineral aggregates are produced by Fe(II)-oxidizing bacteria (*Posth et al. 2010*). In a second step, the influence of Fe(II)-oxidizing bacteria on sorption and co-precipitation of arsenic was investigated. For this, sorption and co-precipitation batch experiments with As(V) and As(III), and both biogenic and abiogenic Fe(III) minerals were set up. The biogenic minerals were produced by Acidovorax sp. BoFeN1, an anaerobic, nitrate-reducing Fe(II)-oxidizing bacteria found in arsenic contaminated aquifers. Freshly prepared GEH material was used for the abiogenic substrate. The minerals were suspended in carbonate-buffered (pH 7) water with a low phosphate concentration (<10 µM) and 8 - 10 mM dissolved Fe(II). Experiments with GEH contained 250 mg solid material/25 mL water (10 g/L suspension or about 2800 m²/L surface). Arsenite or arsenate was added at a final concentration of 0.025 - 10 mM. All sorption experiments were sampled at the start and after 48 h of equilibration time. Co-precipitation experiments were sampled at the start and at the end of Fe(II) oxidation. The dissolved As(V) and As(III) concentrations of the samples were quantified by the collaboration partner at UFZ-Leipzig. On a mass basis, more As(V) and As(III) sorbed per g Fe to

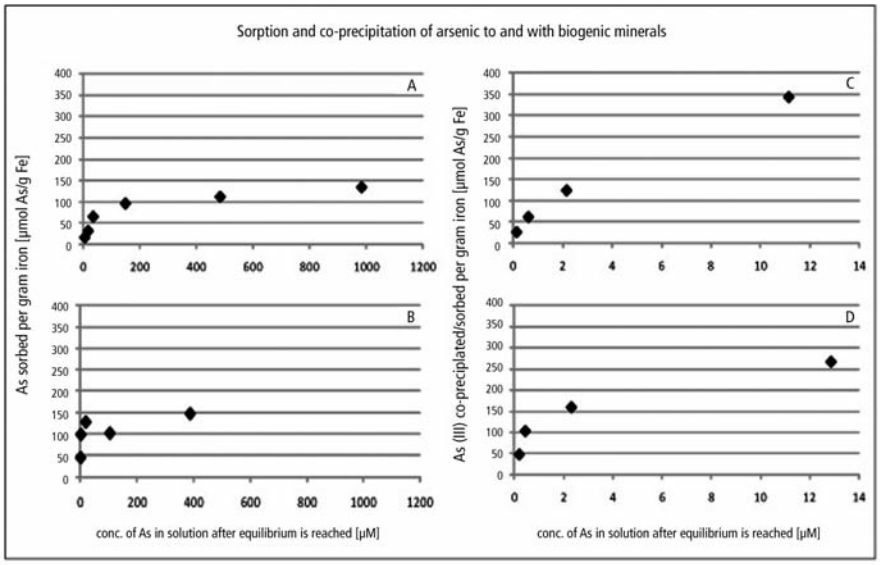

Figure 8: Sorption and co-precipitation of arsenic to and with biogenic minerals. A) sorption of As(III) to biogenic minerals, B) sorption of As(V) to biogenic minerals, C) co-precipitation of As(III) with biogenic minerals, D) co-precipitation of As(V) with biogenic minerals.

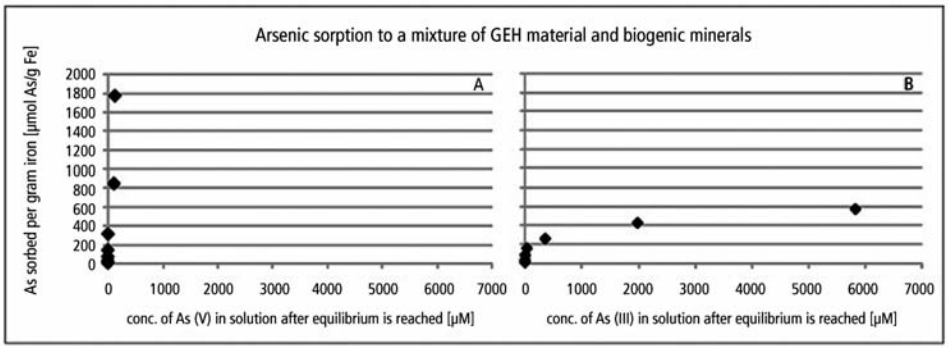

Figure 9: Sorption of arsenic to a mixture of GEH material and biogenic minerals. A) As(V) sorption to GEH material and biogenic minerals (biogenic minerals first precipitated and then added to GEH material before As(V) addition). B) As(III) sorption to GEH material and biogenic minerals (biogenic minerals precipitated in the presence of GEH material before As(III) addition).

GEH material than to the biogenic minerals (Figures 7 and 8). Nearly all As(V) up to an initial As concentration of 10 mM (98.3 - 100.0 % of arsenate added) was immobilized by GEH via sorption, yielding up to 2 mM As(V) sorbed per g Fe in GEH (Fig. 7). Likewise, As(III) is nearly entirely sorbed to GEH material (94.8 - 100.0 % of the amount added yielding up to 1.5 mM As(III) per gram Fe).

Nonetheless, in GEH filter systems, in which nitrate-dependent Fe(II)-oxidizing bacteria have been found, sorption to GEH, sorption to biogenic minerals, and co-precipitation with biogenic minerals are all occurring simultaneously. To approach the complexity of these sorption continuum systems, step-wise experiments were set up. First, the sorption of As(V) to a mixture of GEH and biogenic minerals (biogenic minerals first precipitated then added to the GEH material) revealed that 98.1 – 100 % of the added As(V) was removed (Fig. 9). In this experiment, sorption to the GEH is likely the more important mechanism, and the results are similar to those of sorption of As(V) to GEH alone (up to 2 mM As(V) sorbed per g Fe). Interestingly, in case of precipitation of the biogenic minerals in the presence of the GEH

material, only 39.4 % of As(III) (at the highest As(III) concentration) and up to 100% As(III) at lower As(III) concentrations were removed from solution indicating that the biogenic minerals precipitated in the presence of the GEH material are obviously coating the GEH material and thus lowering its sorption capacity or even preventing sorption of As to the GEH material. Additionally, the cell organic matter may block sorption cites in the biogenic minerals.

In a final experimental set-up, the processes of sorption and co-precipitation are occurring simultaneously as would be the case in a GEH filter system with Fe(II)-oxidizing bacteria. As a result, 96.4 - 99.9 % of As(V) and 97.1 - 99.9 % of As(III) were removed, corresponding to a load of up to 1.8 mM As(V) per g Fe and approximately 1.5 mM As(III) per g Fe. The mixture is still very efficient (Figure 10), but it seems that the participation of microorganisms that form biogenic minerals again reduces the efficiency of the GEH material. Compared to the abiotic systems where As sorbs to GEH, this system removes less arsenic. Our preliminary hypothesis is again that the cell organic matter in the biogenic systems probably blocks sorption sites or changes the surface charges from positive to negative. In order to investigate the influence of organic compounds in the sorption capacity and co-precipitation capacity of As species to GEH and biogenic minerals, further experiments are warranted which focus on the influence of humic substances on sorption capacity of the GEH material. These experiments, as well as column experiments with biogenic minerals and GEH filter material, are currently in progress. As a preliminary conclusion, however, it can be stated from all those results that microbiological activation is not a suitable way to enhance the performance of the GEH material as originally expected.

While all XRF and XRD measurements, adsorption experiments, and microbiological investigations yet mentioned were based on bulk GEH material, contaminant load has been measured by microprobe analysis also on individual used filter grains by the project partner at Mainz University. This analysis revealed that there is a strong inhomogeneity between individual grains in scavenging efficiency for the toxic elements As and V. There are nearly inactive GEH grains with almost no As and V scavenged (e.g., the grain in the upper left corner in Figure 11), and very active grains with a high load in both elements (central grain in Figure 11) but in the same sample batch from the top horizon of a filter bed used for 2 years at the water works station »Schö« (Table 1). The ratio between active and inactive grains is about 1:1 as indicated by a scatterplot of As vs. Si for about 200 analyzed grains (Figure 12). Both the inactive and active grains have a similar Si load but with extremely different effect on their As/V affinity. Differing phase composition (akaganeite/ferrihydrite) as indicated by different Cl concentrations between both grain populations could be a probable reason. This would also explain the difficulties and deviations in receiving representative bulk phase

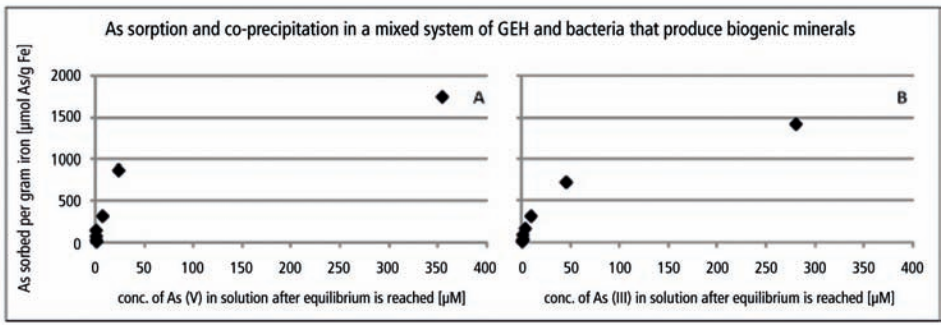

Figure 10: Sorption and co-precipitation of arsenic in a mixed system of GEH and bacteria that produce biogenic minerals. A) As(V) in the mixed system B) As(III) in the mixed system.

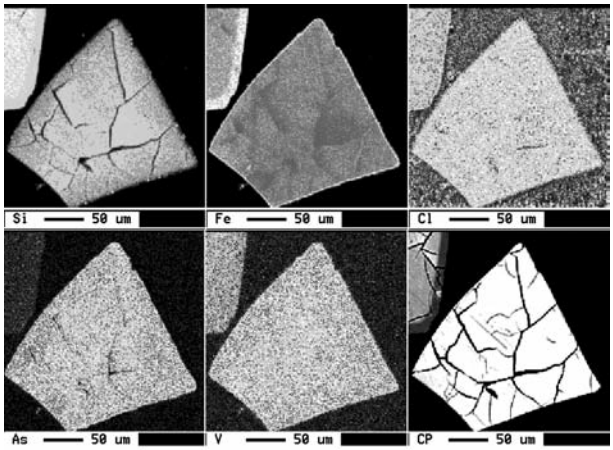

Figure 11: Microprobe element distribution maps for two typical GEH grains sampled in the top horizon of a filter used for 2 years at the water works station »Schö« (Table 1). The lighter are the pixels (or more yellow-red in color), the higher was the element concentration.

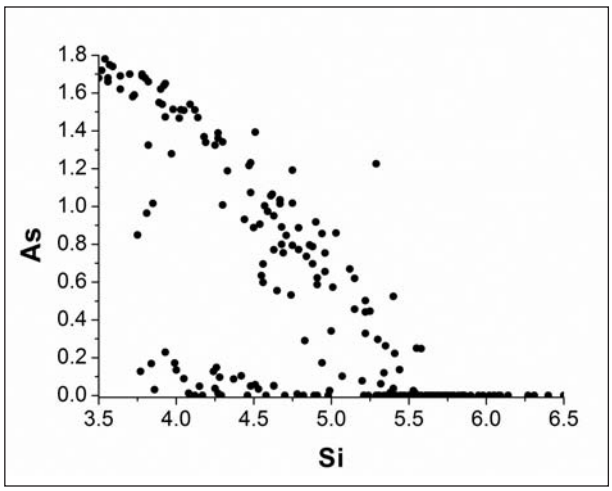

Figure 12: Scatterplot of As vs. Si for 200 analyzed grains sampled in the top horizon of a filter used for 2 years at the water works station »Schö« (arbitrary units of the qualitative microprobe analysis). Note the steep slope of the negative As vs. Si regression curve in between 3.5 and 5.5 Si units, and another less steep but with low to virtually zero As concentrations in between 3.5 and 6.5 Si units. The number of grains in both data populations is about equal.

composition analysis as mentioned above. Verification of this hypothesis by micro-spectroscopic phase analysis on the individual grain scale could potentially become new and unexpected key information how to improve the GEH production process.

Literature

Chida T., Niibori Y., Tochiyama O., Mimura H., Tanaka K. (2007): Deposition rates of polysilicic acid with up to 10^{-3} M calcium ions. Appl. Geochem. 22, 2810–2816.

Daus B., Wennrich R., Weiss H. (2004): Sorption materials for arsenic removal from water: a comparative study. Water Res. 38, 2948-2954.

Hohmann C., Winkler E., Morin G., Kappler A. (2010): Anaerobic Fe(II)-oxidizing bacteria show As resistance and co-precipitate As during Fe(III) mineral precipitation. Environmental Science and Technology, 44, 94-101.

Kersten M., Vlasova N. (2009a): Arsenite adsorption on goethite at elevated temperatures. Appl. Geochem. 24, 32-43.

Kersten M., Vlasova N. (2009b): Silicate adsorption by goethite at elevated temperatures. Chem. Geol. 262, 372-379.

Kersten M., Vlasova N., Posth N., Kappler A., Schurk K., Stanjek H., Daus B., Kolbe F., Wennrich R., Bahr C., Driehaus W. (2009): MicroActiv - Optimization of water purification technology for arsenic and antimony scavenging by microbially-activated Fe-oxide minerals. Report for the 1st Statusseminar Bayreuth, 10 pp.

Köster H.M. (1979): Die chemische Silikatanalyse - Spektralphotometrische, komplexometrische und flammenspektrometrische Analysenmethoden. Springer-Verlag, Berlin, Heidelberg, New York.

Lafferty B.J., Loeppert R.H. (2005): Methyl Arsenic Adsorption and Desorption Behavior on Iron Oxides. Environ. Sci. Technol. 39, 2120-2127.

Miot J., Benzerara K., Morin G., Kappler A., Bernard S., Obst M., Férard C., Skouri-Panet F., Guigner J.M., Posth N., Galvez M., Brown G.E. Jr, Guyot F. (2009): Iron biomineralization by anaerobic neutrophilic iron-oxidizing bacteria. Geochim. Cosmochim. Acta 73, 696-711.

Posth N.R., Huelin S., Konhauser K.O., Kappler A. (2010): Size, density and mineralogy of cell-mineral aggregates formed during anoxygenic phototrophic Fe(II) oxidation. Geochimica Cosmochimica Acta, 74, 3476-3493.

Rahman M.M., Ng J.C., Naidu R. (2009): Chronic exposure of arsenic via drinking water and its adverse health impacts on humans. Environ. Geochem. Health 31, 189-200.

Schmidt G.T., Vlasova N., Zuzaan D., Kersten M., Daus B. (2008): Adsorption mechanism of arsenate by zirconyl-functionalized activated carbon. J. Colloid Interf. Sci. 317, 228-234.

Smith S., Edwards M (2005): The influence of silica and calcium on arsenate sorption to oxide surfaces. J. Water Suppl. AQUA 54, 201-211.

Speitel G.E.Jr., Katz L.E., Chen C.-C., Stokes S., Westerhoff P., Shafieian P. (2010): Surface complexation and dynamic transport modeling of arsenic removal on adsorptive media. AWTP Program Report, WERC Water Research Foundation, Denver CO, USA, 140 pp. (available at: http://www.arsenicpartners.org/3098.pdf).

Sperlich A, Werner A. (2005): Breakthrough behaviour of granular ferric hydroxide (GFH) fixed–bed adsorption filters: Modeling and experimental approaches. Water Res. 39, 1190-1198.

Swedlund P.J., Webster J. (1999): Adsorption and polymerisation of silicic acid on ferrihydrite, and its effect on arsenic adsorption. Water Res. 33, 3413-3422.

Swedlund P.J., Miskelly G.M., McQuillan A.J. (2009): An attenuated total reflectance IR study of silicic acid adsorbed onto a ferric oxyhydroxides surface. Geochim. Cosmochim. Acta 73, 4199-4214.

Von Gunten U. (2008): Can the quality of drinking water be taken for granted? EAWAG News 65e, 4-7.

Zhang J.S., Stanforth R.S., Pehkonen S.O. (2007): Effect of replacing a hydroxyl group with a methyl group on arsenic (V) species adsorption on goethite (α-FeOOH). Colloid Interface Sci. 306, 16-21.

Microstructural Controls on Monosulfide Weathering and Heavy Metal Release (MIMOS)

Pollok K. (1)*, Harries D. (1), Hopf J. (1,2), Etzel K. (1), Chust T. (1), Hochella M.F., Jr. (3), Hellige K. (4), Peiffer S. (4), Langenhorst F. (1)

(1) Universität Bayreuth, Bayerisches Geoinstitut, D-95440 Bayreuth, kilian.pollok@uni-bayreuth.de

(2) Friedrich-Schiller-Universität Jena, Institut für Mikrobiologie, Neugasse 25, D-07743 Jena

(3) Center for NanoBioEarth, Department of Geosciences, Virginia Polytechnic Institute and State University, Blacksburg, Virginia, USA

(4) Universität Bayreuth, Lehrstuhl für Hydrologie, D-95440 Bayreuth

* Coordinator of the project

1. Introduction and summary

The iron monosulfides pyrrhotite ($Fe_{1-x}S$) and mackinawite (tetragonal FeS) are both environmentally important phases linking the iron and sulfide elemental cycle. This report summarizes studies that aim at understanding on the effect of microstructure, mineral chemistry and crystallography of these minerals on the reactivity (*Pollok et al., 2008*) and provides insights towards possible applications.

Pyrrhotite comes a close second after pyrite among the most abundant iron sulfides in crustal rocks and ore deposits including Ni-Cu, Pb-Zn, Au, and platinum-group elements (PGE). The weathering of pyrrhotites contributes to the release of iron and other metals as well as sulfate to surface waters as a part of the acid mine drainage problem. The relevance of this reaction lies in the high reactivity of pyrrhotite (20 to 100 times faster compared to the disulfide pyrite; *Nicholson & Scharer, 1994*) which limits the neutralization of produced sulfidic acid by silicate weathering reactions. Furthermore, many potentially important implications to the fields of geomagnetics, petrology, environmental mineralogy, and technical mineral processing are to be expected if detailed knowledge about structures and phase relations is available. Lately, the flotation behavior of pyrrhotite is attracting more attention as this mineral is an important host for Ni and PGEs (*Becker et al., 2010; Ekmekçi et al., 2010*).

In the first section the coupling between crystallographic structure and composition of pyrrhotite has been studied by the use of transmission electron microscopy (TEM) which has been used for the first time to directly visualize details of the (non-integral) stacking sequences using superstructure diffraction spots. The observations result in a new and versatile description of pyrrhotite superstructures which provide a basis to understand variation in physical properties and reactivity of pyrrhotites. In the second section the relevance of different superstructures in terms of reactivity is directly substantiated for the biologically-enhanced dissolution of a pyrrhotite intergrowth. The difference in dissolution rates betwee the intergrown phases is quantified by using topographic data produced by confocal microscopy providing a new view on the reactivity and weathering patterns of this mineral. The third part deals with the evolution of surface roughness for such reacted and heterogeneous surfaces. To extend our possibilities to generate meaningful data for reactive surface area and, hence, dissolution rates, a new program is introduced, which allows a non-biased statistical evaluation of surface roughness distributions. The concept presented here can be utilized for any kind of topographic data and might be well applicable to other areas of surface science.

Mackinawite is a metastable, nanoparticular phase that forms by precipitation from aqueous solutions at low temperatures. It is a major component of acid volatile sulfide (AVS) compounds, causing black-colored layers in recent anoxic sediments. Mackinawite is therefore an important precursor of sedimentary pyrite and can facilitate in-situ remediation of metals in connection with (biogenic) sulfate reduction in acidic pit lakes and sediments (*Bilek, 2006, Church et al. 2007*). It is known as an effective absorber due to its large specific surface area (*Ohfuji & Rickard, 2006*) but detailed reaction mechanisms important to biogeochemistry are still missing.

The last section provides experimental evidence for the formation mechanisms of sedimentary sulfides via mackinawite under anoxic conditions. The results highlight the importance of iron hydroxide surfaces as the locations of electron transfer for mackinawite formation, but also show the spatial decoupling to pyrite formation. In conclusion, the study provides fundamental data that enables to model basic reactions at geochemical interfaces.

2. Towards a new structural model for NC-pyrrhotites: Structural and chemical characterization of selected samples by electron microscopy

The physical properties of a mineral and the reactivity of a mineral surface are determined by its chemical composition and internal atomic structure. In this respect, non-stoichiometric pyrrhotite is a striking phase because its structure and the physical (e.g. magnetic) properties change dramatically within a small compositional range. A detailed knowledge about the composition-structure relationship as well as the structure-property relationship is needed to gain a fundamental understanding of this environmentally and technically important mineral.

Pyrrhotite has a NiAs-derivative structure that contains sequences of hexagonal close-packed S atom layers stacked in alternation with layers of Fe atoms in octahedral coordination. Non-stoichiometric compositions arise from the presence of vacancies within Fe layers and span the range in-between ~47 to 50 at% Fe (Fe_7S_8 to FeS), whereas most structural complexity occurs in the narrow compositional range between 47 to 48 at% Fe. At temperatures below 300 °C various superstructures are observed in this range due to vacancy ordering among and within Fe layers, resulting in a rather complicated subsolidus phase diagram (e.g., *Nakazawa & Morimoto, 1970*).

Based on a NiAs-type structure of FeS, the well understood monoclinic 4C structure is derived by removing 1/4 of Fe atoms from every second Fe layer, leading to the composition Fe_7S_8. Four vacancy layers are mutually discernible in the stacked arrangement and the resulting sequence of partially vacant (V) and filled (F) Fe layers is $V_AFV_BFV_CFV_DF$. The spacing between V layers of the same type is strictly four times the c-axis repeat of the NiAs substructure (or eight Fe layers).

Structural descriptions of integral NC-pyrrhotite structures can be roughly divided into two approaches using either discrete (0 or 1) or partial Fe site occupancies. The former relates to an idealized extension of the 4C stacking scheme by introducing additional F layers, which increases both the periodicities of the superstructures as well as the Fe/S ratios, while the latter proposes in addition to extended layer stacking a considerable atomic scale disorder of Fe vacancies.

Yamamoto & Nakazawa (1982) developed a superstructure description for an N_c = 5.54 pyrrhotite based on a continuous modulation of (partial) Fe site occupancies. In this model of an aperiodic crystal structure the probability of finding a Fe atom at a given lattice site is governed by a continuous, sinusoid-like modulation function embedded in a four-dimensional superspace formalism. Aperiodicity results from the occupation modulation being incommensurately related to the substructure periodicity. Based on this work *Izaola et al.* (2007) introduced a generalized superspace approach by replacing the continuous occupancy modulation with a step-like function governing discrete site occupancies. By virtue of a »closeness« condition, the model strictly obeys the

sequence of ABCD layering as well as the rule that two V layers must not follow consecutively without an interjacent F layer, resulting in the fixed relation $1/N_c = 2x$ between superstructure N_c value and composition expressed as x in $Fe_{1-x}S$.

A primary motivation for this study was that the reported electron diffraction pattern of non-integral NC-pyrrhotites strongly resemble those seen in certain translation interface modulated binary alloys such as $Au_{3+x}Zn_{1-x}$ (*Amelinckx & Van Dyck, 1992*). In these alloy systems integral superstructures arise in stoichiometric compounds as Au_3Zn from ordering atoms on certain sites of the fcc lattice. Non-stoichiometric compositions and further superstructures are related to variably ordered, non-conservative (»composition-changing«) antiphase boundaries (APBs) of these simple superstructures. Such translation interface modulation (TIM) is characterized by replacement (or splitting) of the simple superstructure diffractions spots (e.g., those of 4C-pyrrhotite) with arrays of satellite reflections – as seen in NC-pyrrhotites.

2.1. Samples and experimental methods

In this study, two natural pyrrhotite samples from geologically different locations were characterized in detail by electron microscopy. Samples were obtained from the Sta. Eulalia mining district in Chihuahua, Mexico (EUL) and from the Nyseter mining area near Grua, Norway (NYS). Ar-ion thinning for transmission electron microscopy (TEM) was carried out using liquid nitrogen cooling or a low angle thinning system. In order to check for preparation artefacts, powdered and ultramicrotomed samples were prepared as well, but no systematic differences in SAED pattern could be detected. N_c values were obtained from selected area electron diffraction (SAED) patterns with typical uncertainties of ±0.01 (2s). TEM superstructure dark-field imaging (SDF) was accomplished by placing an objective aperture of 2.3 nm^{-1} diameter on strong satellite reflections.

2.2. Results - Electron microprobe analysis (EMPA)

Back scatter electron (BSE) imaging of EUL and NYS shows abundant exsolution lamellae in both samples. In sections the lamellae form two sets of lens shaped or sigmoidal bodies inclined towards the [001] direction of host pyrrhotite. Lamellae typically measure <200 µm in length and up to 30 µm in width and are darker in BSE images (Fig. 1a). Quantitative analyses show the lamellae to have compositions near $Fe_{0.875}S$ (or Fe_7S_8) indicative of 4C-pyrrhotite, while the host pyrrhotites' Fe contents are slightly below $Fe_{0.900}S$ (or Fe_9S_{10}) as indicated by x values of 0.106±0.001 (EUL) and 0.102±0.001 (NYS). Contrary to the EUL sample NYS shows a small Ni content of 0.05 to 0.11 wt%. Exsolution of 4C-pyrrhotite from NC-pyrrhotite appears to be quite abundant in nature and is well documented by petrographic methods.

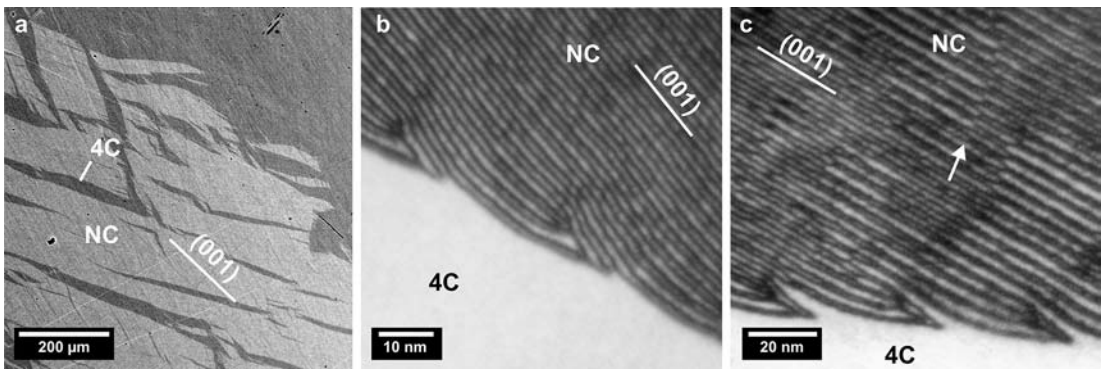

Figure 1: (a) BSE image of 4C/NC intergrowths in sample EUL. (b) TEM-SDF image of the 4C/NC interface in EUL. APBs terminate in eight-fold node structures. (c) TEM-SDF image of the 4C/NC interface in sample NYS. Nearly identical node structures occur at the boundary but additionally changes in APB configurations (arrow) in the NC phase can be seen

2.3. Results - TEM-SAED

The indexing of superstructure satellite reflections is done by applying a (3+1)-dimensional (hklm) scheme analogous to the one adopted by *Yamamoto & Nakazawa* (1982) and commonly used for the description of one-dimensionally modulated structures (Fig. 2). A diffraction vector **g** is thus:

$$\mathbf{g} = h\,\mathbf{a^*} + k\,\mathbf{b^*} + l\,\mathbf{c^*} + m\,\mathbf{q}$$

m is the satellite order of a superstructure reflection and **q** is the modulation vector relating each satellite to a (*hkl*) substructure reflection. **q** is generally parallel or subparallel to **c***. The N_c value of a superstructure is obtained as the length ratio **c***/**q** with c* referring to the NiAs-type subcell ($c^* \approx 1.72$ nm^{-1}). For the EUL and NYS samples coincident N_c values of 4.81-4.87 and 4.78-4.96, respectively, have been obtained. In general, the Nc values compare well to the x values obtained from EMPA assuming the relation $1/N_c = 2x$.

Based on the hypothesis of an APB modulation, the splitting of reflections in SAED patterns obtained from zone axes perpendicular to c allows to calculate average spacings and displacement vectors of APBs (*Amelinckx & Van Dyck, 1992*). The geometrical evaluation of pattern obtained from EUL and NYS suggest spacings of 1.58 to 1.74 nm and a displacement vector $\mathbf{R} = 1/8[001]_{4H}$ (the 4H indexing refers to a hexagonal cell in which the NiAs a and c dimensions are doubled and quadrupled, respectively).

2.4. Results - TEM-SDF

In order to obtain TEM-SDF images from electron beams diffracted by the superstructure, it was found to be most effective to place the objective aperture on the (0004) and (008-4) satellite reflections accessed from near the $[210]_{4H}$ zone axis. The sample foil was tilted such that in the ideal case only diffracted beams in the (00*l*m) reciprocal lattice row were excited. In the NC portions of both the EUL and NYS samples, SDF images reveal dense arrays of dark stripes being aligned parallel to the (001) planes and solely visible in dark-field images using strong superstructure reflections. In EUL the stripes appear more ordered and show less wiggles and irregularities compared to NYS, which displays some weak diffuse diffraction in the area from which the images were obtained. Further, in NYS the configuration of stripes appears to change along certain domain boundaries where the thin stripes, as seen in EUL, change into thicker stripes. The latter dominate the NYS sample and are likely doublets of two stripes being too close to be resolved under the SDF imaging conditions. The average spacing of stripes in EUL is 1.63±0.05 nm and the observed (half-)width of a single stripe is approx. 0.80 nm. Assuming the thick stripes in NYS to be non-resolvable doublets, the average spacing between individual stripes is 1.94±0.10 nm.

The average distance for EUL compares very well with the expected APB spacing as obtained from the SAED pattern geometries and we therefore interpret the dark stripes to be APBs. Based on contrast in dark-field images we can exclude them to be stacking faults or twin boundaries, as the former would be seen with substructure reflections as well and the latter would show intensity differences of domains on either site of the boundary. The larger average spacing in NYS, despite very similar N_c values, is likely due to the higher disorder with larger and more irregular spacings between stripes which bias the mean distance to higher values. The average of 1.94 nm corresponds to an N_c value of approx. 4.7, which is compatible with diffuse satellite reflections seen in some SAED patterns.

Most striking features in SDF images of EUL and NYS are the phase boundaries between 4C- and NC-pyrrhotite where the stripes form complicated but remarkably similar node structures in which the stripes terminate. When the phase interface is oriented mostly parallel to the stripes, no nodes occur directly at the interface, but occasionally appear nearby within the NC phase, often associated with crystallographic edge dislocations having the Burgers vector **b** = [001] of the NiAs cell. In all cases of node structures we observed eight stripes to terminate in a single node.

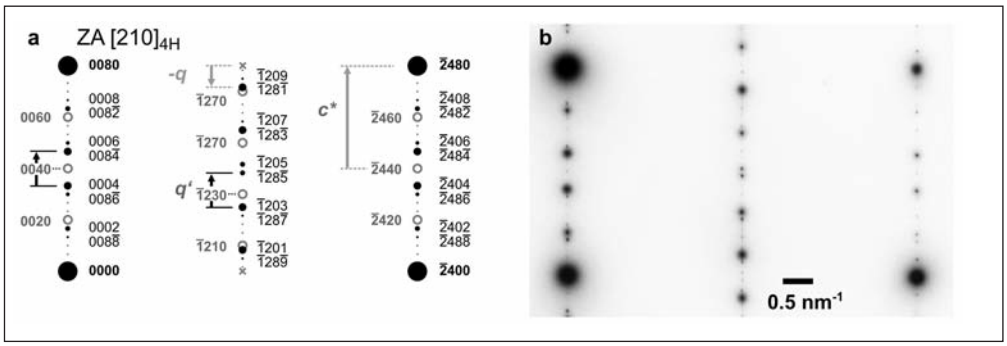

Figure 2: Diffraction patterns of non-integral NC-pyrrhotite. (a) Schematic representation of zone axis [210] for N_c = 4.85. Grey open circles/indices represent 4C reflections, crosses mark the (generally absent) 4C reflections used for superstructure indexing. (b) Experimental SAED pattern of NYS with N_c = 4.84±0.01

The behavior of stripes in the observed node structures and adjacent 4C-pyrrhotite strongly endorses our interpretation of them being non-conservative APBs of the 4C structure. Their orientation is fully compatible with the inferred displacement vector **R** = $1/8[001]_{4H}$ which creates double layers of completely filled Fe positions as opposed to single layers being present in the 4C structure. The eight-fold nodes facilitate the reconstruction of the 4C phases from the APB modulated NC phase and directly support the proposed displacement vector $1/8[001]_{4H}$ as its eight-fold multiple will be the c dimension of the hexagonal 4C unit cell (see discussion section). Apparently the highly similar node configurations represent a self-organization towards an energetically optimal phase interface.

2.5. Discussion

Our TEM observations provide compelling evidence that the structural diversity of non-integral NC-pyrrhotites can be explained in terms of a TIM structure model. The translation interfaces are APBs based on the Fe sublattice of 4C-pyrrhotite. This model bears resemblance to previously suggested »out-of-step« and anti-phase defect models (*Pierce & Buseck, 1974*) but is more precise on the actual nature of the involved translation interfaces. On the other hand, the superspace approach of *Izaola et al. (2007)* is fully compatible with our TIM model. In essence, this superspace model produces discretely modulated superstructures by inserting additional F layers into the basic 4C layer sequence, producing either periodic or aperiodic (but uniform) stacking sequences parallel to (001). Because the so produced double F layers carry an Fe excess, the resulting phases will have higher Fe/S ratios than 4C-pyrrhotite and follow strictly the relation $1/N_c = 2x$ as spacings between double layers are evenly distributed.

For a structure with N_c = 4.8, which is a simple representation for the host NC-pyrrhotite in our EUL and NYS samples, it is possible to derive two well ordered stacking schemes: $(DSSDS)_4$ and $(DDSSS)_4$, where D represents double F layers and S single F layers, intercalated with the four vacancy bearing layers. The $(DSSDS)_4$ sequence can be derived via the superspace model of *Izaola et al.* (2007) and is uniform, while the $(DDSSS)_4$ sequence cannot be obtained from the model and has less equally spaced D layers, leading to slightly less order while maintaining the same average vacancy-vacancy distance.

The observed D layer or APB arrangements in EUL are alike the well ordered $(DSSDS)_4$ sequence, while in NYS domains relating to both stacking schemes coexist as indicated by the changes in stripe configuration. Here the domains containing the thicker, non-resolvable stripes may correspond to the $(DDSSS)_4$ stakking in which the closest spacing between D layers or APBs is approx. 0.86 nm and thus more or less equal to the half-width of a single stripe as observed in EUL. The average ~1.72 nm D layer spacing of the idealized $(DSSDS)_4$ sequence compares well with the average stripe and APB spacings in EUL as obtained from

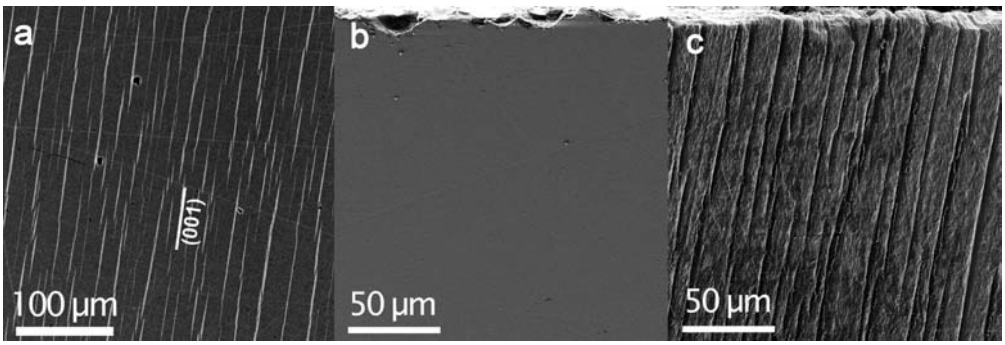

Figure 3: a) BSE image of the TYS sample. Bright lamellae contain 2 wt% more iron than the matrix. b) SE image of the surface of the abiotically reacted pyrrhotite cubes after 40 days which shows almost no dissolution. c) SE image of the pyrrhotite surface reacted with *A. ferrooxidans* after 40 days. Deep trenches formed at the position of the stoichiometric FeS lamellae

SDF images and SAED patterns, respectively, and consistently reproduces the observed slightly non-equal spacings in the bulk NC phase. It appears reasonable to assume that in case of NYS the energetic difference between both arrangements of D layers in the $(DSSDS)_4$ and $(DDSSS)_4$ stacking variants are very small and either the structure is observed on a transition to a more ordered state as in EUL or the elevated Ni content exerts some control on vacancy arrangements.

So far the discussion focused on an idealized layer stacking involving parallel layer arrangements. SDF images clearly shows that this ideal situation is virtually never fulfilled in the studied samples as stripes and therefore APBs are slightly wavy, corrugated and often non-parallel. Changes in stacking schemes at given Nc values as well as disorder introduced by bent APBs will not produce strong effects in SAED patterns. For the $(DSSDS)_4$ and $(DDSSS)_4$ stakking schemes the diffraction pattern geometries will be the same with only moderate differences in spot intensities, likely being hidden by dynamical diffraction effects. Increasing mesoscale disorder of APBs will first lead to vanishing higher order satellite reflections and gradually lead to streaky diffraction along the **c*** direction when a quasi-periodicity is no longer maintained. While a D layer in the ideal layer model is always an APB of the Fe sublattice the converse is not strictly true as isolated APBs are capable of moving more or less freely through the crystal and can have even in the confinement of a modulated structure a much more dynamical behavior as represented by a static layer model. Therefore, describing the layer stacking as a TIM structure of densely arranged APBs offers much better prospects of understanding the behavior and properties of non-integral NC-pyrrhotites.

The need of a more dynamical model clearly becomes apparent when trying to understand the node structures observed at NC/4C phase interfaces. The termination of eight stripes equivalent to eight APBs in a single node is necessary to reconstruct the 4C structure from an NC structure with well ordered V layer stakking. Because the stacking of V layers on the left side strictly obeys the ABCD sequence, the termination creates a sequence fault where two VF layers follow on each other. Consequently, two APBs have to terminate either at a perfect dislocation with $\mathbf{b} = [001]_{NiAs} = 1/4[001]_{4H}$, which removes a pair of VF layers, or 4 pairs of APBs have to terminate close-by such that the eight $1/8[001]_{4H}$ displacement vectors add up to the 4C lattice repeat. Both variants and combinations thereof are seen in our samples and we suggest that the observed node configurations facilitate an energetically most favorable state when there are no or few dislocations involved.

Based on the TIM model we suggest that there is no significant difference between integral and non-integral pyrrhotites and both types

can be understood as part of a continuum of structures in-between Fe_7S_8 and (at least) $Fe_{11}S_{12}$, in which variable Fe contents are governed by changes in densities and ordering states of APBs. Based on the presented data and preliminary data on other natural pyrrhotite samples we currently do not see evidence for preferred stability of integral NC-pyrrhotites in exsolution association with 4C-pyrrhotite, but the true phase relations may be obscured by slow diffusion kinetics below 220 °C, where NC-pyrrhotites first appear (*Nakazawa & Morimoto, 1970*). However, the very sharp compositional gradients at the 4C/NC interfaces in our EUL and NYS samples point to well equilibrated assemblages. Therefore, the association of $N_c \approx 4.85$ pyrrhotite with exsolved 4C-pyrrhotite in two of our samples, as well as the coexistence of $N_c = 4.88$ pyrrhotite and 4C-pyrrhotite observed by *Morimoto et al.* (1975), points to a favored stability of NC-pyrrhotites within the range of $N_c = 4.8$ to 4.9 – at least with regards to typical temperatures of the uppermost crust, where the samples resided for geological timescales.

The insight into complexity in the bulk structure and the applied TIM model can lead to a better understanding of physical properties and the reactivity of surfaces. Due to the rather two dimensional, layer-like structure of pyrrhotites one clear expectation is a pronounced anisotropy of surface properties. Preliminary experimental results indicate that reaction speeds on basal (001) faces are considerably different than on prismatic (*hk0*) surfaces. Owing to pyrrhotite's excessively variable magnetic and physicochemical properties and widespread occurrence in rocks and ore deposits, many potentially important implications to the fields of geomagnetics, petrology, environmental mineralogy, and technical mineral processing (e.g. pyrrhotite flotation) are to be expected when the presented detailed characterization of structures and phase relations is applied.

3. Structural controls on the alteration of pyrrhotite by Acidithiobacillus ferrooxidans under acidic conditons

Based on the detailed characterization procedures described above, a well-directed study on the reactivity of pyrrhotite intergrowth in experiments with acidophilic microorganisms was conducted. Acidophilic microorganisms play a dominant role in acid mine drainage (AMD) and for the metal recovery from low-grade ores by bioleaching applications. A number of studies focused on the reaction paths of chemical and biological metal sulfide oxidation (*Rawlings, 2002; Schippers, 2004*). However, experimental studies on the biologically-enhanced pyrrhotite oxidation are still scarce (see *Belzile et al.* 2004 for review) or focus on bioleaching applications of low grade ores (*Ke & Li, 2006; Jiang et al., 2007*), but clearly indicate the catalytic effect of microorgansms without reporting a reliable characterization of the starting material and dissolution rates. *Schippers et al*. (2007) provides a potential pyrrhotite oxidation rate measured in a mine tailing using microcalorimetry, which suggests that natural rates can exceed laboratory rates by up to 4 orders of magnitude. Beside the enhancing effect of microbial consortia, pyrrhotite dissolution may be also influenced by the reactivity and intergrowth texture of different superstructures. *Janzen et al.* (2000) studied a number of pyrrhotite samples from different localities and determined the relative proportions of so-called monoclinic (mainly 4C) and hexagonal (NC) pyrrhotite. No systematic trend in dissolution rates were found, however, information about the intergrowth texture is missing for these samples.

Acidithiobacillus ferrooxidans, an acidophilic proteobacteria that catalyses the oxidation of ferrous iron, elemental sulfur and reduced sulfur compounds is by far the best characterized bioleaching microorganism and has been used in the presented study. Cells of *A. ferrooxidans* produce an exopolysaccharide (EPS) layer to attach to the sulfide mineral surface (*Gehrke et al., 1998*) and this attachment is viewed as a process by which the bacterial membrane components interact directly with metal and

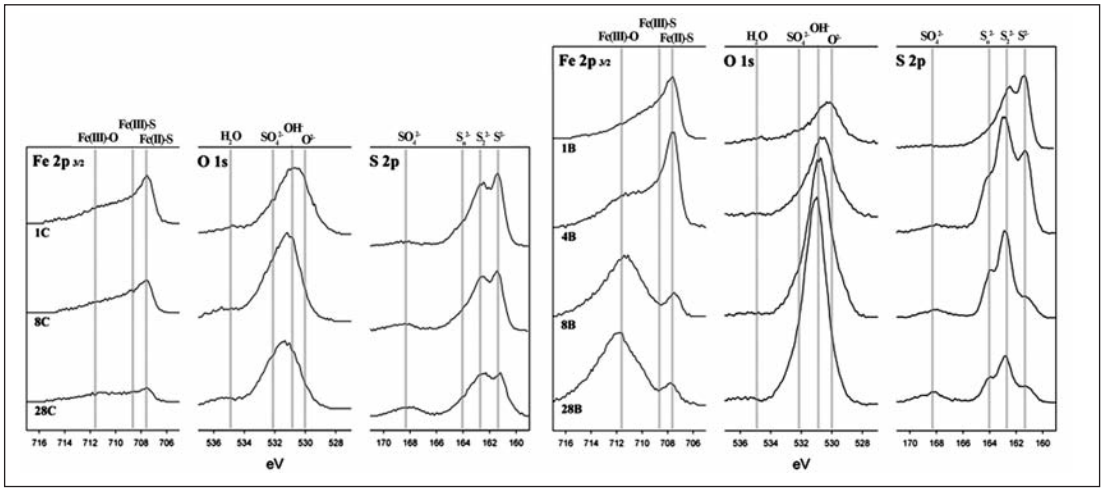

Figure 4: Overlays of the Fe $2p_{3/2}$, O 1*s* and S *2p* narrow region scans of pyrrhotite surfaces abiotic control (left) and biotic (right) experiments. Labels denote the duration of the experiments

sulfur of the mineral by an enzymatic type of mechanism (*Sand et al. 1995*).

In this study X-ray photoelectron spectroscopy (XPS), scanning electron microscopy (SEM), and confocal microscopy have been used to trace the chemical and morphological changes at the surface of a well characterized pyrrhotite sample. Surface topography has employed to quantify a differential dissolution rate between intergrown pyrrhotites.

3.1. Samples and experimental methods

A pyrrhotite from Tysfjord region, Norway (TYS) was used in this study. The TYS sample shows a dense population of 1-3 µm wide exsolution lamellae with a common orientation parallel to (001). They appear brighter in BSE images compared to the matrix indicating a higher Fe/S ratio (Fig. 3a). Quantitative analyses place them close to stoichiometric FeS (troilite). The matrix pyrrhotite of the TYS sample has a composition close to $Fe_{0.900}S$ (or Fe_9S_{10}) with x values of 0.096±0.001 and thus, the lamellae contain about 2 wt% more iron then the matrix.

Polished cubes (3x3x3 mm) of TYS pyrrhotite were dissolved in presence of *Acidithiobacillus ferrooxidans* at pH 2 over 40 days with an abiotic control in parallel. *A. ferrooxidans* ATCC 19859, obtained from the American Type Culture Collection (ATCC, Manassas, VA), was routinely cultivated as a pre-culture in ATCC medium 2039 at 28°C for five days on a rotary shaker (300 rpm). For the inoculation of the experiments 10 µl pre-culture (approx. 2×10^3 cells/ml) was directly used. Cultures for the experiments were grown in 50 ml mineral salt solution with 0.4 g each of $(NH_4)_2SO_4$, K_2HPO_4, and $MgSO_4\times7H_2O$ per liter. Cubes were removed from the batch experiments after 1, 4, 7, 14, 17, 21, 28 and 40 days, respectively.

XPS was performed on a PHI Quantera SXM-03 Scanning XPS Microprobe using an Al Kα X-ray source with a highly focused beam (<9 microns). High resolution scans of the Fe 2p, S 2p, and O 1s peaks were used to determine the bond and valence state information. XPS reference binding energies for pyrrhotite provided by *Legrand et al.* (2005) were used to assign and fit the spectra.

The topography of selected surfaces was measured by the confocal 3D microscopy system µsurf custom (Nanofocus AG, Oberhausen). It consist of a monochromatic LED light source (λ = 505 nm), a helically-shaped arrangement of pinholes (Nipkow-Disk), a stage with piezo module for z movement and a megapixel CCD camera. The objective used (numerical aperture 0.9) provides 160 µm x 160 µm field of view with a resolution of 10 nm in z and about 500 nm in x/y.

3.2. Results

A. ferrooxidans develops a visible biofilm on

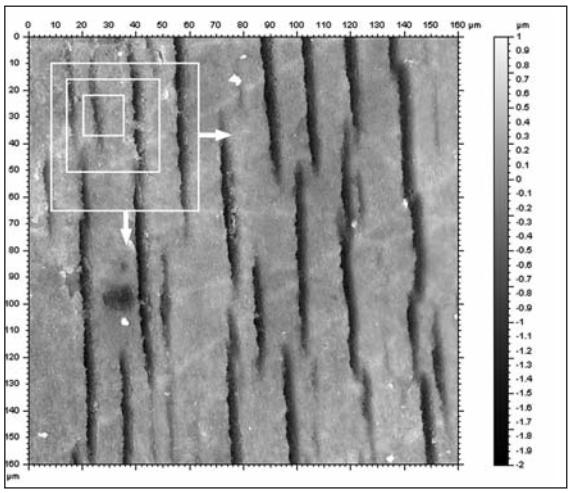

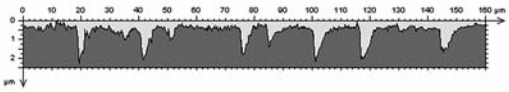

Figure 5: Surface of the TYS sample after biologically-enhanced dissolution measured for 28 days measured by confocal microscopy. The height of the matrix NC-pyrrhotite (~0.5 µm) was used as reference height to determine the differential dissolution rate from the dissolved volume of the 2C-lamellae. The squares illustrate the principle of roughness parameter calculation as function of sampling size performed with ROUGHNECK.
The upper profile clearly shows the non-symmetrical shape of the trenches which is explained by the inclined intersection of the lamellae with the surface

the pyrrhotite cubes after approximately 5 days of incubation. After 9 days the whitish biofilm covered the entire pyrrhotite cubes and grew slowly until the experiment was finally stopped at 40 days. After removing the biofilm by a washing procedure the color has changed to dark blue/black and the reflectivity from shiny to matt. In contrast, the control pyrrhotite cubes (abiotic) were still shiny golden in all experiments with only minor changes in reflectivity. XPS analyses (Fig. 4) reveal a significantly more oxidized surface in the biotic experiment with a clear shift from Fe(II)-S to Fe(III)-O bonding. Compared to the control experiment, the surface is more hydroxylated and shows even traces of sulfate. SEM images (Fig. 3) of the pyrrhotite surface exposed to A. ferrooxidans reveal long and deep trenches which start to develop already after 4 days of experiment. The position of the trenches is identical to the troilite lamellae indicating that the reactivity of the lamellae is significantly higher than the surrounding NC-pyrrhotite. Trenches reach depths of about 2 µm and a width of 3 µm as determined by confocal microscopy measurements after 28 days (Fig. 5). Height profiles suggest that the lamellae are inclined to the dissolving surfaces which lead to the nonsymmetrical shape of trenches. Although information of the original surface height is missing, the 3D topographic data can provide a differential dissolution rate of the 2C-pyrrhotite compared to the NC-pyrrhotite by using the matrix surface as a reference height. Five topographic images taken from surfaces after 21 and 28 days resulted in a differential dissolution rate of $8.8\pm1.2\times10^{-9}$ and $1.2\pm0.3\times10^{-8}$ mol $m^{-2}s^{-1}$, respectively.

3.3. Discussion

The dissolution experiments clearly show the catalyzing effect of microorganisms at conditions that are unfavorable for chemical dissolution. The XPS data indicates a fast and extensive oxidation of the biologically altered surface with dominating of Fe(III)-O bonds as well as some sulfate which points to the formation of a iron hydroxide layer (possibly FeOOH). However, this does not result in a passivation of the surface as indicated by a continuous deepening of the 2C lamellae which possible can be explained by the presence of EPS and a regeneration of ferric iron by the bacteria. For the first time, the clear difference in reactivity between two pyrrhotite superstructure (2C and NC) has been shown by the presented experiments. A direct and an indirect mechanism for biologically-enhanced dissolution have been proposed in the literature. For the direct mechanism, bacteria are attached to the surface surrounded by EPS which provides complexed ferric iron (*Rodriguez-Leiva & Tributsch, 1988*). The indirect mechanism interprets dissolution as an inorganic process where non-attached bacteria only maintain a certain ferric iron concentration which accelerates the dissolution (*Rodriguez et al., 2003*). Whether the difference in dissolution rate is facilitated by a preferred attachment of bacteria due to the different iron content or are caused by diffe-

rences in reactivity of troilite and NC-pyrrhotite alone is not yet been conclusively evaluated and will be subject of further activity. In any case, the lamellar structure of the trenches can not be interpreted as a primary microbial biosignatures because it is originally caused by the exsolution process during equilibration of the pyrrhotite sample and acts like a template during dissolution.

In any case, the differential dissolution rate is already higher than all reported abiotic dissolution rates and highlights the significance of the structural variability and intergrowth texture. When we combine the differential dissolution rate with the only available biotic dissolution rate for pyrrhotite under acidic conditions (8×10^{-9} mol $m^{-2}s^{-1}$) reported in *Belzile et al.* (2004), the resulting net dissolution rate is about one order of magnitude higher than reported rates in the absence of additional ferrous Fe. Further accelerating factors towards the observed rates include the combined effect of bacterial consortia (combinations of iron- and sulfur-oxidizer) as well as the increase of reactive surface area by the deepening of the trenches.

4. From surface morphology to rates: An automated routine to evaluate converged roughness parameters of heterogeneous surfaces

An increase of surface roughness during biologically-enhanced dissolution of pyrrhotite which, in turn, affects the dissolution rate was caused by both the microbial activity and the sample heterogeneity. Two components contribute to the surface roughness evolution of the TYS sample, namely, the alteration of the NC matrix and the deepening of trenches at the 2C lamellae. The high differential dissolution rate may be at least partly explained by increasing surface area. For the presented surfaces (Fig. 5) we are therefore interested in the evolution of surface roughness for the matrix, the lamellae and the combined surface of the biologically dissolved pyrrhotite surface, respectively.

In geosciences, rates are usually determined from dissolution studies (either flow through or batch experiments) using a size fraction of ground and sieved starting material by measuring the change in fluid chemistry as a function of time. The surface area of the starting material is commonly determined by the BET method and used as a constant to normalize rates. Recently, topographic methods have been introduced to directly measure sulfide dissolution rates and surface roughness (*Asta et al., 2008*) and offer new insides into the reaction mechanisms and surface reactivity. Furthermore, it allows a systematic determination of surface roughness parameters.

As statistical quantities roughness parameters are strongly dependent on the field of view of the used technique or the sampling size. The concept of »converged roughness parameter« (*Fischer & Lüttge, 2007*) was shown to be very useful to characterize certain surface building blocks by employing recurrent (squared) bisections of the measuring field with an edge length of a. A surface parameter is defined as converged when a flat slope is found in the convergence graph (roughness parameter versus edge length a). Converged parameters intrinsically depend on the choice of »representative« areas for their analysis. Furthermore, artificial measuring points may lead to an overestimation of roughness parameters. Here, we present the newly developed program ROUGHNECK, which calculates a number of surface roughness parameters from topographic data as function of sampling size allowing to analyze and visualize roughness parameter distributions.

4.1. The program ROUGHNECK

The program ROUGHNECK utilizes the common Surface Data Format (SDF) (*Blunt & Stout, 2001*) as input and output file format and is a stand-alone application that can be used on Windows and Linux systems. Our input files produced by confocal microscopy consist of 984x984 points representing a 160x160 µm field of view. For this study a quality criteria of a minimum of 99% of measured points was used for the topographic data. The residual non-measured points were linearly interpolated. The following 3D roughness parameters are implemented so far: the roughness average S_a, the root-mean-square roughness S_q, the

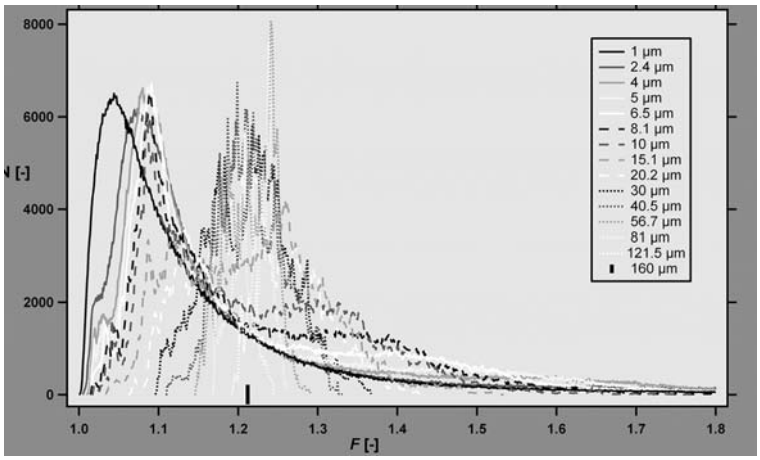

Figure 6: *F* value distributions for various squared sampling areas with a given edge length. With increasing sampling size the maximum of the curves is shifted to higher *F* values. However, the transition from low values around 1.05-1.1 to values around 1.2 is clearly visible and used in the convergence graph (Fig. 7a). For some curves (e.g. *a* = 4 µm) up to 3 maxima can be located indicating the heterogeneity of surface components

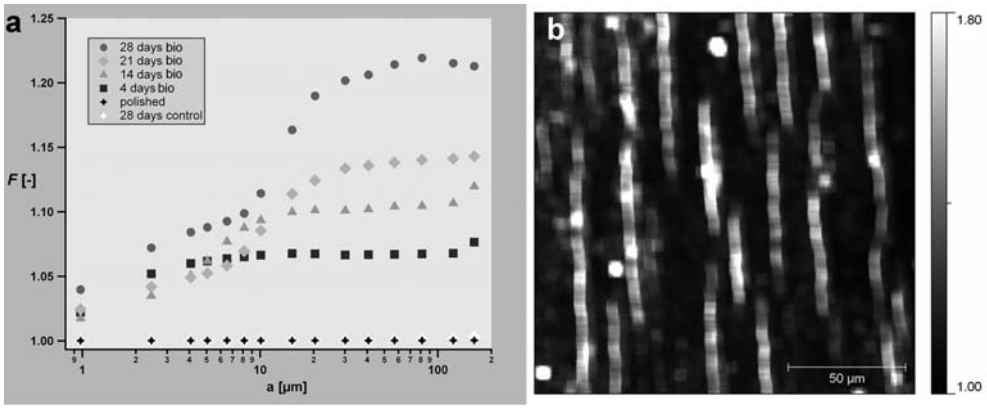

Figure 7: a) Evolution of *F* as function of the edge length of the squared sampling area calculated for fresh and reacted pyrrhotite surfaces. F at larger sampling size (>10 µm) is controlled by the deepening of 2C lamellae. b) Spatial distribution of *F* values for a squared sampling size with edge length *a*=4 µm. High *F* values (~1.6) can be found at the positions of the dissolved 2C lamellae. Since these areas represent only a small portion of the entire field of view, they are not detectable in the histogram. Very high *F* values originate from overlying particles (cf. Fig. 5), but they do not alter the converged roughness parameter determined from the histogram

peak-to-peak height S_z, the ten-point-height S_{10z}, the root-mean-square-gradient S_{dq}, the surface-skewness S_{sk}, the surface-kurtosis S_{ku}, and the surface area ratio F. The program uses freely selectable edge lengths for the desired sampling area, which is moved pixel by pixel over the entire field of view (cf. Fig. 5).

4.2. Evaluation of ROUGHNECK outputs

The surface area ratio, $F=A_{3D}/A_{2D}$, which describes the surface area of a three dimensional surface normalized by the two dimensional (projected) surface, is used as an example parameter to illustrate the statistical procedure. A perfectly flat surface will result in $F=1$, while a rough surface results in $F>1$. This parameter is a so-called hybrid surface parameter because it does not mainly depend on the amplitude but is more sensitive to the high frequency modulations of the surface as it is measured by the slope between adjacent surface points.

ROUGHNECK has been used to calculate the converged F parameters of the biologically dissolved pyrrhotite surface after 28 days (Fig. 5). The distribution of roughness parameters (here frequency *N* vs. *F*) can be plotted as histogram by applying discrete bins (Fig. 6a). The maxima of the distributions show the roughness value for a significant portion of the measured surface. For heterogeneous surfaces, a number of maxima may indicate various components with different surface roughness. In general, the maximum *F* value increases with increasing sampling area. At small scale (*a*=1 to 10 µm),

the first maxima represent only the roughness of the NC pyrrhotite matrix which dissolves slower than the 2C lamellae. At larger scale (*a*=15 to100 µm) the *F* value includes contributions from both because the spacing between the lamellae is smaller than the edge length of the sampling area.

The maxima of each distribution can be translated into a convergence graph plotting the *F* value of the maxima versus the sampling length *a*. Comparing predominant roughness values as a function of time allows to trace the increase in surface roughness of the NC matrix alone (*a*=1 to 10 µm) as well as the evolution of roughness for the entire surface (*a*=15 to100 µm). The output data for every sampling area can also be visualized providing a spatial roughness parameter distribution (Fig. 6b). This is particularly useful if certain surface components, like the locations of the former 2C lamellae, represent only a small portion of the entire surface and are hence not well represented in the histogram. From the roughness distribution image (*a*=4 µm) a roughness parameter for the 2C lamellae of 1.6 can be determined. In turn, this also validates that the roughness parameter distribution (Fig. 6a) is not sensitive for artefacts like overlying particles or inaccurately measured surface points.

5. The reaction pathway of secondary iron sulfide formation under anoxic condition: An experimental study on the reaction of lepidocrocite with dissolved sulfide

AMD waters are typically characterized by high amounts of ferric iron and sulphate. The formation of secondary iron sulfides in the subsurface is an important pathway to reduce the contaminant concentration and to raise the pH of overlying waters (*Bilek, 2006*). In this respect, the interaction between dissolved sulfide and ferric oxides can be regarded as a key reaction leading ultimately to pyrite formation (*Canfield et al., 1992, Poulton et al., 2004*), but knowledge on the pathways and on controlling factors is still limited. Here, results from batch experiments on the reaction between lepidocrocite and dissolved sulfide under anoxic conditions are presented with a special emphasis on the characterization of nanocrystalline products by TEM forming at different time steps.

5.1. Materials, experimental setup and methods

Kinetic batch experiments were conducted by mixing lepidocrocite (25 mmol/L) and different concentrations of dissolved sulfide at room temperature and a constant pH of 7 within an anoxic glove box. After 1-2 hours, 24 hours,

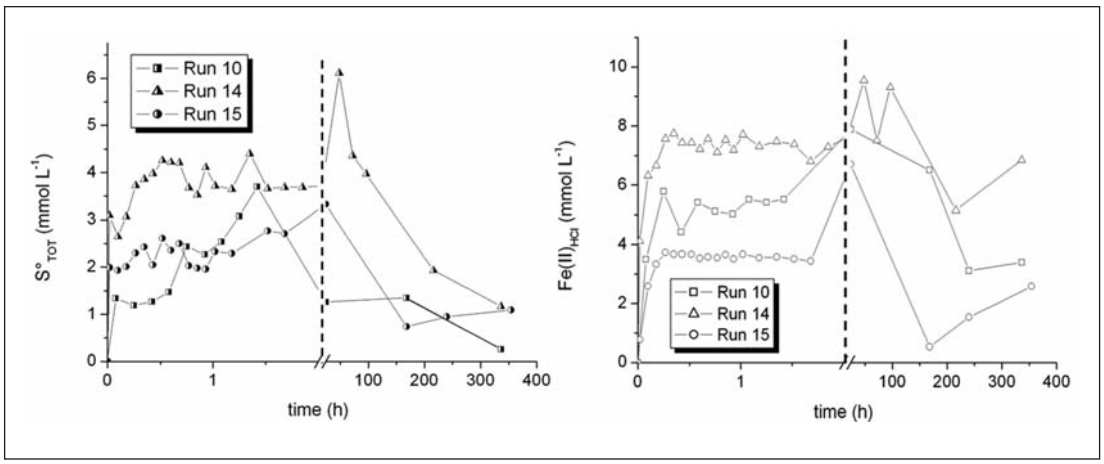

Figure 8: Evolution of elemental sulfur (left) and acid extractable ferrous iron (right) during two weeks of reaction for selected experimental runs. The initial sulfide concentration in run 10 and 14 was twice as the concentration in run 15. Mackinawite formation is rapid within the first hours of the experiments, whereas pyrite formation is relatively slow, starts after 2 days and continued to the end of the run

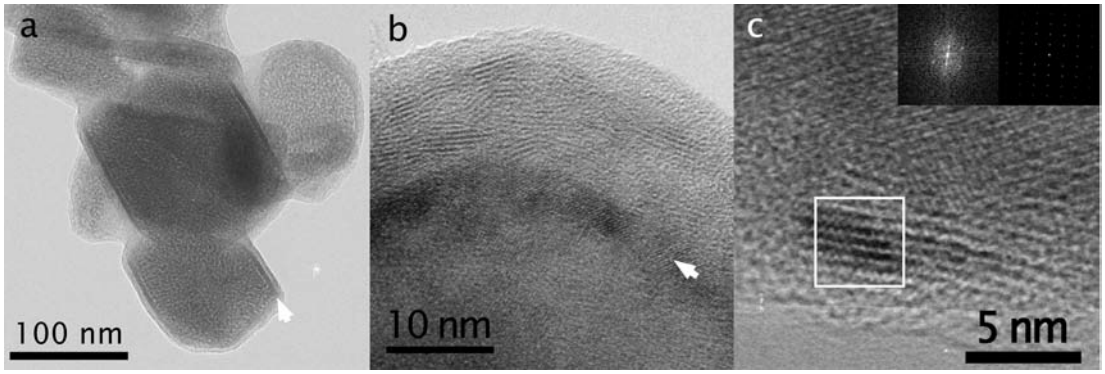

Figure 9: Bright field (a) and high resolution (b,c) TEM images of lepidocrocite crystals with sulfur-rich rims after 2 hours of reaction. The spotted contrast on lepidocrocite grains in (a) is due to nanocrystalline mackinawite. In (b) characteristic (001) and (111) lattice fringes of mackinawite (0.52 and 0.23nm, respectively) are visible in the outer rim. A continuous intermediate layer (arrow) shows fringes matching d_{220} of magnetite/maghemite (arrow). This layer can also be noticed in (a). A nanocrystal of mackinawite in [010] zone axis orientation is shown in (c) together with its calculated FFT and a simulated diffraction pattern as inset

1 week and 2 weeks, respectively, dissolved Fe(II) and S(-II), Fe(II) extractable with 0.5 N HCl, S°, and the total iron content were determined by wet chemistry extraction. At different time steps aliquots of the reacting suspension were analyzed by TEM, XRD and Mössbauer spectroscopy. In order to limit oxidation in air during TEM sample preparation the suspension was first sampled in gas-tight vials. A drop of solution was then taken with a syringe and put onto a Lacey carbon-coated copper grid. The grid was immediately transferred to the TEM holder and inserted into the high vacuum of the TEM. The short exposure of the sample to air can be limited to 1-2 minutes at maximum with this procedure.

5.2. Results

The reaction can be divided into three phases on the basis of wet chemistry (Fig. 8) and TEM observations (Figs. 9 and 10). In the first minutes of the reaction (0-15min) dissolved sulfide is rapidly consumed. It is partly oxidized to S° species in solution and partly consumed by initial mackinawite formation. In a second phase (15-120 min) a continuous but slower formation of S° is observed while acid extractable Fe(II) remained constant. TEM measurements revealed the occurrence of a mackinawite rim covering the lepidocrocite crystals that was separate from the lepidocrocite surface by an interfacial magnetite layer (Fig. 9). The magnetite layer can be seen as an intermediate stage linking two reactions, the formation of mackinawite which reduces ferric iron at the lepidocrocite surface on one hand and the transport of electrons in the deeper regions of the lepidocrocite bulk crystal which facilitates reductive dissolution and mackinawite rim growth and the other hand. The third phase is characterized by a decrease of acid extractable Fe(II) and S° and results in pyrite formation together with some magnetite (2-14 days). TEM measurements indicate that mackinawite completely dissolves from the surface of lepidocrocite while the precipitation of pyrite occurs separately from the lepidocrocite surface. The pyrite formation is coupled to mackinawite dissolution and probably accompanied by the formation of FeS clusters that serve as precursors. The conversion of mackinawite to pyrite was traced by TEM at 72 hours, 1 and 2 weeks. The mackinawite rims get gradually thinner and more corrugated with time. After 48 hours amorphous regions composed of iron and sulfur in variable concentration can be found between lepidocrocite grains. Pyrite grains reach diameters between 200 and 500 nm after 2 weeks and commonly show striking cubic or octahedral outlines (Fig. 10). However, the grains are composed of smaller cubic building blocks which point to a formation by oriented aggregation. In addition to pyrite, some magnetite grains similar in size and shape could be

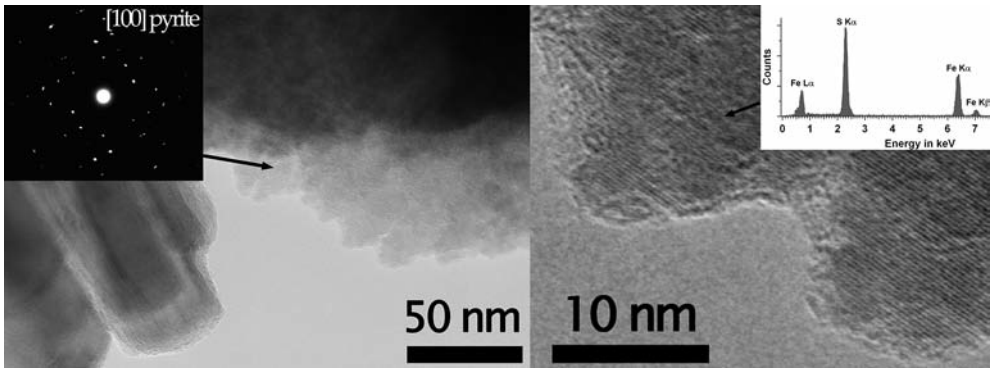

Figure 10: High resolution images, electron diffraction pattern and EDX spectra of pyrite. Note the aggregative nature of the grain consisting of cubic building blocks. Slight misorientations are also reflected in the diffraction pattern

identified by STEM-EDX and electron diffraction as well.

5.3. Discussion

The temporal evolution of the chemical species concentrations and solid phases indicate that the reaction progress is highly dynamic. TEM demonstrates that several phases form during the reaction towards pyrite. On the basis of the observed concentrations a number of balanced chemical equations can be formulated involving sorbed iron species as well as polysulfites. However, it is obvious that the system is kinetically controlled towards chemical equilibration (pyrite formation) due to the slow reductive dissolution process and the redox disproportionation. This study has provided novel insights into the redox processes occurring at the surface and in the vicinity of the lepidocrocite crystals and reveals the occurrence of magnetite and mackinawite in the initial phase of the reaction covering the lepidocrocite surface. It further demonstrates that dissolution of makkinawite occurs prior to formation of pyrite presumably being followed by further reaction with polysulfides in the absence of dissolved sulfide. It has also demonstrated that the kinetics of precursor formation from reductive dissolution of ferric (hydr)oxides by hydrogen sulfide and of subsequent pyrite formation are kinetically decoupled. This observation implies that in iron-rich aqueous systems of periodical sulfide formation (e.g. movement of the capillary fringe in ground waters) ferric oxides may undergo »charging« with reduced substances that may lead to pyrite (and magnetite) formation even in the absence of dissolved sulfide. This reactions sequence has also implications for the retention of toxic metal by adsorption on nanocrystalline mackinawite which may get mobilized by further reaction to pyrite.

6. Conclusion

The most important scientific insights obtained within the MIMOS project are:

(i) A new structural model (TIM model) has been successfully applied to non-stoichiometric NC-pyrrhotite. It well explains important structural details that are observed in electron diffraction patterns and dark-field images and can lead to a better understanding of surface and bulk physical properties of pyrrhotite relevant to geomagnetics, petrology, environmental mineralogy, and technical mineral processing.

(ii) Differences in reactivity caused by small structural and chemical variations have been directly proven for biologically-enhanced dissolution of pyrrhotite. The intergrowth texture has therefore a direct influence on the dissolution rate by a continuous increase of reactive surface area. This result is relevant for the assessment of the weathering rates of pyrrhotite tailings and bioleaching applications.

(iii) The evolution of surface area was quantified by combining topographic data and a

statistical evaluation of surface roughness using the newly developed program ROUGHNECK for heterogeneous surfaces. This approach provides new prospects for mineral dissolution studies as well as for more general topics dealing with surface alteration like corrosion.

(iv) Analytical TEM was successfully applied to tracing the reaction pathway of iron sulfide formation. The new results are relevant for our understanding of processes and element distributions at geochemical boundaries which can help to decipher successful remediation strategies for polluted waters and soils.

References

Amelinckx, S. & Van Dyck, D. (1992) Electron diffraction effects due to modulated structures. Electron diffraction techniques, IUCr/Oxford Science Publications, 2, 309-373.

Asta, M.P., Cama, J., Soler, J.M., Arvidson, R.S. & Lüttge, A. (2008) Interferometric study of pyrite surface reactivity in acidic conditions. Am. Mineral., 93, 508-519.

Becker, M., de Villiers, J. & Bradshaw, D. (2010) The flotation of magnetic and non-magnetic pyrrhotite from selected nickel ore deposits. Miner. Eng., in press, doi:10.1016/j.mineng.2010.07.002

Belzile, N., Chen Y., Cai, M. & Li, Y. (2004) A review on pyrrhotite oxidation. Journal of Geochemical Exploration, 84, 65-76.

Blunt, L. & Stout, K.J. (2001) EC Project Final Report »Development of a Basis for 3D Surface Roughness Standards« SMT4-CT98-2209.

Bilek, F. (2006) Column tests to enhance suphide precipitation with liquid organic electron donators to remediate AMD-influenced groundwater. Environ. Geol., 49, 674-683.

Canfield D. E., Raiswell R. & Bottrell S. (1992) The reactivity of sedimentary iron minerals toward sulphide. Am. J. Sci., 292, 659-683.

Church, C.D., Wilkin, R.T., Alpers, C.A., Rye, R. O. & McCleskey, R.B. (2007) Microbial sulfate reduction and metal attenuation in pH 4 acid mine water. Geochem. Transac., doi:10.1186/1467-4866-8-10.

Ekmekçi, Z., Becker, M., Bagci Tekes, E. & Bragshaw, D. (2010) An impedance study of the adsorption of CuSO4 and SIBX on pyrrhotite samples of different provenances. Miner. Eng., in press, doi:10.1016/j.mineng.2010.02.007

Fischer, C. & Lüttge, A. (2007) Converged surface roughness parameters – A new tool to quantify rock surface morphology and reactivity alteration. Am. J. Sci. 2007, 307, 955-973.

Gehrke, T., Telegdi, J., Thierry, D. & Sand, W. (1998) Importance of extracellular polymeric substances from Thiobacillus ferrooxidans for bioleaching. Appl. Environ. Microbiol., 64, 2743 – 2747.

Izaola, Z., Gonzalez, S., Elcoro, L., Perez-Mato, J.M., Madariaga, G. & Garcia, A. (2007) Revision of pyrrhotite structures within a common superspace model. Acta Cryst. B, 63, 693-702.

Janzen, M.P., Nicholson, R.V. & Scharer, J.M. (2000) Pyrrhotite reaction kinetics: reaction rates for oxidation by oxygen, ferric iron, and for nonoxidative dissolution. Geochim. Cosmochim. Acta 64, 1511 –1522.

Jiang, L., Zhou, H.Y. & Peng, X.T. (2007) Bioxidation of pyrite, chalcopyrite and pyrrhotite by Acidithiobacillus ferrooxidans. Chin. Sci. Bull., 52, 2702-2714.

Ke, J. & Li, H. (2006) Bacterial leaching of nikkel-bearing pyrrhotite. Hydrometallurgy, 82, 172-175.

Legrand, D.L., Bancroft, G.M. & Nesbitt, H.W. (1995) Oxidation/alteration of pentlandite and pyrrhotite surfaces at pH 9.3: Part 1. Assignment of XPS spectra and chemical trends. Am. Min., 90, 1042-1054.

Morimoto, N., Gyobu, A., Tsukuma, K. & Koto, K. (1975) Superstructure and nonstoichiometry of intermediate pyrrhotite. Am. Min., 60, 240-248.

Nakazawa, H. & Morimoto, N. (1970) Pyrrhotite phase relations below 320°C. Proc. Japan Acad., 46, 678-683.

Nicholson, R.V. & Scharer, J.M. (1994): Laboratory studies of pyrrhotite oxidation kinetics. In: Environmental geochemistry of sulfide oxidation. Alpers C.N., Blowes D.W. (eds.), .ACS Symp. Series 550, 14-30.

Ohfuji, H. & Rickard, D. (2006) High resolution transmission electron microscopic study of synthetic nanocrystalline mackinawite. Earth and Planetary Science Letters, 241, 227-233.

Pierce, L. & Buseck, P.R. (1974) Electron imaging of pyrrhotite superstructures. Science, 186, 1209-1212.

Pollok, K., Langenhorst, F., Hopf, J., Kothe, E., Geisler, T., Putnis, C.V. & Putnis, A. (2008) Microstructural Controls on Monosulfide Weathering and Heavy Metal Release (MIMOS), GEOTECHNOLOGIEN Science Report, 12, 79-88.

Poulton S.W., Krom, D.M. & Raiswell R. (2004) A revised scheme for the reactivity of iron (oxyhydr)oxide minerals towards dissolved sulfide. Geochim. Cosmochim. Acta, 68, 3703-3715.

Rawlings, D.E. (2002) Heavy metal mining using microbes. Annual Reviews in Microbiology, 56, 65–91.

Rodriguez, Y., Ballester, A., Blazquez, M. A. & Munoz, J. A. (2003) Study of bacterial attachment during the bioleaching of pyrite, chalcopyrite and sphalerite. Geomicrobiol. J. 20, 131–141.

Rodriguez-Leiva, M. & Tributsch, H. (1988) Morphology of bacterial leaching patterns by Thiobacillus ferrooxidans on synthetic pyrite. Arch. Microbiol. 149, 401–405.

Sand W., Gehrke, T., Hallman, R. & Schippers, A. (1995) Sulfur chemistry, biofilm, and the (in)direct attack mechanism – a critical evaluation of bacterial leaching. Appl. Microbiol. Biotechnol., 43, 961-966.

Schippers, A. (2004) Biogeochemistry of metal sulfide oxidation in mining environments, sediments and soils. In:Amend, J.P., Edwards, K.J., Lyons, T.W. (Eds.), Sulfur Biogeochemistry—Past and Present. Special Paper, vol. 379. Geological Society of America, Boulder, Colorado, pp. 49-62.

Schippers, A., Kock, D., Schwartz, M., Böttcher, M.E., Vogel, H. & Hagger, M. (2007) Geomicrobiological and geochemical investigation of a pyrrhotite-containing mine waste tailings dam near Selebi-Phikwe in Botswana. J. Geochem. Expl., 92, 151-158.

Yamamoto, A. & Nakazawa, H. (1982) Modulated structure of the NC-type (N = 5.5) pyrrhotite, Fe1-xS. Acta Cryst. A, 38(1), 79-86.

Author's Index

V

W

Y

Z

GEOTECHNOLOGIEN Science Reports – Already published/Editions

No. 1 Gas Hydrates in the Geosystem – Status Seminar, GEOMAR Research Centre Kiel, 6–7 May 2002, Programme & Abstracts, 151 pages.

No. 2 Information Systems in Earth Management – Kick-Off-Meeting, University of Hannover, 19 February 2003, Projects, 65 pages.

No. 3 Observation of the System Earth from Space – Status Seminar, BLVA Munich, 12–13 June 2003, Programme & Abstracts, 199 pages.

No. 4 Information Systems in Earth Management – Status Seminar, RWTH Aachen University, 23–24 March 2004, Programme & Abstracts, 100 pages.

No. 5 Continental Margins – Earth's Focal Points of Usage and Hazard Potential – Status Seminar, GeoForschungsZentrum (GFZ) Potsdam, 9–10 June 2005, Programme & Abstracts, 112 pages.

No. 6 Investigation, Utilization and Protection of the Underground – CO_2-Storage in Geological Formations, Technologies for an Underground Survey Areas – Kick-Off-Meeting, Bundesanstalt für Geowissenschaften und Rohstoffe (BGR) Hannover, 22–23 September 2005, Programme & Abstracts, 144 pages.

No. 7 Gas Hydrates in the Geosystem – The German National Research Programme on Gas Hydrates, Results from the First Funding Period (2001–2004), 219 pages.

No. 8 Information Systems in Earth Management – From Science to Application, Results from the First Funding Period (2002–2005), 103 pages.

No. 9 1. French-German Symposium on Geological Storage of CO_2, Juni 21./22. 2007, GeoForschungsZentrum Potsdam, Abstracts, 202 pages.

No. 10 Early Warning Systems in Earth Management – Kick-Off-Meeting, Technical University Karlsruhe, 10 October 2007, Programme & Abstracts, 136 pages.

No. 11 Observation of the System Earth from Space – Status Seminar, 22–23 November 2007, Bavarian Academy of Sciences and Humanities, Munich, Programme & Abstracts, 194 pages.

No. 12 Mineral Surfaces – From Atomic Processes to Industrial Application – Kick-Off-Meeting, 13–14 October 2008, Ludwig-Maximilians Universtität, Munich, Programme & Abstracts, 133 pages.

No. 13 Early Warning Systems in Earth Management – Status Seminar, 12–13 October 2009 Technische Universität München, Programme & Abstracts, 165 pages.

No. 14 Die dauerhafte geologische Speicherung von CO_2 in Deutschland – Aktuelle Forschungsergebnisse und Perspektiven, Herausgegeben von: Ludwig Stroink, J. Peter Gerling, Michael Kühn, Frank R. Schilling, 140 Seiten.

No. 15 Early Warning Systems for Transportation Infrastructures, Workshop 9-10 February 2009, Fraunhofer IITB Karlsruhe, Karlsruhe Institute of Technology (KIT), 160 p.

Mineral Surfaces – From Atomic Processes to Industrial Application

In the frame of the R&D-programme GEOTECHNOLOGIEN thirteen joint interdisciplinary projects have been launched in April 2008. The object of research is the better understanding of the multiple physical and chemical reactions at mineral surfaces. The abstract volume summarizes the scientific results presented during the status seminar at the Johannes Gutenberg University in Mainz, Germany in October 2010.

Research activities focus on different applications of geomaterials:

– reactions on external and internal interfaces (e. g., immobilization of toxic elements/compounds and radioactive irradiated phases) and bio-mineralization such as biomimetic functional materials as well as bone implants.

– development of high technology and its applications for the exploration of the Earth's interior on the one hand and the synthesis of new materials (e. g. deformation hardening, ultra hard phases) on the other.

Bundesministerium für Bildung und Forschung

DFG

The GEOTECHNOLOGIEN programme is funded by the Federal Ministry for Education and Research (BMBF) and the German Research Council (DFG)

ISSN: 1619-7399